

148

(NASA-CR-126753) SOLAR SYSTEM APPLICATIONS  
OF MIE THEORY AND OF RADIATIVE TRANSFER OF  
POLARIZED LIGHT L.P. Whitehill (Cornell  
Univ.) Mar. 1972 293 p

CSCL 20F

31

N72-25624

G3/23 15508

Unclas

DRA

# CORNELL UNIVERSITY

*Center for Radiophysics and Space Research*

ITHACA, N. Y.

[REDACTED]

Reproduced by  
NATIONAL TECHNICAL  
INFORMATION SERVICE  
U S Department of Commerce  
Springfield VA 22151

[REDACTED]

CENTER FOR RADIOPHYSICS AND SPACE RESEARCH  
CORNELL UNIVERSITY  
ITHACA, NEW YORK

March 1972

CRSR 483

SOLAR SYSTEM APPLICATIONS OF MIE  
THEORY AND OF RADIATIVE TRANSFER  
OF POLARIZED LIGHT

Laird Peter Whitehill

## BIOGRAPHICAL SKETCH

The author was born on Manhattan Island on January 16, 1945. He went to school there until he was 20 years old, attending Stuyvesant High School and Columbia University School of Engineering where he received a Bachelor of Science in Electrical Engineering in June 1965. While at Columbia he was honored as a Deans Scholar and by his election to Eta Kappa Nu and Tau Beta Pi. He entered graduate school at Cornell University in September 1965 where he studied astronomy graduating in May 1972.

## ACKNOWLEDGEMENTS

I wish to express my deep gratitude to Dr. Carl Sagan whose interest, guidance, and financial and moral support were indispensable in the successful execution of this work. I would also like to thank Dr. James Pollack for the many hours that he worked with me and the considerable physical insight that he shared with me.

I am grateful to Dr. T. G. Northrup of the NASA Space Flight Center in Greenbelt, Md. for the computer time used to run the large programs of the thesis and to Dr. James Hansen of the Goddard Institute for Space Studies in New York City who was instrumental in the development of the doubling program. I wish to thank them both for their encouragement and hospitality during my visits.

I thank Dr. G.S.S. Ludford for serving on my special committee and Dr. M.J. Campbell for the impetus he provided the lunar radar depolarization model.

Mrs. B. Boettcher prepared the numerous graphs; Mrs. M. Wanlass and Mrs. M. Szymanski typed a portion of the thesis; Mr. K. Perine helped key punch graphical data. I thank them for their help.

This research was supported in part by NASA NGR 33-010-101, NASA NGR 33-101-082, by the Atmospheric Sciences Section, National Science Foundation under Grant GA-23945 and by a NASA traineeship.



## TABLE OF CONTENTS

### Part I

#### MULTIPLE SCATTERING OF POLARIZED LIGHT BY ANISOTROPICALLY SCATTERING SPHERICAL PARTICLES IN A PLANE PARALLEL MEDIUM OF ARBITRARY OPTICAL THICKNESS-THEORY

	<u>page</u>
I Scattering from a Single Particle-The Stokes Parameters	2
II Reflection and Transmission Matrices from a Single Scattering Layer and their Symmetry Properties	21
III Reflection and Transmission Matrices from a Multiple Scattering Layer--The Doubling Method	26
IV The Doubling Equations--Fourier Components and Symmetry Properties	32
V Elimination of Unnecessary Computations through the use of Symmetry Relations	47
VI A Collage of Time Saving Devices	51

### Part II

#### THEORETICAL CALCULATIONS OF DISK INTEGRATED AND DISK RESOLVED POLARIZATION OF PLANETARY ATMOSPHERES

	<u>page</u>
I Introduction	59
II Polarization as a Function of Position on a Planetary Disk-Theory	62
III Polarization and Intensity Integrated over the Disk of a Planet-Theory	70
IV Regional and Disk Integrated Polarization-Results	77
1. Accuracy	78
2. Results	80
A. The Rayleigh Phase Matrix	80

Table of Contents (cont'd)

	<u>page</u>
B. A Forward Scattering Non-Rayleigh Phase Matrix	114
C. Venus at 1 Micron Wavelength	132
a. Theory	132
b. Comparison with Observations	137
V Localized Polarimetric Observations of Jupiter and Venus--Discussion	153
1. Jupiter	154
2. Venus	157

Part III

RADAR OBSERVATIONS OF THE MOON AND THEIR INTERPRETATION:  
A MULTIPLE SCATTERING APPROACH

	<u>page</u>
I Introduction	168
II The Observations and Previous Interpretations	173
1. Cross Section	174
2. Delay Measurements	183
3. Delay Doppler Measurements	187
4. Discrete Model vs. Homogeneous Model	194
III The Difference between the Single Scattering Model and Reality and its Influence on the Multiple Scattering Results	197
IV Single Scattering-Calculations	205
V Scattering Matrix for Buried Rocks	209
VI Scattering Matrix for a Crater	216
VII The Matrix Elements and the Radar Experiments	224
VIII The Angular Variables-Observations and Calculations Compared	229

Table of Contents (cont'd)

	<u>page</u>
IX The Single Scattering Albedo-The Pivotal Point of the Model	259
X The Total Diffuse Cross Section of the Moon	270
1. Diffuse Cross Section-Theory	270
2. The Fresh Crater Distribution Function	273
3. The Total Diffuse Cross Section	277
4. The Wavelength Dependence	279
5. Maria-Highland differences and Implications for Future Radar Experiments	283

## Part I

# MULTIPLE SCATTERING OF POLARIZED LIGHT BY ANISOTROPICALLY SCATTERING SPHERICAL PARTICLES IN A PLANE PARALLEL MEDIUM OF ARBITRARY OPTICAL THICKNESS-THEORY

### Abstract

A theory of the multiple scattering of polarized light is described using the doubling method of van de Hulst. The concept of the Stokes parameters is derived and used to develop the form of the scattering phase matrix of a single particle. The diffuse reflection and transmission matrices of a single scattering plane parallel atmosphere is expressed as a function of the phase matrix and the symmetry properties of these matrices are examined. Four matrices are required to describe scattering and transmission instead of the usual two as in intensity only theory. The scattering matrix that results from the addition of two identical layers is derived. By this doubling method the scattering and transmission matrices of layers of arbitrary optical thickness can be derived. The doubling equations are then rewritten in terms of their fourier components. Computation time is reduced since each fourier component doubles independently. Computation time is also reduced through the use of symmetry properties as well as by other methods discussed.

## I Scattering from a Single Particle - The Stokes Parameters

In this section we will develop a method to fully describe the state of polarization of an arbitrarily polarized parallel beam of light. We shall show how to represent the scattering from a single particle in terms of the Stokes matrix and the Stokes vector. Some physical insights into the meaning of the Stokes vector shall also be developed. In the interests of brevity many results and theorems on polarized light will not be proved, since they are the result of the work of others. The reader is referred to Chandrasekhar's<sup>1</sup> book, Radiative Transfer (herein abbreviated R.T.), for further discussion of some points.

An arbitrary beam of light can be regarded as a mixture of a completely polarized beam and a completely unpolarized independent beam. We mean by unpolarized and independent that the electric fields, resolved along two perpendicular vectors normal to the direction of propagation, that is, in the transverse plane, will show no permanent phase correlations with each other and will have equal amplitudes. The perpendicular electric vectors of the polarized beam, while having no permanent phase, do retain a permanent phase difference  $\delta$ .

Let  $\alpha$  and  $\beta$  be the time varying uncorrelated phases of the electric fields of the unpolarized beam. Let "l" and "r" refer to directions parallel and perpendicular respectively to a plane, as yet unspecified, which contains the direction of propagation.

These directions then lie in the plane transverse to the direction of propagation. The sense of the two unit vectors  $\hat{e}_1$  and  $\hat{e}_r$  is chosen such that  $\hat{e}_r \times \hat{e}_1$  is in the direction of propagation. Then the beam may be represented by the real part of the complex electric vector  $\hat{E}(t)$ .

$$\hat{E}(t) = \hat{E}_r(t)\hat{e}_r + \hat{E}_1(t)\hat{e}_1$$

1.1

$$= (E_r e^{i\delta} + E_u e^{i\alpha}) e^{i\omega t} \hat{e}_r + (E_1 + E_u e^{i\beta}) e^{i\omega t} \hat{e}_1$$

$E_v$  is the amplitude of the unpolarized component of the electric field. The symbol  $\hat{\phantom{x}}$  means a complex quantity and  $*$  will mean complex conjugate.

The four quantities  $E_r$ ,  $E_1$ ,  $E_u$  and  $\delta$  determine the state of polarization. Because of their unsymmetric nature, another set of quantities is preferred. These are a set of parameters similar to a set introduced by Sir George Stokes in 1852. They form a representation commonly called the Stokes vector

$$\bar{I} = [I_1, I_r, U, V]$$

The meaning of these four quantities is next defined. In what follows the symbol  $\langle \rangle$  means the time average of the quantity within the brackets. Thus for example  $\langle e^{i\alpha} \cdot e^{i\beta} \rangle = 0$  and  $\langle \hat{E}_1 \cdot \hat{E}_u e^{i\alpha} \rangle = 0$ . Then

$$I_1 \equiv \langle \hat{E}_1 \cdot \hat{E}_1^* \rangle = E_1^2 + E_u^2$$

1.2

$$I_r \equiv \langle \hat{E}_r \cdot \hat{E}_r^* \rangle = E_r^2 + E_u^2$$

$$U \equiv 2\text{Re}\langle \hat{E}_r \cdot \hat{E}_1^* \rangle = 2E_1 E_r \cos \delta$$

1.2

$$V \equiv 2\text{Im}\langle \hat{E}_r \cdot \hat{E}_1^* \rangle = 2E_1 E_r \sin \delta$$

Care must be taken in the sign of  $V$  as a minus sign can easily be mislaid. Here  $\delta$  is the amount that  $\hat{E}_r$  leads  $\hat{E}_1$  when viewed against the direction of propagation.

An alternate set of Stokes parameters is the set  $[I, Q, U, V]$ . They are related to the previous set by the relations:

$$I = I_1 + I_r$$

$$Q = I_1 - I_r$$

They will be used interchangeably with the first set whenever they will help simplify an expression. The first set, however, will be preferred in the equations we shall see later.

Some discussion of the physical meaning of the Stokes parameters at this time would be in order. Assume that the beam is completely polarized. Then  $E_u$  is zero. The end point of the electric vector

$$\hat{E}(t) = (E_r e^{i(\delta + \omega t)})\hat{e}_r + E_1 e^{i\omega t}\hat{e}_1$$

sweeps out an ellipse in space, figure 1.1. The ellipse is tilted by an angle  $\chi$ , which is sometimes referred to as the plane of polarization.  $\chi$  is positive when measured clockwise from  $\hat{e}_1$ ,  $\tan 2\chi = U/Q$ . Note also that for a fully polarized beam  $I^2 = Q^2 + U^2 + V^2$ .

The ratio of the semimajor axes of the ellipse,  $\tan \beta$ ,

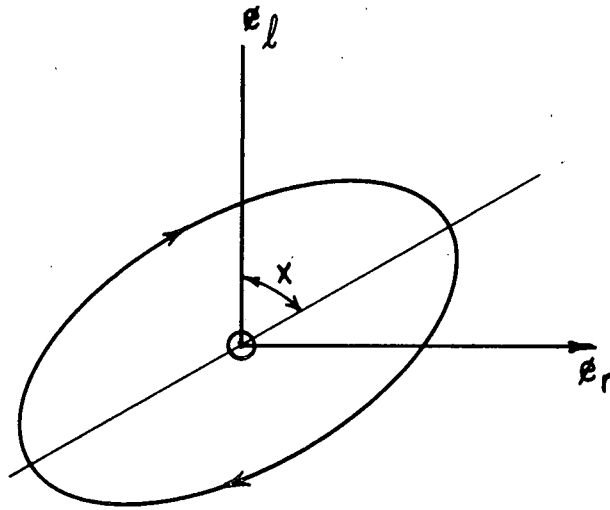


Figure 1.1 Elliptical polarization.

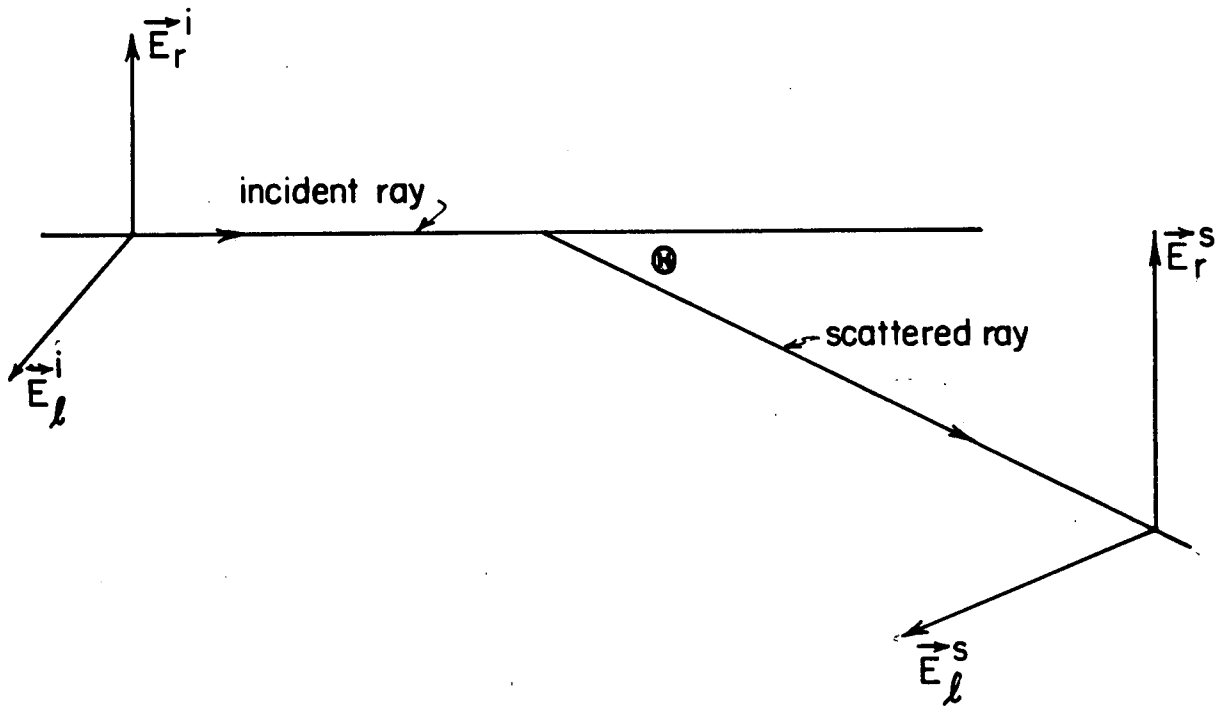


Figure 1.2 The scattering event in the coordinate system of the scattering plane.



is given by

$$\sin 2\beta = \frac{V}{\sqrt{Q^2 + U^2 + V^2}}$$

See R.T. p25-28 for derivation.

For natural, unpolarized, light  $Q = U = V = 0$ . Complete linear polarization occurs when  $I = \pm Q$  and  $U = V = 0$ . Complete circular polarization occurs when  $\hat{E}_r$  leads or lags  $\hat{E}_l$  by  $90^\circ$  and there is no unpolarized component. Then  $I = \pm V$  and  $Q = U = 0$ . The polarization is right handed or left handed as the sign of  $V$  is positive or negative respectively. Right handed polarization means that when viewed against the direction of propagation the electric vector turns in a clockwise direction.

The previous relations were skipped over rather quickly without any derivation. They are useful relations but the mathematics necessary to derive them is not worth repeating as they can be found in the references cited. Of more importance to later work is some physical rather than mathematical insight into the Stokes parameters. It is already apparent, because of the representation chosen that  $Q$  represents the excess of parallel over perpendicular linearly polarized light. It is less obvious that both  $U$  and  $V$  lend themselves to the same kind of interpretation.

If we chose 2 new perpendicular axes "q" and "p" rotated  $45^\circ$  from "l" and "r" then it can be shown that  $U$  is the excess of "q" over "p" linearly polarized light.  $V$ , as we shall show, is the excess of right handed over left handed circularly polarized light.

To do this we chose a new set of unit vectors to replace those of equation 1.1. If we choose  $\delta = \pi/2$ ,  $E_o = E_r = E_l$ ,  $E_u = 0$ , then  $V = I$ ,  $U = Q = 0$  and we have a right handed circularly polarized beam  $E_o(\phi_l + i\phi_r)e^{i\omega t}$ . This leads us to the choice of 2 new unit vectors  $\phi_+$  and  $\phi_-$  defined by

$$\phi_{\pm} = \frac{\phi_l \pm i\phi_r}{\sqrt{2}}.$$

In terms of these new basis vectors we may represent an arbitrarily polarized beam in an alternate way

$$\begin{aligned} \hat{E}(t) = & (E_+ e^{i\delta} + E_- + E_u(e^{i\alpha} + e^{i\beta}))e^{i\omega t}\phi_l \\ 1.3 \quad & + i(E_+ e^{i\delta} - E_- + E_u(e^{i\alpha} - e^{i\beta}))e^{i\omega t}\phi_r. \end{aligned}$$

This also allows circular and linear representations to be interrelated.

Now from equation 1.2,

$$\begin{aligned} V &= 2\text{Im}\langle \hat{E}_r \cdot \hat{E}_l^* \rangle \\ &= E_+^2 - E_-^2. \end{aligned}$$

Thus we see  $V$  is the amount by which right handed circular polarization exceeds left handed circular polarization.

Now let us describe the transformation of the Stokes parameters due to scattering off a single spherical particle.

Consider a parallel beam of light having an arbitrary state of polarization incident on the particle. The situation is shown in figure 1.2.

Now we define "r" and "l" to be directions perpendicular and parallel to the scattering plane defined by incident ray

"i" and scattered ray "s".  $\theta$  is the scattering angle and is zero for undeflected light.

For spherical particles the transformation properties of the scattering process can be described in terms of electric fields by

$$1.4 \quad \begin{pmatrix} \hat{E}_1^s(\theta) \\ \hat{E}_r^s(\theta) \end{pmatrix} = \begin{pmatrix} \hat{A}_1(\theta) & 0 \\ 0 & \hat{A}_2(\theta) \end{pmatrix} \begin{pmatrix} \hat{E}_1^i \\ \hat{E}_r^i \end{pmatrix}$$

$\hat{A}_1$  and  $\hat{A}_2$  are complex function of  $\theta$  having no time dependence. The off diagonal terms are zero only for particles having spherical symmetry. For any other type of particle they are not zero. Spherical particles rarely occur in nature, but unfortunately we cannot easily calculate these four quantities unless we assume the particles are spherical. This will be assumed in all that follows.

We will now derive the transformation matrix for the Stokes parameters thus putting equation 1.4 in a more facile form. From the definitions in equation 1.2 we have

$$\begin{aligned} I_1^s &= \langle \hat{E}_1^s \cdot \hat{E}_1^{s*} \rangle = (\hat{A}_1 \cdot \hat{A}_1^*) I_1^i \\ I_r^s &= \langle \hat{E}_r^s \cdot \hat{E}_r^{s*} \rangle = (\hat{A}_2 \cdot \hat{A}_2^*) I_r^i \\ U^s &= 2\text{Re} \langle \hat{E}_r^s \cdot \hat{E}_1^s \rangle \\ &= \text{Re}(\hat{A}_2 \cdot \hat{A}_1^*) U^i - \text{Im}(\hat{A}_2 \cdot \hat{A}_1) V^i \\ V^s &= 2\text{Im} \langle \hat{E}_r^s \cdot \hat{E}_1^{s*} \rangle \\ &= \text{Im}(\hat{A}_2 \cdot \hat{A}_1^*) U^i + \text{Re}(\hat{A}_2 \cdot \hat{A}_1) V^i \end{aligned}$$

This follows from the following easily deriveable identities:

$$\text{Re}(\hat{X} \cdot \hat{Y}) = \text{Re}(\hat{X})\text{Re}(\hat{Y}) - \text{Im}(\hat{X})\text{Im}(\hat{Y})$$

$$\text{Im}(\hat{X} \cdot \hat{Y}) = \text{Im}(\hat{X})\text{Re}(\hat{Y}) + \text{Re}(\hat{X})\text{Im}(\hat{Y}) \quad .$$

We can now write down the transformation law that describes the changes in the stokes vector of the outgoing wave due to the scattering from a single spherical particle:

$$\begin{matrix} & \bar{\mathbf{I}}^S = \bar{\mathbf{P}}(\theta) \cdot \mathbf{I}^i \\ 1.5 \quad \begin{pmatrix} I_1^S \\ I_r^S \\ U^S \\ V^S \end{pmatrix} = & \begin{pmatrix} P_1 & 0 & 0 & 0 \\ 0 & P_2 & 0 & 0 \\ 0 & 0 & P_3 & -P_4 \\ 0 & 0 & P_4 & P_3 \end{pmatrix} & \begin{pmatrix} I_1^i \\ I_r^i \\ U^i \\ V^i \end{pmatrix} \end{matrix}$$

where

$$P_1(\theta) = \hat{A}_1 \cdot \hat{A}_1^*$$

$$P_2(\theta) = A_2 \cdot A_2^*$$

$$P_3(\theta) = \text{Re}(\hat{A}_2 \cdot \hat{A}_1^*)$$

$$P_4(\theta) = \text{Im}(\hat{A}_2 \cdot \hat{A}_1^*) \quad .$$

These functions,  $P_i(\theta)$ , are also functions of the real and imaginary parts of the index of refraction, the size of the particle and the wavelength of observation. They were produced by a Mie program written by J. V. Dave<sup>2</sup> which is available upon request from I.B.M. We defer until later a discussion of Mie theory since it would interrupt the development we have started.

At this point however it is useful to change our point of view from single scattering on a single particle to single scattering on many particles. In the computer program that parallels this theoretical development we use for  $P_i$  the Stokes matrix elements averaged over a poly-dispersion of particles.

In doing this we make many assumptions. The spherical particle is replaced with a spherical volume element large enough to contain a statistically homogeneous collection of particles which perform random motions in time scales short enough so that there are no permanent phase correlations in the radiation scattered off the various particles during the period of observation.

Otherwise the scattering theory would have to be expressed in terms of the complex amplitudes  $\hat{A}_1$  and  $\hat{A}_2$  instead of the intensity coefficients  $P_1$ . In the case of scattering from stationary objects such as radar return from boulders on the moon the above assumption does not hold. In this case, however, the use of intensities rather than complex amplitudes can be justified by introducing an ensemble average over a small portion of the surface. Then if the surface moves, i.e. a rotating planet, the procession of the scattering elements across the line of sight is equivalent to a time average that can by the application of ergodicity, be set equal to the average over the distribution of scatterers. R. Ruffine<sup>3</sup> has shown that replacing time averages with ensemble averages results in an error of less than 10% for the radar cross sections predicted for 600 sec integrations of the radar return. The error in the measurements will generally be higher for the applications we shall have since instrumental calibration of the radar is only good generally to  $\pm 3$  db.

We implicitly make some further assumptions as to the character of the spherical volume element. We assume that we can

take the volume large enough to encompass a statistically representative sample of particles, yet small enough so that there is no difference in intensity or polarization between light illuminating the front and rear hemispheres. When we begin discussing multiple scattering we will also assume the particles are far enough apart so that each particle is illuminated by plane waves. These properties are hard to realize in practice but scattering theory generally gives good results in spite of this.

So far in our discussion we have referred the Stokes matrix to a set of axes defined by the scattering plane, the plane formed by the incident and scattered rays. But the scattering plane has no particular orientation in space and changes for successive scattering events. We will need to describe the scattering event in terms of a fixed coordinate system, independent of the scattering plane. To that end we will need a law for rotation of the axes about the direction of propagation.

Assume that the axes along which we measure the polarization properties has been rotated in the clockwise direction by an angle  $\phi$ , figure 1.3.

Note that in figure 1.3 the direction of propagation is out of the page. This is the convention we shall use, that is, the Stokes parameters will always be referred to propagation towards the observer.

The rotational transformation for the electric fields now



becomes

$$1.6 \quad \begin{pmatrix} \hat{E}_x \\ \hat{E}_y \end{pmatrix} = \begin{pmatrix} \cos \phi & \sin \phi \\ -\sin \phi & \cos \phi \end{pmatrix} \begin{pmatrix} \hat{E}_l \\ \hat{E}_r \end{pmatrix}$$

since  $\hat{E}$  is a spacial vector.

We will now derive the rotational transformation for the Stokes vector. Writing equation 1.2 in terms of the new axes X and Y we have

$$1.7 \quad \begin{aligned} I_x &= \langle \hat{E}_x \cdot \hat{E}_x^* \rangle \\ I_y &= \langle \hat{E}_y \cdot \hat{E}_y^* \rangle \\ U_\phi &= 2\text{Re} \langle \hat{E}_y \cdot \hat{E}_x^* \rangle \\ V_\phi &= 2\text{Im} \langle \hat{E}_y \cdot \hat{E}_x^* \rangle \end{aligned}$$

Now substituting equation 1.6 in equation 1.7 and using the definitions of  $I_l$ ,  $I_r$ ,  $U$ , and  $V$  from equation 1.2.

$$1.8 \quad \begin{aligned} I_x &= \cos^2 \phi I_l + \sin^2 \phi I_r + \frac{1}{2} \sin 2\phi U \\ I_y &= \sin^2 \phi I_l + \cos^2 \phi I_r - \frac{1}{2} \sin 2\phi U \\ U_\phi &= -\sin 2\phi I_l + \sin 2\phi I_r + \cos 2\phi U \\ V_\phi &= V \end{aligned}$$

Thus rotating the axes of observation through an angle  $\phi$



in the clockwise direction has the effect of subjecting the Stokes vector,  $\bar{I}$ , to the transformation  $\bar{L}(\phi)$ .

$$\bar{I}_\phi = \bar{L}(\phi)\bar{I}$$

where

$$1.9 \quad \bar{L}(\phi) = \begin{pmatrix} \cos^2\phi & \sin^2\phi & \frac{1}{2}\sin 2\phi & 0 \\ \sin^2\phi & \cos^2\phi & -\frac{1}{2}\sin 2\phi & 0 \\ -\sin 2\phi & \sin 2\phi & \cos 2\phi & 0 \\ 0 & 0 & 0 & 0 \end{pmatrix}$$

We are now prepared to describe the scattering in a coordinate system independent of the scattering plane. The scattering process in the new coordinate system is shown in figure 1.4.

Light in the meridian plane  $OX_1Z$  enters the diagram at  $X_1$  making an angle  $\theta'$  with the local normal,  $OZ$ , to the x-y plane. It is scattered at  $O$ , and leaves at  $X_2$  traveling in the meridian plane  $OX_2Z$ , with an angle of emergence  $\theta$ . The definition of the variables we shall use are clearly marked on the diagram but they still need some discussion. A consistent definition of azimuthal directions is needed because azimuth related considerations are the source of more errors than all other considerations combined. (For intensity only calculations, on the other hand, azimuth does not require special attention.) We shall take as our definition of azimuth the angle in the x-y plane, measured from the arbitrary x axis, made by that meridian plane of the beam through which the

radiation entered the sphere, or, extending backwards along the direction of propagation, would have entered the sphere. On the other hand we measure  $\theta$  and  $\theta'$  from the points at which the light actually does pierce the sphere. In this we use a different convention than is usual, but it has the advantage of making the scattering and transmission matrices that we shall introduce later on more similar in notation and symmetry properties to the phase matrix. This is a decision based originally on computer considerations alone since in this way the computer program algorithm is more similar to the equations on which it is based.

Until now the abbreviations "l" and "r" in the Stokes vector has referred to directions parallel and perpendicular to the scattering plane  $X_1OX_2$ . If we now redefine "l" and "r" as being directions parallel and perpendicular to the meridian plane that the beam is in, then we must rewrite the Stokes matrix in terms of this new definition.  $\bar{I}^1(\theta', \phi')$  can be transformed to the directions necessary for using the Stokes matrix in equation 1.5 by applying to it the linear transformation  $\bar{L}(i_1)$ , where  $i_1$  is the angle between the scattering plane  $X_1OX_2$  and the meridian plane  $OX_1Z$  through the point  $X_1(=\theta', \phi')$ . The resulting expression

$$1.10 \quad \bar{P}(\psi) \bar{L}(i_1) \bar{I}^1$$

describes the Stokes vector at  $P_2$  in terms of direction parallel and perpendicular to the plane of scattering. Note that

for convenience  $\psi$  has been written to replace  $\pi-\theta$ . To transform 1.10 to our new set of coordinate axes, we must apply  $\bar{L}(-i_2)$  where  $i_2$  is the angle at the point  $X_2(=\theta, \phi)$  between the meridian plane  $OX_2Z$  and the scattering plane  $X_1OX_2$ .

The angles  $i_1$  and  $-i_2$  used in the rotation of coordinates are not immediately obvious. In deriving then we must remember the convention that all angles are positive if the direction of rotation is clockwise when the direction of propagation is towards the observer. We must also carefully follow the directions "l" and "r" in the scattering plane and rotate "l" into the meridian plane so that it points upwards in figure 1.4.

The equation for the scattering process in the new coordinate system now becomes

$$1.11 \quad \bar{I}^S = \bar{L}(-i_2) \bar{P}(\psi) \bar{L}(i_1) \bar{I}^1$$

$$\bar{I}^S(\theta, \phi) = \bar{R}(\theta, \theta', \phi' - \phi) \bar{I}^1(\theta', \phi')$$

where

$$1.12 \quad R = \begin{pmatrix} \cos^2 i_2 & \sin^2 i_2 & -\frac{1}{2} \sin 2i_2 & 0 \\ \sin^2 i_2 & \cos^2 i_2 & +\frac{1}{2} \sin 2i_2 & 0 \\ +\sin 2i_2 & -\sin 2i_2 & \cos 2i_2 & 0 \\ 0 & 0 & 0 & 0 \end{pmatrix}$$

$$X = \begin{pmatrix} P_1(\psi) & 0 & 0 & 0 \\ 0 & P_2(\psi) & 0 & 0 \\ 0 & 0 & P_3(\psi) & -P_4(\psi) \\ 0 & 0 & +P_4(\psi) & P_3(\psi) \end{pmatrix}$$

$$X \begin{pmatrix} \cos^2 i_1 & \sin^2 i_1 & +\frac{1}{2}\sin 2i_1 & 0 \\ \sin^2 i_1 & \cos^2 i_1 & -\frac{1}{2}\sin 2i_1 & 0 \\ -\sin 2i_1 & +\sin 2i_1 & \cos 2i_1 & 0 \\ 0 & 0 & 0 & 1 \end{pmatrix}$$

Unfortunately there are no simple relations between the variables  $i_1, i_2, \psi$  and  $\theta, \phi, \theta', \phi'$ . From spherical geometry we get the following results.

$$1.13 \quad \psi = \cos^{-1}(\cos \theta \cos \theta' - \sin \theta \sin \theta' \cos \Delta \phi)$$

$$\sin i_2 = -\sin \theta' \frac{\sin \Delta \phi}{\sin \psi}; \quad \sin i_1 = -\sin \theta \frac{\sin \Delta \phi}{\sin \psi}$$

$$\cos i_2 = \frac{\cos \theta' - \cos \theta \cos \psi}{\sin \theta \sin \psi}; \quad \cos i_1 = \frac{\cos \theta - \cos \theta' \cos \psi}{\sin \theta' \sin \psi}$$

where  $\Delta \phi = \phi' - \phi$  and we have used the results

$$\cos(X+\pi) = -\cos X$$

$$\sin(X+\pi) = -\sin X$$

We shall write out equation 1.12 in full since we will need to refer to individual terms later on when we discuss symmetry relations and fourier coefficients. For the convenience of later discussion we make the change of variable  $\mu \rightarrow \cos \theta$  and  $\mu' \rightarrow \cos \theta'$ . Define  $\bar{R}'$  by

$$\bar{R}(\mu, \mu', \phi' - \phi) = \bar{Q} \cdot \bar{R}'(\mu, \mu', \phi' - \phi)$$

where  $\bar{Q}$  is the diagonal matrix

$$\begin{pmatrix} 1 & 0 & 0 & 0 \\ 0 & 1 & 0 & 0 \\ 0 & 0 & 2 & 0 \\ 0 & 0 & 0 & 2 \end{pmatrix}$$

The need for  $\bar{\bar{Q}}$  arises out of the non-symmetrical nature of  $I_1$ ,  $I_r$  on the one hand and  $U, V$  on the other. The matrix  $\bar{\bar{R}}$  is defined in terms of its components as

$$\begin{aligned}
 R'_{11} &= P_1 \cos^2 i_1 \cos^2 i_2 + P_2 \sin^2 i_1 \sin^2 i_2 + \frac{1}{2} P_3 \sin 2i_1 \sin 2i_2 \\
 R'_{12} &= P_1 \sin^2 i_1 \cos^2 i_2 + P_2 \cos^2 i_1 \sin^2 i_2 - \frac{1}{2} P_3 \sin 2i_1 \sin 2i_2 \\
 R'_{21} &= P_1 \sin^2 i_2 \cos^2 i_1 + P_2 \cos^2 i_2 \sin^2 i_1 - \frac{1}{2} P_3 \sin 2i_2 \sin 2i_1 \\
 R'_{22} &= P_1 \sin^2 i_1 \sin^2 i_2 + P_2 \cos^2 i_1 \cos^2 i_2 + \frac{1}{2} P_3 \sin 2i_1 \sin 2i_2 \\
 R'_{33} &= \frac{1}{4} P_1 \sin 2i_1 \sin 2i_2 + \frac{1}{4} P^2 \sin 2i_1 \sin 2i_2 + \frac{1}{2} P_3 \cos 2i_1 \cos 2i_2 \\
 R'_{34} &= -\frac{1}{2} P_4 \cos 2i_2 \\
 R'_{43} &= +\frac{1}{2} P_4 \cos 2i_1 \\
 R'_{44} &= \frac{1}{2} P_3
 \end{aligned}
 \tag{1.14a}$$

$$\begin{aligned}
 R'_{13} &= \frac{1}{2} (P_1 \sin 2i_1 \cos^2 i_1 - P_2 \sin 2i_1 \sin^2 i_2 - P_3 \cos 2i_1 \sin 2i_2) \\
 R'_{31} &= \frac{1}{2} (P_1 \sin 2i_2 \cos^2 i_1 - P_2 \sin 2i_2 \sin^2 i_1 - P_3 \cos 2i_2 \sin 2i_1) \\
 R'_{23} &= \frac{1}{2} (P_1 \sin 2i_1 \sin^2 i_2 - P_2 \sin 2i_1 \cos^2 i_2 + P_3 \cos 2i_1 \sin 2i_2) \\
 R'_{32} &= \frac{1}{2} (P_1 \sin 2i_2 \sin^2 i_1 - P_2 \sin 2i_2 \cos^2 i_1 + P_3 \cos 2i_2 \sin 2i_1) \\
 R'_{14} &= +\frac{1}{2} P_4 \sin 2i_2 \\
 R'_{41} &= -\frac{1}{2} P_4 \sin 2i_1 \\
 R'_{24} &= -\frac{1}{2} P_4 \sin 2i_2 \\
 R'_{42} &= +\frac{1}{2} P_3 \sin 2i_1
 \end{aligned}
 \tag{1.14b}$$

The components have been separated into two groups for ease of discussion of their different properties later on. We shall call matrix  $\bar{\bar{R}}$ , the phase matrix.

We shall not discuss the symmetry properties at length since an extensive treatment has been published by J. W. Hovenier.<sup>4</sup>

He uses the [I,Q,U,V] representation of the Stokes vector so his phase matrix is different in form than the one we have derived. In addition, because of different definitions of  $\theta, \theta'$  and  $\phi$ , his symmetry relations for the phase matrix are different than ours. However, his definition of the  $\mu, \mu'$ , and  $\phi$  of the scattering and transmission matrices, which we shall introduce soon, is the same and so we may compare our equations with his directly. Hovenier has derived all of the symmetry properties of the phase, scattering and transmission matrices. Of these we will only need a few. They all follow from equations 1.13 and 1.14 and a casual examination is all that is necessary to convince oneself of the validity of any one of them.

I have found it more convenient, conceptually, to visualize the symmetry properties of the phase matrix in terms of three unorthodox symmetry operators X,Y,Z.

$$1.15 \quad X = \begin{pmatrix} + & + & + & - \\ + & + & + & - \\ + & + & + & - \\ - & - & - & + \end{pmatrix}, \quad Y = \begin{pmatrix} + & + & - & + \\ + & + & - & + \\ - & - & + & - \\ + & + & - & + \end{pmatrix}, \quad Z = \begin{pmatrix} + & + & - & - \\ + & + & - & - \\ - & - & + & + \\ - & - & + & + \end{pmatrix}$$

As an example of their use, the action of X on an arbitrary matrix A is written  $B = X * A$  and defined in terms of components by  $B_{ij} = X_{ij} A_{ij}$ , summation not implied. Thus X,Y,Z can be regarded as templates to be placed over the matrix to indicate sign changes. Under this definition  $X * Y = Z$ . We shall indicate by the tilde,  $\sim$ , the transpose of a matrix.

$$1.16a \quad R'(\mu, \mu', \phi - \phi') = Z * R'(\mu, \mu', \phi' - \phi)$$

$$1.16b \quad R'(\mu', \mu, \phi' - \phi) = X * \tilde{R}'(\mu, \mu', \phi' - \phi)$$

$$1.16c \quad R'(-\mu', +\mu, \phi' - \phi) = Y * \tilde{R}'(-\mu, +\mu', \phi' - \phi)$$

$$1.16d \quad R'(-\mu, -\mu', \phi - \phi') = R'(+\mu, \mu', \phi' - \phi')$$

Equation 1.16a expresses the fact that those elements which have a minus sign in matrix Z are odd functions of  $\phi' - \phi$ , and those with a plus sign are even functions of  $\phi' - \phi$ . This will be important later on when we fourier analyze each matrix element. The odd functions will be expressable as a sine expansion and the even functions as a cosine expansion. Equations 1.16b and 1.16c are of interest theoretically, but we shall use them just to reduce redundancy and thus increase the speed of the computer computation.

## II Reflection and Transmission Matrices from a Single Scattering Layer and their Symmetry Properties.

In this section we shall derive the diffuse reflection and transmission properties of a single scattering, plane parallel atmosphere. These will be expressed as functions of the phase matrix we have already derived. We shall also examine the symmetry properties of these matrices with a view towards removing computational redundancy later on. We will find that we need four of these matrices instead of the usual two for intensity only calculations.

Consider a parallel beam of light of net flux

$$\pi \bar{F} = \pi(F_1, F_r, F_u, F_v)$$

per unit area normal to the direction of the beam in the four Stokes parameters, incident from above in the direction  $(\mu', \phi')$ , on a plane parallel atmosphere of optical depth  $\tau$ . The distinction "from above" is important. We wish to express the laws of diffuse reflection and transmission in terms of a scattering matrix  $\bar{S}(\tau; \mu, \mu', \phi' - \phi)$  and a transmission matrix  $\bar{T}(\tau; \mu, \mu', \phi' - \phi)$  such that the intensity reflected upwards and the intensity transmitted downwards are given by

$$\bar{I}(0; \mu, \phi; \mu', \phi') = \frac{1}{4\mu} \bar{S}(\tau; \mu, \mu', \phi' - \phi) \bar{F}$$

1.17

$$\text{and } \bar{I}(\tau, -\mu, \phi; \mu', \phi') = \frac{1}{4\mu} \bar{T}(\tau; \mu, \mu', \phi' - \phi) \bar{F}.$$

The factor  $1/\mu$  has been added to insure similar symmetry properties to those mentioned for the phase matrix.



We shall now derive  $\bar{S}$  and  $\bar{T}$  for light that has been scattered only once in the layer. Consider that portion of the atmosphere between  $\tau'$  and  $\tau' + d\tau'$ . At that depth a fraction  $e^{-\tau'/\mu'}$  will have penetrated without having undergone scattering in the atmosphere above. The contribution to the diffuse light in the direction  $(\mu, \phi)$  from the reduced intensity that penetrates to this depth and is scattered is

$$e^{-\tau'/\mu'} \bar{R}(\mu, \mu', \phi' - \phi) \frac{\pi \bar{F}}{4\pi} \frac{d\tau'}{\mu}$$

where  $\bar{R}$  is the phase matrix given, by equation 1.14.

A fraction  $e^{-\tau'/\mu}$  emerges from the layer in the direction  $(\mu, \phi)$  without undergoing further scattering. Thus the contribution to the diffuse intensity in the direction  $(\mu, \phi)$  from light that has been scattered once between  $\tau'$  and  $\tau' + d\tau'$  is

$$\frac{e^{-\tau'/\mu} e^{-\tau'/\mu'}}{4\mu} \bar{R}(\mu, \mu', \phi' - \phi) d\tau' \quad . \quad \text{See R.T., page 145.}$$

The total intensity from a layer of optical depth  $\tau$  is just the integral of this expression over  $\tau'$

$$I(0; \mu, \phi; \mu', \phi') = \frac{[1 - e^{-\tau(\frac{1}{\mu} + \frac{1}{\mu'})}]}{4\mu} (\frac{1}{\mu} + \frac{1}{\mu'})^{-1} \bar{R}(\mu, \mu', \phi' - \phi) \bar{F}$$

In a similar manner we can derive the diffuse intensity transmitted down in the direction  $(-\mu, \phi)$ . We find

$$I(\tau; -\mu, \phi; \mu', \phi') = \frac{[e^{-\tau/\mu} - e^{-\tau/\mu'}](\frac{1}{\mu'} - \frac{1}{\mu})^{-1}}{4\mu} \bar{R}(-\mu, \mu', \phi' - \phi) \bar{F}.$$

We can now write down the scattering and transmission matrices for singly scattered light.

$$\begin{aligned} \bar{S}(\tau; \mu, \mu', \phi' - \phi) &= (\frac{1}{\mu} + \frac{1}{\mu'})^{-1} [1 - e^{-\tau(\frac{1}{\mu} + \frac{1}{\mu'})}] \bar{R}(\mu, \mu', \phi' - \phi) \\ 1.18 \quad \bar{T}(\tau; \mu, \mu', \phi' - \phi) &= (\frac{1}{\mu'} - \frac{1}{\mu})^{-1} [e^{-\tau/\mu} - e^{-\tau/\mu'}] \bar{R}(-\mu, \mu', \phi' - \phi) \end{aligned}$$

In the limit as  $\tau \rightarrow 0$ , the coefficients of  $\bar{R}$  in equations 1.18 are just  $\tau$  for both  $\bar{S}$  and  $\bar{T}$ . Notice that interchanging  $\mu$  and  $\mu'$  in equations 1.18 does not change the value of the coefficients.

We shall now discuss the symmetry properties of the scattering and transmission matrices  $\bar{S}'$  and  $\bar{T}'$  defined in terms of  $\bar{S}$  and  $\bar{T}$  by

$$\begin{aligned} \bar{S} &= \bar{Q} \cdot \bar{S}' \\ \bar{T} &= \bar{Q} \cdot \bar{T}' \end{aligned}$$

We shall give the same names to both the primed and unprimed matrices. It will be clear from the context which is meant.

From equations 1.16 we may write down immediately the results

$$\begin{aligned} \bar{S}'(\mu, \mu', \phi - \phi') &= \bar{Z} * \bar{S}'(\mu, \mu', \phi' - \phi) \\ 1.19a \quad \bar{T}'(\mu, \mu', \phi - \phi') &= \bar{Z} * \bar{T}'(\mu, \mu', \phi' - \phi) \end{aligned}$$

$$1.19b \quad \bar{S}'(\mu', \mu, \phi' - \phi) = \bar{X} * \bar{S}'(\mu, \mu', \phi' - \phi)$$

$$1.19c \quad \bar{T}'(\mu', \mu, \phi' - \phi) = \bar{Y} * \bar{T}'(\mu, \mu', \phi' - \phi)$$

So far we have discussed two of the four matrices that will be needed. The need for the other two results from the fact that  $\bar{S}$  and  $\bar{T}$  cannot express the reflection and transmission of radiation incident from below the layer. This fact has sometimes been overlooked in the literature where it generally assumed that intensity equations are completely generalizable to polarization equations. Specifically, it was overlooked in Chandrasekhar's Radiative Transfer, where he states on page 170 that his invariance equations for intensity can be generalized to polarization by replacing the functions  $S$  and  $T$  by the matrices  $\bar{S}$  and  $\bar{T}$ .

To allow for this case we define two new matrices.  $\bar{S}^*$  and  $\bar{T}^*$  such that the light scattered downwards from below is

$$1.20a \quad \bar{I}(\tau; -\mu, \phi; -\mu', \phi') = \frac{1}{4\mu} \bar{S}^*(\tau; \mu, \mu', \phi' - \phi) \bar{F}.$$

and the light transmitted upwards from below is

$$1.20b. \quad \bar{I}(0; \mu, \phi; -\mu', \phi') = \frac{1}{4\mu} \bar{T}^*(\tau; \mu, \mu', \phi' - \phi) \bar{F}.$$

We can express  $\bar{S}^*$  and  $\bar{T}^*$  in terms of  $\bar{S}$  and  $\bar{T}$  if we make use of the properties of the original phase matrix. From 1.16d we have

$$1.21a \quad \bar{S}^{*'}(\mu, \mu', \phi' - \phi) = \bar{S}'(\mu, \mu', \phi - \phi')$$

and

$$1.21b \quad \bar{\bar{T}}^{*'}(\mu, \mu', \phi' - \phi) = \bar{\bar{T}}'(\mu, \mu', \phi - \phi')$$

Physically, the need for  $\bar{\bar{S}}^{*}$  and  $\bar{\bar{T}}^{*}$  as well as the reversal of the azimuth direction comes about because the use of the unstarred matrices to express scattering from below would result in measuring azimuth in the opposite direction than scattering from above. The definition of azimuth is tied to the direction of propagation.

The symmetry relationships for  $\bar{\bar{S}}^{*}$  and  $\bar{\bar{T}}^{*}$  are exactly the same as those for  $\bar{\bar{S}}$  and  $\bar{\bar{T}}$  expressed in equations 1.19.

### III Reflection and Transmission Matrices from a Multiple Scattering Layer -- The Doubling Method.

We now have four matrices which completely describe the reflection and transmission properties of a single scattering plane parallel layer of any optical thickness. In this next section we shall see how to combine two identical layers using a generalization of Van de Hulst's<sup>5</sup> doubling method. We will then have the reflection and transmission matrices of a layer of twice the optical thickness which multiply scatters the light between the top and bottom halves. If we begin the doubling with a layer whose optical thickness is so small that only single scattering is present, we can derive the multiple scattering properties of a layer of any optical thickness by a sufficient number of doublings.

To derive the generalized doubling method it will be convenient to define some shorthand notation. We assume the incident intensity to be a parallel beam of net flux  $\pi\bar{F}$  in the four Stokes parameters. It is a delta function in direction and we write it

$$\bar{I} = \pi\bar{F}\delta(\mu-\mu_o, \phi-\phi_o)$$

$$\text{or } \bar{I} = \pi\bar{F}\delta$$

The diffuse intensity reflected from and transmitted through the layer is

$$\bar{I}^S = \bar{S}(\mu, \mu_o, \phi_o - \phi) \frac{\bar{F}}{4\mu}$$

$$\bar{I}^t = \bar{T}(\mu, \mu_o, \phi_o - \phi) \frac{F}{4\mu}$$

or

$$\bar{I}^s = \frac{1}{4\mu} \bar{S} \bar{F}$$

$$\bar{I}^t = \frac{1}{4\mu} \bar{T} \bar{F}$$

Matrix multiplication is implied. If a diffuse intensity  $I(\mu_o, \phi_o)$  is incident on a layer the diffuse intensity reflected and transmitted will be

$$\bar{I}^s = \frac{1}{4\pi\mu} \int_0^1 \int_0^{2\pi} \bar{S}(\mu, \mu', \phi' - \phi) \bar{I}(\mu', \phi') d\mu' d\phi'$$

$$\bar{I}^t = \frac{1}{4\pi\mu} \int_0^1 \int_0^{2\pi} \bar{T}(\mu, \mu', \phi' - \phi) \bar{I}(\mu', \phi') d\mu' d\phi'$$

We will write this as

$$\bar{I}^s = \frac{1}{4\mu} \bar{S} \cdot \bar{I}$$

$$\bar{I}^t = \frac{1}{4\mu} \bar{T} \cdot \bar{I}$$

where the symbol " $\cdot$ " means

$$\frac{1}{\pi} \int_0^1 \int_0^{2\pi} d\mu' d\phi'.$$

It also will be useful to define another operation " $\circ$ " defined by

$$\frac{1}{\pi} \int_0^1 \int_0^{2\pi} \frac{1}{4\mu'} d\mu' d\phi'$$

so that we may write

$$\frac{1}{4\pi\mu} \int_0^1 \int_0^{2\pi} \bar{S}(\mu, \mu', \phi' - \phi) \frac{\bar{T}}{4\mu'}(\mu', \mu_o, \phi_o - \phi') d\mu' d\phi'$$

as

$$\frac{1}{4\mu} \bar{S} \circ \bar{T}$$

It can easily be seen that associative rules hold for the operators " $\cdot$ " and " $\circ$ ". Thus for example

$$\bar{S} \circ \bar{T} \circ \bar{S} = \bar{S} \circ (\bar{T} \circ \bar{S}) = (\bar{S} \circ \bar{T}) \circ \bar{S}$$

$$\bar{S} \circ \bar{T} \bar{F} = (\bar{S} \circ \bar{T}) \bar{F} = \bar{S} \circ (\bar{T} \bar{F})$$

and

$$\bar{S} \circ \bar{T} \cdot \bar{I} = (\bar{S} \circ \bar{T}) \cdot \bar{I} = \bar{S} \circ (\bar{T} \cdot \bar{I})$$

Now consider the situation in figure 1.5. Two layers of identical scattering properties are placed together. It is required to find the scattering properties of the two layers combined. Light is incident from the direction  $(\mu_0, \phi_0)$  with intensity  $\bar{I}^1 = \pi \bar{F} \delta$ . The diffuse intensity that is reflected from the upper layer due to  $\bar{I}^1$  is

$$\bar{P}_1 = \frac{1}{4\mu} \bar{S} \cdot \bar{I}^1 = \frac{1}{4\mu} \bar{S} \bar{F}$$

The intensity, both diffuse and direct, transmitted down through the upper layer is

$$\begin{aligned} \bar{D}_1 &= \bar{I}^1 e^{-\tau/\mu_0} + \frac{1}{4\mu} \bar{T} \cdot \bar{I}^1 \\ &= \pi \bar{F} \delta e^{-\tau/\mu_0} + \frac{1}{4\mu} \bar{T} \bar{F} \end{aligned}$$

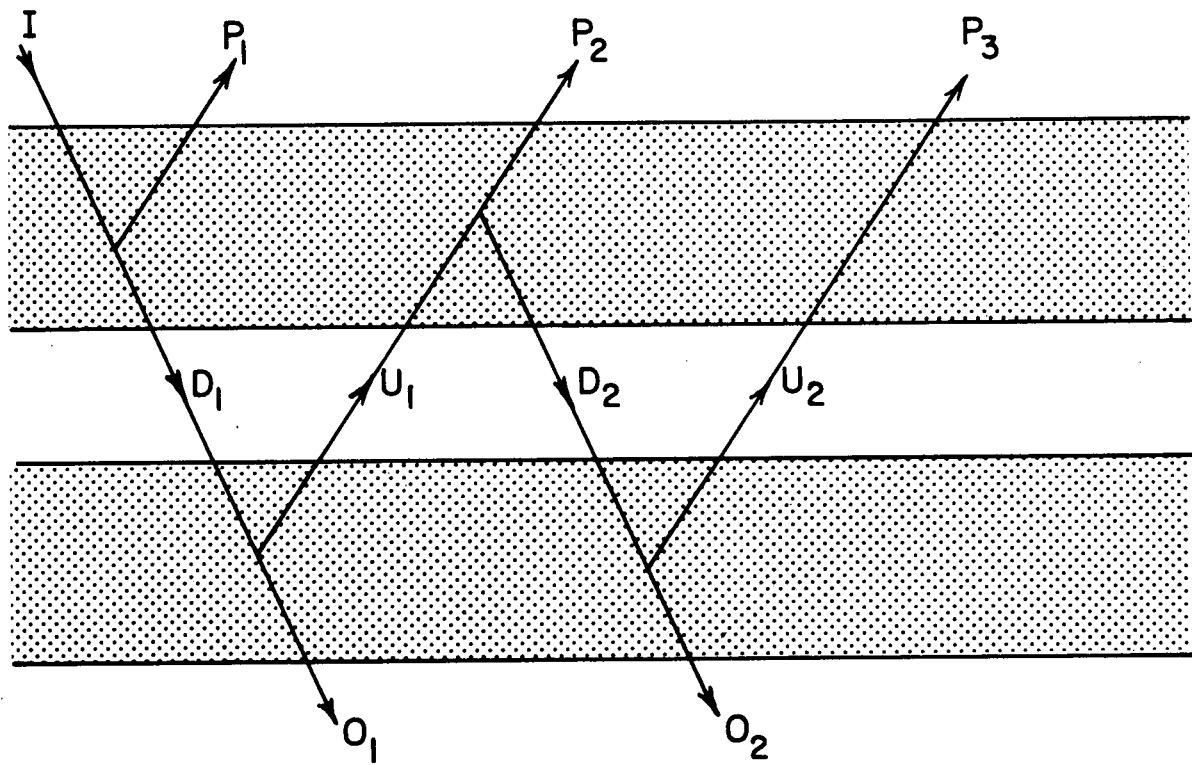


Figure 1.5 Scattering from the sum of two layers.



The intensity transmitted through the lower layer is

$$\begin{aligned}\bar{O}_1 &= e^{-\tau/\mu} \bar{D}_1 + \frac{1}{4\mu} \bar{T} \cdot \bar{D}_1 \\ &= \pi \bar{F} \delta e^{-2\tau/\mu_0} + \frac{e^{-\tau/\mu}}{4\mu} \bar{T} \bar{F} + \frac{e^{-\tau/\mu_0}}{4\mu} \bar{T} \bar{F} + \frac{1}{4\mu} \bar{T} \circ \bar{T} \bar{F}\end{aligned}$$

The diffuse intensity scattered upwards by the lower layer is

$$\begin{aligned}\bar{U}_1 &= \frac{1}{4\mu} \bar{S} \cdot \bar{D}_1 \\ &= \frac{e^{-\tau/\mu_0}}{4\mu} \bar{S} \bar{F} + \frac{1}{4\mu} \bar{S} \circ \bar{T} \bar{F}\end{aligned}$$

The diffuse intensity transmitted upwards by the upper layer is

$$\begin{aligned}\bar{P}_2 &= \bar{U}_1 e^{-\tau/\mu} + \frac{1}{4\mu} \bar{T}^* \cdot \bar{U}_1 \\ &= \frac{e^{-\tau/\mu} e^{-\tau/\mu_0}}{4\mu} \bar{S} \bar{F} + \frac{e^{-\tau/\mu}}{4\mu} \bar{S} \circ \bar{T} \bar{F} \\ &\quad + \frac{e^{-\tau/\mu_0}}{4\mu} \bar{T}^* \circ \bar{S} \bar{F} + \frac{1}{4\mu} \bar{T}^* \circ \bar{S} \circ \bar{T} \bar{F}\end{aligned}$$

The diffuse intensity produced by  $\bar{U}_1$  scattered downwards by the upper layer is

$$\begin{aligned}\bar{D}_2 &= \frac{1}{4\mu} \bar{S}^* \cdot \bar{U}_1 \\ &= \frac{e^{-\tau/\mu_0}}{4\mu} \bar{S}^* \circ \bar{S} \bar{F} + \frac{1}{4\mu} \bar{S}^* \circ \bar{S} \circ \bar{T} \bar{F}\end{aligned}$$

The diffuse intensity produced by  $\bar{D}_2$  transmitted downwards by the lower layer is

$$\begin{aligned}
\bar{O}_2 &= \bar{D}_2 e^{-\tau/\mu} + \frac{1}{4\mu} \bar{T} \cdot \bar{D}_2 \\
&= \frac{1}{4\mu} e^{-\tau/\mu_0} e^{-\tau/\mu} \bar{S}^* \circ \bar{S} \bar{F} + \frac{1}{4\mu} e^{-\tau/\mu} \bar{S}^* \circ \bar{S} \circ \bar{T} \bar{F} \\
&+ \frac{1}{4\mu} e^{-\tau/\mu_0} \bar{T} \circ \bar{S}^* \circ \bar{S} \bar{F} + \frac{1}{4\mu} \bar{T} \circ \bar{S}^* \circ \bar{S} \circ \bar{T} \bar{F}
\end{aligned}$$

Continuing in this way we find the reflected and transmitted intensities from the two layers combined. Ignoring the directly transmitted light,  $\pi F \delta e^{-2\tau/\mu_0}$ , we may now write down immediately the reflection and transmission matrices of the two layers combined. They are

$$\begin{aligned}
1.22a \quad S(2\tau) &= S + e^{-\tau/\mu} \Sigma_1 e^{-\tau/\mu_0} + e^{-\tau/\mu} \Sigma_1 \circ T \\
&+ e^{-\tau/\mu_0} T^* \circ \Sigma_1 + T^* \circ \Sigma_1 \circ T
\end{aligned}$$

$$\begin{aligned}
1.22b \quad T(2\tau) &= T(e^{-\tau/\mu} + e^{-\tau/\mu_0}) + T \circ T \\
&+ e^{-\tau/\mu} \Sigma_2 e^{-\tau/\mu_0} + e^{-\tau/\mu} \Sigma_2 \circ T \\
&+ e^{-\tau/\mu_0} T \circ \Sigma_2 + T \circ \Sigma_2 \circ T
\end{aligned}$$

where  $\Sigma_1 = S + S \circ S^* \circ S + S \circ S^* \circ S \circ S^* \circ S + \dots$

and  $\Sigma_2 = S^* \circ S + S^* \circ S \circ S^* \circ S + \dots$

Equations 22 are the doubling equations. Note that  $\Sigma_2 = S^* \circ \Sigma_1$ . We have dropped the double lines above the matrices since it will be clear from now on that matrices are implied.

#### IV The Doubling Equations - Fourier Components and Symmetry Properties

It might seem now that the problem of combining layers is completely solved. In theory these equations could be programmed into a computer and solved numerically. In practice it is impossible. Present state of the art computers are completely incapable of producing accurate answers from these equations for large optical depths and non-Rayleigh phase functions given any reasonable time limit. The rest of the discussion of the doubling equations, therefore, is directed, as its main purpose, to save computer time.

We shall see how to rewrite the doubling equations in terms of the fourier components of the reflection and transmission matrices. We will find that each fourier component doubles independently. We shall also rewrite the symmetry equations for these fourier matrices so that we may see which computations in the doubling equations are redundant.

In order to motivate the analysis of the matrices into their fourier components, let us compare the amount of computation necessary for both methods. Let  $M$  be the number of fourier components, let  $I$  be the number of integration points in the  $\mu$  integration and let  $K$  be the number of integration points in the  $\phi$  integration. We would expect that  $K \sim I$ . Then the double integral in  $\phi$  and  $\mu$  would require

$$N_{\phi} = 4^3 \times I^3 \times K^2 = 4^3 \times I^5 \text{ operations, symmetry considerations neglected.}$$
 The cubed term arises because  $I$  operations are

needed to integrate each of the  $I^2$  sets of points at which the function is defined in  $\mu, \mu_0$  space. The single integral that will appear in the fourier analysed equations requires

$N_M = 4^3 \times I^3 \times M$  operations. In the case of Rayleigh scattering, reasonable answers are obtained for  $I \sim 4$ .  $M$  is exactly 3. Thus there is a factor of 5 improvement in computer time for the simplest realistic case. This improvement factor increases markedly if the answers are required at more  $\phi$  points since the fourier components can be recombined at any set of  $\phi$  points. The improvement increases also as the phase function becomes more anisotropic.

Consider the four matrices  $S, S^*, T,$  and  $T^*$ . Equations 1.21 and 1.19a show that all four have the same symmetry with respect to  $\phi$ , that is, the terms marked with a "+" sign in symmetry operator matrix  $Z$ , reproduced below, are even functions of  $\phi$  and those marked with a "-" sign are odd functions of  $\phi$ .

$$Z = \begin{pmatrix} + & + & - & - \\ + & + & - & - \\ - & - & + & + \\ - & - & + & + \end{pmatrix}$$

We may then expand the even terms in a cosine expansion and the odd terms in a sine expansion.

The fourier analysis will take some discussion. Normally the  $m^{\text{th}}$  fourier coefficient of a function is obtained by integrating the function times  $\frac{\sin}{\cos}(m\phi)$  over the range of interest. However this operation has to be done numerically and a moment's consideration will reveal that as  $m$  increases the number of integration points, which must be much greater than  $m$ , must

increase as well, no matter how smooth the function. This seems to be requiring more information from the function than should be needed.

There exists another, not well known, approach by which even functions having fourier coefficients up to order  $N$  and odd functions having fourier coefficients up to order  $N-1$  can be analyzed using exactly  $N+1$  evenly spaced points. Assume we have an even or odd function  $f(X)$  with a period  $2\pi$  and which is known at  $2N+1$  equally spaced points from  $-\pi$  to  $\pi$ . Denote the  $2N$  points from  $-\pi$  to  $\pi$  by  $X_1 = i \times \frac{\pi}{N}$ ,  $i = -(N-1), \dots, N$  where we have not included  $-\pi$  in the set since  $f(-\pi) = f(\pi)$  implies that  $-\pi$  is not an independent point. If  $f(X)$  can be resolved exactly using  $2N-1$  fourier coefficients in sine and cosine then we may write

$$1.23 \quad f(X_1) = a_0 + \sum_{k=1}^{N-1} a_k \frac{\sin(kX_1)}{\cos(kX_1)}$$

(The method below using  $2N$  points gives enough information to determine  $a_N$  for the cosine term so that  $2N$  points would yield  $2N$  coefficients. However we will require sine and cosine fourier coefficients of similar orders so that the  $N^{\text{th}}$  order cosine coefficient will not be of use to us here. The neglect of  $a_N$  in 1.23 will still permit the other  $a_k$ 's to be found uniquely.)

Conventionally we would multiply by  $\cos mX$  or  $\sin mX$  and integrate. Instead,

$$\sum_1 f(X_1) \frac{\sin(mX_1)}{\cos(mX_1)} = a_0 \sum_1 \frac{\sin(mX_1)}{\cos(mX_1)} + \sum_{k=1}^{N-1} a_k \sum_1 \frac{\sin(kX_1)}{\cos(kX_1)} \frac{\sin(mX_1)}{\cos(mX_1)}$$

where  $\sum_{i=1}^N = \sum_{i=-(N-1)}^N$ .

It is possible to prove the following relations:

$$\sum_{i=1}^N \cos kX_i \cos mX_i = 0 \quad m \neq k$$

$$\sum_{i=1}^N \sin kX_i \sin mX_i = 0 \quad m \neq k$$

$$\sum_{i=1}^N \sin^2 kX_i = N \quad k \neq 0$$

$$\sum_{i=1}^N \cos^2 kX_i = N \quad k \neq 0, N$$

$$\sum_{i=1}^N \cos^2 NX_i = \sum_{i=1}^N 1 = 2N$$

Then we have immediately

$$a_0 = \frac{1}{2N} \sum_{i=-(N-1)}^N f(X_i), \quad f(X) \text{ even}$$

$$a_0 = 0, \quad f(X) \text{ odd}$$

$$a_m = \frac{1}{N} \sum_{i=-(N-1)}^N f(X_i) \frac{\sin(mX_i)}{\cos(mX_i)}$$

Since  $f(X_i)$  is even or odd in  $X$  we may write

$$a_m = \frac{2}{N} \sum_{i=0}^N b_i f(X_i) \frac{\sin(mX_i)}{\cos(mX_i)}$$

$$\text{where } b_i = 1 \quad i \neq 0, N$$

$$b_i = 1/2 \quad i = 0, N$$

$$a_0 = \frac{1}{N} \sum_{i=0}^N b_i f(X_i), \quad f(X) \text{ even}$$

$$= 0, \quad f(X) \text{ odd.}$$

It will be convenient notationally if we redefine the coefficients  $a_m$  to be

$$1.24 \quad a_m = \frac{1}{2N} \sum_{i=0}^N b_i f(X_i) \frac{\sin}{\cos} (mX_i), \quad m = 0, \dots, N-1.$$

We must rewrite equation 1.23 in terms of this new definition of  $a_m$ . Equation 1.23 now takes the form

$$1.24 \quad f(X) = \sum_{m=0}^{N-1} (4 - 2\delta_{0m}) a_m \frac{\sin}{\cos} (mX)$$

We are now ready to proceed with the fourier analysis of the matrices themselves. We have shown how to compute the fourier component numerically. Under the definition of the fourier components given by equations 1.24 and 1.25 we rewrite the standard fourier analysis-synthesis equations as

$$1.26 \quad f(\phi) = \sum_m f f^m (4 - 2\delta_{0m}) \frac{\sin}{\cos} (m\phi)$$

$$\text{where } f f^m = \frac{1}{4\pi} \int_0^{2\pi} f(\phi) \frac{\sin}{\cos} (m\phi) d\phi$$

Consider now as an example the equation

$$1.27 \quad \bar{A} = \bar{S} \circ \bar{T}$$

$$\text{or } \bar{A}(\phi_0 - \phi) = \frac{1}{\pi} \int_0^1 \int_0^{2\pi} \bar{S}(\phi' - \phi) \bar{T}(\phi_0 - \phi') d\phi' \frac{d\mu'}{4\mu}$$

The variable  $\mu, \mu'$ , and  $\mu_0$  have been suppressed for convenience. Matrix multiplication is implied.

The inner integral is the integral over  $\phi$  of 64 separate functions. If we write both S and T in the form of equation 1.26 and denote the fourier coefficients by  $\overline{SS}^m$  and  $\overline{TT}^m$  then, equation 1.27 becomes

$$1.28 \quad \sum_m \overline{AA}^m d_m \frac{\sin}{\cos}(m(\phi_0 - \phi)) =$$

$$\frac{1}{\pi} \int_0^1 \int_0^{2\pi} \sum_m \overline{SS}^m d_m \frac{\sin}{\cos}(m(\phi' - \phi)) \sum_m \overline{TT}^m d_m \frac{\sin}{\cos}(m(\phi_0 - \phi')) d\phi' \frac{d\mu'}{4\mu} \quad \text{where}$$

$$d_m = (4 - 2\delta_{0m}) .$$

Equation 1.28 needs some explanation. The equation is still a matrix equation with matrix multiplication implied between all the  $\overline{SS}^m$  and  $\overline{TT}^m$  terms. The term  $\frac{\sin}{\cos}$  now means that each component should be expanded in cosine or sine depending on whether it is even or odd. Equation 1.28 leads immediately to the statement that all fourier components double independently. To prove it, the equation must be written out in full and use made of the standard orthogonality relations between cosine and sine. We will not do that here since the proof is as tedious as it is obvious.

The 64 separate expressions on the right side of equation 1.28 are each of the form

$$\frac{1}{\pi} \int_0^1 \int_0^{2\pi} \overline{SS}_{ik}^m \overline{TT}_{kj}^m d_m^2 \frac{\sin}{\cos}(m(\phi' - \phi)) \frac{\sin}{\cos}(m(\phi_0 - \phi')) d\phi' \frac{d\mu'}{4\mu} \quad \text{before summa-}$$



tion over  $k$  is performed.

There are 4 possible integrals indicated here. Their values are, neglecting the constant coefficients,

$$\begin{aligned}
 \int \sin \sin d\phi' &= -\pi \cos m (\phi_0 - \phi) \\
 \int \cos \cos d\phi &= 4\pi \cos m (\phi_0 - \phi) / d_m \\
 1.30 \quad \int \sin \cos d\phi' &= \pi \sin m (\phi_0 - \phi) \\
 \int \cos \sin d\phi' &= \pi \sin m (\phi_0 - \phi)
 \end{aligned}$$

The factor  $4/d_m$  ( $=1, m \neq 0$ ;  $=2, m=0$ ) appears only for the 'cos cos' term, but we may multiply the 3 other terms by it since they all contain 'sin' terms in either the right or left side of the equal signs and their coefficients are zero for  $m=0$ .

It is not immediately obvious that only cosine terms will appear in the matrix elements marked "+" in matrix  $Z$  or that only sine terms will appear in the matrix elements marked "-". This, however, is the case and can be seen only by careful checking of each of the 64 terms with the aid of equation 1.30.

We may therefore now write the analog of equation 1.27 in terms of its fourier components and matrix elements as

$$1.31 \quad AA_{ij}^m = \int_0^1 \sum_{k=1}^4 SS_{ik}^m r_{ikj} TT_{kj}^m \frac{du'}{u'}$$

where  $r_{ikj} = -1$

$$\begin{aligned}
 \text{for } \{i;j;k\} &= \{i=1,2; j=3,4; k=1,2\} \\
 &\quad \{i=3,4; j=1,2; k=3,4\}
 \end{aligned}$$

and  $r_{ijk} = +1$  for all other  $i, j, k$ .  $r_{ijk}$  follows from equation 1.30 when note is taken of the position of sin and cos terms in the matrices. Then with this new definition of matrix multiplication we may write equation 1.31 as a matrix equation

$$1.32 \quad \overline{AA}^m = \int_0^1 \overline{SS}^m * \overline{TT}^m \frac{d\mu'}{\mu'}$$

where "\*" stands for fourier component matrix multiplication as defined in equation 1.31. If we define a new operator ":" by

$$1.33 \quad \overline{SS}^m : \overline{TT}^m = \int_0^1 \overline{SS}^m * \overline{TT}^m \frac{d\mu'}{\mu'}$$

then we can rewrite the doubling equations 1.22 in terms of the fourier matrices. Because of our choice of conventions in the fourier analysis (see equation 26), the equations have exactly the same form with "o" replaced by ":" and single letters replaced by double letters. We will write then again in their new form, suppressing the double bar and "m" for convenience.

$$1.34a \quad \begin{aligned} SS(2\tau) = & SS + e^{-\tau/\mu} \Sigma \Sigma_1 e^{-\tau/\mu_0} + e^{-\tau/\mu} \Sigma \Sigma_1 : TT \\ & + e^{-\tau/\mu_0} TT* : \Sigma \Sigma_1 + TT* : \Sigma \Sigma_1 : TT. \end{aligned}$$

$$1.34b \quad \begin{aligned} TT(2\tau) = & TT(e^{-\tau/\mu} + e^{-\tau/\mu_0}) + TT : TT \\ & + e^{-\tau/\mu} \Sigma \Sigma_2 e^{-\tau/\mu_0} + e^{-\tau/\mu} \Sigma \Sigma_2 : TT \\ & + e^{-\tau/\mu_0} TT : \Sigma \Sigma_2 + TT : \Sigma \Sigma_2 : TT \end{aligned}$$

1.35a where  $\Sigma\Sigma_1 = SS + SS^* : SS^* : SS + . . .$

1.35b and  $\Sigma\Sigma_2 = SS^* : \Sigma\Sigma_1 = SS^* : SS + SS^* : SS : SS^* : SS \dots$

Once again the associative rule can be shown to hold. Equations 1.34 and 1.35 are an exact analog of the intensity only equations derived by Hansen<sup>6</sup>.

The symmetry relations for the fourier scattering and transmission matrices can be written down immediately from equations 1.19 and 1.21.

$$1.36a \quad SS'(\mu', \mu) = X * \overset{\sim}{SS'}(\mu, \mu')$$

$$1.36b \quad TT'(\mu', \mu) = Y * \overset{\sim}{TT'}(\mu, \mu')$$

$$1.36c \quad SS'^*(\mu, \mu') = Z * SS'(\mu, \mu')$$

$$1.36d \quad TT'^*(\mu, \mu') = Z * TT'(\mu, \mu')$$

Here again we use the prime to denote the matrices before multiplication by  $\bar{Q}$ ,  $\sim$  means the transpose and the operator sign  $*$  means the term by term multiplication by the sign of the symmetry operators X, Y, Z.

#### The $\bar{\Sigma}\bar{\Sigma}$ Matrices

The doubling equations are not quite complete. We must show how to evaluate the infinite series involved in the definitions of  $\Sigma\Sigma_1$  and  $\Sigma\Sigma_2$ . Physically each term in  $\Sigma\Sigma_1$  and  $\Sigma\Sigma_2$  represents the diffuse intensity of the radiation at each bounce between the upper and lower layers. Intuitively we expect the ratio of the components of two successive terms to approach some limit independent of  $\mu$  and  $\mu_0$ . This turns out to be the case.

Let  $\bar{C}^i = \langle \bar{\Sigma}\bar{\Sigma}_1^{i+1} / \bar{\Sigma}\bar{\Sigma}_1 \rangle$  where  $\bar{\Sigma}\bar{\Sigma}_1^i$  is the  $i^{\text{th}}$  term in the expansion 1.35a. The division is performed for each matrix

element at each  $\mu$  and  $\mu_0$ . The average  $\langle \rangle$  is performed for each matrix element over  $\mu$  and  $\mu_0$  with equal weight given to each  $(\mu, \mu_0)$ . Thus  $\overline{C}^1$  is a matrix of 16 scalar quantities, each independent of  $(\mu, \mu_0)$ .

When it has been determined that  $C^1$  is indeed the limit of successive ratios and hence independent of "i" we may write

$$1.37 \quad \Sigma \Sigma_1 = \Sigma \Sigma_1^1 = \Sigma \Sigma_1^2 + \dots + \frac{1}{1-C} \Sigma \Sigma_1^i$$

$$\text{and} \quad \Sigma \Sigma_2 = SS^* : \Sigma \Sigma_1.$$

The division  $\frac{1}{1-C}$  is performed for each of the 16 matrix elements.

The determination  $\overline{C}^1 = \overline{C}$  while simple in concept is difficult computationally. The problem arises because the ratio  $\Sigma \Sigma_1^{i+1} / \Sigma \Sigma_1^i$  does not approach a constant independent of  $\mu, \mu_0$  very well, or quick enough in some cases. Sometimes, as in the case of Rayleigh scattering the ratio is of two zero matrices. This must be tested for and the ratio set equal to zero since division by zero causes interrupts in the execution of the computer program. Sometimes, however, for Rayleigh and Rayleigh-like scattering, the divisor is zero, while the dividend is not. This arises because, in the case of Rayleigh scattering at least, a finite number of points has been used to describe the Stokes parameters defined at an infinite number of points. The fourier terms that are computed for theoretically zero elements are not always evaluated to be exactly zero. This possibility among many others must be tested for and the ratio set to zero if the dividend is small enough. If the dividend is not small

enough, the next term in the series is computed and the process repeated.

For small optical depths a frequent problem arises. The ratio is not only not constant, but changes sign with  $\mu, \mu_0$ . It would be meaningless to compute an average in this case. Fortunately after a few (usually one or two) terms, the terms  $\Sigma \Sigma_1^i$  are so small compared with  $\Sigma \Sigma_1^1$  that they may be disregarded. Since the IBM 360 is only accurate to 6 places in single precision I have set this tolerance ratio to  $10^{-6}$ . As the optical depth increases this problem of sign change still exists but disappears in all cases tested so far before the 4th or 5th term.

For larger optical depths,  $\tau \gtrsim 5$ , another problem arises. Some of the terms in the matrix  $C^i$  oscillate back or forth around the limit, converging very slowly in the 3rd decimal place. Again we are fortunate because the difference that the oscillation causes in  $\Sigma \Sigma_1$  can usually be brought below  $10^{-6}$  with less than 5 terms.

There is yet another problem which must be dealt with. The ratio  $C^i$  approaches the limit rather quickly in most cases. However there are points in the ratio  $\Sigma \Sigma^{i+1} / \Sigma \Sigma^i$  which are either much greater or much less than  $C^i$ . As "i" increases these differences decrease. In the testing therefore we must make sure that truncation of the series with the first few terms does not impose a false value on  $\Sigma \Sigma_1$  at a few points. This is done by not allowing the series to terminate until the difference caused by accepting the maximum and minimum values for the ratios as  $C^i$  is less than  $10^{-6}$ . This is perhaps unnecessarily strict but

the amount of testing necessary to reduce the restriction and improve confidence in less demanding tests is prohibitive on the IBM 360/65 with the funds available. The testing subroutine can sometimes take as much time as the computation of a term  $\Sigma_1^1$ . In the future it will be possible to have the computer "learn" where to truncate the series from previous runs, thus saving considerable computer time.

Before concluding this section it would be worthwhile to mention some of the properties of the matrix  $C$ . Not all the properties of  $C$  has been investigated since that was not the intention in getting the program working. But a few have been noticed. For  $m=0$  as  $\tau$  gets larger the 4 non zero terms 11,12, 21,22 approach the same limit. The other 4 non-zero terms 33, 34,43,44 appear not to do so and in fact each term approaches its own limit. (The ratio for symmetrical terms like 34 and 43 are always identical). It is possible that these 4 terms do approach the same limit as  $\tau$  gets larger and " $i$ " increases, but if so it converges much more slowly than the first 4. In any case we would not expect them to converge to the same limit as the first 4 because for  $m=0$ , the sine terms are zero and the 4X4 matrix equations become reduceable to two 2X2 independent matrix equations.

For  $m \neq 0$  the matrix  $C$  approaches a constant, that is, all 16 terms have the same ratio. This effect was noted as  $\tau$  gets large, but it is possible that in fact the approach to a constant occurs for all  $\tau$  as " $i$ " increases.

One other effect may be noted in the matrix  $C$ . The integrations necessary in these computations have not yet been discussed with reference to the computer, but it is obvious that we must use a finite number of integration points. If we have chosen too few points to correctly perform the integrations, the problem will become most apparent in  $C$  for  $m = 0$  when the single scattering albedo is exactly 1. As  $\tau$  gets large  $C$  increases. Too few integration points result in  $C$  becoming greater than 1. At this point the computation ceases to have any meaning, and the answers for a few doublings back can be expected to be grossly inaccurate. Even if we were to use an infinite number of integration points we expect that as  $\tau \rightarrow \infty$  the answers become more and more inaccurate. This is due to the loss of accuracy in the ratio  $1/1-C$  as  $C$  approaches 1 with only 6 significant figures.

#### The Numerical Integration Scheme

The doubling equations as written yield the scattering and transmission matrices at any optical depth with complete accuracy. No approximations have been made in their derivation. The loss of accuracy occurs in the algorithm for programming the equations into a digital computer. Theoretically at least we may choose the initial optical depth small enough so that no loss of accuracy results in assuming only single scattering exists in the initial scattering and transmission matrices.

The integration scheme we have chosen is the method of Gaussian quadrature. Consider the integral

$$I = \int_0^1 F(x) dx.$$

This may be approximated by

$$I \approx \sum_{i=1}^N F(x_i) a_i$$

where  $a_i$  is a suitably chosen weight at  $x_i$ . If  $a_i$  is chosen as  $(x_{i+1} - x_{i-1})/2$ , that is, the distance between the midpoints of the intervals on either side of  $x_i$ , the effect is to evaluate the integral by computing the area under the trapezoids formed by joining the points with straight lines. The choice of  $x_i$  is arbitrary in this case.

Gaussian quadrature is much more sophisticated than this, in that the points are chosen a priori given the number of points, but basically the weights  $a_i$  may still be thought of as an interval around  $x_i$ .

There is no need to derive the properties of Gaussian integration as many books have sections on it (see, for example, R.T., p. 61). It is sufficient to note that it is an extremely powerful method capable of evaluating exactly the integral of any polynomial of order  $r \leq 2n - 1$  with only  $n$  points and their respective weights. It is still suprisingly accurate if  $r > 2n - 1$ . Unless otherwise mentioned, Gaussian quadrature will be used in evaluating all future integrals that occur. If the integration interval is other than  $(0,1)$ , say  $(a,b)$  then we must choose the points  $y_i$  and the weights  $b_i$  according to the scaling laws



$$1.38 \quad y_1 = a + (b-a)x_1$$

$$b_1 = (b-a) a_1$$

where  $x_1$  and  $a_1$  are the points and the weights on the interval  $(0,1)$ .

## V Elimination of Unnecessary Computations Through the Use of Symmetry Relations.

As we have seen previously, we may express some of the components of the scattering and transmission matrices in terms of other components of the same matrices. Changing our point of view from analytic to digital means that there exists some redundancy in the information content of the multidimensional arrays that are the digital analog of the scattering and transmission matrices. While there is no convenient way to reduce the space these arrays require in the computer, we can reduce the computations necessary to fill the space.

Equations 1.36 are the basis of this reduction. We need only assume one other fact in order to proceed. The symmetry properties were derived from the single scattering matrices. It is by no means obvious that these properties will continue to hold for large optical thickness. This however is true and we shall assume it implicitly henceforth. It was checked numerically in test runs of the program and served as a continuous check of conceptual mistakes in the creation of the computer program.

From equations 1.36 we have, in component form,

$$\begin{aligned}
 SS'_{ij}(\mu', \mu) &= X_{ij} SS'_{ji}(\mu, \mu') \\
 TT'_{ij}(\mu', \mu) &= Y_{ij} TT'_{ji}(\mu, \mu') \\
 SS^*_{ij}(\mu, \mu') &= Z_{ij} SS^*_{ij}(\mu, \mu') \\
 TT^*_{ij}(\mu, \mu') &= Z_{ij} TT^*_{ij}(\mu, \mu').
 \end{aligned}$$

1.39

From this we see that SS and TT need only be calculated for little more than half the matrix before all the information is computed. However that is not the whole story.

Each term in the doubling equations is, of course, computed separately. It is natural to assume that each term in the equations has the same symmetry as the term on the left hand side of the equals sign. This is not the case.

A posteriori this is obvious. Such is the wonders of hindsight. Consider the terms of the form  $e^{-\tau/\mu} \Sigma\Sigma_1 : TT$  and  $e^{-\tau/\mu_0} TT^* : \Sigma\Sigma_1$  in the SS equation. The remarks here apply equally to similar terms in the TT equation. These are the only terms in the equation which do not share the symmetrical form of the other terms. In examining the computer representation of these terms it was found that instead of each term being symmetrical with respect to itself, it was the sum of the terms that had this property. Moreover each term appeared to be expressible in terms of the other. We will now derive this property.

Consider the term  $\Sigma\Sigma_1 : TT$ . It is logical to assume that  $\Sigma\Sigma_1$  has the same symmetry as the term on the left hand side -- that of SS. This will not be proved, but the assertion has been checked numerically. The statement that  $\Sigma\Sigma_2$  has the same symmetry as TT is true also and has been checked as well.

The term  $\Sigma\Sigma_1 : TT$  may be written in component form as

$$(\Sigma\Sigma_1 : TT)_{ij}(\mu, \mu_0) = Q_1 \int_0^1 \sum_k \left( \Sigma\Sigma'_1{}_{ik}(\mu, \mu') r_{ijk} Q_k TT'_{kj}(\mu', \mu_0) \right) \frac{d\mu'}{\mu'}$$

where we have noted that the matrix  $Q$  may be written slightly ambiguously as  $Q_i$ . We could write it as a full matrix,  $Q_{i1} \delta_{i1}$ , but this would necessitate expressing another full matrix multiplication in the equation. If we let  $Q_{i1} = Q_i$  we must make sure that  $Q$  performs its intended function -- multiplication of the 3<sup>rd</sup> and 4<sup>th</sup> rows by 2. The appearance of  $Q$  in the equations occurs when we go from unprimed to primed terms.

$$\begin{aligned}
 &= Q_j \int_0^1 \sum_k \left( \Sigma \Sigma'_{ki}(\mu', \mu) X_{ki} r_{ikj} Q_k Y_{kj} TT'_{jk}(\mu_0, \mu') \right) \frac{d\mu'}{\mu'} \\
 &= Q_j \int_0^1 \sum_k \left( TT'^*_{jk}(\mu_0, \mu') Y_{kj} Z_{kj} r_{ikj} Q_k X_{ki} \Sigma \Sigma'_{ki}(\mu', \mu) \right) \frac{d\mu'}{\mu'}
 \end{aligned}$$

Now  $Y_{kj} Z_{kj} = X_{kj}$  since multiplication of these symmetry matrices is component by component. Then we have  $X_{kj} X_{ki}$  or  $X_{ik} X_{kj}$ .

A quick check by matrix multiplication shows that in fact

$$X_{ik} X_{kj} = X_{ij} \text{ independent of } k, \text{ summation over } k \text{ not implied.}$$

The right hand side of the equation may now be written

$$\begin{aligned}
 &= X_{ij} \int_0^1 \sum_k \left( TT'^*_{jk}(\mu_0, \mu') r_{ikj} \Sigma \Sigma'_{ki}(\mu', \mu) \right) \frac{d\mu'}{\mu'} \\
 &= X_{ij} (TT^* : \Sigma \Sigma_1)_{j1}(\mu_0, \mu).
 \end{aligned}$$

In matrix form we have proved

$$1.40 \quad \overline{\Sigma \Sigma}_1 : \overline{TT}(\mu, \mu_0) = X * \overline{TT}^* : \overline{\Sigma \Sigma}_1(\mu_0, \mu).$$

In a similar manner we may show that

$$1.41 \quad \overline{\Sigma \Sigma}_2 : \overline{TT}(\mu, \mu_0) = Y * \overline{TT}^* : \overline{\Sigma \Sigma}_2(\mu_0, \mu).$$

Thus we need only compute one of these sets of terms in full before the other becomes known.

The proof that the symmetry properties of SS and TT for single scattering continues to hold true for multiple scattering can be done with considerations such as those above. Each of the terms (or pairs of terms as noted above) in the doubling equations must be examined to show that they have the same symmetry properties as the matrix on the left hand side. Then if the optical depth of the initial layer is taken to be small enough so that single scattering prevails to any degree of accuracy, we may show by induction that the single scattering symmetry properties hold true for any optical depth and hence for multiple scattering.

## VI. A Collage of Time Saving Devices

The doubling equations which we have derived still need much discussion if we are to use them intelligently. There is still much we can do to reduce the time required to execute the computer program. The interplay between time and accuracy is the game we shall play. In this section we shall develop a method to significantly reduce computation time with no sacrifice in accuracy through the removal of single scattering from the computations. We shall discuss the effects of the number of fourier coefficients used, the number of Gauss points and the number of  $\phi$  points used in the fourier analysis. We shall also discuss the effect of making the initial and final optical depth a function of the number,  $m$ , of each fourier coefficient. We will find it useful to define a generalized single scattering albedo  $\tilde{\omega}_o^m$  which will help us gauge the importance of any fourier component in the final answer.

### Generalized Single Scattering Albedo

The single scattering albedo as generally defined is just a measure of the ratio of the energy scattered to the energy incident in any scattering event. In terms of our notation it is

$$1.42 \quad \tilde{\omega}_o = \frac{1}{4\pi} \int_0^{2\pi} \int_0^\pi \left( \frac{p_1(\theta) + p_2(\theta)}{2} \right) \sin \theta d\theta d\phi.$$

If we express  $\tilde{\omega}_o$  as an integral in  $\mu, \mu', \phi$  space of the fourier analyzed phase matrix we find that only the 1<sup>st</sup> fourier matrix gives a non-zero contribution.

We have shown how to get  $\overline{SS}^m$  and  $\overline{TT}^m$ . If we let  $\overline{SS}_u^m$  and  $\overline{TT}_u^m$  stand for the matrices unadjusted by the coefficients that converted them from a phase matrix to scattering and transmission matrices (see equation 1.18) then the set  $\{\overline{SS}_u^m, \overline{TT}_u^m\}$  represents the fourier analysed phase matrix.  $SS_u^m$  and  $TT_u^m$  represent respectively light scattered in the backward and forward hemispheres. In terms of the phase matrix  $\overline{R}$  of equation 1.14,

$$\tilde{\omega}_o(\mu) = \frac{1}{4\pi} \int_0^{2\pi} \int_{-1}^1 R(\mu, \mu', \phi' - \phi) d\mu d\phi' .$$

Here, and similarly in what follows, unbarred terms like  $R$  mean  $(R_{11} + R_{12} + R_{21} + R_{22})/2$ , a representation of the scattered intensity for unpolarized light incident.

$$\tilde{\omega}_o(\mu) = \frac{1}{4\pi} \int_0^{2\pi} \int_0^1 \{S_u(\mu, \mu', \phi' - \phi) + T_u(\mu, \mu', \phi' - \phi)\} d\mu' d\phi'$$

where the  $u$  stands for unadjusted by the coefficients of equation 1.18. Now writing  $S_u$  and  $T_u$  in terms of their fourier coefficients according to the formula of equation 1.26, and noting that  $\int_0^{2\pi} \cos m\phi d\phi = 0$ ,  $m \neq 0$

$$1.43 \quad \tilde{\omega}_o(\mu) = \int_0^1 \{SS_u^o(\mu, \mu') + TT_u^o(\mu, \mu')\} d\mu' .$$

We have written  $\tilde{\omega}_o(\mu)$  although theoretically we would expect  $\tilde{\omega}_o(\mu) = \tilde{\omega}_o$ , a constant. But what we have in practice is a measure of the accuracy of the fourier analysis, and the gaussian integration. If we have chosen too few  $\phi$  points to accurately describe the phase matrix or if we are using insufficient gauss points in the integration, the deficiency shows

up most markedly in  $\tilde{\omega}_0(\mu)$ . Experience has shown that a very good feel for the accuracy of the doubling computations can be gotten from the degree to which  $\tilde{\omega}_0(\mu)$  departs from  $\tilde{\omega}_0$ . Unhappily  $\tilde{\omega}_0(\mu)$  depends upon 2 parameters and there is no easy way to separate their effects other than vary each one separately. In practice both were varied together according to intuition based on limited experience.

Equation 1.43 leads immediately to the generalization for  $m \neq 0$ .

$$1.44 \quad \tilde{\omega}_0^m(\mu) = \int_0^1 \{ |SS_u^m(\mu, \mu')| + |TT_u^m(\mu, \mu')| \} d\mu'$$

The absolute value signs grew out of the fact that the second fourier coefficient for rayleigh scattering ( $m=1$ ) gives  $\tilde{\omega}_0^1(\mu) = 0$ , although each term by itself produces a non-zero integral. Oddly enough the answers are the same with or without the absolute value signs for all non-rayleigh scattering laws tested.

Clearly  $\tilde{\omega}_0^m(\mu)$  does not have the same physical meaning as the  $m = 0$  term. For  $m \neq 0$  we find that it is not a constant but a function of  $\mu$  (as advertised). Just the same, however, it can serve as a guide to guessing three other accuracy parameters -- specifically  $M$ , the number of fourier terms needed,  $\tau_1^m$ , the initial optical depth for each  $m$ , and  $\tau_F^m$  the optical depth at which the results for a semi-infinite atmosphere are reached.

It is found that  $\langle \tilde{\omega}_0^m(\mu) \rangle$ , an eyeball average over  $\mu$ , decreases with increasing  $m$ . There are exceptions to this rule,



but the deviation from monotonic is usually small. Since the doubling equations for each  $m$  takes no note of the value of  $m$  we expect that statements made about the effect of  $\tilde{\omega}_0$  on the importance of various orders of scattering carry over to some degree for  $\langle \tilde{\omega}_0^m(\mu) \rangle$ .

Since 8 of the 16 terms are zero for  $m = 0$ , there is in fact a difference. However the doubling equations written for intensity only contain only cosine terms, none of which are zero for  $m = 0$ , and thus the above statement appears to be more accurate when applied to intensity only. Much of the polarization is due to simple scattering and this, as we shall see, is dealt with in a manner that makes  $M$  effectively infinite for single scattering. Then any decision we make on the basis of  $\langle \tilde{\omega}_0^m(\mu) \rangle$  in our choice of  $M$ ,  $\tau_i^m$ , and  $\tau_F^m$  will not affect the polarization any more than it does the intensity.

As we have noted  $\langle \tilde{\omega}_0^m(\mu) \rangle$  decreases as  $m$  increases. This means that the importance of secondary and higher order scattering diminishes with respect to single scattering. We may therefore expect that increasing the initial optical depth,  $\tau_i^m$ , as  $m$  increases will increase the speed of the solution with little sacrifice to accuracy. Eventually for each optical depth,  $\tau$ , of interest an  $m = M - 1$  is reached beyond which  $\tau_i^m = \tau$ . Then we only need compute  $M$  fourier terms if we account for the single scattering due to terms  $m \geq M$ . We do this by a method due to Hansen and Pollack<sup>7</sup> for doubling equations in the intensity only case.

$$1.45 \quad \bar{S}(\tau; \mu, \mu'; \phi' - \phi) = \sum_{m=0}^{m-1} \frac{\bar{S}S^m(\tau; \mu, \mu') - \bar{S}S_s^m(\tau; \mu, \mu')}{\sin m(\phi' - \phi)} \cos m(\phi' - \phi) \\ + \bar{S}_s(\tau; \mu, \mu'; \phi' - \phi) ,$$

where  $S_s$  is the scattering matrix due to single scattering at optical depth  $\tau$ , and  $\{SS_s^m\}$  are the  $M$  fourier components of  $S_s$ . Equation 1.45 permits a reduction in computer time by as much as a factor of 4.

The decrease of  $\langle \omega_0^m(\mu) \rangle$  with  $m$  permits additional time to be saved for calculations to large optical depths. The approach to a semi-infinite atmosphere is achieved at  $\tau \leq 8$  for all  $m > 0$ . Terms with  $\mu, \mu' \rightarrow 0$  approach this limit at lower optical depths than terms with  $\mu, \mu' \rightarrow 1$ . Radiation entering or leaving the scattering layer near normal incidence is much more likely to feel the effect of deeper particles than radiation at grazing angles which is affected more by single scattering in the upper layers.

Not all of the values in fourier scattering arrays contribute significantly to the integrations in the doubling equations. In the case of "intensity only" equations we find that as  $m$  increases terms with  $\mu, \mu' \rightarrow 0$  are much larger than  $\mu, \mu' \rightarrow 1$ . Thus we may decrease the number of gauss points actually used in the integration,  $K_m$ , until as  $m \rightarrow M$  only the terms with  $\mu, \mu' \sim 0$  are used. With the addition of polarization the situation is more complicated, although the same time saving method is valid. For  $m = 0$  we have in fact  $(\mu, \mu' \rightarrow 1) \gg (\mu, \mu' \rightarrow 0)$  for all 16 terms. As  $m$  becomes large this trend reverses itself to become

$(\mu, \mu' \rightarrow 1) < (\mu, \mu' \rightarrow 0)$  for all 16 terms. The complication arises because each of the 16 terms does not reach this limit in the same way or at the same rate. Polarization calculations, it appears, require more care in the selection of  $K_m$  than do intensity calculations.

#### REFERENCES - I

1. S. Chandrasekhar, Radiative Transfer, Dover Book Co., Inc., New York (1960)
2. J.D. Dave, Program # 360-D-174002, I.B.M. Programming Dept.
3. R. Ruffine, J.G.R., 72, 4069 (1967)
4. J.W. Hovenier, J. of Atmos. Sci., 26, 488 (1969)
5. H.C. van de Hulst, A New Look at Multiple Scattering, Mimeographed Report, NASA, Institute for Space Studies, New York (1963)
6. J.E. Hansen, Ap.J., 155, 565 (1969)
7. J.E. Hansen and J.B. Pollack, J. Atmos. Sci., 27, 265 (1970)

## Part II

### THEORETICAL CALCULATIONS OF DISK INTEGRATED AND DISK RESOLVED POLARIZATION OF PLANETARY ATMOSPHERES

#### Abstract

The theory developed in Part I is used to calculate the disk resolved polarization of model atmospheres as a function of phase angle. The theory of the integration of the Stokes parameters over the illuminated disk of the planet is presented. The polarization as a function of position on the disk is shown superimposed on the planetary disk drawn for various phase angles for three different types of phase matrices, including the Rayleigh phase matrix and one that matches the phase variation of Venus at 1 micron wavelength. Comparison of the disk resolved Venus observations with calculations is good. Disk integrated results are given as well. The effect of the single scattering albedo of the scatterers is investigated. The polarization observations of Venus and Jupiter are discussed in the light of general principles that have been inferred from examination of the results of the model calculations. Disk resolved polarization observations may be an unharvested field of useful information.

## I INTRODUCTION

Most of what we have learned about the planets has been learned from the light they reflect. By far most of the efforts to understand the planets to date have concentrated on some aspect of the reflected intensities. The polarization of the light has gone by comparatively unexplored by observer and theorist alike. This gap in our knowledge was caused by a singular inability to interpret the observations. We attempt to further develop this capability in the present paper.

Polarization in planetary atmospheres is a difficult subject to treat. Only recently, with the availability of high speed electronic computers has it been possible to attempt polarization calculations at all. The inclusion of polarization in radiative transfer computations requires an increase in computer time of a factor of 27 to 64 depending on the algorithm chosen.

The computational expense of these calculations has been a major factor in determining the content of the work that follows. It was not possible to do extensive model calculations, both because of the many computer runs necessary and the lack of an interactive capability caused by the physical distance between the programmer and the computer. The program was designed but never run on an

I.B.M. 360/65 at Cornell University and run on an I.B.M. 360/91 at the Goddard Space Flight Center in Maryland.

We shall explore the radiative transfer calculations from the input stage of a single scattering phase function to the output stage which describes the disk integrated and localized disk polarizations. Extensive use is made of the theory and associated computer program developed in Part I of this thesis. The computations are made for semi-infinite atmospheres with the single scattering albedo as a parameter. In addition to the planetary phase angle dependence of the polarization of the entire planet, we give many diagrams of the polarization across the planetary disk. Both the total polarization and the polarization of light scattered more than once will be explored.

We investigate three different types of phase functions including the Rayleigh phase function and one that matches the phase variation of Venus at 1 micron wavelength. The discussion of the three cases is intended to be instructive rather than exhaustive. The behavior of the polarization is discussed in detail so that a good a priori knowledge can be derived for planetary polarization from the single scattering information alone. Many observational effects that at first sight appear strange will be seen to be rather easily understood. The work here should help to provide

a basis for future model calculations and the interpretation of future observations, including the Grand Tour observations of the outer planets.

The next two sections describe the computational procedure; section IV gives the results for the three cases studied; and section V discusses some of the observations in light of what was learned in section IV.



## II. POLARIZATION AS A FUNCTION OF POSITION ON A PLANETARY DISK--THEORY

It is usual to discuss the results of radiative transfer calculations for plane parallel layers in terms of three parameters,  $\theta$ ,  $\theta'$ , and  $\Delta\phi$  where  $\theta$  and  $\theta'$  are, respectively, the angles of emergence and incidence and  $\Delta\phi$  is an azimuthal coordinate. These are the variables of the scattering matrix function  $\bar{S}(\theta, \theta', \phi' - \phi)$  that was derived in Part I of this thesis. Typically one coordinate is held constant and results are given in the other two coordinates. The figures thus produced are rarely capable of being immediately interpreted in a planetocentric coordinate system. With the addition of polarization and its intimate dependence on the azimuthal coordinate, the usefulness of such figures is reduced, for most astronomical purposes. Tables of values such as those of Coulson et al. (1960) for a finite Rayleigh atmosphere require extensive interpolation in one, two, or three dimensions to describe the state of polarization of light reflected from a given spot on the disk for a given planetary phase angle.

In this section, therefore, we will show how to describe the intensity and polarization of light reflected from a planetary disk as a function of phase angle and position on the disk. By doing this we can gain additional

physical insight into the effects of multiple scattering, since the phase angle of a planet is just  $180^\circ$  minus the scattering angle for single scattering,  $\theta$ . Thus every point on the disk scatters the light to the observer through the same angle and the polarization due the single scattering alone is everywhere the same across the disk.

Before discussing the planetary geometry, let us review the use and meaning of the Stokes intensity  $\bar{I}(\theta, \theta', \phi' - \phi)$ . As defined in Part I of this thesis  $\theta$  and  $\theta'$  are angles of emergence and incidence respectively, measured from the local normal. The local normal and the direction of propagation define the meridian planes of emergence and incidence, respectively. The azimuth is measured from an arbitrary direction and is positive in a counterclockwise direction, when seen from above. (In the convention of Part I, azimuth is measured from the direction where the radiation appears to have entered the scattering event. This introduces a factor of  $\pi$  radians in figure 1.4. The convention is the same below.) The azimuth of the observer and source are  $\phi - \pi$  and  $\phi'$  respectively. Thus propagation back to the observer corresponds to  $\phi' - \phi = -\pi$  and  $\phi' - \phi$  is negative over the upper disk of the planet shown in figure 2.1, discussed below. (The minus sign here corresponds directly to the adventitious decision to display the planetary disk as a

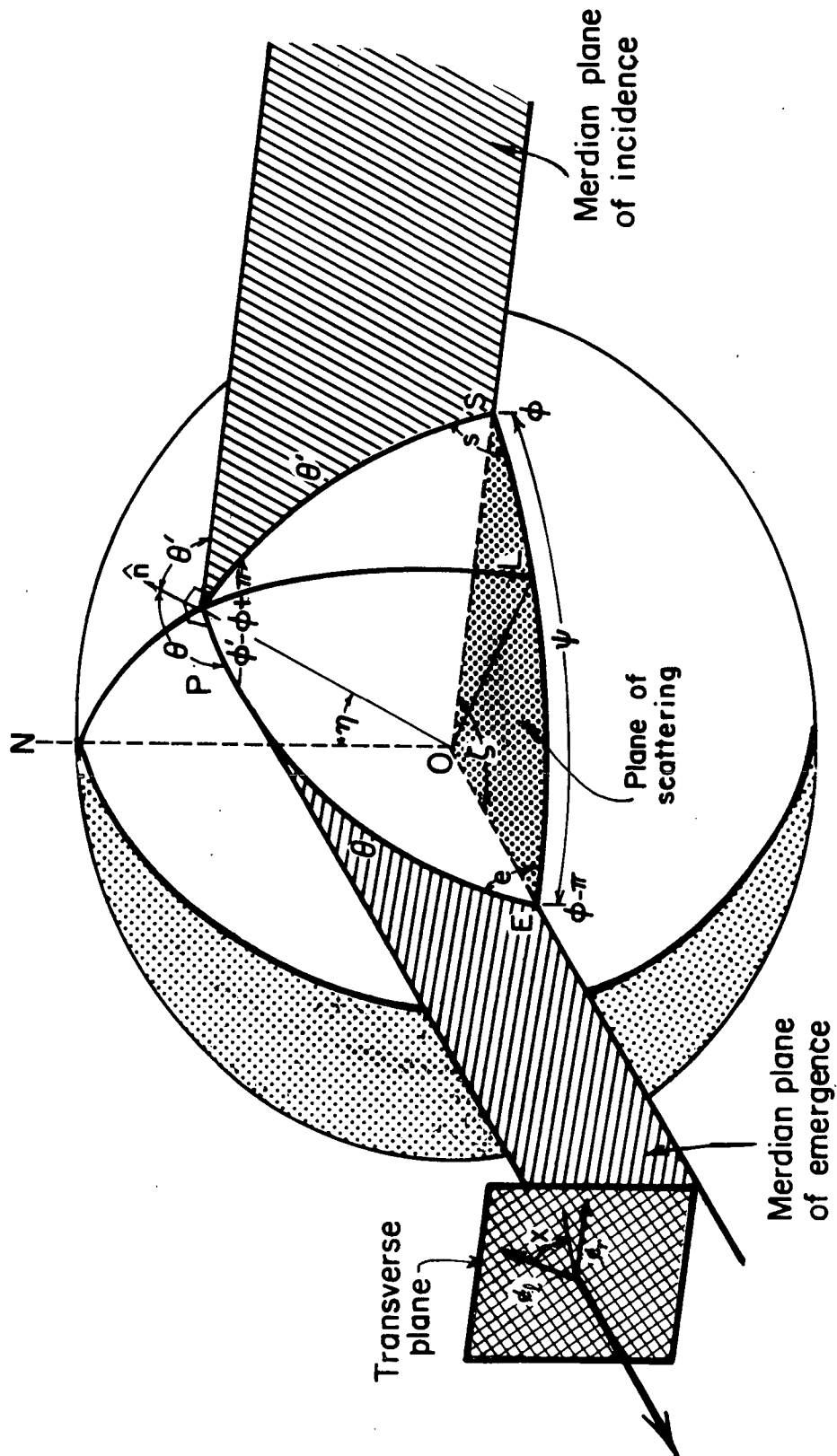


Figure 2.1 Geometry of scattering from a planetary disk. Subearth point is E, subsun is S, and scattering event is at P. The direction of polarization is given by  $\chi$ , measured from  $e_1$ , a unit vector parallel to the plane of emergence.

function of negative phase angles, i.e., the earth-planet-sun angles of Venus before inferior conjunction.)

Figure 1.4 of Part I develops the scattering event in a non-planetary geometry. The direction in the plane transverse to the direction of propagation in which the intensity is maximum is called the direction (or plane) of polarization. It is an angle  $\chi$  measured in a clockwise direction from a vector,  $\phi_1$ , in the transverse plane that is parallel to the meridian plane of emergence, propagation towards the observer. See figure 1.1 of Part I for a simple picture.

The angle  $\chi$  is given by

$$2.1 \quad \tan 2\chi = U/Q$$

where  $U$  and  $Q$  are components of the Stokes intensity vector  $\bar{I}[I, Q, U, V]$ , and

$$2.2 \quad Q = I_l - I_r$$

where  $l$  and  $r$  refer, respectively, to directions parallel and perpendicular to the meridian plane.

The previous discussion while conceived of in terms of figure 1.4 should now be reread when considering figure 2.1 which give a picture of the geometry of scattering from a planetary atmosphere seen at a phase angle  $\Psi = \pi - \theta$ , where  $\theta$  is the scattering angle of the single scattering phase function. The subsun point is at S, the subearth point at E and the scattering takes place at P. Vectors

$\phi_1 = \hat{n}$  and  $\phi_r$  are parallel and perpendicular to the plane of emergence and lie in the transverse plane. The angles  $\theta$ ,  $\theta'$  and  $\phi' - \phi + \pi$  are clearly indicated. Angle  $e$  at  $E$  can be considered a planetary azimuth coordinate since when viewed along  $EO$  all great circles beginning at  $E$  appear as radial lines. Vector  $\phi_1$ , parallel to the plane of emergence, is therefore radial as viewed by the observer. Thus angle  $\chi$ , the polarization direction, is measured from the radial direction as seen by the observer.

The geometry of angle  $\chi$  once again points up the difficulty of obtaining a physical insight from graphs of  $\chi$  versus  $\theta, \theta'$ , or  $\Delta\phi$ . For example, if the polarization is everywhere normal to the scattering plane  $EOS$ ,  $\chi$  varies across the disk, even though the quantity  $\chi - e$  is a constant. It was decided therefore to display the computer results as a function of  $e$  and  $\theta$ . The printed output gave the quantities  $\chi$  and  $\chi - e$  as a function of  $e$  and  $\theta$ . When the polarization is radial  $\chi = 0$ ; when it is tangential to the limb  $\chi = \pm\pi/2$ . On the other hand when  $\chi - e = 0$  the polarization is normal to the scattering plane; when  $\chi - e = \pm\pi/2$  it is parallel.

Positive (or negative) polarization is a term that suffers from some ambiguity. It is usually meant to express the fact that the electric vector normal (or parallel) to the scattering plane is greater than the par-

allel (or normal) vector. It is a term that is unambiguous in the context of single scattering, for then no planes are defined besides the scattering plane. In the context of a planetary atmosphere, however, the meaning of the term is confused by the presence of the plane of emergence with respect to whose direction the polarization is measured. We then may mean radial when we say positive or tangential when we say negative. To avoid confusion we will henceforth qualify "positive" or "negative" with "radial" or "tangential" whenever necessary.

Also note that for single scattering the polarization across the disk can be only positive or negative, whereas for multiple scattering it can be positive, negative, radial positive, tangential negative or anything in between, although these cases are by far most often encountered observationally and theoretically. On the other hand the polarization integrated over a uniform sphere must again be either positive or negative because then only the earth-planet-sun plane is defined.

It remains now to detail the equations for the degree of polarization,  $P$ , and the direction of polarization  $\chi$ . The degree of polarization at  $(e, \theta)$  is a mathematically positive quantity and is given by

$$2.3 \quad P = \frac{(Q^2 + U^2 + V^2)^{\frac{1}{2}}}{I}$$

I, Q, U, V are the four components of the Stokes vector. The degree of linear polarization,  $P_L$ , is what we usually measure however.

$$2.4 \quad P_L = \frac{(Q^2 + U^2)^{\frac{1}{2}}}{I}$$

$P_L \approx P$  for the cases that we have calculated, the degree of circular polarization,  $P_C$ , usually being small.

$$2.5 \quad P_C = \frac{V}{I}$$

The polarization direction for linear polarization is given by equation 2.1.

Before ending this section it is necessary for completeness to describe the transformation  $(\theta, \theta', \Delta\phi) \rightarrow (e, \theta, \Psi)$ . We also discuss the interpolation necessary to derive  $\bar{I}(e, \theta, \Psi)$  from  $\bar{I}(\theta, \theta', \Delta\phi)$ , the output of the computer program.

Spherical geometry gives

$$\begin{aligned} \cos\Psi &= \cos\theta \cos\theta' + \sin\theta \sin\theta' \cos(\phi' - \phi + \pi) \\ 2.6 \quad &= \cos\theta \cos\theta' - \sin\theta \sin\theta' \cos(\Delta\phi) \\ \Delta\phi &= \phi' - \phi \end{aligned}$$

Also,

$$2.7 \quad \cos(e) = \frac{\cos\theta' - \cos\theta \cos\Psi}{\sin\theta \sin\Psi}$$

A set of  $(\theta, \theta', \Delta\phi)$  points is then related to a set of  $(e, \theta, \Psi)$  points. Thus  $I(e, \theta, \Psi)$  is known, but not necessarily at the  $e_o, \Psi_o$  points desired. We must therefore interpolate in 2 dimensions in  $e, \Psi$  space to obtain the results at  $e_o, \Psi_o$ . We now discuss such a scheme.

We are handicapped by the fact that  $e, \Psi$  space is not uniformly filled with known points. This has two consequences. First, none of the conventional interpolation schemes will work. Second, large errors are introduced at place where the data is sparse.

The interpolation scheme we employ here is a modified Lagrangian interpolation. The method produces a function of two variable that is restricted such that it passes through the 9 points nearest to the required point. The formula is

$$f(e_o, \Psi_o) = \sum_{i=1}^3 \sum_{j=1}^3 f(e_i, \Psi_j) \times \prod_{n \neq i}^3 \frac{(e_o - e_n)}{(e_i - e_n)} \times \prod_{m \neq j}^3 \frac{(\Psi_o - \Psi_m)}{(\Psi_j - \Psi_m)}$$

Equation 2.8 produces quite reliable results. It appears that  $3^2$  is the optimum number of points for a good fit, because more points introduce uncontrolled spurious oscillations of the fitting function. The results from equation 2.8 degrade considerably when either or both required points are outside the known grid of points. This occurs at the limb of the planet and at large phase angles.



### III POLARIZATION AND INTENSITY INTEGRATED OVER THE DISK OF A PLANET-THEORY

The theory of the integrated diffuse intensity of a planetary disk is well known. The addition of polarization considerations complicates matters by requiring a rotation of the coordinate system at each point on the disk before the standard equations may be applied. We shall discuss below the integration of the Stokes quantities over the disk, as well as the algorithm used to produce the computer code.

To perform an integration over the disk we must first rotate the coordinate system in which the Stokes vector is defined into one that is independent of the position on the disk. Let this new coordinate system be the directions in the transverse plane of figure 2.1 that are parallel and perpendicular to the scattering plane EOS. The axes of observation must then be rotated by  $\pi/2 - e = \rho$  in a counterclockwise direction. The effect of rotation of the coordinate axes is to subject  $\bar{I}_p$ , the Stokes vector in the coordinate system defined at P, to the transformation

$$2.9 \quad \begin{pmatrix} I \\ Q \\ U \\ V \end{pmatrix} = \begin{pmatrix} 1 & 0 & 0 & 0 \\ 0 & -\cos 2e & -\sin 2e & 0 \\ 0 & \sin 2e & -\cos 2e & 0 \\ 0 & 0 & 0 & 1 \end{pmatrix} \begin{pmatrix} I_p \\ Q_p \\ U_p \\ V_p \end{pmatrix}$$

Only integration over the upper half of the disk is required if we include the result that integration over both halves yields  $U = V = 0$ . Every point  $P_u$  on the upper half has a mirror point  $P_l$  on the lower half with  $\theta$  and  $\theta'$  the same, but with a difference in sign in the angles  $e$  and  $e'$ . The Stokes parameters  $I$  and  $Q$  are even functions of  $\Delta\phi$  but  $U$  and  $V$  are odd. (See Part I of the thesis). The result of adding the Stokes intensity at  $P_u$  and  $P_l$  is, in the new coordinate system,

$$2.10 \quad \begin{pmatrix} I \\ Q \\ U \\ V \end{pmatrix} = 2 \begin{pmatrix} 1 & 0 & 0 & 0 \\ 0 & -\cos 2e & -\sin 2e & 0 \\ 0 & 0 & 0 & 0 \\ 0 & 0 & 0 & 0 \end{pmatrix} \begin{pmatrix} I_p \\ Q_p \\ U_p \\ V_p \end{pmatrix}$$

Note that we would only expect to observe circular polarization, the  $V$  term, if the observations were to be made over half the disk.

The rest of the treatment of the disk integration can now proceed along well traveled paths. The only refinement is that we write  $I_1$  in place of  $I$  in the standard equations, where  $I_1 = I$  and  $I_2 = Q$ . Below we shall briefly discuss the Bond albedo,  $A_B$ , the geometric albedo,  $p$ , the phase integral,  $q$ , and the phase variation of intensity,  $p(\Psi)$ .

The Bond albedo is the measure of the total energy reflected from the planet and equals the ratio of the total

energy reflected by the planet to the total energy incident. The derivation of  $A_B$  will not be pursued here since many sources are available for a complete discussion (most recently, Kattawar and Adams, 1971). It is

$$2.11 \quad A_B = p_1(0)q$$

where

$$2.12 \quad p_1(\Psi) = \frac{1}{\pi F} (\cos \Psi + 1) \int_0^1 (1-\beta^2)^{\frac{1}{2}} d\beta \int_{-1}^1 I_1(\beta, \xi) d\xi$$

$$\text{where} \quad \beta = \cos \eta$$

$$\text{and} \quad \xi = \frac{2 \sin \zeta}{(\cos \Psi + 1)} + \frac{(\cos \Psi - 1)}{(\cos \Psi + 1)}$$

and  $\eta$  and  $\zeta$  are related to  $\theta$  and  $\theta'$  by the equations

$$\cos \theta' = \sin \eta \cos(\zeta - \Psi)$$

$$\cos \theta = \sin \eta \cos \zeta$$

The phase integral used in equation 2.11 above is defined as

$$2.13 \quad q = 2 \int_0^\pi \frac{p_1(\Psi)}{p_1(0)} \sin \Psi \, d\Psi.$$

The angles  $\zeta$ ,  $\eta$ , and  $\Psi$  are defined in figure 2.1.

The degree of polarization at any phase angle  $\Psi$ , is then

$$2.14 \quad P_L = \frac{p_2(\Psi)}{p_1(\Psi)}$$

Note that since  $U = 0$  the direction of polarization can be

only perpendicular or parallel to the scattering plane, corresponding to whether  $P_L$  is positive or negative respectively. This is the same property displayed by single scattering from a sphere, and indeed, the planet may be regarded as a very large uniform sphere in no way different in scattering geometry from the particles of which it is composed.

The algorithm developed to evaluate equation 2.12 was, it turns out, not optimally conceived. The accuracy of the results is not as high as would be expected considering the number of integration points used. The accuracy will be discussed at the beginning of section IV. The failure to iterate on the integration scheme was the result of the physical distance between the computer used to develop the program and the computer used to test and run it. Accuracy tests were not possible at Cornell.

The integration in  $(\xi, \beta)$  space was performed using only those points on the disk that corresponded to the Gaussian points in the variable  $\mu$  at which the functions were known. This left  $\mu'$  and  $\Delta\phi$  free to follow the path of integration. Two dimensional interpolation in these variables was necessary at every integration point. The integration was performed in two steps. First the integral was evaluated over  $\beta$ --i.e., over angle  $\eta$  in figure 2.1. Parabolic sections were fitted to the points along NPL ( the line of longitude through P ), and the integra-

tion performed analytically. The integration over  $\xi$  was done similarly. Only those  $\xi$  values were used that corresponded to  $\cos\zeta = \mu$ , where  $\mu$  is a Gaussian point, thus insuring that the integration over  $\beta$  included a point on the equator.

This scheme was deemed preferable to a three dimensional interpolation which would be necessary to find the values of the function at points dictated by a sophisticated quadrature scheme. Kattawar and Adams (1971), for example, use Chebyshev polynomials of the second kind over  $\xi$  and Legendre-Gauss quadrature over  $\beta$ . They do not indicate, however, how they evaluate the functions at these points. It is possible that the integration scheme described here can be improved, but it is adequate for many planetary atmosphere problems.

The integration over the disk was checked using a code that does not require interpolation and gives  $A_B$  and  $p = p_1(0)$  very exactly via Gaussian quadrature. Thus  $q$  is accurately known and the integral of  $p_1(\Psi)$  in equation 2.13 may be checked against a more exact value.

After the definition of  $p$  given by Russell (1916),  $p$  is the ratio of the observed brightness of the planet at full phase to that of a flat disk of the same size illuminated and viewed normally and reflecting all the incident

light by Lambert's law. Thus

$$2.15 \quad p = \frac{\int_0^{2\pi} \int_0^1 I(\mu=\mu'; \phi' - \phi = \pi) r^2 \mu d\mu d\phi}{\pi r^2 F}$$

$$2.16 \quad I(\mu) = \frac{S(\mu)F}{4\mu}$$

and hence

$$2.17 \quad p = \frac{1}{2} \int_0^1 S(\mu) d\mu$$

(This is a factor of 4 smaller than the radar cross section of a planet with the same scattering function.) The integral in equation 2.17 can be formed accurately since the points required for the Gaussian quadrature are just those points at which the function was calculated.

The Bond albedo is the integral over all positions on the disk of the energy flux reflected into all directions from each point, divided by the incident energy. Thus

$$2.18 \quad A_B = \frac{\int_0^{2\pi} ds \int_0^1 r^2 d\mu' \int_0^{2\pi} d\phi \int_0^1 I(\mu, \mu', \phi) \mu d\mu}{\pi r^2 \pi F}$$

From equation 1.26 we have

$$2.19 \quad I = \frac{F}{4\mu} S = \frac{F}{4\mu} \sum_{m=0}^N SS^m \cdot (4 - 2\delta_{0m}) \cdot \cos(m\phi)$$

Only the  $m = 0$  term survives the integration over  $\phi$ .

Equation 2.18 reduces to

$$2.20 \quad A_B = 2 \int_0^1 \int_0^1 SS^\circ(\mu, \mu') d\mu d\mu'$$

This again is accurately computable by Gaussian quadrature.

#### IV REGIONAL AND DISK INTEGRATED POLARIZATION-RESULTS

This section represents a set of tentative steps leading to a fuller understanding of polarization in planetary atmospheres. Until now, no theoretical work has shown the distribution of polarization over a planetary disk, and the appearance of the disk in polarized light was virtually unknown. Those measurements that have been made have had no theoretical framework with which to compare, and thus a wealth of information goes uninterpreted, unsifted for possible information content. It is hoped that the discussion here will help to provide a basis for understanding some of the more general polarization effects displayed by a planetary atmosphere.

Unfortunately, it was not possible to make a comprehensive survey of the effects of different phase functions. The polarization program requires about 4 minutes for the Rayleigh phase function and up to 15 minutes or more for the forward scattering phase functions studied. The computations were performed on an I.B.M. 360/91 (a very fast machine). Computer time allotments limited the number of times the program could be run and the physical distance between the programmer and the computer limited the number of iterations. Thus the sample of phase functions studied is not comprehensive. It is hoped that it is representative.



We have chosen to display below both disk integrated and disk resolved results for three phase matrices, selected from a larger set of similar phase matrices with differing  $\tilde{\omega}_0$ 's. In each of the following three subsections we give these comprehensive results as well as displaying the variation of the disk integrated quantities with  $\tilde{\omega}_0$ . Both the total light scattered, designated by "T", and the multiply light with single scattering removed, "M", will be investigated.

The three phase matrices A, B, and C will be discussed thoroughly in their respective subsections. Briefly, Case A corresponds to Rayleigh scattering; Case B to a forward scattering phase function the polarization curve of which exhibits two neutral points between  $0^\circ$  and  $180^\circ$ ; and Case C to a forward scattering negatively polarized phase function which matches the disk integrated polarization of Venus at 1. micron wavelength.

A complete table of A, p, q,  $q/p(50^\circ)$  (Russell's rule) for all the calculated cases as a function of  $\tilde{\omega}_0$  is given in the Appendix.

### 1. Accuracy

Rayleigh scattering for  $\tau = 1$  was compared with the tables of Coulson et al.(1960) with agreement to four places. The doubling program was also checked by comparing the results

for an arbitrary phase function with the results obtained by Hansen (private communication) for the same phase function. There again the agreement was to better than 4 places, although Hansen's computer program was derived independently using the doubling method originally suggested by Van de Hulst (1963). At the Gaussian points we expect an accuracy of  $\pm 0.01\%$  in the percent polarization. Interpolation over the disk gives an accuracy of  $\pm 1.05\%$  for polarization greater than  $0.05\%$ . This was estimated by noting that the interpolated single scattering polarization should be constant over the disk. Integration over the disk is accurate to  $\pm 1.01\%$  or  $\pm 0.2\%$ , whichever is higher, for  $0 < \Psi < 140^\circ$ , and  $\pm 1.2\%$  or  $\pm 1.0\%$  for  $140^\circ < \Psi < 160^\circ$ . Beyond  $160^\circ$ , we do not accept the integrated results at all. Disk integrated accuracy was estimated by internal checking and by comparison with the table of Kattawar and Adams (1971) for disk integrated Rayleigh scattering for  $\tau = 10 \neq \infty$ . All error estimates are approximate since they depend on the phase function being studied as well as the phase angle and position on the disk.

Rayleigh scattering with  $\tilde{\omega}_0 = 1$  gave a Bond Albedo of 0.99 not 1.0 as would be expected. This is the product of using single precision arithmetic with only six significant figures and the loss of accuracy associated with dividing by the difference of two numbers quite close to unity when  $\tilde{\omega}_0 = 1$ .

Figure 2.2 shows the phase variation of Venus at  $1\mu$  as calculated by Hansen (1971) and myself. Input parameters to the Mie program were supplied by Hansen, and  $\tilde{\omega}_0$  was chosen to match the Bond albedo of the planet following Hansen's method. The comparison, however, can only be considered approximate, for Hansen later modified his best fit parameters in the published graphs. Figure 2.2 lends greater confidence to the results below. The solid line is Hansen's results, the circles have been calculated here and the data points give the observations of Coeffen and Gehrels (1969).

## 2. Results

### A The Rayleigh Phase Matrix

Rayleigh scattering is the most thoroughly worked area of radiative transfer theory, with the exception of isotropic scattering. It holds this distinction both because it has the simplest realistic phase function (requiring only 3 Fourier components and 6 Gaussian quadrature points for comparison with Coulson et al.'s (1960) tables) and because it is the case to which the phase function of any scatterer returns as the wavelength is increased. It is also important at short wavelengths for the upper molecular layers of many planetary atmospheres attain appreciable optical depths in the ultraviolet.

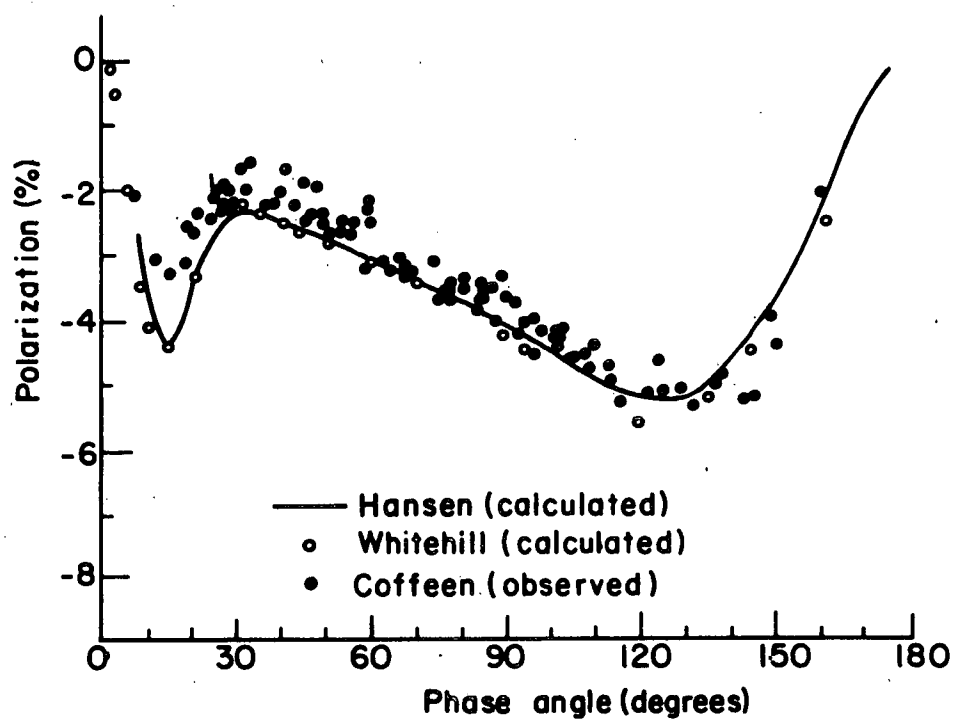


Figure 2.2 The disk integrated polarization of Venus at  $0.99\ \mu$  as observed by Coffeen and Gehrels (1969a), as calculated by Hansen (1971) and as calculated here using preliminary parameters supplied by Hansen.

Treatments of Rayleigh scattering range from the analytical discussion by Chandrasekhar (1960) to a set of tables for the three non-zero Stokes parameters published by Coulson et al. (1960). Faster computers capable of handling more complex scattering functions have led to a decreased interest in Rayleigh scattering, and yet the ease of data handling that these computers provide has increased interest in disk integrated Rayleigh calculations. Hansen (1971) published graphs of disk integrated polarizations as a function of optical depth. In a more extended treatment Kattawar and Adams (1971) have published tables of disk integrated polarizations and intensities as a function of optical depth and ground albedo.

To the body of knowledge on Rayleigh scattering we add below the polarizations across the disk of a semi-infinite Rayleigh atmosphere. Results at selected phase angles and non-unity single scattering albedos are also included. Concurrent with the multiple scattering figures is a set of figures with the single scattering removed, included to dispell the convenient but incorrect idea that light scattered more than once is unpolarized, as well as to better understand the effects seen in the total light.

The figures showing the Rayleigh planetary disk are given at the end of this subsection. Figures 2.4 - 2.13

show the percent polarization and direction of polarization for a single scattering albedo,  $\tilde{\omega}_0$ , equal to 1 for phase angles from  $1^\circ$  to  $160^\circ$ . The upper figures give polarization of the total light, T, scattered from each point whereas the lower figures give the polarization of the light, M, that has been scattered more than once.

Figure 2.14 - 2.19 show the influence of  $\tilde{\omega}_0$ . The upper and lower figures correspond to  $\tilde{\omega}_0 = 1.0$  and  $\tilde{\omega}_0 = 0.9$ , respectively, for T light. Figure 2.20 gives the T polarization for  $\tilde{\omega}_0 = 0.99$  at the largest phase angle run,  $170^\circ$ .

A word about the graphical representation. The polarization at a given point Q is given by the length of the arrow that begins at Q. Q is indicated by a small + sign. The end of the arrow has a small arrowhead which begins after the length corresponding to the polarization. At small phase angles where the polarization is small near the center of the disk, a portion of the physical disk has been removed and replaced by an insert with an expanded scale. The scale of the percent polarization changes with phase angle, but an attempt has been made to keep the scale relatively constant for a range of phase angles. The points at which data is presented changes with phase angle. This accounts for anomalies that are sometimes seen when a point wanders too close to the limb or pole. The points were chosen according to the following scheme: For a given value of  $\theta$  (corresponding to a Gauss-

ian point) values are given a 7 equally spaced points in the angle  $e$  over the interval between  $e = 0$  and the value of  $e$  where the circle of constant  $\theta$  intersects the terminator or equator. If the circle of constant  $\theta$  intersects the terminator, the interval in  $e$  is reduced somewhat so that no point falls on the terminator. The above scheme accounts for the migration of data points in the direction of the sun's motion as the phase angle  $\Psi$  changes. Another slight modification may be noticed. For small phase angles and radial polarization angle  $e$  was shifted by a maximum of  $5^\circ$ , the shift increasing as  $\theta$  increases. This increase the visibility of the arrows somewhat.

The scales of the drawings were chosen for rapid comprehension rather than maximum data content. Each drawing is accompanied by a scale whose physical length does not change in any of the figures. The value next to the scale indicates the percent polarization corresponding to the scale length. The center of the disk is drawn to an expanded scale for many figures at small phase angles.

The drawings were produced on a Calcomp Plotter from data punched by hand on cards. The plotter can only draw lines in one of eight directions so that lines at other angles must be drawn as combinations of small sections of lines in the quantized directions. This produces breaks in the lines which de-

grades the accuracy somewhat while at the same time providing a visual guide to the departure of an arrow from true vertical or true horizontal.

The polarization for T and M has been normalized to the value of the respective intensity due to T or M. This has the advantage of showing the polarization caused by secondary scattering alone, but has the disadvantage that the two figures for T and M at a given phase angle are not additive without the addition of a multiplicative factor at each point. Normalization to the same intensity would be preferable, but this iteration was not performed.

Let us describe the general behavior of the T polarization as  $\Psi$  increases. Subsequently we will discuss and explain the points raised here, as well as the behavior of the M polarization. The figures for T and M are drawn to the same scale in all cases. It will be helpful to the reader to glance through the figures now and during the discussion.

Starting with figure 2.4 for  $\Psi = 1^\circ$  we see that the polarization is everywhere radial, and definitely non-zero, contrary to the expectations of some. It is only as a result of the disk integration that the polarization approaches zero at zero phase. The percentage increases radially outwards, reaching a maximum of about 8% at a radial distance of 0.97 and then decreases to zero at the limbs. The M polarization is also radial but increases monotonically at the limb is ap-



proached, achieving an average maximum of 30%. As the phase angle increases the polarization begins to change from the situation at zero phase, the change spreading outwards from the subearth point. At  $\Psi = 12^\circ$  we begin to notice that the polarization at the center of the disk has increased and is becoming perpendicular to the earth-planet-sun plane (the equatorial plane in the figures). This continues until at  $\Psi = 60^\circ$  the directions have become virtually perpendicular to this plane and the percentages have become more equal over the disk, with the edges of the illuminated disk still possessing the strongest polarization. The absolute maximum is approached at the pole. The polarization everywhere increases monotonically with  $\Psi$  until a maximum is reached near  $90^\circ$ , the scale reduction from  $60^\circ$  to  $120^\circ$  masking this somewhat.

Beyond  $90^\circ$  the polarization decreases again, while becoming increasingly radial at the center of the illuminated crescent, the radial nature spreading to the terminator and limb as  $\Psi$  increases. At  $160^\circ$ , the largest phase angle calculated for  $\tilde{\omega}_0 = 1$ , the appearance is mostly radial with the exception of an area very near the terminator.

The scales for  $60^\circ$ - $120^\circ$  and for  $140^\circ$ - $160^\circ$  are reduced by factors of 0.16 and 0.44 relative to the scale from  $1^\circ$ - $30^\circ$ . The inserts are enlarged by 4.0.

The pictures with single scattering removed, M, are similar to the T pictures but show an increased tendency to

the radial direction at all phase angles. For  $\Psi = 160^\circ$  the M polarization is larger than the T polarization, but it should be remembered here that the actual intensity is greatly diminished. What can be learned from all of this? We are most interested in what we can generalize to all phase functions. The discussion below has in fact resulted from a comparison of this case to two distinctly non-Rayleigh cases which we discuss later. Thus there is a high probability that the general points we make are truly general. The discussion, in places, relies on a simple picture of secondary scattering and to this extent we are treading on soft ground. Understanding multiple scattering and its profusion of different scattering geometries in successive scattering events is not easy, and we shall be content if our simple explanations are sufficiently indicative.

Before we begin let us make a few points about polarization in general. The main point we wish to emphasize is that the arrows we have drawn are arrows, not vectors in the usual sense. Thus for light of the same intensity and degree of polarization, two arrows at right angles cancel and two parallel arrows add to one of the same length. If these arrows make an angle of  $\chi_1$  and  $\chi_2$  with the meridian plane of emergence the resulting polarization is reduced by the factor  $\cos(\chi_1 - \chi_2)$ . Percent polarizations cannot be combined unless the intensities are known as well.

One further reminder: The scattering matrix  $\bar{\bar{S}}$  where  $\bar{I} = \bar{\bar{S}} \cdot \bar{F} / 4\mu$  has 16 components, 8 of them even and 8 of them odd in  $\Delta\phi$ . Thus we note, from the discussion in Part I of the thesis, that for unpolarized light incident, I and Q are cosine functions of  $\Delta\phi$  and U and V are sine functions.

This brings us to the radial polarization at small phase angles. At every point on the disk then  $\phi' - \phi + \pi$ , the angle between the earth-point point-sun lines (see figure 2.1) , is close to zero yielding  $U \approx 0$ . Now

$$2.21 \quad \tan 2\chi = U/Q$$

so that  $\chi = 0^\circ$  or  $90^\circ$  depending on whether Q is positive or negative respectively.  $\chi$  is measured from radial lines drawn from the subearth point and so the polarization is either radial positive ( $\chi=0^\circ$ ) or tangential negative ( $\chi=90^\circ$ ). We will discuss the choice between radial and tangential shortly.

Another equally valid though less mathematical point of view is that at zero phase angle no scattering plane is defined and the only defined directions are radial lines and concentric circles. The direction of polarization is thus determined by symmetry. We shall see that we have a very good measure of what we mean by the ambiguous term, "degree of symmetry" in

$$2.22 \quad (1 - \sin \Delta\phi) \equiv s$$

where  $s$  is defined as the symmetry factor. At zero phase  $s = 1$  across the disk.

The question now is why radial positive rather than tangential negative. A hint of the answer is in our decision to use the words positive and negative in reference to these directions. The answer will be found in the secondary and multiple scattering and the fact that the polarization of the single scattering phase function is positive at all scattering angles. We discuss this in detail below.

The polarization at the center of the disk must be zero at zero phase. At the limbs it must be zero as well since the glancing angles of incidence and reflection insure that only single scattering is important. The symmetry of single particle backscattering implies that light scattered back in the direction of incidence is unpolarized if the scatterers are spherical. Thus another question, implicit in the previous question, is why there is any polarization at all at zero phase. This too is a result of multiple scattering, as we shall see.

Let us try to describe a secondary scattering event. Consider a point on the disk  $P$  a distance  $\theta$  from the sub-earth point  $E$  at a phase angle of zero. The scattering geometry is shown in figure 2.3 and is observed from above the subearth-subsun point  $E, S$ . We assume for simplicity that all secondary scattering at  $P$  arises from points along

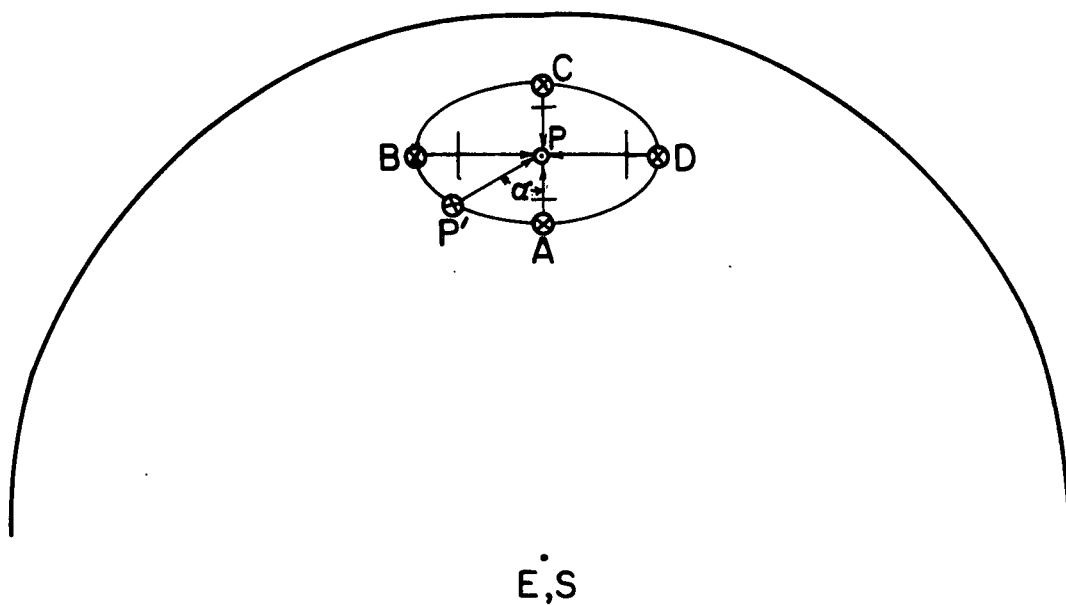


Figure 2.3 Geometry of a simplified set of secondary scattering events at phase angle  $\psi = 0$ . Light is initially incident at A, B, C, D, and P' and is scattered again at P. The short lines normal to the radii from P suggest the direction and magnitude or the polarization of the light scattered from A, B, C, and D toward P for the Rayleigh phase function. Distance P E corresponds to  $\theta$  as in figure 2.1. Angle  $\gamma$  at P' between the observer and P' P is not shown.

concentric circles around P lying at or near the surface. ABCDA is one such small circle. The illumination at any point P' on the circle is the same and arrives making an angle  $\theta$  with the local normal. The light is scattered once at P' through an angle  $\gamma$  (not shown, due to the geometry) and arrives at P polarized due to the scattering at P'. The magnitude and direction of the induced polarization is indicated on the figure for 4 selected points A, B, C, and D. Rayleigh scattering is assumed.

The light is scattered again at P through an angle  $\pi - \gamma$ , and the polarization is changed once more. If it is realized that for both scattering events at P' and P the plane of polarization is normal to the plane of the paper through P'P then it is apparent that the light emerging from P will be polarized perpendicular to P'P for positive polarization at P and P'. As P' moves about the circle the scattering angle  $\gamma$  goes from a minimum of  $\pi/2 - \theta$  at C to a maximum of  $\pi/2 + \theta$  at A passing through  $\pi/2$  at B and D. At  $\pi/2$  the polarization is a maximum for the Rayleigh phase function. Thus we see that the polarization induced by secondary scattering lies in a radial direction.

We can see now also why the polarization increases as we move away from the center of the disk. Near the center of the disk the range of scattering angles decreases and approaches  $\pi/2$  for all points P'. Then the polarization is

more nearly equal at A, B, C, and D and cancels to a large extent. At the limbs the cancellation is less effective and the secondary polarization is large.

A more general point can be made. At zero phase (and, less accurately, at small phase angles as well) the polarization observed is the result of averaging (in the sense described below) the polarization over all scattering angles from  $\pi/2-\theta$  to  $\pi/2+\theta$ , when the plane of polarization and intensity are properly accounted for.

It is not our purpose here to develop these concepts beyond the intuitive. Yet it is possible to describe mathematically the previous discussion and we do so below. The derivation is lengthy and complex geometrically so only the results are given. Let  $p_1(\gamma)$  and  $p_2(\gamma)$  represent the components of the single scattering phase matrix such that

$$2.23 \quad \begin{pmatrix} I^S \\ Q^S \end{pmatrix} = \begin{pmatrix} p_1 & p_2 \\ p_2 & p_1 \end{pmatrix} \begin{pmatrix} I^i \\ Q^i \end{pmatrix}.$$

Then for unpolarized light incident the polarization after two scattering events as described above is given by

$$2.24 \quad P = Q/I$$

$$\text{where} \quad I = \int_0^{2\pi} \{p_1(\gamma)p_1(\pi-\gamma) + p_2(\gamma)p_2(\pi-\gamma)\} d\alpha$$

$$\text{and} \quad Q = - \int_0^{2\pi} \{p_1(\gamma)p_2(\pi-\gamma) + p_2(\gamma)p_1(\pi-\gamma)\} \cos 2\delta \, d\alpha$$

and where

$$\cos \gamma = \sin \theta \cos \alpha$$

$$\tan \delta = \sec \theta \tan \alpha$$

$\alpha$  is given in figure 2.3.  $\delta$  is an angle similar to  $\alpha$  but measured in the plane of the paper. If  $P$  is positive the polarization is radial, and tangential if it is negative.

At larger phase angles we saw the polarization increase most rapidly at the center of the disk all the while becoming increasingly positive. The increase in the polarization is due to both single and multiple scattering, and is too complex to discuss intuitively other than to remark that we would expect it to change from zero. The change in the direction of polarization is at first sight difficult to understand because naively we might feel that orientation of the direction of polarization to directions defined by a scattering plane is a single scattering phenomenon and single scattering should be smallest near the center of the disk. A glance at the T and M figures for  $\Psi=12^\circ$  and  $\Psi=20^\circ$  shows that, contrary to expectations, the orientation change is due to multiple scattering, the single scattering of course helping as well as  $\Psi$  increases.

We can gain a better feel for this change in direction if we look at the "symmetry" of the scattering situation. The subearth and subsun points, E and S, become increasingly separated as  $\Psi$  increases. Near disk center the concept of "rad-



ial" loses its meaning for we must specify radial to what, E or S. At the limbs the question is less important because the polarization can point towards the general direction of E and S and still retain a radial character. Loosely, we can say that scattering at the edge of the disk is more "symmetrical" than near the center. Near the center the symmetry factor  $s$  (given by equation 2.22) is variable and not equal to 1; near the edges it is nearly 1 at all points.

The symmetry factor works as an intuitive crutch because it is directly related to  $U$ . When  $s = \pm 1$ ,  $U$ , an odd function of  $\Delta\phi$ , is zero and the polarization, according to equation 2.21 must be radial or tangential.  $U$  increases most rapidly near the center of the disk for there  $\Delta\phi$  increases most rapidly as  $\Psi$  increases. Thus  $\chi$  is not zero, and the polarization can no longer be radial.

It is by no means obvious why  $U$  should vary in such a way to make the orientation perpendicular to the scattering plane rather than just variable. A general statement that can be made is that at intermediate phase angles multiple scattering, even with single scattering removed, remembers the orientation of the plane of single scattering quite well, especially near disk center. We shall see this again in the other two phase functions we have investigated.

At  $60^\circ$  and  $90^\circ$  the direction of polarization is rather accurately perpendicular to the scattering plane, due to

the large single scattering polarization. The M polarization shows this too, as we have mentioned, but is less strongly polarized.

The increasingly radial nature at  $\Psi = 120^\circ, 140^\circ, 160^\circ$  is due again to  $U \rightarrow 0$  or to  $s \rightarrow -1$  for all points on the disk. It is difficult to see, but the change towards radial is slower at the limb and terminator, due to a competition between single and multiple scattering, the single scattering becoming increasingly important for grazing angles. We shall see a more vivid example of this in subsection B.

The enhancement of single scattering by grazing angles of incidence and reflection is further emphasized by the polarization enhancements at the poles. There both scattering directions are grazing and multiple scattering is smallest.

The previous discussion dealt with Rayleigh scattering for a single scattering albedo  $\tilde{\omega}_0 = 1$ . Figures 2.14 to 2.19 compare  $\tilde{\omega}_0 = 1$  with  $\tilde{\omega}_0 = 0.9$  for T scattering. It is interesting that both sets of figures should be so similar, considering that the Bond albedo for  $\tilde{\omega}_0 = (1.0, 0.9)$  is  $(1.0, 0.48)$  respectively. For  $\tilde{\omega}_0 = 0.9$  and small phase angles the polarization is larger near the center of the disk, the increase spreading to the limbs towards  $\Psi = 90^\circ$ . Near the poles, however, the polarization changes little with  $\tilde{\omega}_0$  for all phase angles.

These effects are just the result of the decreased dilution of the single scattering polarization by multiple scattering, where it must be borne in mind that the multiply scattered component is itself significantly polarized, and is in fact larger than the singly scattered component over large portions of the disk at large and small phase angles. The dilution is greatest near disk center for  $\Psi \gtrsim 0$ , accounting for the change there. At intermediate phase angles the single scattering polarization is high and the more weakly polarized M component causes less dilution than for  $\tilde{\omega}_0 = 1$ .

Finally in this section on Rayleigh scattering we deal with a graph for  $\tilde{\omega}_0 = 0.99$  and  $\Psi = 170^\circ$ , figure 2.20. This is included because the recent calculations of Kattawar and Adams (1971) have shown that the disk integrated polarization is actually negative for  $\Psi > 164^\circ$ . Figure 2.20 is the only computed case which falls in this range. Our own calculations for the disk integrated polarization at  $170^\circ$  gives a positive value there, but our integration scheme most certainly is unreliable at such large phase angles.

How then can we explain negative polarization from positively polarizing particles? The answer lies with the geometry. At  $\Psi = 170^\circ$  the arrows are decidedly more radial than at  $\Psi = 160^\circ$ . For the radial positive regional polarization to yield a positive disk integrated polarization the positively polarized intensity (the component Q of the Stokes

vector) obtained by integrating from the poles to latitude  $\pm 45^\circ$  must be greater than the negatively polarized intensity obtained by integrating from latitude  $\pm 45^\circ$  to the equator. But for truly radial polarization this is not possible, for there is a greater integrated flux from the equatorial regions than from the poles due to the geometry. Thus positively polarizing particles should always yield a region of negative polarization at very large phase angles. A similar statement applies to negatively polarizing particles. The phase angle at which the reversal occurs is a function of the degree of forward scattering. For Rayleigh scattering the reversal occurs near  $164^\circ$  while for cases B and C a reversal is not yet apparent at  $170^\circ$  judging from the non-radial and non-tangential polarization that is seen in the figures.

In figure 2.21 we give the disk integrated polarization of a Rayleigh scattering planet of infinite optical depth as a function of phase angle and single scattering albedo. For  $\tilde{\omega}_0 \rightarrow 0$  only the polarization of the single scattering phase function is important and we have included this case for comparison. While the calculations are accurate to within  $\pm 2\%$  polarization beyond  $140^\circ$ , we do not display results beyond  $135^\circ$  because we want to discourage comparison for the purpose of accuracy testing in this region.

Both the T and M polarization increase with decreasing  $\tilde{\omega}_0$  because the dilution by the lesser polarized higher orders is less since their intensity is less.

An unsuccessful attempt was made to derive the multiple scattering results from a knowledge of the single scattering polarization and the total intensity. The interested reader is referred to Hovenier (1971) for a successful attempt using singly and doubly scattered light.

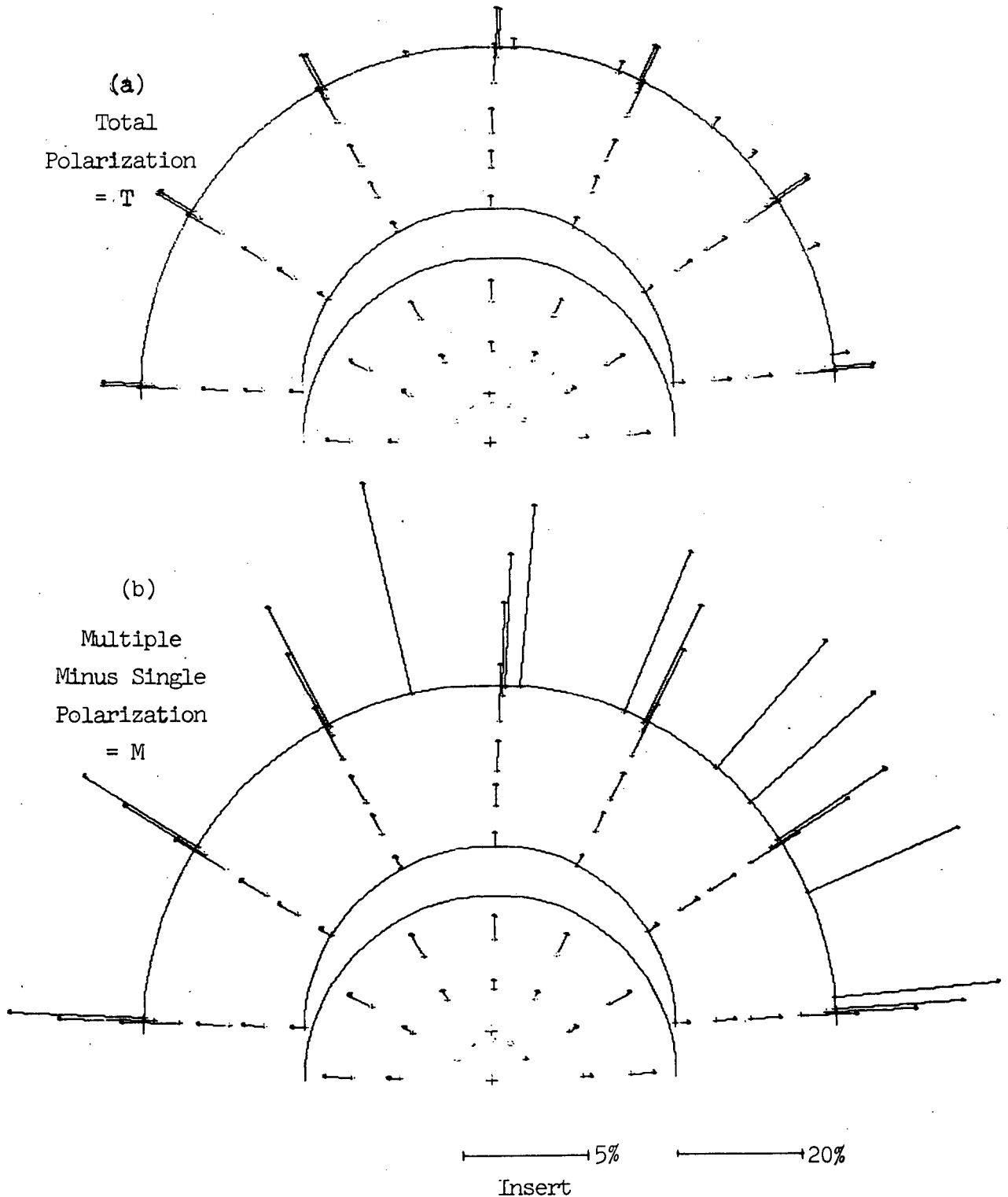


Figure 2.4 Rayleigh scattering across the disk of a semi-infinite planetary atmosphere with single scattering albedo  $\tilde{\omega}_0 = 1$ ; (a) gives polarization of total light scattered = T; (b) gives polarization of light scattered more than once = M. Length of arrow indicates magnitude of polarization. Direction of arrow gives orientation of electric vector maximum. A portion of the disk is shown with an expanded scale. For a more detailed description see text. Phase Angle  $\psi = 1^\circ$ .

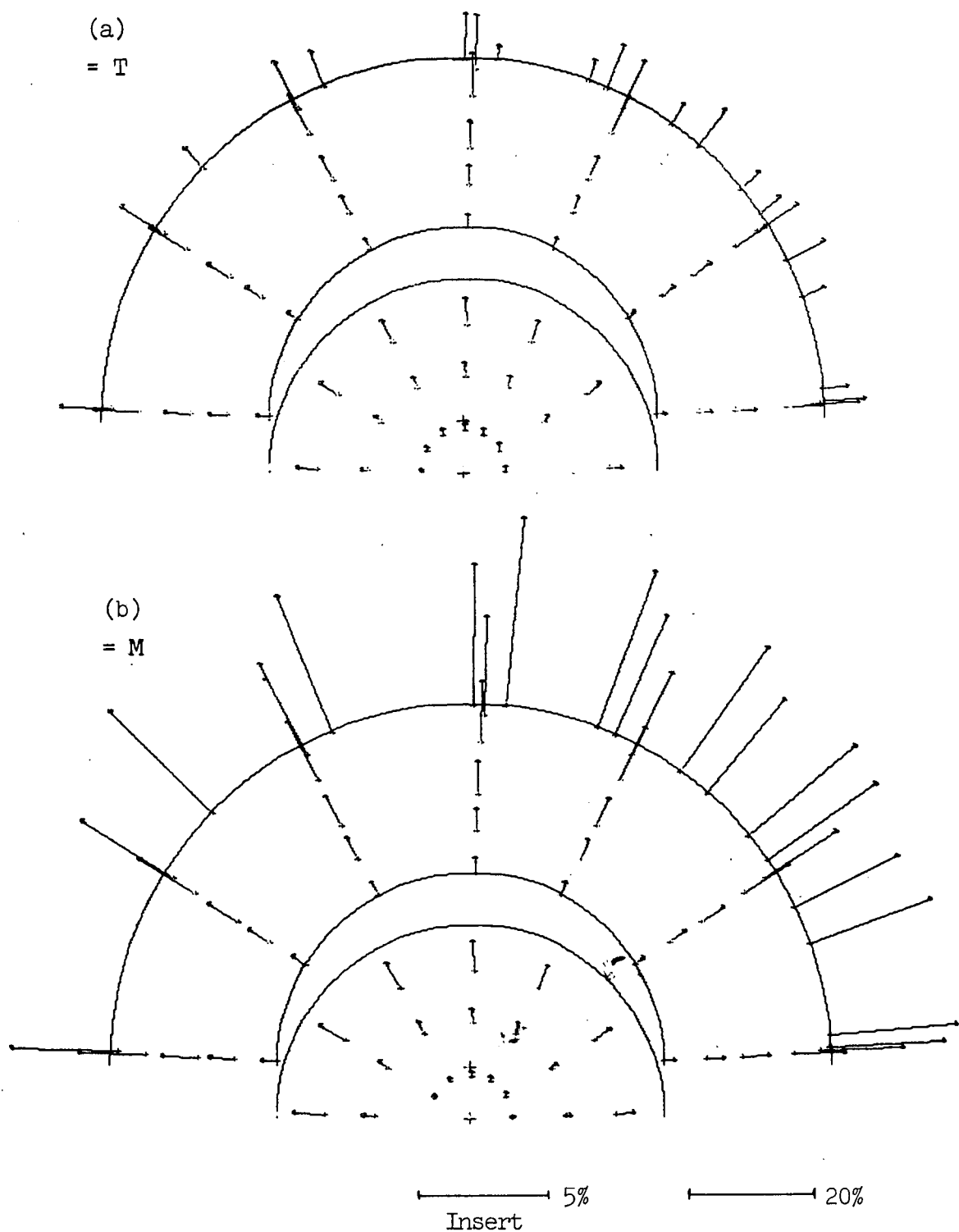


Figure 2.5 Rayleigh scattering,  $\tilde{\omega}_0 = 1$ ; (a) = T; (b) = M;  $\psi = 6^\circ$ . Note radial positive character. M polarization is non-zero and greater in fact than the T polarization.

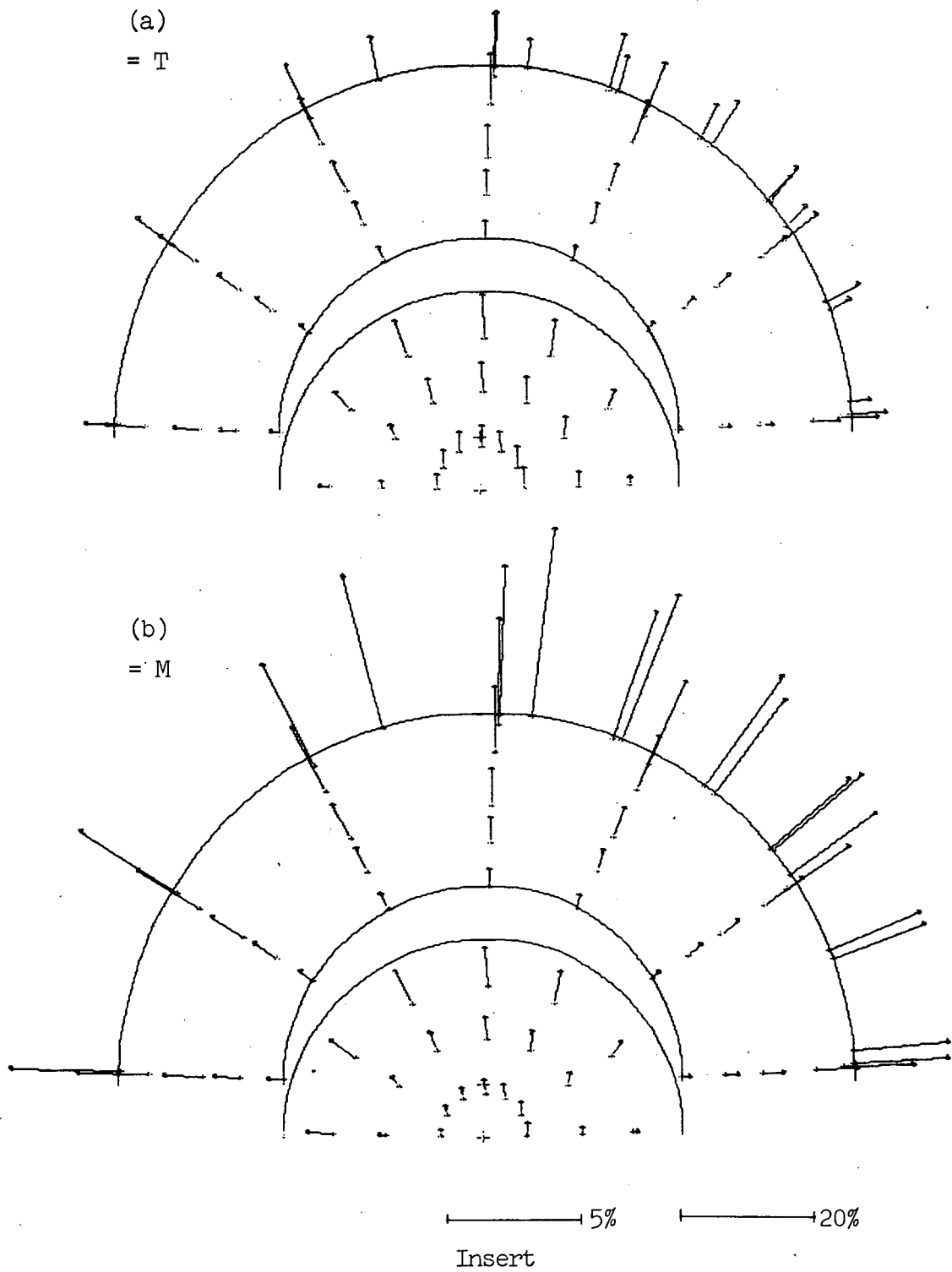


Figure 2.6 Rayleigh scattering,  $\tilde{\omega}_0 = 1$ ; (a) = T; (b) = M;  $\psi = 12^\circ$ . Note increase at center of disk and associated change towards positive, (normal to scattering plane).



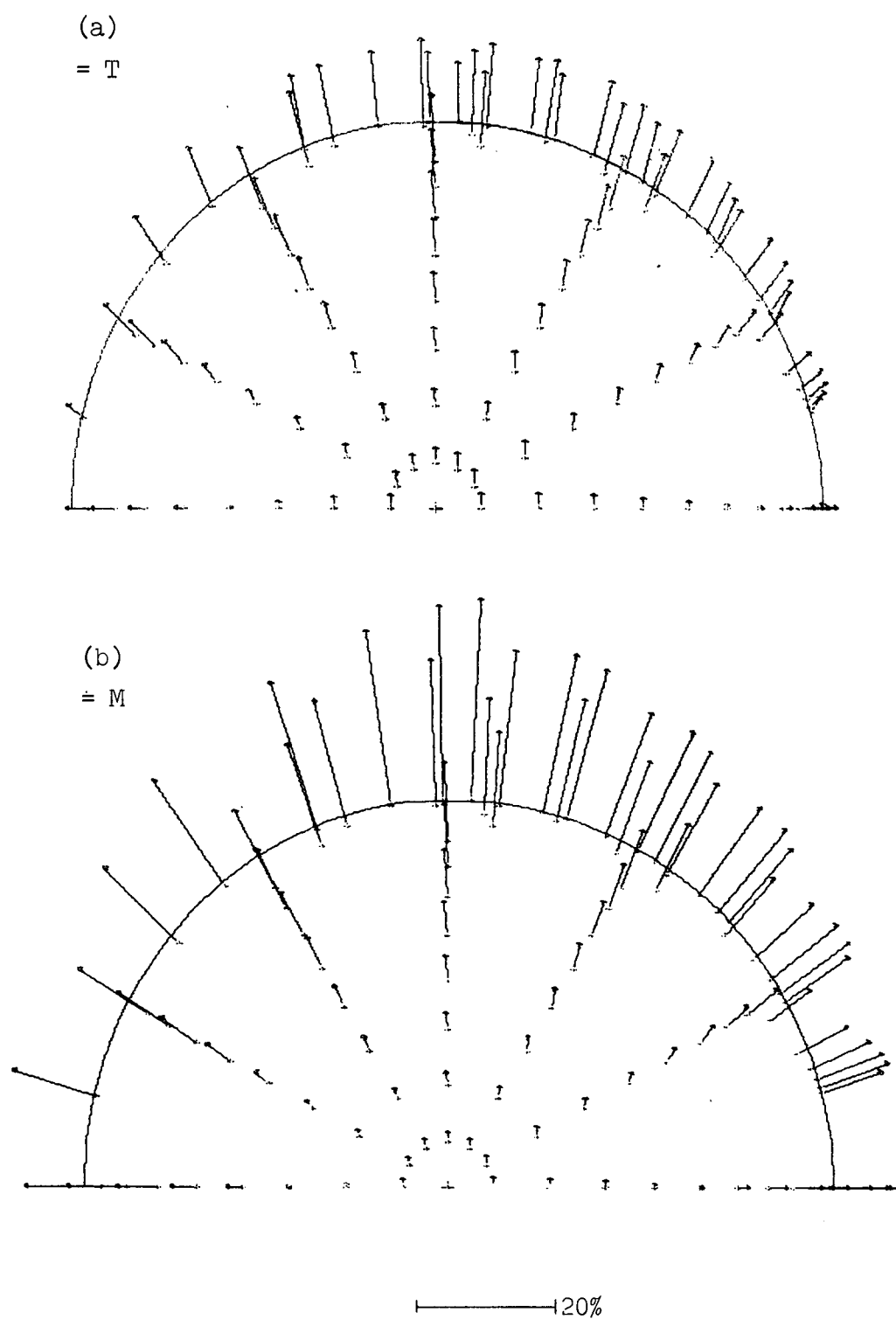


Figure 2.7  $\psi = 20^\circ$ . Center of disk is positive, limbs are radial positive.

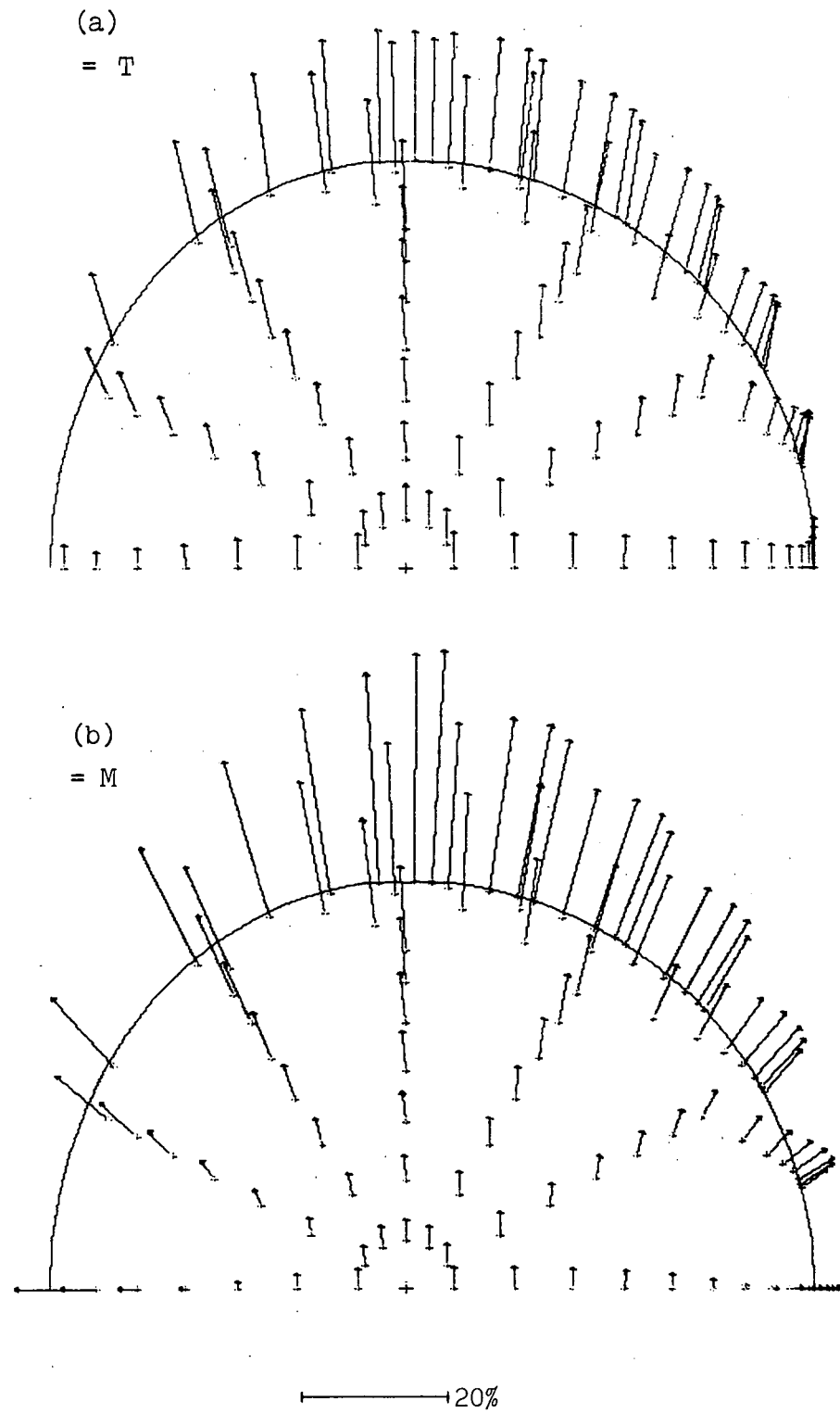
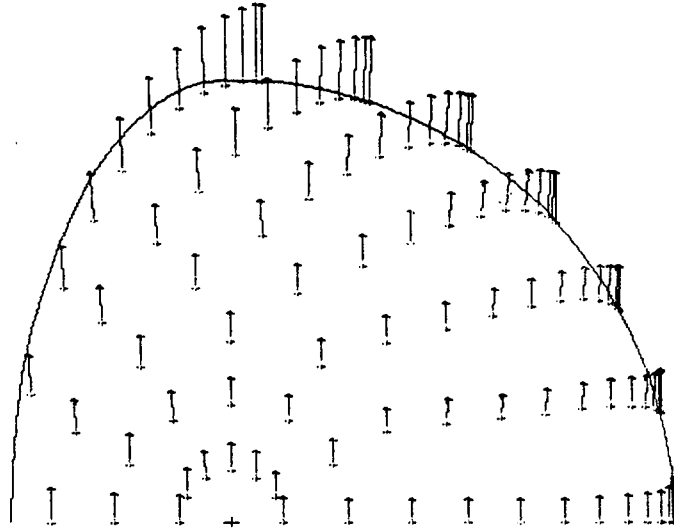
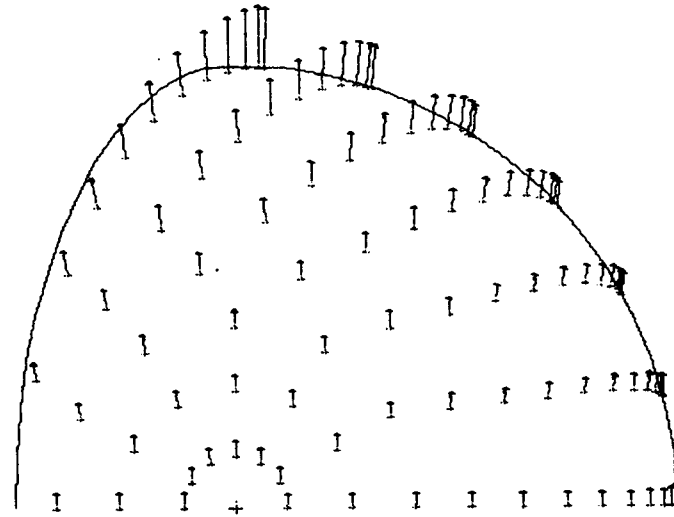


Figure 2.8  $\psi = 30^\circ$ . Increased polarization at pole. Both T and M are positive at center.

(a)  
= T

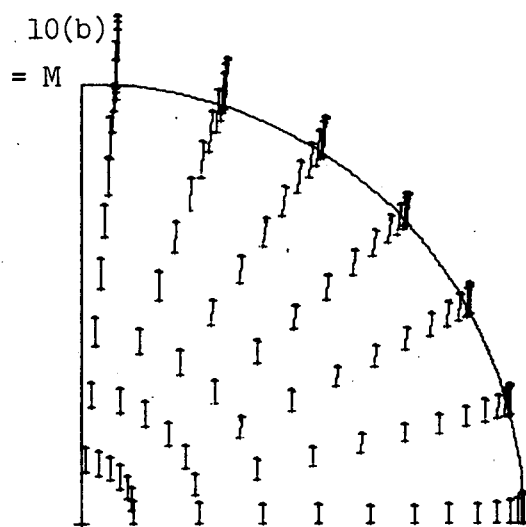
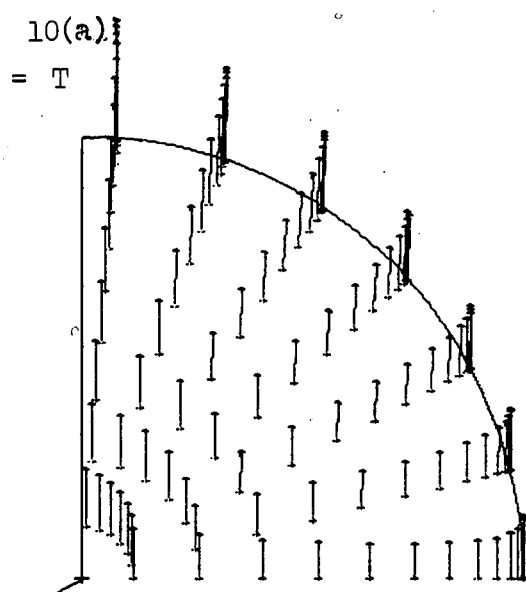


(b)  
= M

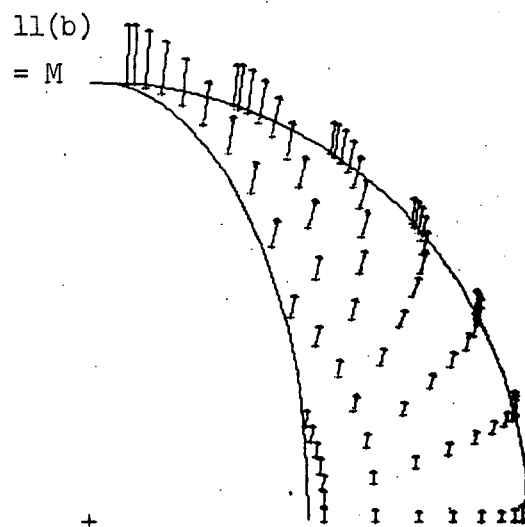
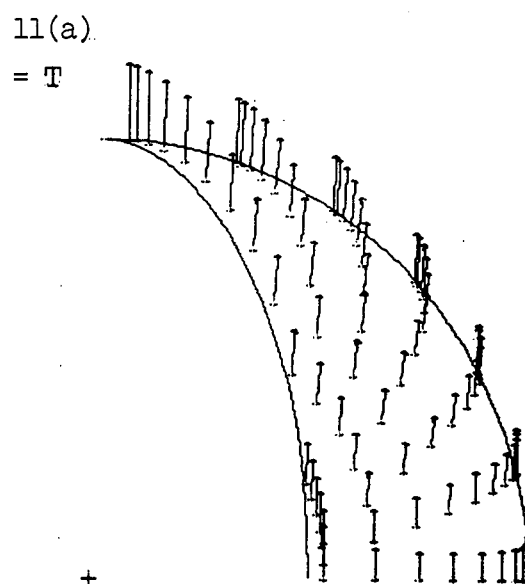


120%

Figure 2.9  $\psi = 60^\circ$ . Both T and M have their electric vector maximum normal to the scattering plane in this view of the planet at a gibbous phase. Note scale change. Scale changes can be easily followed by noting the length of the scale does not change for any of the graphs.



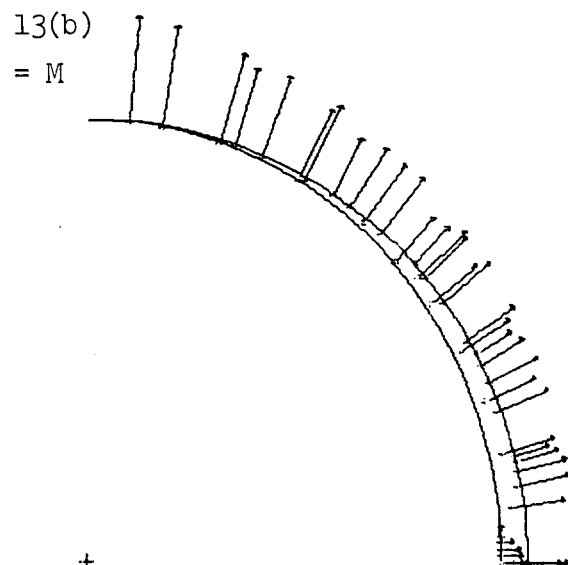
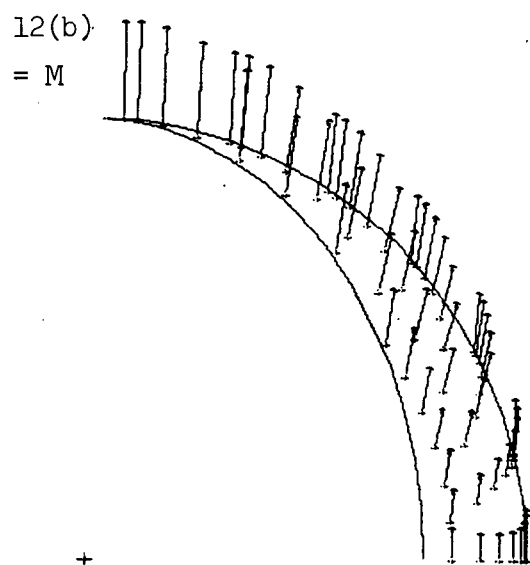
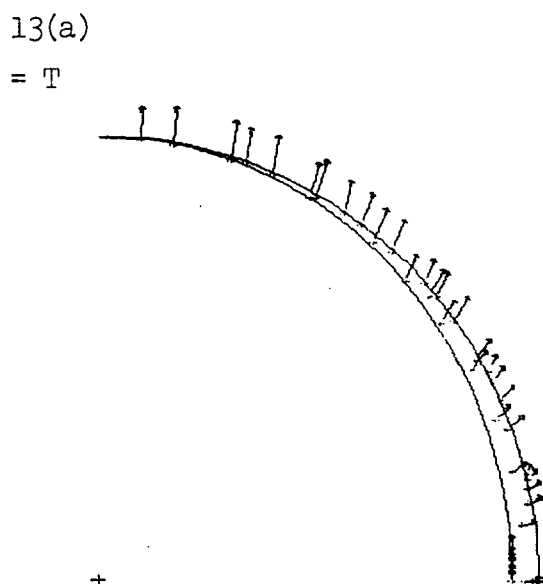
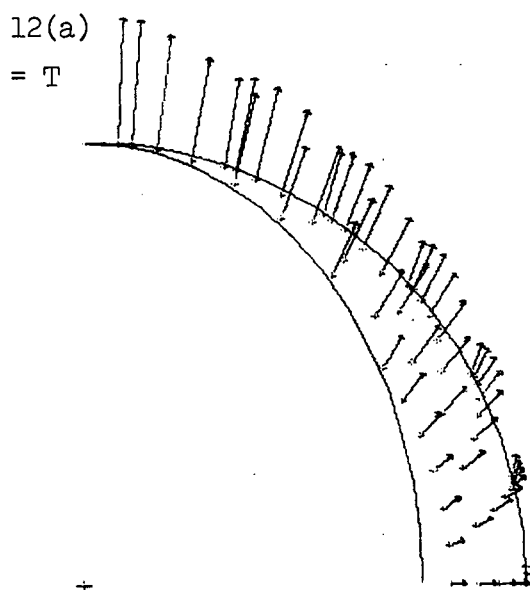
120%



120%

Figure 2.10  $\psi = 90^\circ$ . At this phase angle, Rayleigh scattering gives 100% polarization for single scattering.

Figure 2.11  $\psi = 120^\circ$ . Maximum deviation from positive direction is  $9^\circ$  in the T polarization.



45%

45%

Figure 2.12  $\psi = 140^\circ$ . Approaching radial positive again, Maximum T deviation from positive direction is  $15^\circ$ , at center of visible crescent. Note scale change.

Figure 2.13  $\psi = 160^\circ$ . Mostly radial positive; more apparent in M polarization than in T polarization.

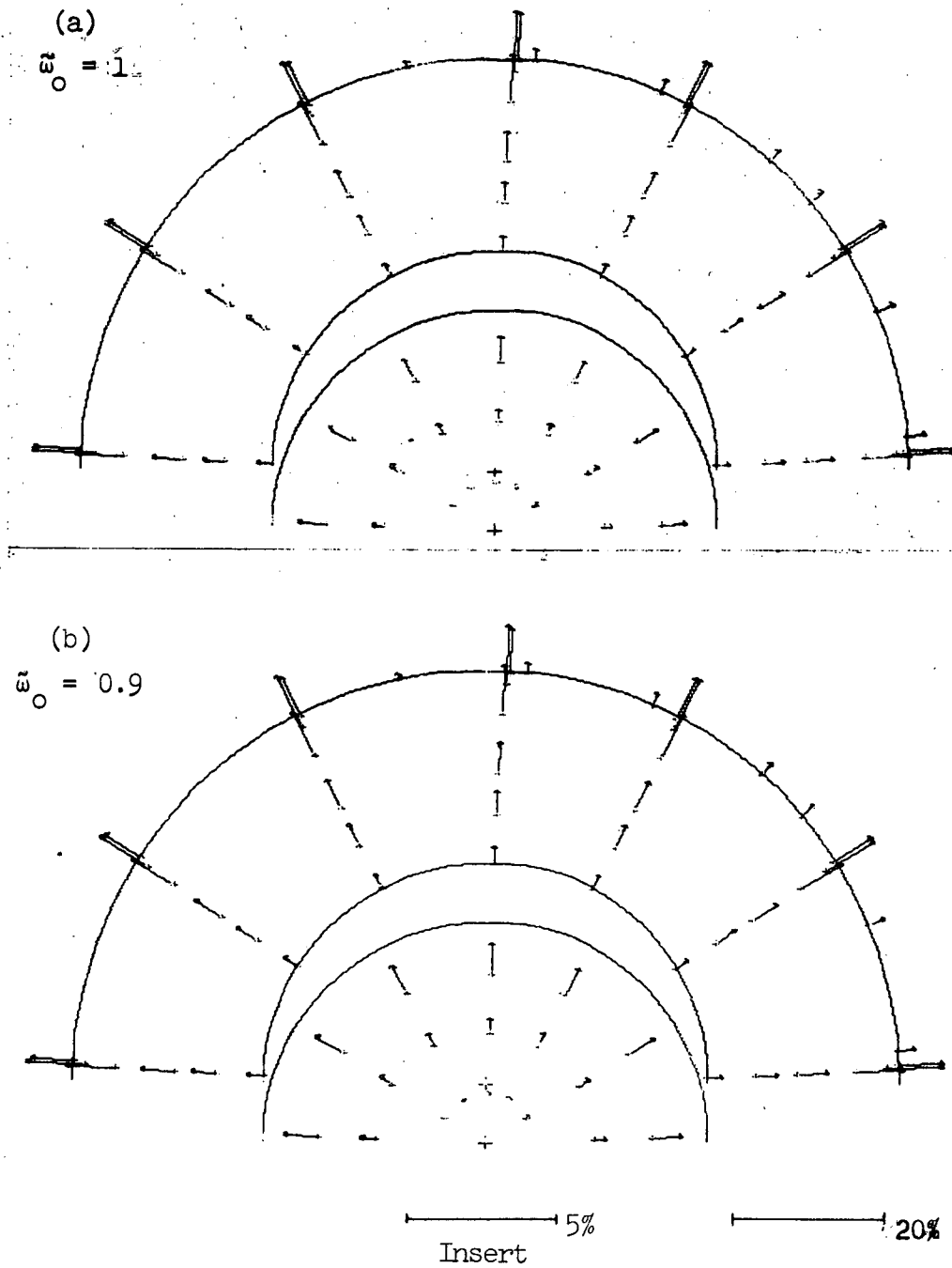


Figure 2.14 Rayleigh scattering in a semi-infinite atmosphere at two different  $\tilde{\omega}_0$ 's. Upper (a) is for  $\tilde{\omega}_0 = 1$ ; lower (b) is for  $\tilde{\omega}_0 = 0.9$ ; corresponding to Bond Albedos of 1 and 0.48 respectively. Note striking near equality.  $\psi = 1^\circ$ .

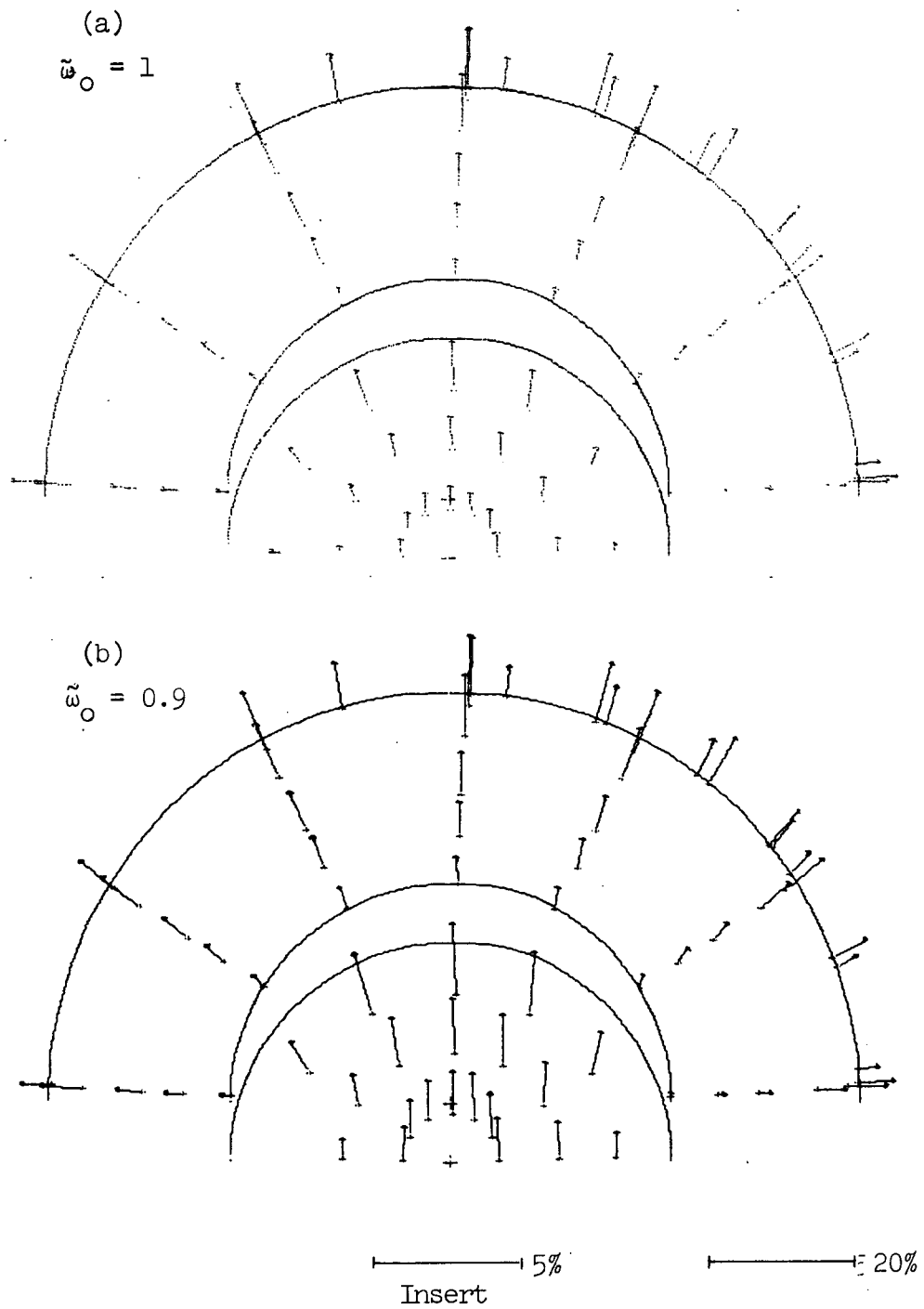


Figure 2.15 Rayleigh scattering (a)  $\tilde{\omega}_0 = 1$ ; (b)  $\tilde{\omega}_0 = 0.9$ ;  $\psi = 12^\circ$ . Central portion of disk are most affected by change in  $\tilde{\omega}_0$ .

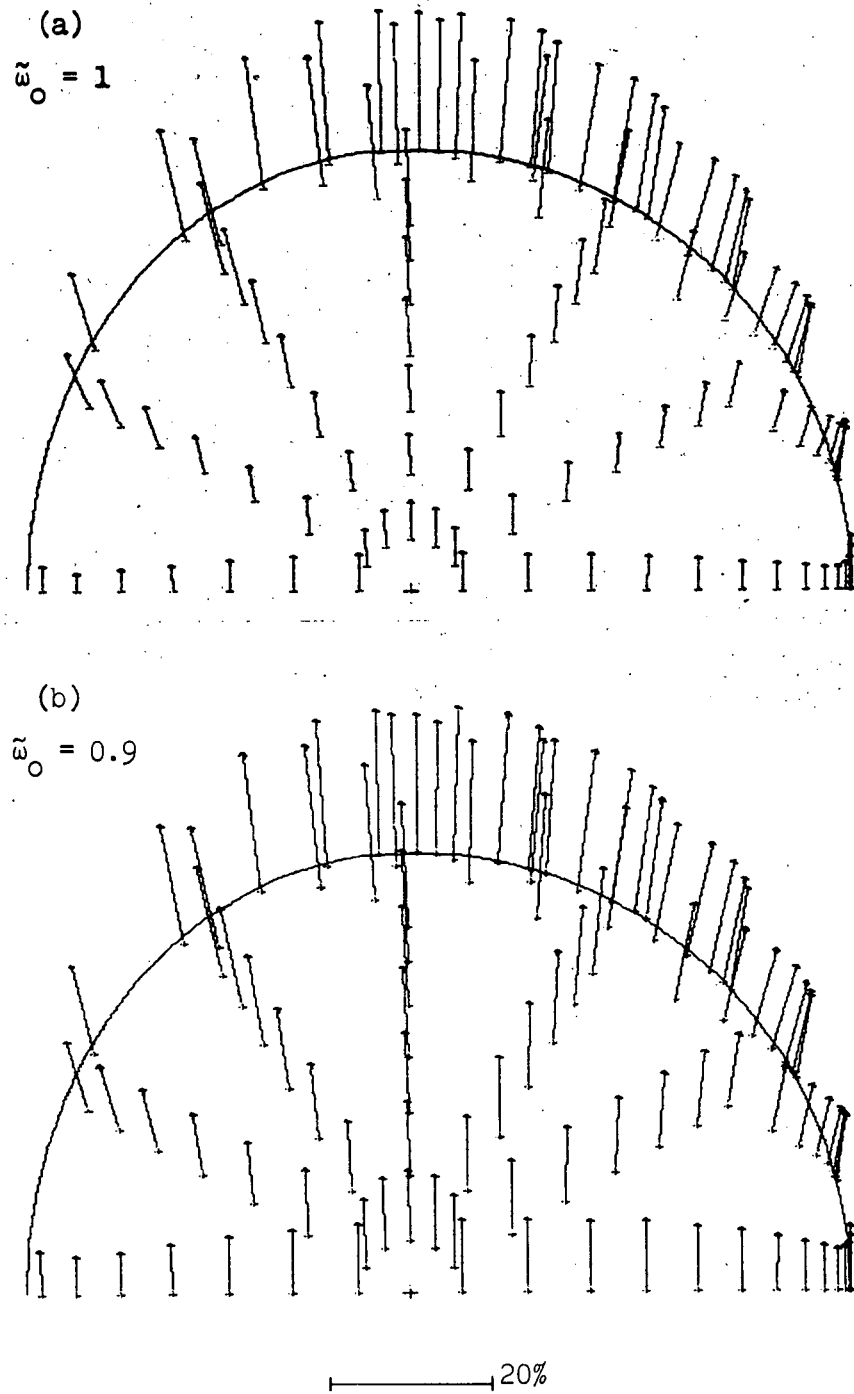
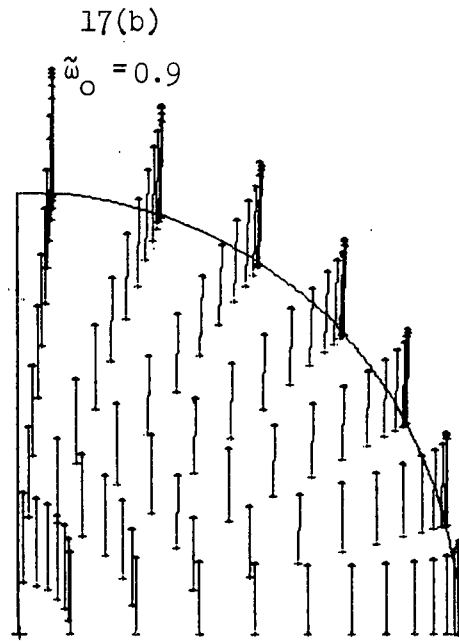
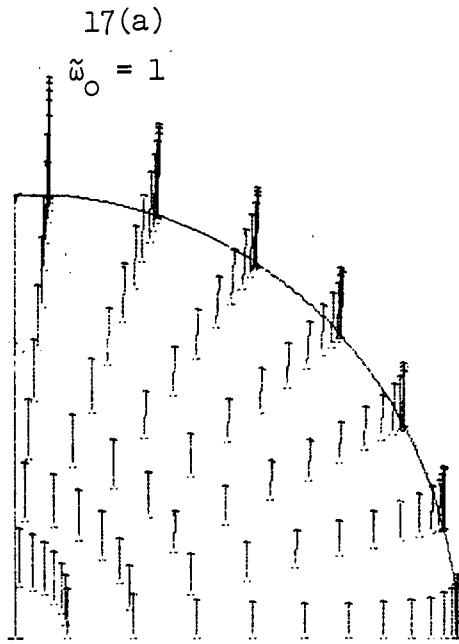
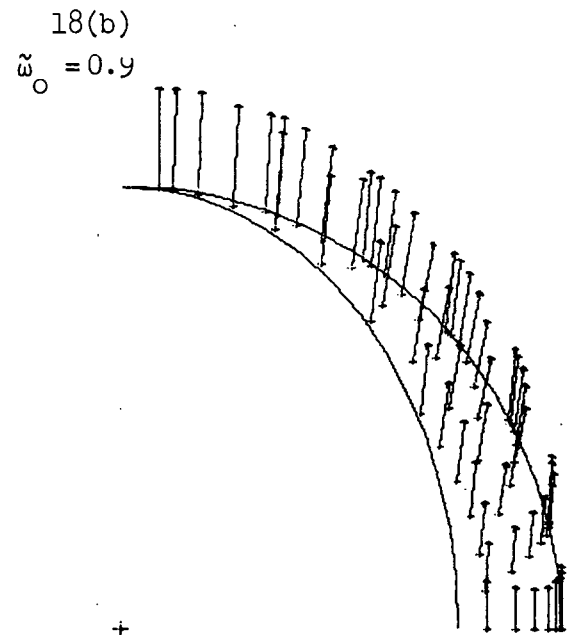
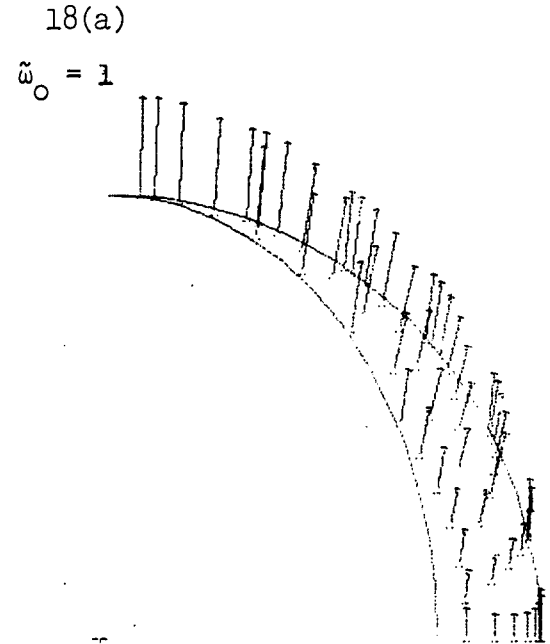


Figure 2.16 Rayleigh scattering (a)  $\tilde{\omega}_0 = 1$ ; (b)  $\tilde{\omega}_0 = 0.9$ ;  $\psi = 30^\circ$ . Central portions of disk are most affected by change in  $\tilde{\omega}_0$ .





120%



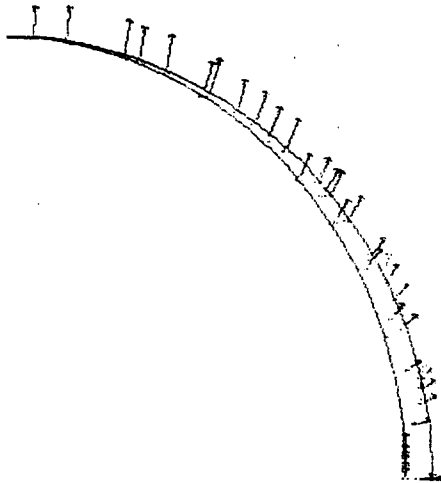
45%

Figure 2.17 Rayleigh scattering (a)  $\tilde{\omega}_0 = 1$ ; (b)  $\tilde{\omega}_0 = 0.9$ ;  $\psi = 90^\circ$ . Influence of  $\tilde{\omega}_0$  is smallest at pole.

Figure 2.18 Rayleigh scattering (a)  $\tilde{\omega}_0 = 1$ ; (b)  $\tilde{\omega}_0 = 0.9$ ;  $\psi = 140^\circ$ . Influence of  $\tilde{\omega}_0$  is smallest at pole.

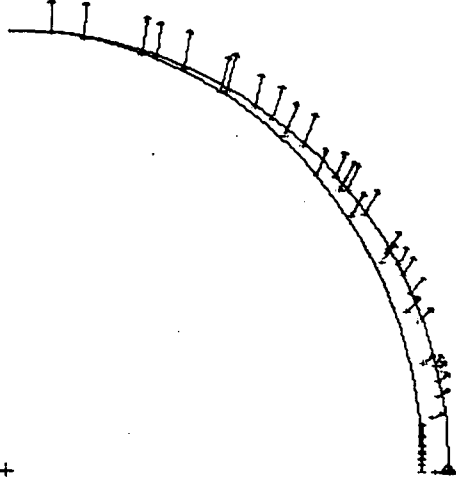
19(a)

$$\tilde{\omega}_0 = 1$$



19(b)

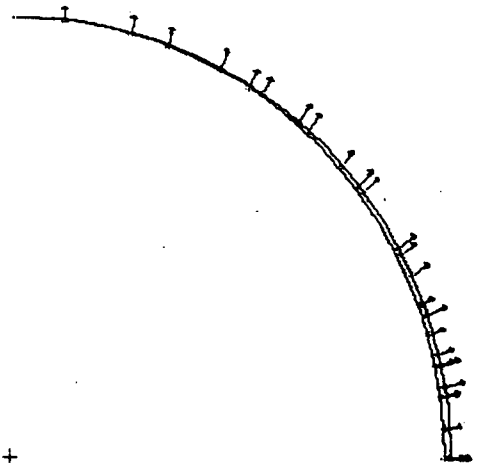
$$\tilde{\omega}_0 = 0.9$$



+

45%

20



+

45%

Figure 2.19 Rayleigh scattering (a)  $\tilde{\omega}_0 = 1$ ; (b)  $\tilde{\omega}_0 = 0.9$ ;  $\psi = 160^\circ$ . Influence of  $\tilde{\omega}_0$  is smallest at pole.

Figure 2.20 Rayleigh scattering  $\tilde{\omega}_0 = 0.99$ ; T.  $\psi = 170^\circ$ . At this phase angle integrated polarization has been shown to be negative, although detailed appearance is radial positive. See text for explanation.

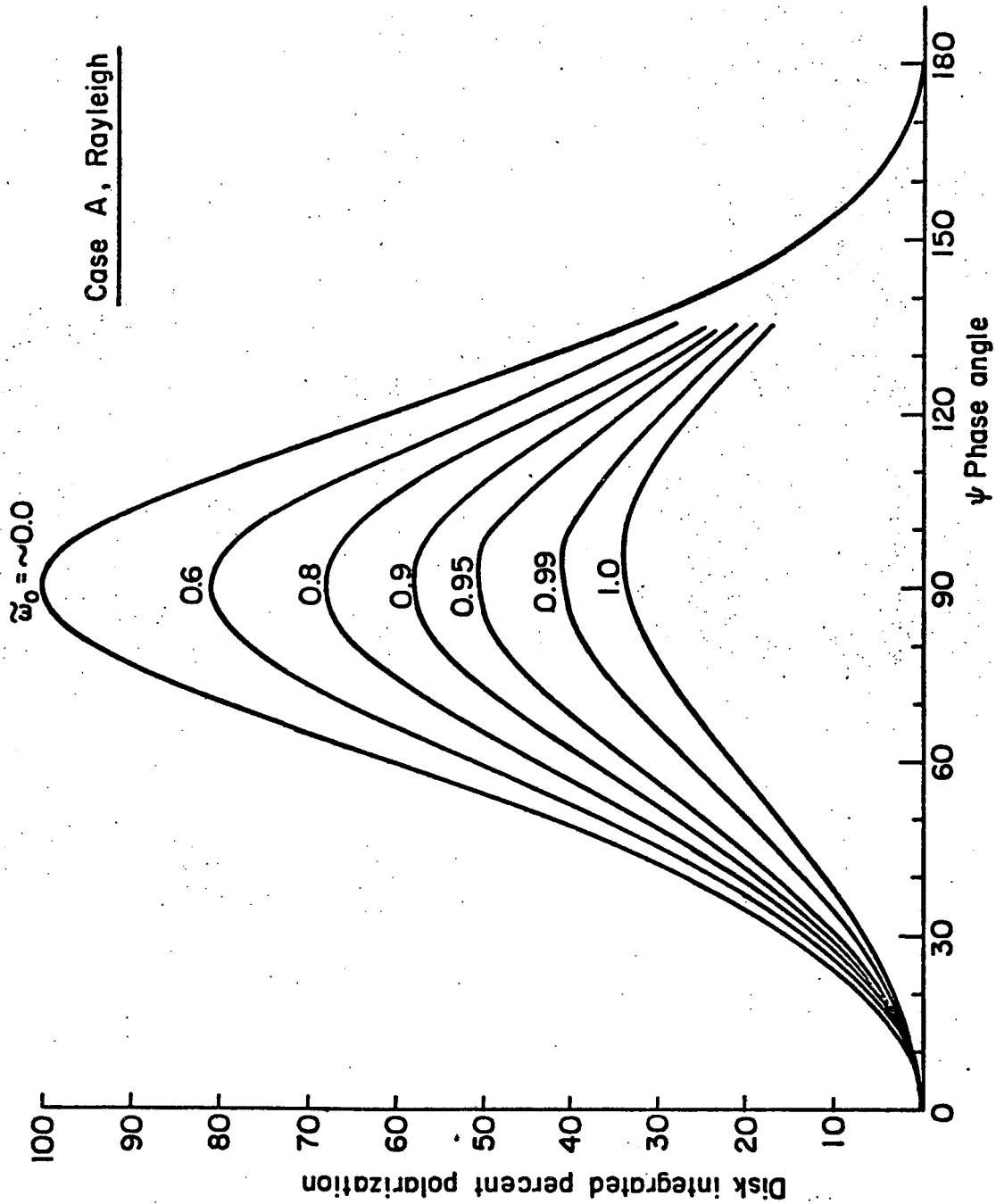


Figure 2.21 Disk integrated polarization of a semi-infinite Rayleigh scattering atmosphere with single scattering albedo,  $\tilde{\omega}_0$ , as a parameter. Calculations beyond  $\psi = 135^\circ$  are not considered accurate enough to be displayed here.

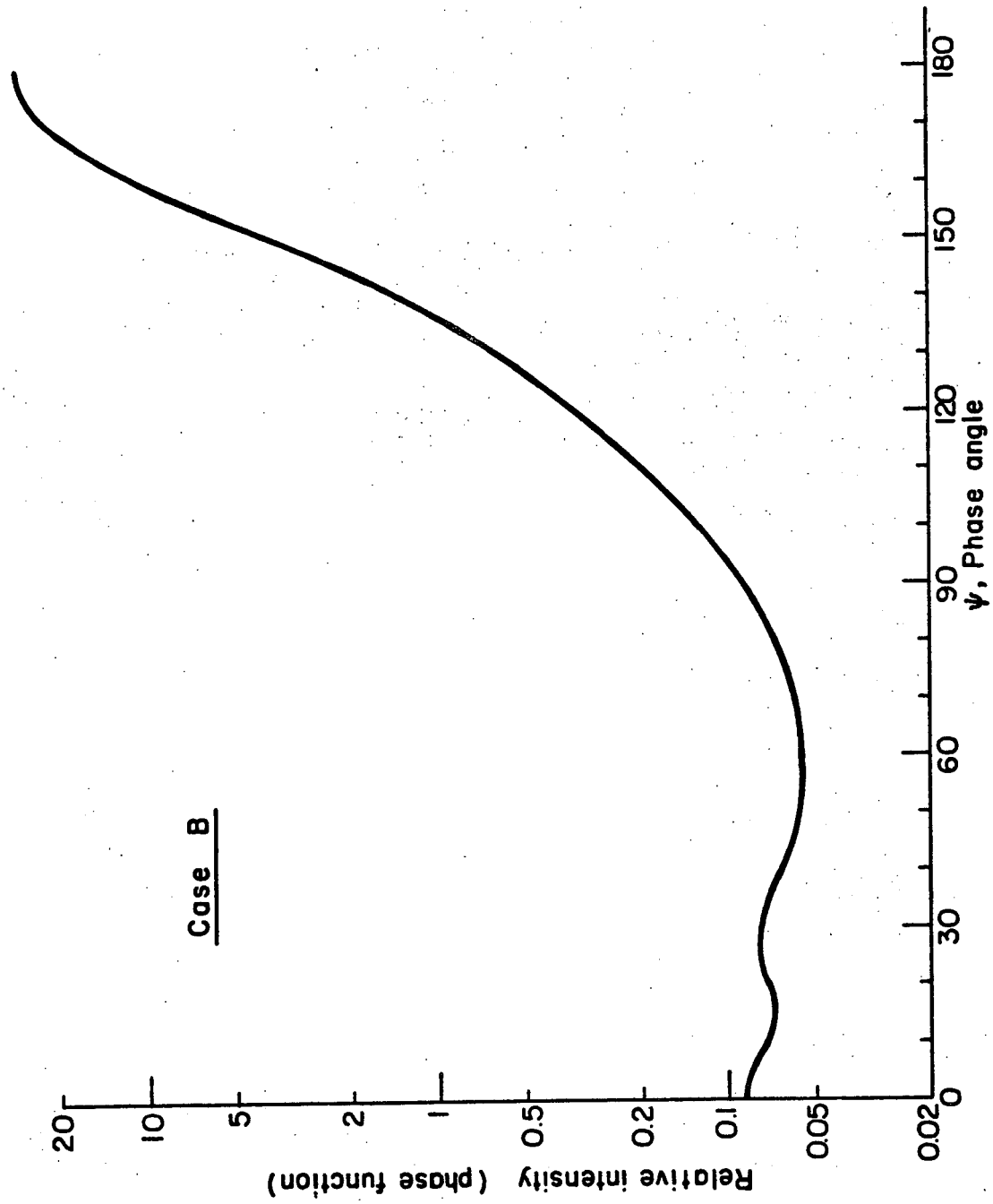


Figure 2.22 Single scattering phase function for case B. Phase angle  $\approx 180^\circ$  - scattering angle.

## B A Forward Scattering Non-Rayleigh Phase Matrix

This phase function is important because it is the only one of the three we discuss which displays both positive and negative polarization, possessing in fact two null points besides the ones at  $0^\circ$  and  $180^\circ$  (see figure 2.23). It is also non-Rayleigh and elongated in the forward direction, as shown in figure 2.22.

The disk integrated polarization also displays two neutral points, and we shall investigate the disk behavior near these points. We will see how the direction of polarization is affected by phase angle and position on the disk for both T and M polarization. We will find that many of the statements made about Rayleigh scattering apply here as well, although different in detail.

For completeness we give below some of the details of the phase function. Its forward elongation is characterized by the average of  $\cos\theta$  over the phase function  $\langle \cos\theta \rangle = 0.84$ , whereas  $\langle \cos\theta \rangle = 0.0$  for Rayleigh scattering. It has a positive polarization at intermediate phase angles, but is negative for small and large values of  $\Psi$ . See figures 2.22 and 2.23 at the end of this subsection. Results are displayed for  $\tau = \infty$  and an arbitrary choice of  $\tilde{\omega}_0 = 0.997$  corresponding to a Bond albedo of 0.73.

The set of parameters necessary to reproduce the phase function from the Mie theory follows. We chose  $\tilde{n} = 1.31 + 0.01$

and a distribution of particle sizes according to the function

$$2.25 \quad n(a) = Aa^{\beta} \exp(-ba^{\gamma})$$

the modified gamma function used by Deirmendjian (1969) to describe real distributions. Here we chose  $\beta = 1$ ,  $\gamma = 3$  and  $b = 1/3$ . This choice of parameters does not correspond to any of the normally selected cloud and haze particle distribution functions (Deirmendjian, 1969), the distribution function decreasing slowly for small particles, and abruptly for large particles. The choice resulted from a keypunching error-- $a^{\beta}$  was computed as  $a\beta$  so that the exponent of  $a$  was 1. A choice of  $\lambda = 2.02$  results in an average size parameter  $\bar{\alpha} = 5.00$ . ( $\bar{\alpha}$  is an average of  $\alpha = 2\pi a/\lambda$  over  $n(a)$  weighted by the scattering cross section,  $\pi a^2 Q_s$ , as calculated in the Mie theory. That is

$$\bar{\alpha} = \frac{\int \alpha \pi a^2 n(a) Q_s(\alpha) da}{\int \pi a^2 n(a) Q_s(\alpha) da}$$

The above parameter choices result in intensity and polarization phase functions which are quite ordinary, although more Rayleigh-like than  $\bar{\alpha} = 5.00$  would normally imply and more Rayleigh-like than we desired a priori.

Figures 2.24 - 2.34 show the disk T and M polarization for selected phase angles. Note that the scale varies over many of the pictures and that almost nowhere is the polarization as strong as that for Case A. The polarization at small phase angles is so small--in fact on the order of 0.1%--that limiting accuracy has been approached. However, the fairly continuous behavior of the polarization over phase

angle and disk position increases the confidence in the results. Typical polarization observations are accurate to  $\pm 0.1\%$ .

First let us note those qualities that this scattering law has in common with the Rayleigh law. The polarization is radial for small phase angles changing to vertical as the the phase angle and polarization increase. Beyond  $170^\circ$  the polarization is tangential, a result of negative polarization. Radial or tangential polarization is a result of symmetry, as we have said before. We also see that the change from radial occurs near the center of the disk first, the orientation to the directions defined by the scattering plane becoming better near the limbs as  $\Psi$  increases. This was explained in terms of symmetry properties in case A.

There are many additional properties that did not appear on the Rayleigh planet, aside from the behavior at the neutral points. The polarization stays oriented to the scattering plane, i.e., positive or negative even until  $\Psi = 160^\circ$ , whereas we saw a radial character developing near  $\Psi = 120^\circ$  for case A. The explanation for this can be found in the forward scattering behavior of the phase function, which produces a larger single scattering intensity at large  $\Psi$ . (See figure 2.35, where the disk integrated intensities for cases A and B are compared.) Note also that the M polarization as well displays the same characteristics. Since the M light has suffered

ed comparatively fewer scatterings to reach the upper boundary of the atmosphere than for Rayleigh scattering, and the polarization is less tangential here (radial, for case A). This means that the radial character is a result of losing the orientation of the scattering plane in many scattering events. It is interesting to note that secondary and tertiary scattering have such a good memory of the scattering geometry. We will see this phenomenon repeated in case C.

In view of this, it may be possible to obtain particle size and composition information from the phase angle at which a planet gives radial or tangential polarization.

Another phenomenon that was noticed in case A is the averaging quality of secondary scattering. This is dramatically seen here, for in figure 2.36 we notice that the disk integrated T polarization is negative for small phase angles as in the single scattering polarization (figure 2.23), but the M polarization is positive during the entire negative branch. The positive polarization comes from the large positive branch at intermediate  $\Psi$ 's. The appearance of the disk near the maximum negative excursion of the T polarization is shown in figure 2.26.

Figure 2.27 shows the polarization at  $\Psi = 15^\circ$ , near the neutral point at  $\Psi = 16^\circ$ . Figure 2.28 for  $\Psi = 21^\circ$  displays the planet at a point where the single scattering polarization is almost zero. The polarization across the disk



at the value of  $\Psi$  where the single scattering polarization is maximum can be found in figure 2.29. This does not correspond to the maximum in the disk integrated polarization, which is displaced towards larger  $\Psi$ .

We also include some diagrams near the second null of the phase function occurring at  $\Psi = 123^\circ$ . At  $\Psi = 120^\circ$  (figure 2.30) the T polarization is zero, while for  $\Psi = 126^\circ$  it is negative. At  $\Psi = 120^\circ$  the effect of single scattering can be seen in the positive polarization at the limb and terminator (here the phase function gives positive polarization), while the averaging of the forward scattering negative polarization can be seen in the center of the disk. The multiple versus single scattering competition was noted for Rayleigh scattering as well.

From  $123^\circ$  to  $180^\circ$  the single scattering polarization is negative and the electric vector maximum becomes parallel to the scattering plane. We have also included  $\Psi = 173^\circ$  where the polarization, though extremely small, has become tangential negative. This is most visible in the M diagram, but since the M intensity is small, the T diagram does not show it on this scale.

Finally in figure 2.37 we give the variation of the disk integrated T polarization with  $\tilde{\omega}_0$ . As we would expect, the largest phase angles are least affected by the variation, for there the multiple scattering dilution is reduced.

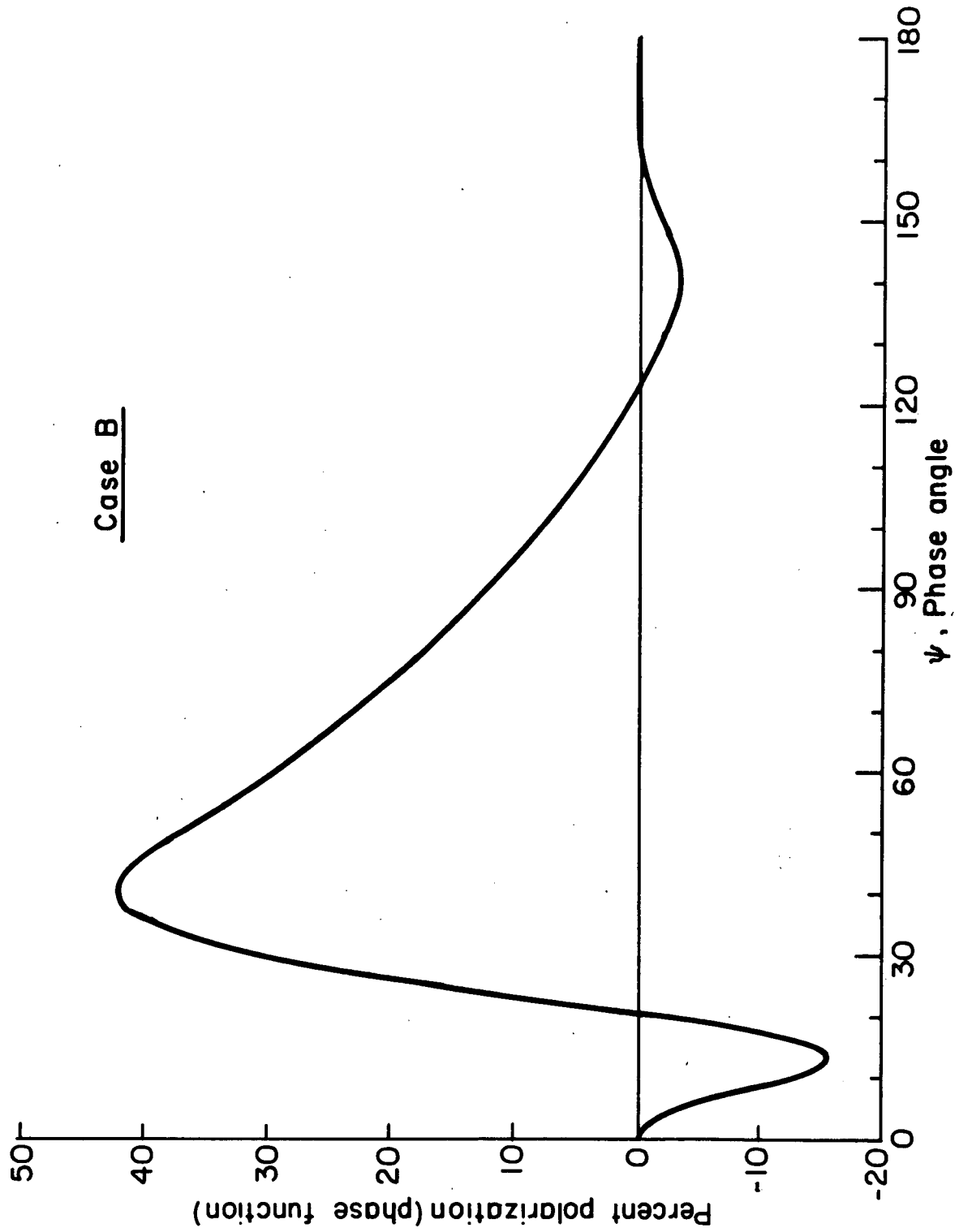


Figure 2.23 Single scattering polarization for case B. The neutral points occur at  $21^\circ$  and  $123^\circ$ .

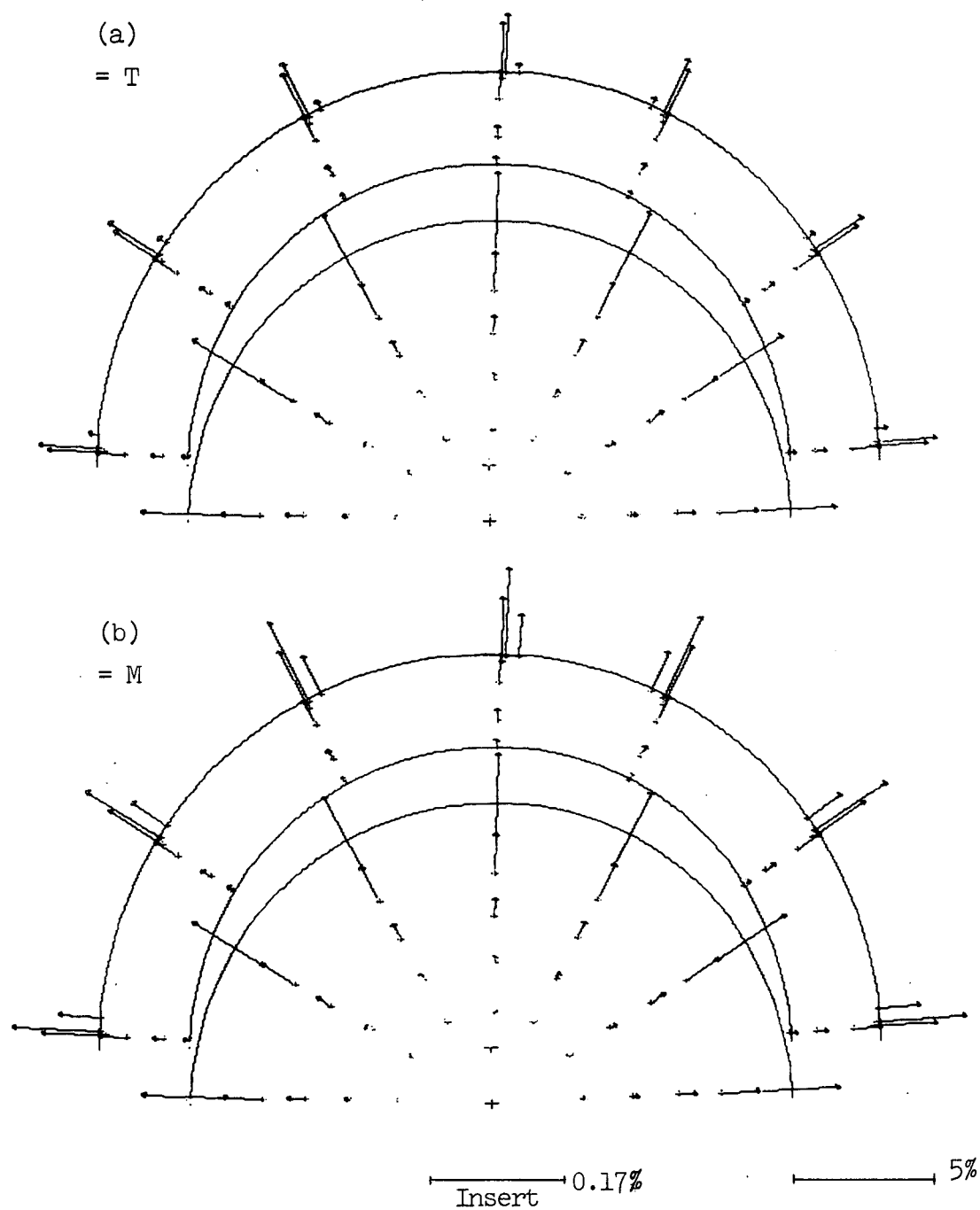


Figure 2.24 Case B. Polarization across disk for a forward scattering phase function as described in the text and in figure 2.22 and 2.23. Note the greatly enlarged scale as compared to the Rayleigh case. The scale of the central portion of the disk has been expanded. The single scattering polarization is negative until  $21^\circ$ . Upper (a) = T; lower (b) = M;  $\psi = 0^\circ$ .

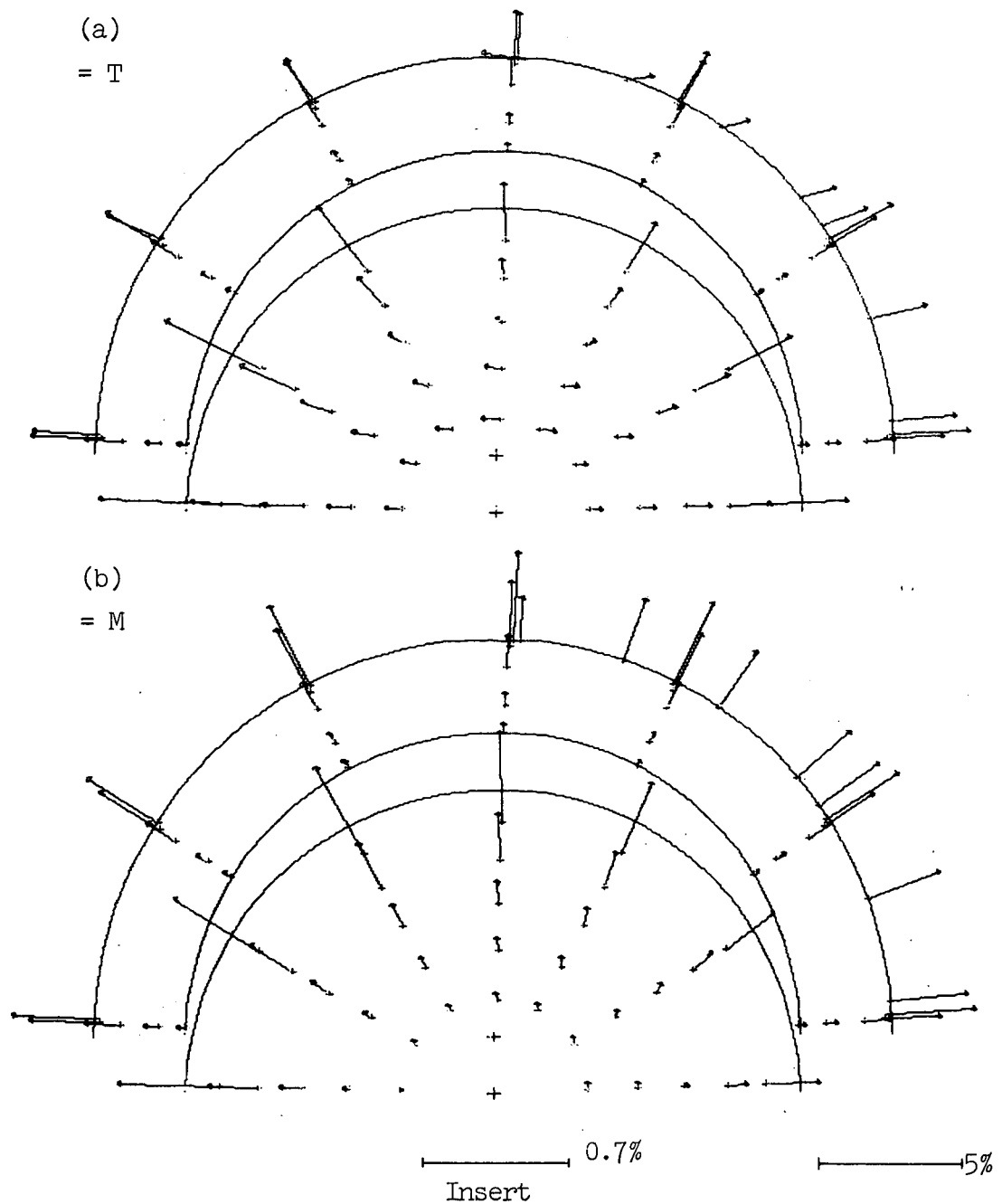


Figure 2.25 Case B.  $\psi = 3^\circ$ . T polarization changes from negative near center to radial positive to negative on sunward limb. M polarization, an average over all phase angles in the sense described in the text, is radial positive.

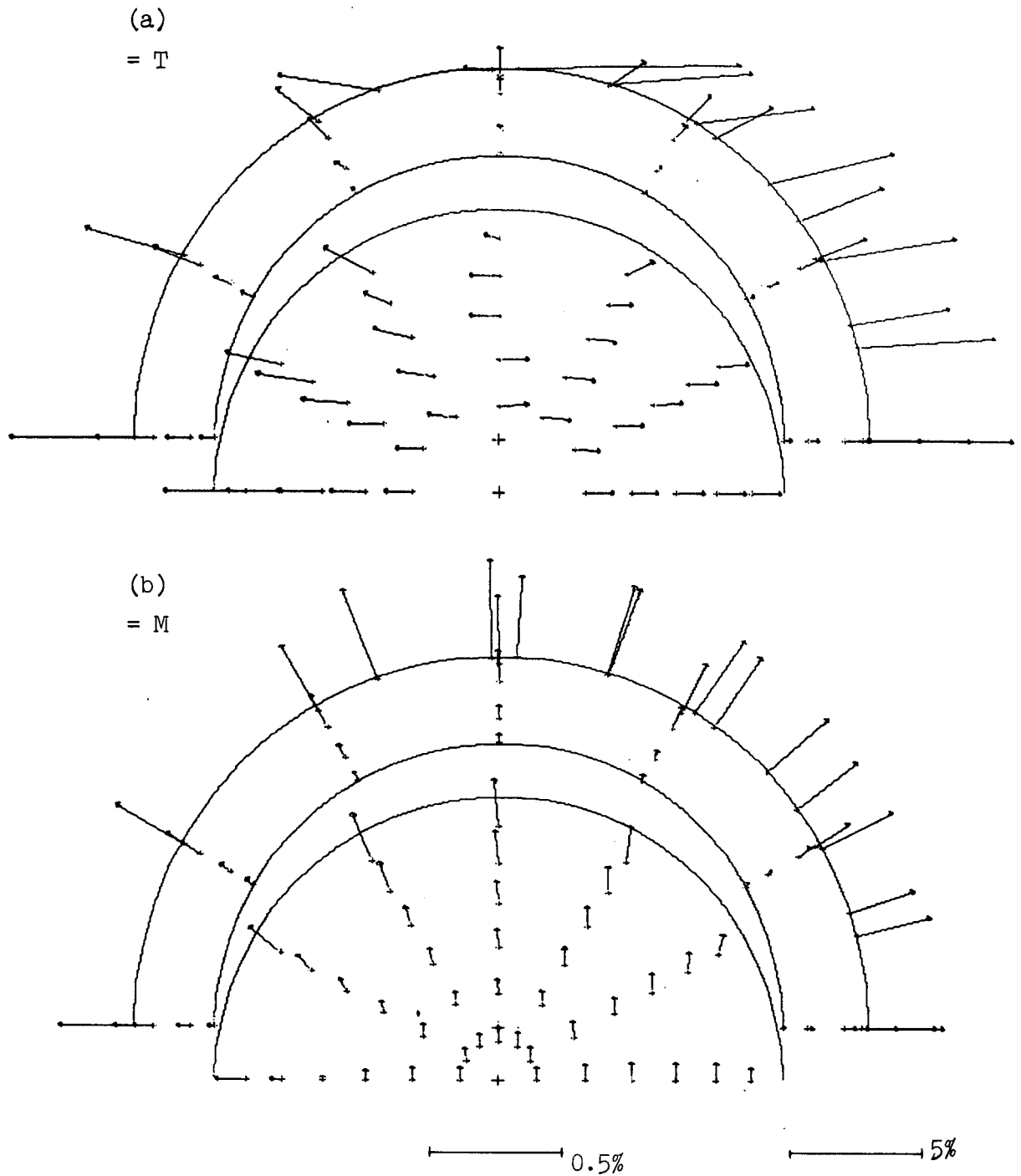


Figure 2.26 Case B.  $\psi = 9^\circ$ . T polarization is negative near center of disk, yet M polarization is positive. Single scattering polarization is -11% and becomes increasingly negative until  $\psi = 15^\circ$ ; disk integrated T polarization is -0.1% and peaks here; disk integrated M polarization is +0.1% and is increasing.

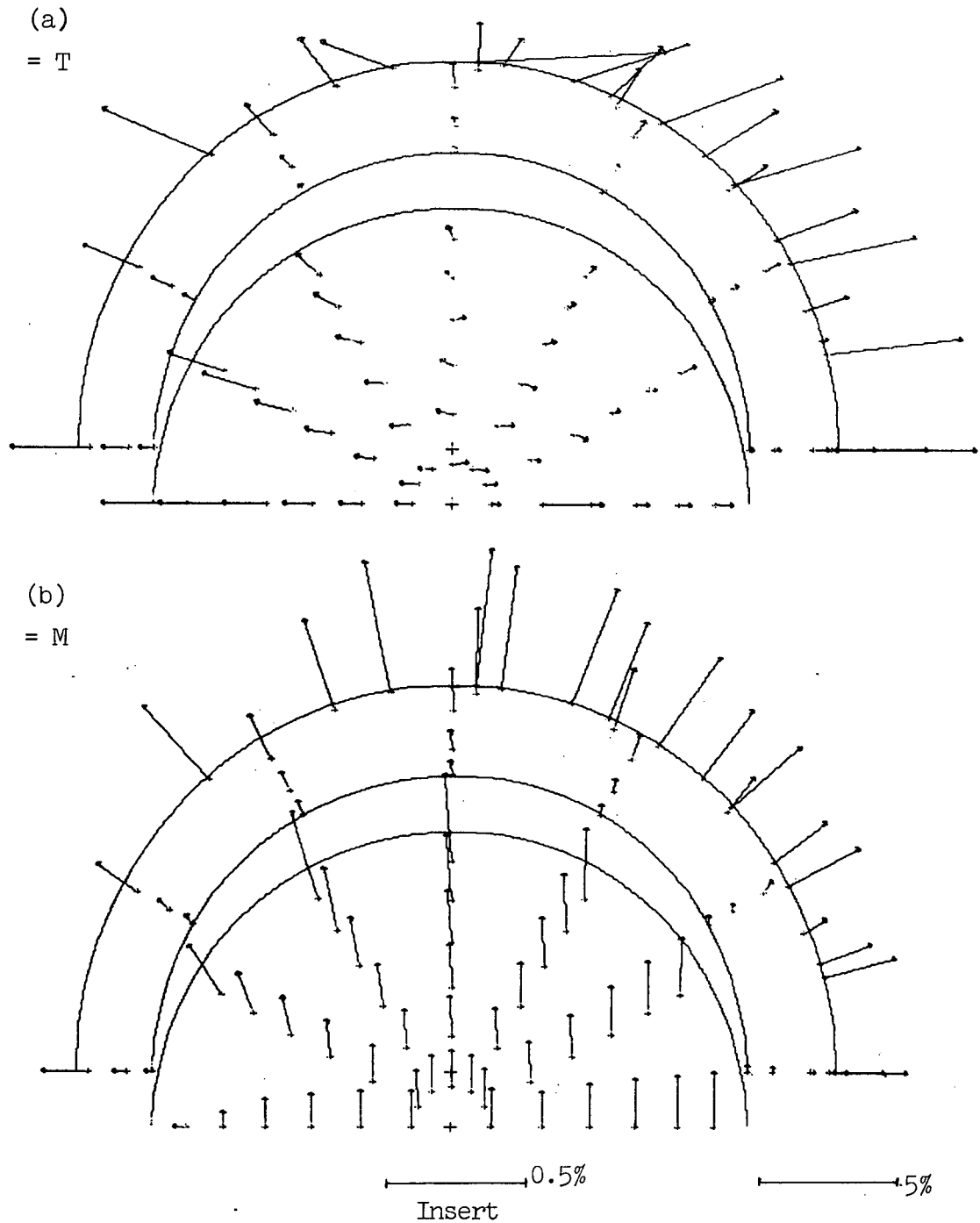


Figure 2.27 Case B.  $\psi = 15^\circ$ . Single scattering polarization reaches a maximum negative value of  $-15\%$  here; integrated T polarization is almost zero, accounting for the chaotic appearance.

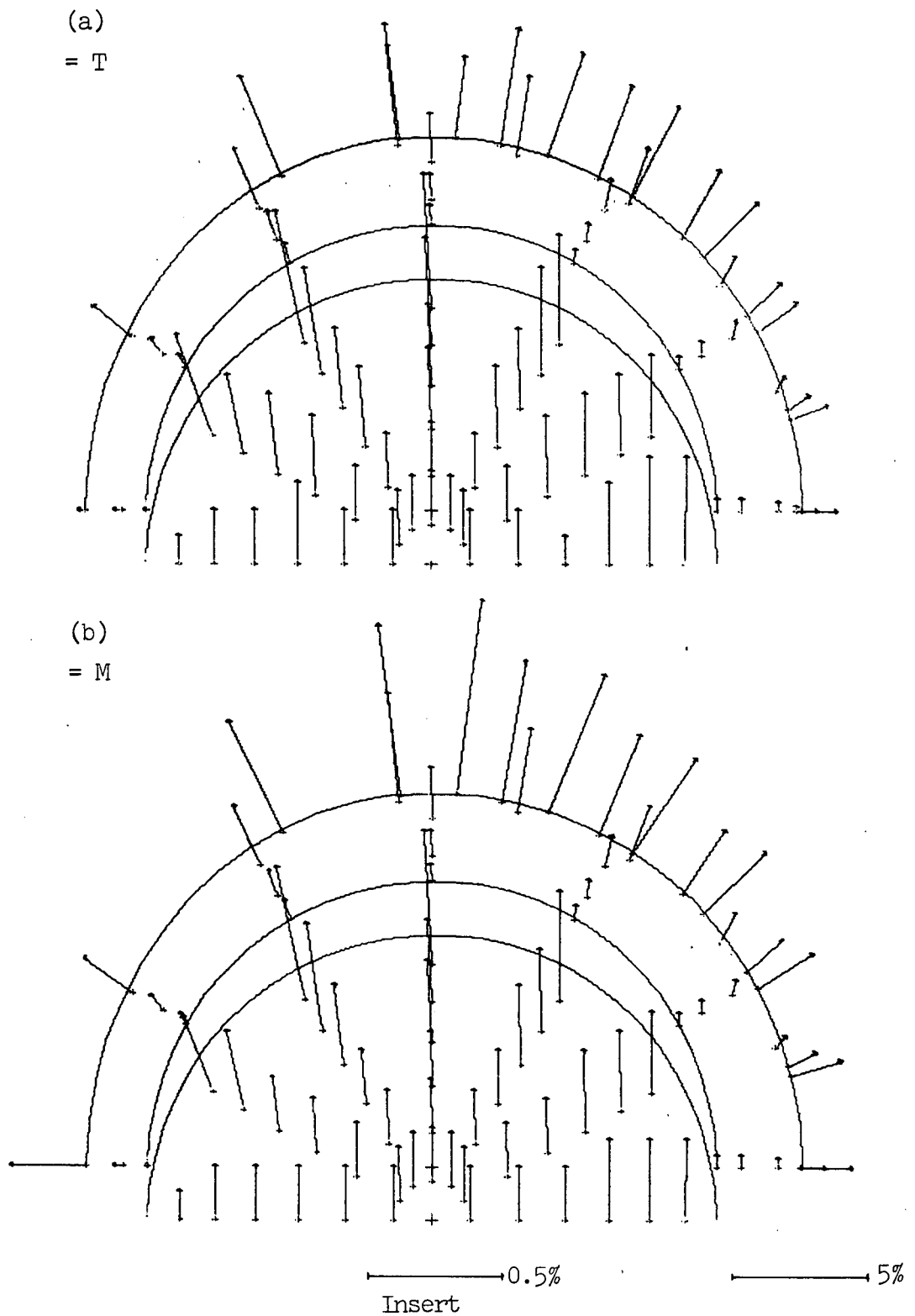
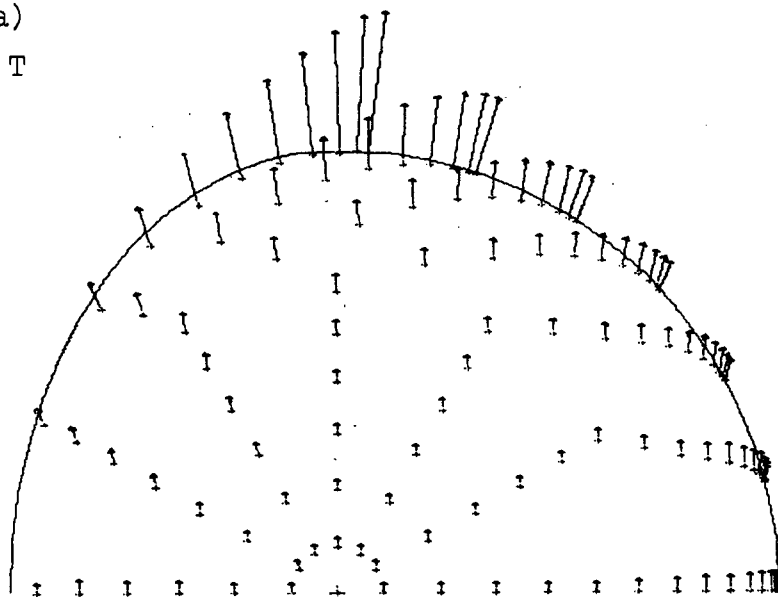


Figure 2.28 Case B.  $\psi = 21^\circ$ . Integrated  $T = M$  at this phase angle. Single scattering polarization is zero, yet polarization at center of disk is normal to single scattering plane.

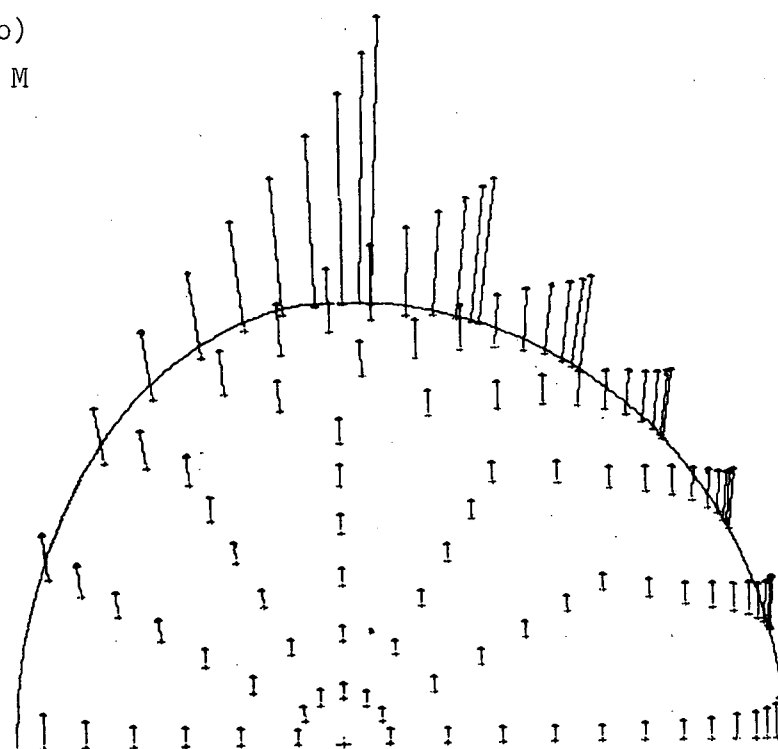
(a)

= T



(b)

= M



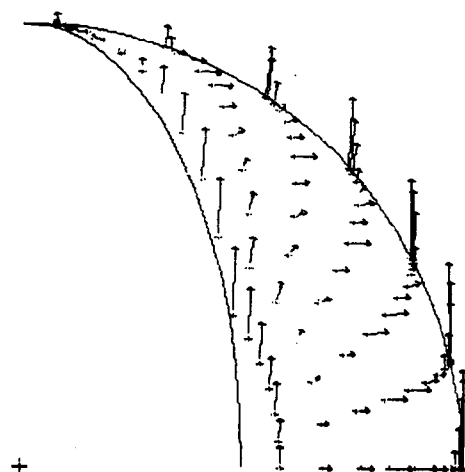
————— 15%

Figure 2.29 Case B.  $\psi = 42^\circ$ . Corresponding to maximum single scattering polarization of 42%. Note scale reduction here and the different scales in the following figures.

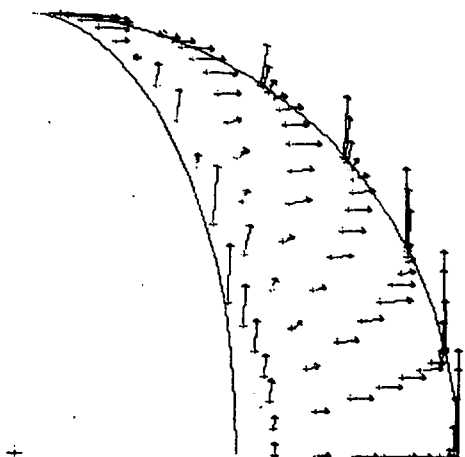


30(a)

= T



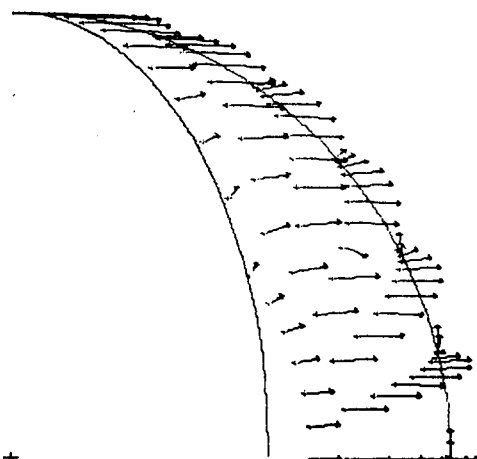
30(b) = M



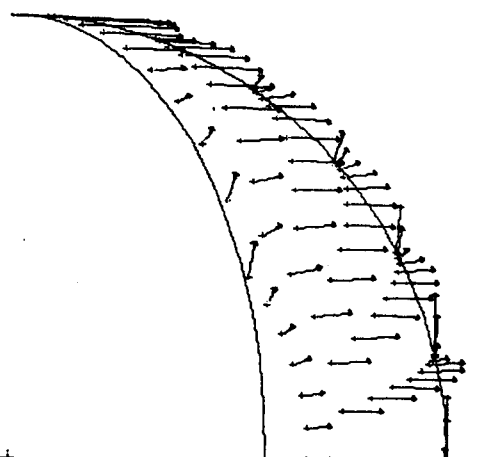
1.7%

31(a)

= T



31(b) = M



1.7%

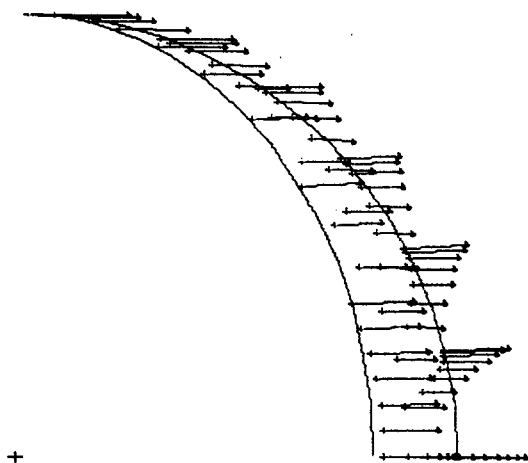
Figure 2.30 Case B.  $\psi = 120^\circ$ . Near second null of phase function at  $123^\circ$ .

The effect of a single scattering polarization of +1% can be seen at limb and terminator. T polarization = 0%, M polarization = -0.15%. Note variable direction of polarization.

Figure 2.31 Case B.  $\psi = 126^\circ$ . Polarization on other side of single scattering null. Most polarizations are negative.

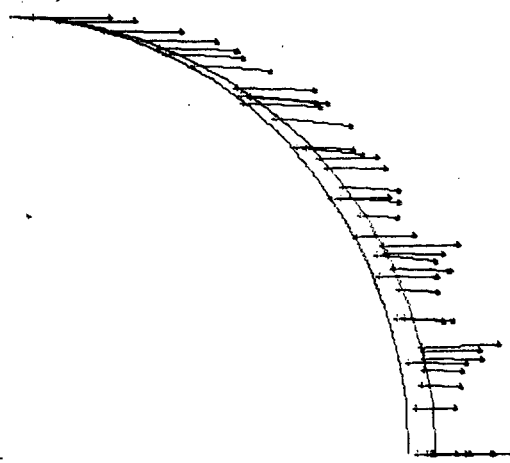
32(a)

= T



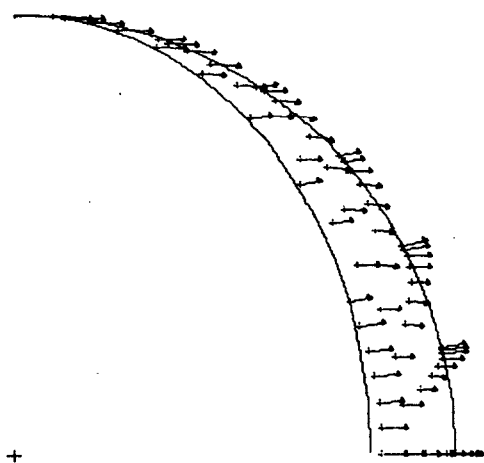
33(a)

= T



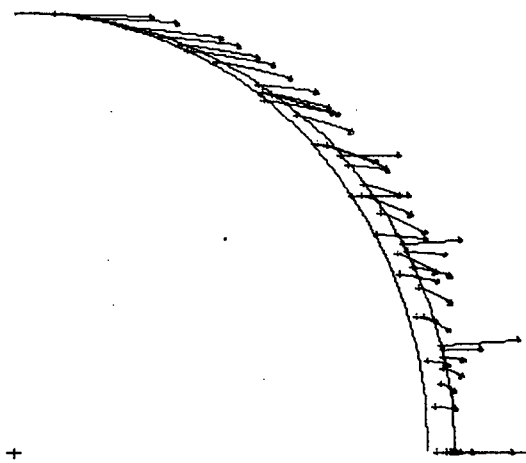
32(b)

= M



33(b)

= M



0.5%

0.83%

Figure 2.32 Case B.  $\psi = 144^\circ$ . T polarization is uniformly negative although M polarization shows deviations towards tangential negative.

Figure 2.33 Case B.  $\psi = 160^\circ$ . Tangential negative characteristics appear in M polarization more so than in T polarization.

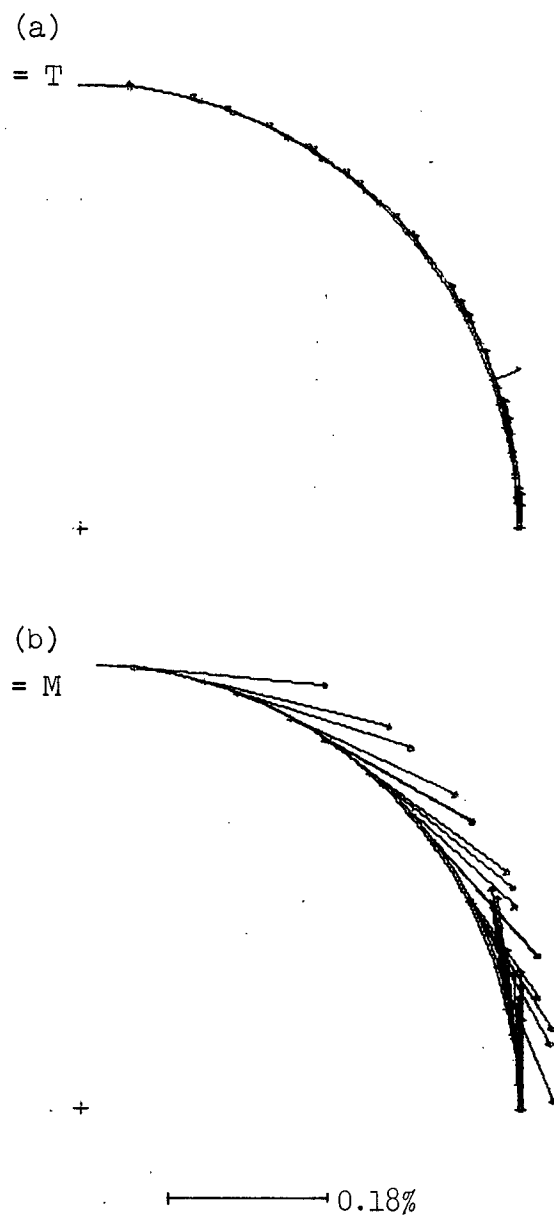


Figure 2.34. Case B.  $\psi = 173^\circ$ . T polarization is very small, but tangential negative. M polarization is obviously tangential negative, but intensity is very small.

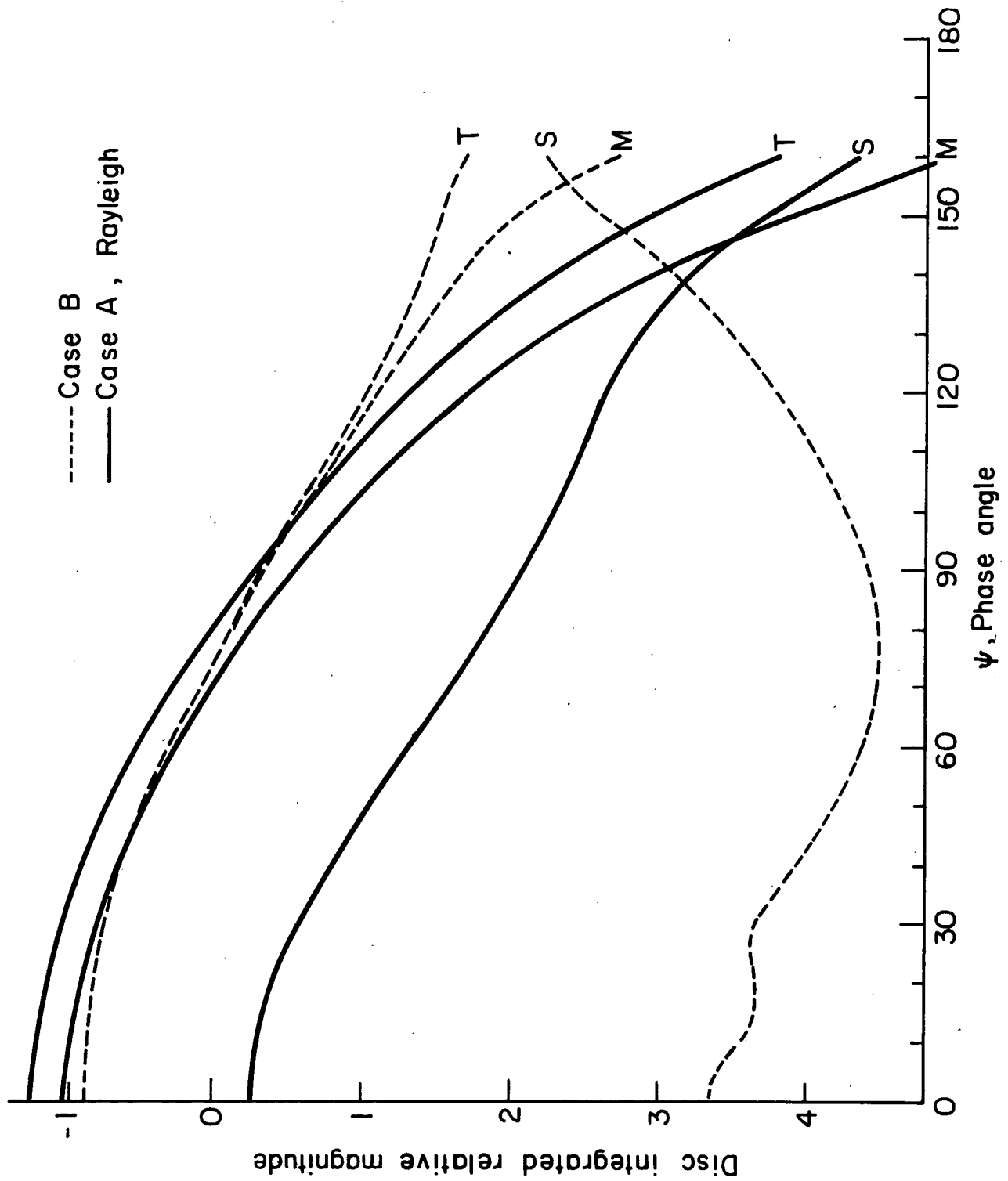


Figure 2.35 Disk integrated relative magnitude of planet for cases A and B. Total intensity, T, intensity of light scattered more than once, M, and single scattering intensity, S, are indicated.

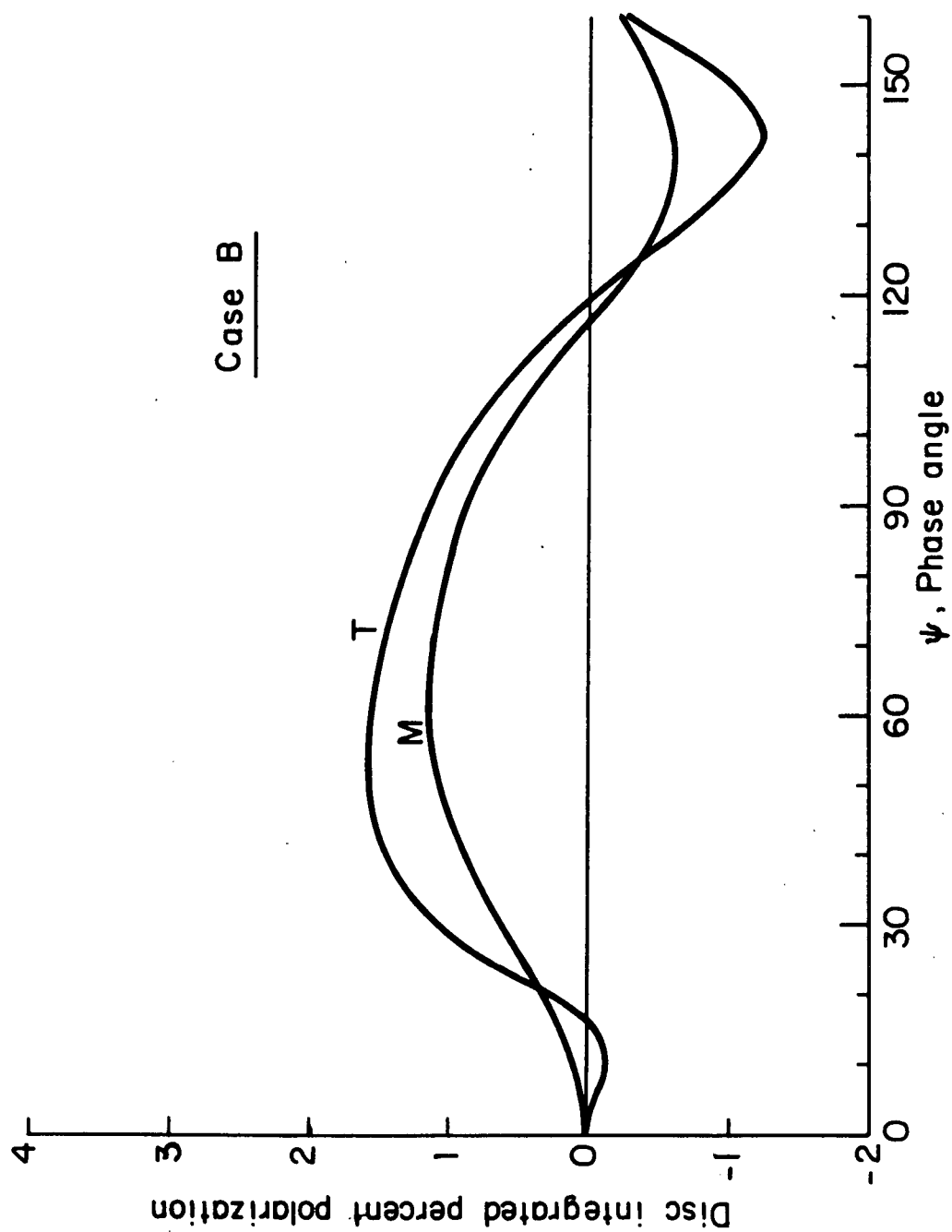


Figure 2.36 Disk integrated polarization for case B. T and M polarizations indicated. The neutral points occur at  $16^\circ$  and  $120^\circ$  for the T polarization. M polarization is positive at small phase angles.

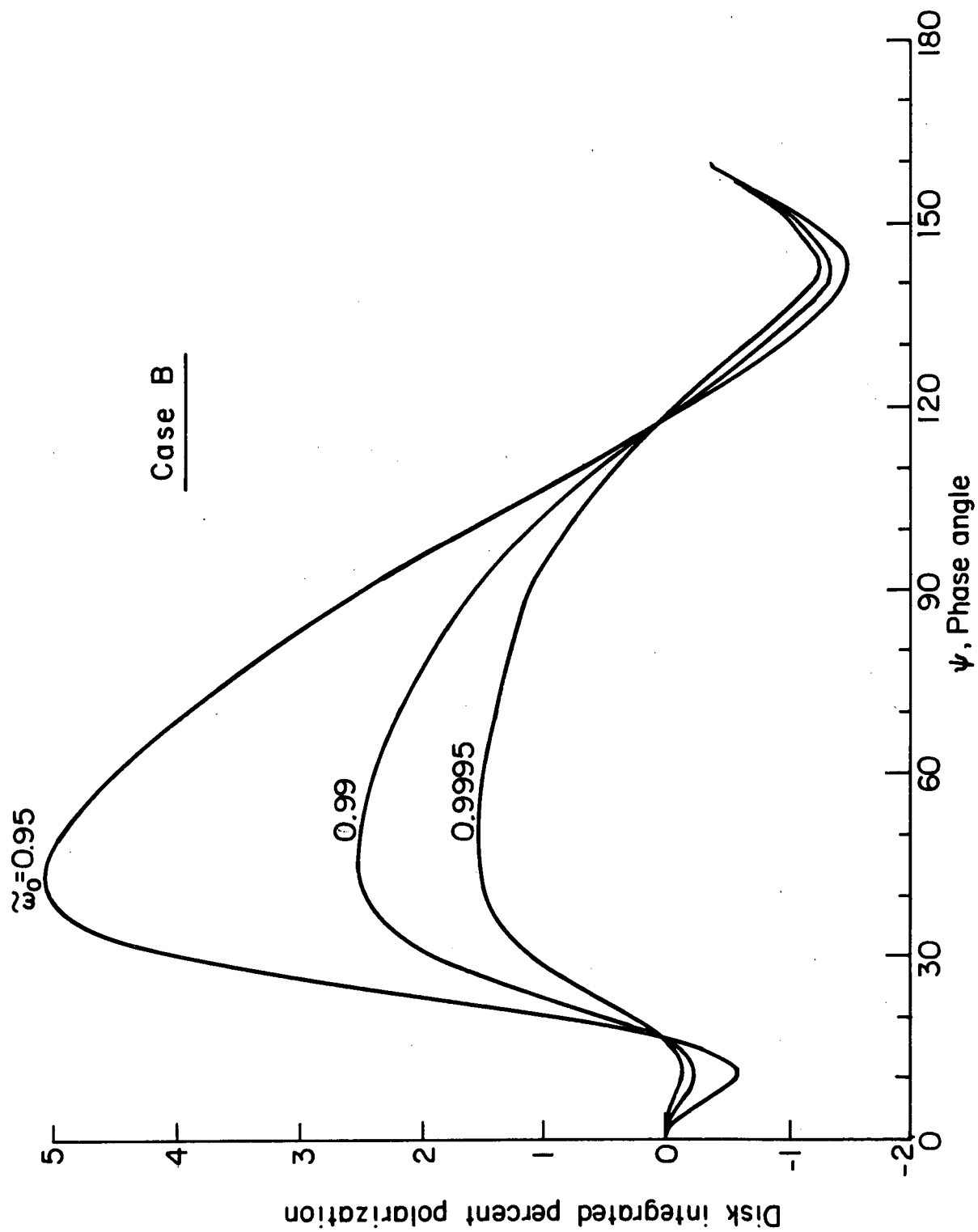


Figure 2.37 Disk integrated T polarization for case B.  $\omega_0$  parameter.

## C Venus at 1 Micron Wavelength

### a. Theory

The composition of the clouds of Venus is still an enigma, despite 2 American and 4 Russian probes to the veiled planet. Water ice, CO<sub>2</sub> ice and suspended dust particles have been proposed, as well as a host of other constituents, among them carbon suboxide, ferrous chloride dihydrate and polywater (Sagan, 1971).

Recently Hansen (1971) suggested a model for the cloud particles which is both startling in its conclusions and powerful in its evidence. He calculates that the particles are round, hence in a liquid state, that they have a mean radius near 1 micron and that their index of refraction is  $n=1.45\pm0.02$ . This was derived from a model which fits the phase and wavelength dependence of the disk integrated polarization.

If Hansen's phase function is correct, then it should also be able to match the polarization across the disk measured by Coffeen and Gehrels (1969). This would be an additional test of the model. Alternately, we may assume that the phase function is correct and look for secondary effects. Both procedures will be explored here.

A description of the derivation and form of the phase function follows. We chose  $n = 1.45$  and the particle size distribution according to equation 2.25 with  $\beta = 6$ ,  $\gamma = 1$ ,

and  $b = 8$ . This gives a mode radius  $r_c = 0.75\mu$  which is smaller than the value  $r_c = 1.1\mu$  finally chosen by Hansen for a best fit. As we saw at the beginning of section IV, this affects the integrated results only slightly, and very little indeed at  $\Psi = 60^\circ$  and  $\Psi = 77^\circ$  where Coffeen has data at  $1\mu$  wavelength. The wavelength was chosen to be  $1\mu$ . Funds did not permit calculations at other wavelengths observed by Coffeen.

The single scattering albedo was chosen using van de Hulst and Grossman's (1968) similarity relations as a first and only iteration to give a Bond albedo equal to that of Venus at  $1\mu$ . A choice of  $\tilde{\omega}_0 = 0.9995$  gave  $A_B = 0.91$ , slightly higher than, but with the error bars of, the value  $A_B = 0.89$  observed by Irvine (1968).

The phase function calculated by the Mie theory for the above input parameters has an average size parameter of  $\bar{\alpha} = 6.6$ , and therefore is peaked in the forward direction. It is peaked in the backward direction as well so that  $\langle \cos\theta \rangle = 0.69$ , slightly less than case B which had a smaller  $\bar{\alpha}$ . Figures 2.38 and 2.39 at the end of this subsection show the single scattering intensity and polarization as a function of  $\Psi = \pi -$  scattering angle.

To discuss the disk polarization we should first note some of the features in the single scattering polarization. The polarization is always negative having a very strong



maximum = -54% at  $\Psi = 10^\circ$ , a relative minimum at  $\Psi = 28^\circ$  and a broad maximum near  $\Psi = 50^\circ$ , decreasing monotonically (in absolute value) to 0% at  $\Psi = 180^\circ$ .

Departing from our previous procedure of discussing the disk integrated results last, let us look at figure 2.40 which shows the results of that calculation for T and M polarizations. We notice immediately that the M polarization does not have a relative maximum corresponding to the maximum at  $\Psi = 10^\circ$  of the phase function itself, although some effect is seen. This once again is the result of the averaging process we discussed previously. The peaks in the T polarization are displaced towards larger  $\Psi$  because of this. We may also note that the total polarization has another maximum, not contained in the phase function. This is due to a competition between the increasing importance of the forward single scattering at grazing angles, and the decreasing polarization.

It may be noticed that both cases B and C had large single scattering negative polarizations near  $10^\circ$ , yet in case C the integrated effect is much more prominent. Note also that the polarization across the disk is much greater near zero phase for case C than for case B. Averaging over the positive and negative branches of the polarization curve could have produced the small polarization that is observed in case B. It is difficult to separate the effect of the averaging process from other causes, however, for it appears that the

differences in the magnitude of the polarization between cases B and C could be due to the larger single scattering backscattering in case C. (Compare figures 2.36 and 2.40 for the polarization and figures 2.35 and 2.41 for the integrated intensities.) The large polarization of case C at small phase angles has an important affect on the direction of the polarization across the disk, as we will see very shortly.

The variation of the T polarization with  $\tilde{\omega}_0$  has been calculated for this case as well; we display it without comment in figure 2.42.

Figures 2.43 to 2.51 show the appearance of the degree of polarization across the disk of Venus at 1 micron wavelength for our model. Figures 2.52 and 2.53 compare these calculations with Coffeen's observations at two phase angles. The scale is the same for all phase angles. Note that here, since the single scattering polarization is always negative, we may read "tangential" for "radial" when comparing this case to cases A and B.

It will be noticed immediately that for the total intensity tangential polarization is practically absent for  $\Psi > 6^\circ$ .  $\Psi = 0^\circ$  was not calculated, but we would expect it to be tangential there from symmetry alone. Comparing this case with case A for Rayleigh scattering, the absence of tangential polarization is striking. From the previous discus-

sion we would attribute this to large single scattering intensity at large phase angles.

The tangential polarization, although overwhelmed by the single scattering polarization, is present in the M polarization at both large and small phase angles. In fact the total behavior of the M polarization is very similar to what we observed for Rayleigh scattering. The large M polarizations near the poles will be observed to be tangent to the disk at all points.

The absence of tangential or radial polarization over a large range of phase angles including the region near zero phase is quite an important result. It is most probably true of all atmospheric models containing particles whose average radii is larger than the wavelength, although we have not made enough computations to be positive. Rayleigh scattering and scattering from large particles can thus be distinguished at a glance by the direction of polarization at small non-zero phase angles. We believe that the general characteristic of large transparent particles of enhanced polarization in the region of enhanced backscattering intensity quickly destroys the radial polarization as the phase angle increase from zero.\* More computations will be needed to determine

---

\*The polarization and intensity peak characteristic of the primary rainbow for  $\bar{\alpha} \gg 1$  is only marginally present in the phase function for Venus at 1 micron. The position of the rainbow moves towards smaller phase angles as  $\bar{\alpha}$  decreases (and as the index of refraction increases). For  $n=1.45$  the primary rainbow should appear at  $38^\circ$ , but the polarization peak here appears at  $10^\circ$  and the intensity peak at  $19^\circ$ .

how well this effect alone can give information on the particle size and index of refraction. The importance of the intensity peak on the polarization direction must also be determined for a complete understanding.

b. Comparison with Observations

The model that we have been discussing is significant because it is able to match the disk integrated polarization of Venus at 1 micron as well as at other wavelengths. As we shall see now, the model also is consistent with polarizations measured at selected points on the disk, lending further weight to Hansen's (1971) conclusions. (Hansen has proposed that the clouds of Venus are composed of particles with  $n = 1.45 \pm 0.02$  and  $\bar{a} \approx 1\mu$ ).

Unfortunately the polarization calculations we have performed can be related directly to observations only in the limiting case of measurements made with a resolution element far smaller than the size of the disk. The actual resolution element used by Coffeen and Gehrels (1969) did not satisfy this condition. Thus to compare these observations with our calculations an integration over a small portion of the disk, allowing for seeing effects, would have to be performed. This was not done and consequently in comparing our results with observations the following must be kept in mind. Near the terminator and limb, and especially at

their intersection, the pole, the polarization increases more rapidly than elsewhere, while the intensity decreases. Thus any integration that does not fairly weight these areas will tend to overestimate the polarization. Our crude integration made use of only data similar to the data in the figures and overestimates the polarization where noted above.

Figures 2.52 and 2.53 compare the observations and calculations. The circles show the area of the measuring aperture, not allowing for seeing effects, which are considerable when observing Venus. The upper and lower numbers give the observations and computations respectively. The lines drawn through the data circles indicate the observed direction of the electric vector maximum. In the intermediate limb regions between the pole and equator Coffeen observed that the direction of polarization is more nearly parallel to the limb, being deviated in that direction by an average of  $5^\circ$ . Our calculations show a deviation of  $4^\circ$ . The plane of polarization is rather well fitted elsewhere on the disk as well. A good agreement is also found for the magnitude of the polarization except near the limb and especially pole as discussed previously.

The comparison, within the computational limitations we have mentioned, and the observational variability discussed in the next section, supports the following statement: the detailed structure of the planetary scattering may be

satisfied as well by Hansen's atmospheric model. This is encouraging for it means that if we believe Hansen's model, we may begin to model the regional departures from the average. Thus cloud top altitudes, variabilities in the index of refraction, particle size distribution and particle shape could be mapped though the effects may be difficult to separate in practice.

The preceding discussion does not confirm Hansen's model, though it does argue in its favor. We believe that Hansen's model stands strongly by itself, if we apply the test of Occum's Razor, for it is the simplest explanation to fit all the data. A two layer model should be investigated, however, for it is not clear that a two layer model with different indexes of refraction or particle size distributions can not do the job as well. A two layer model should be investigated for an index of refraction of 1.45 is difficult to explain while  $1.33 + 1.50$  is not.

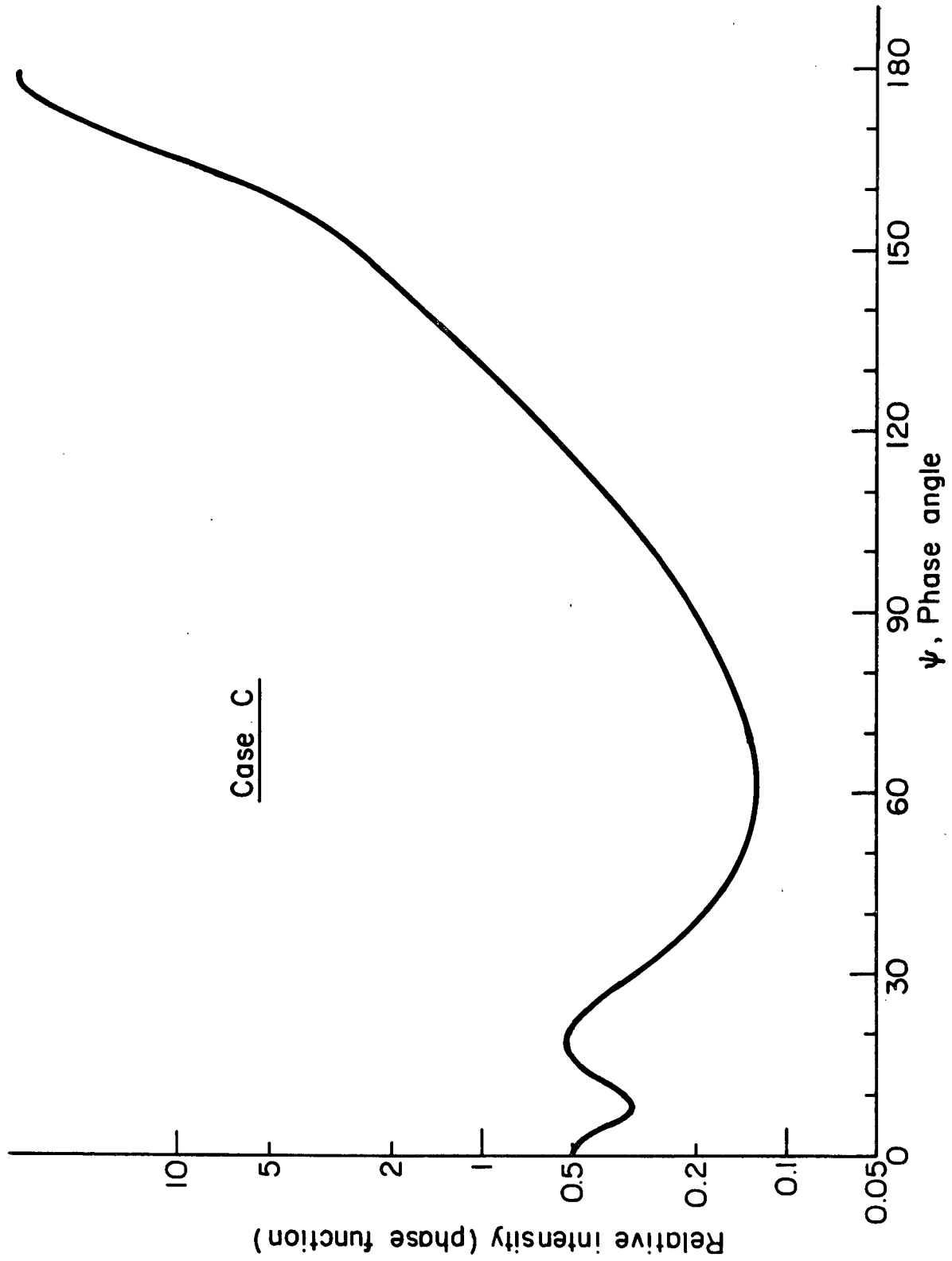


Figure 2.38 Single scattering phase function for case C.

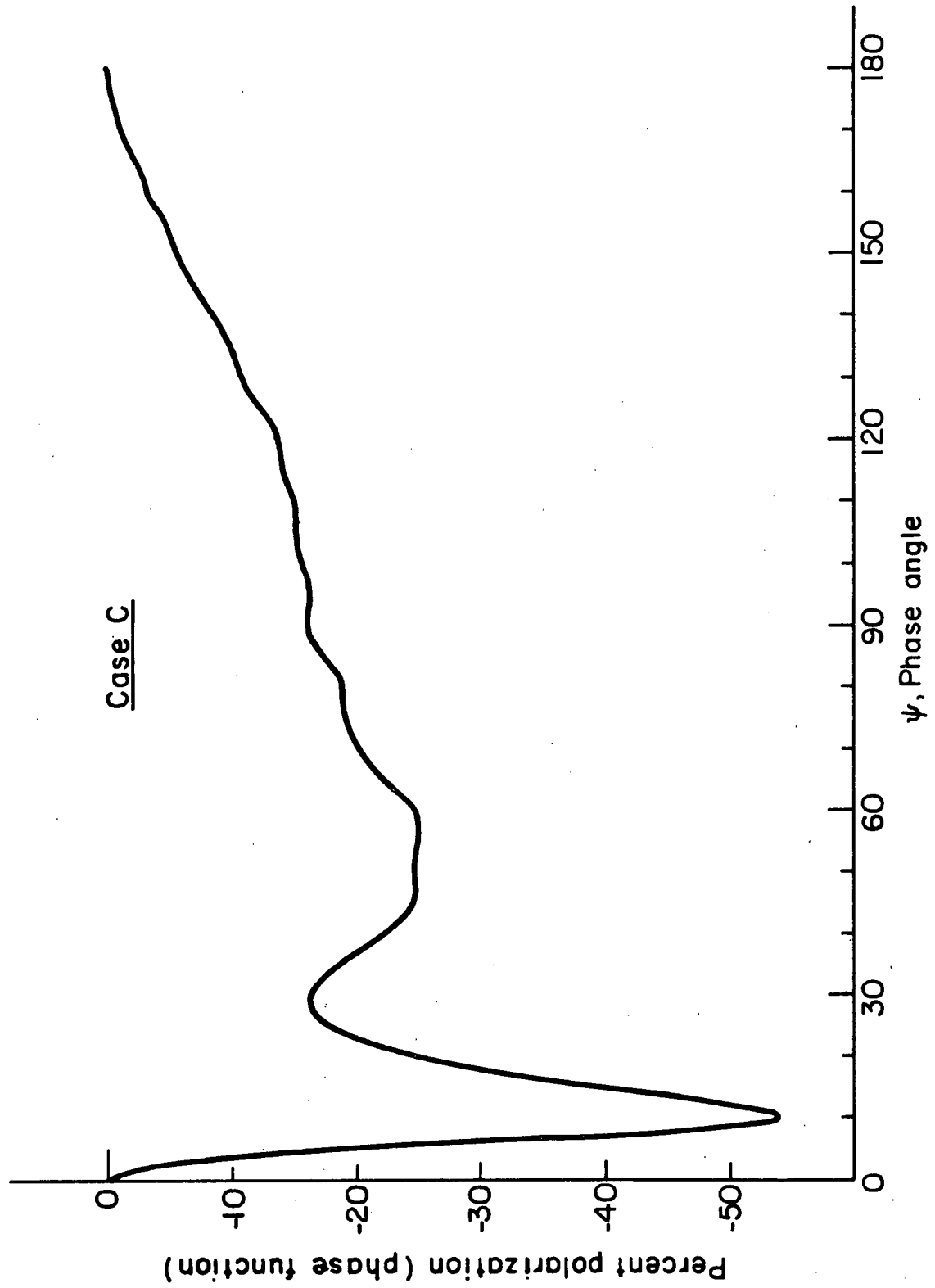


Figure 2.39 Single scattering polarization for case C.



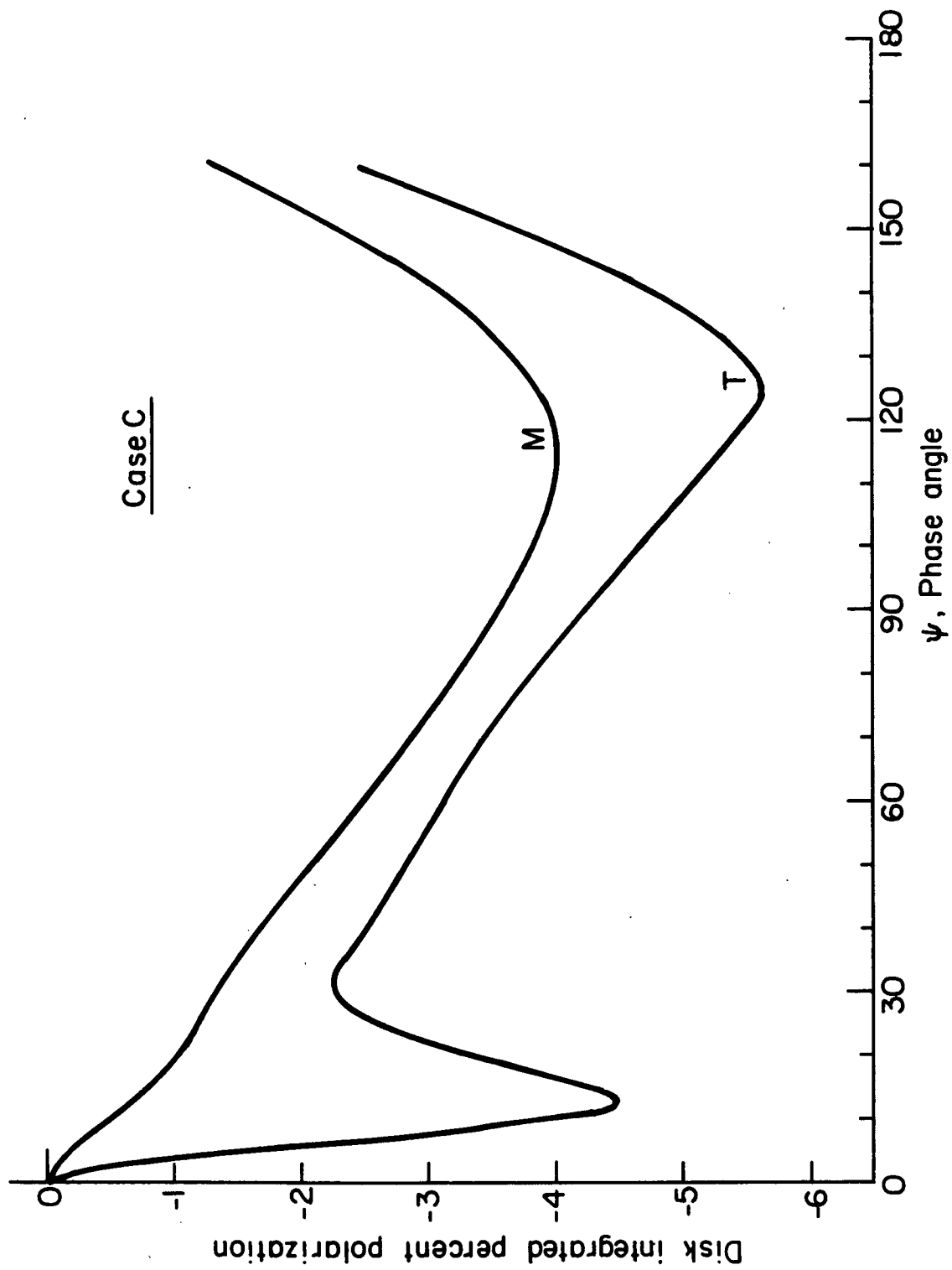


Figure 2.40 Disk integrated polarization for case C. Both T and M polarizations are included.

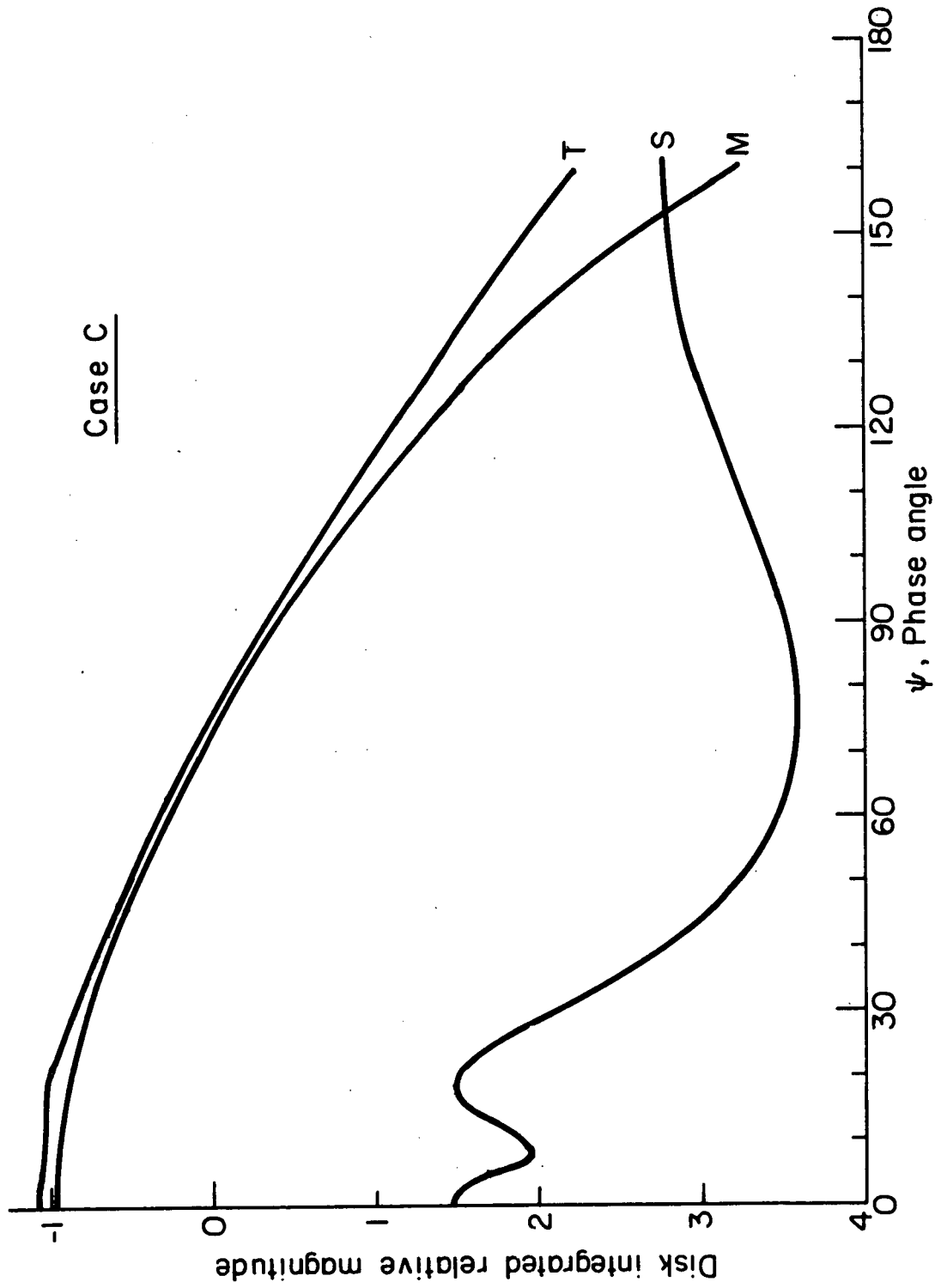


Figure 2.41 Disk integrated relative magnitude of planet for case C. T, M, and S magnitudes are shown.

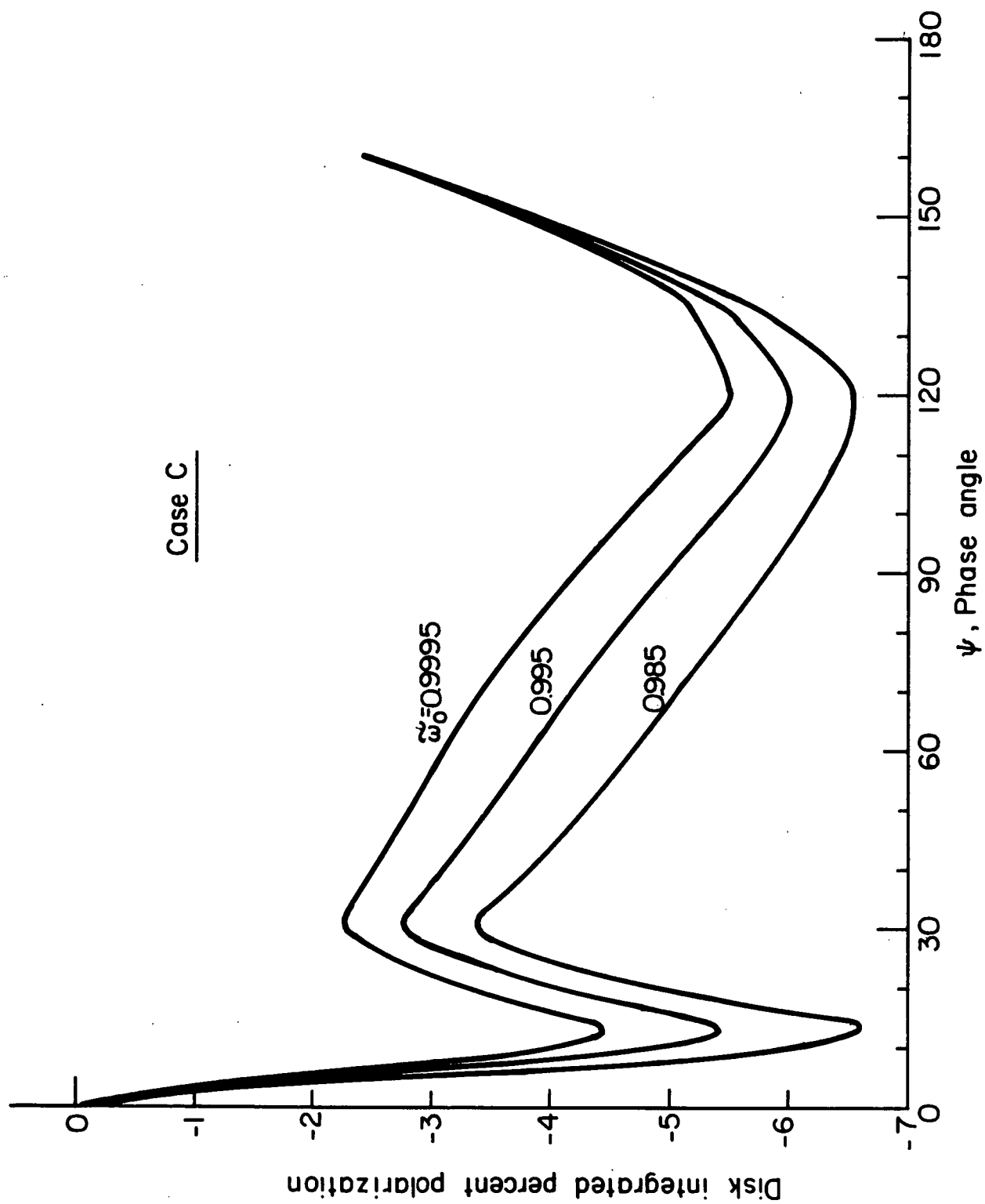


Figure 2.42 Disk integrated T polarization for case C.  $\omega_0$  parameter.

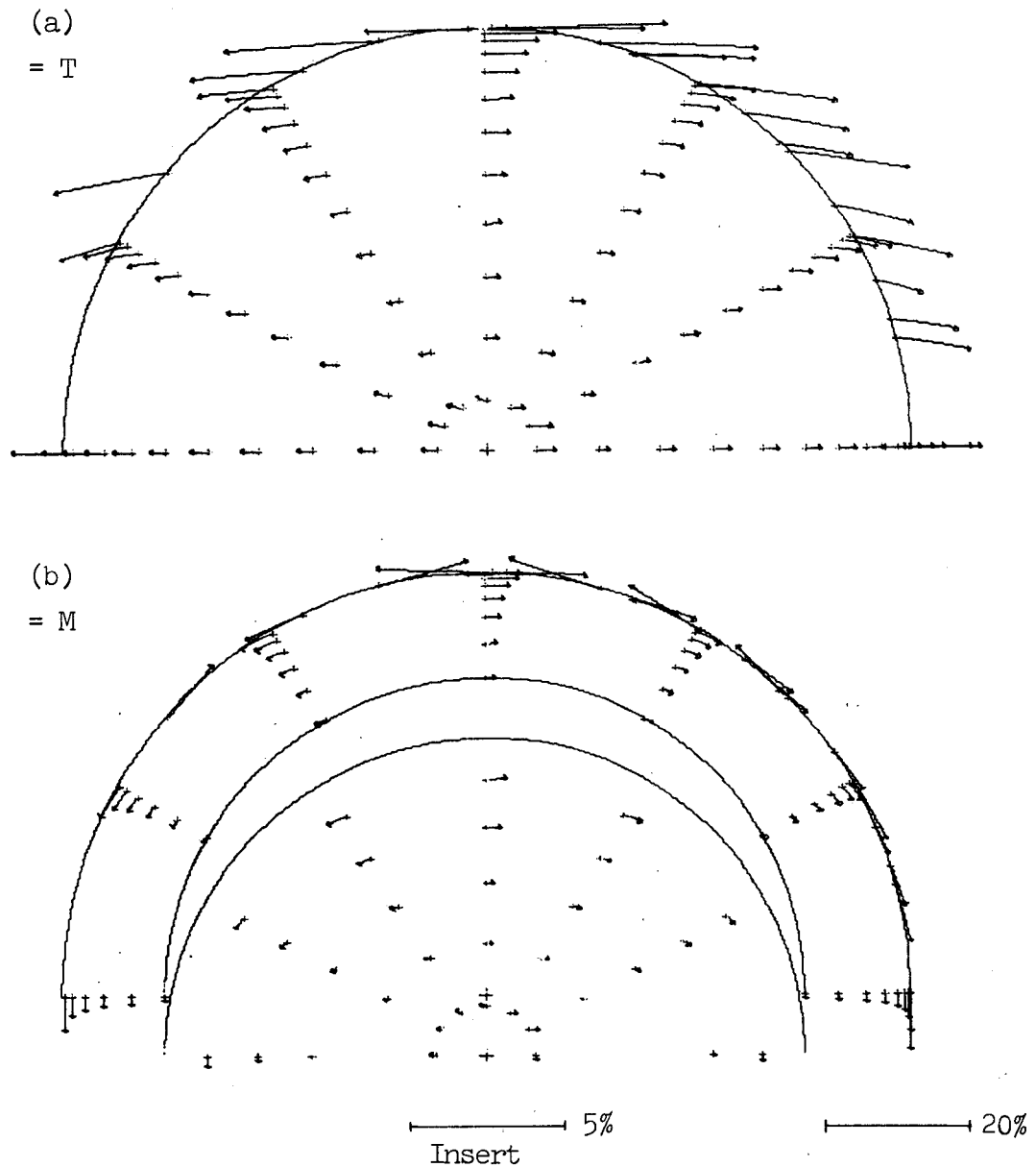


Figure 2.43 Case C. Forward scattering phase function which matches disk integrated phase variation of Venus at one micron.  $\psi = 6^\circ$ . Upper (a) = T; lower (b) = M. T polarization is mostly negative, M polarization is tangential negative. Scale is the same for all phase angles and is equal to the scale for Rayleigh scattering with  $\psi = 30^\circ$ .

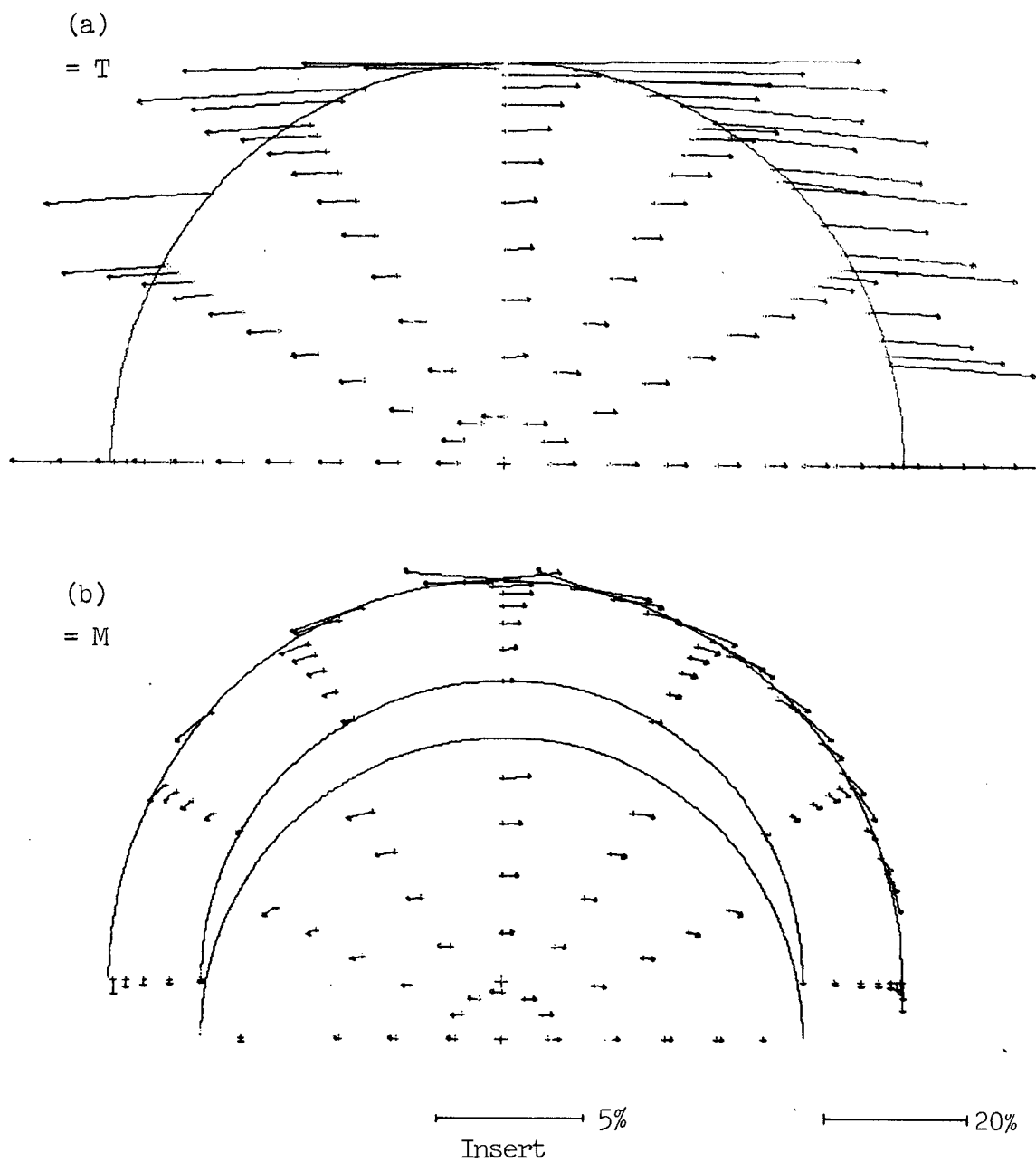


Figure 2.44 Case C.  $\psi = 11^\circ$ , where phase function has a polarization peak of -54%. M polarization unchanged from  $\psi = 6^\circ$ , except near the center where it is larger and more negatively directed, similar to the behavior of the Rayleigh phase function.

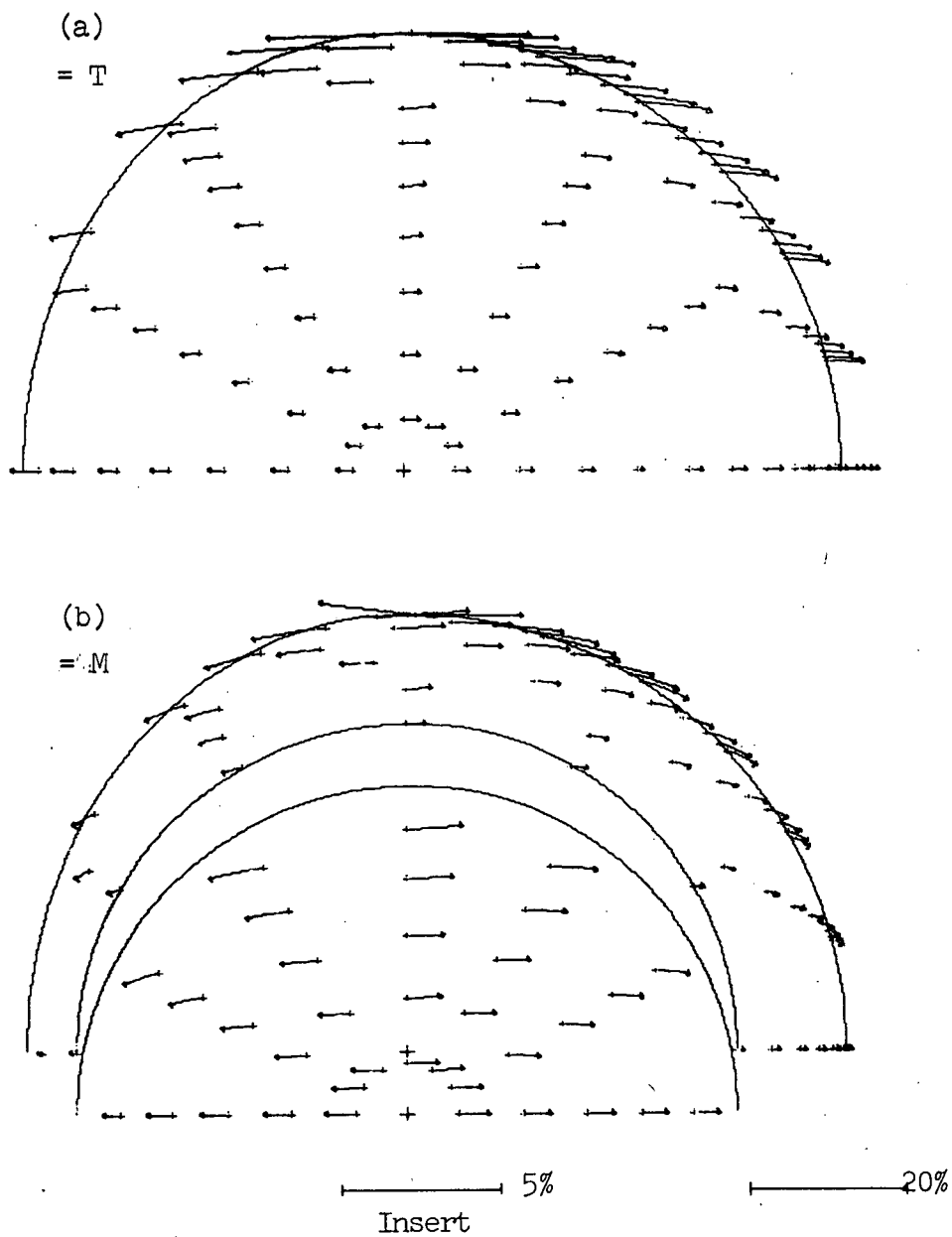


Figure 2.45 Case C.  $\psi = 30^\circ$ , near minimum of absolute value of T polarization. The T polarization is largely negatively directed at this and other phase angles shown. Contrast this with the radial directivity of Rayleigh scattering at similar large and small phase angles.

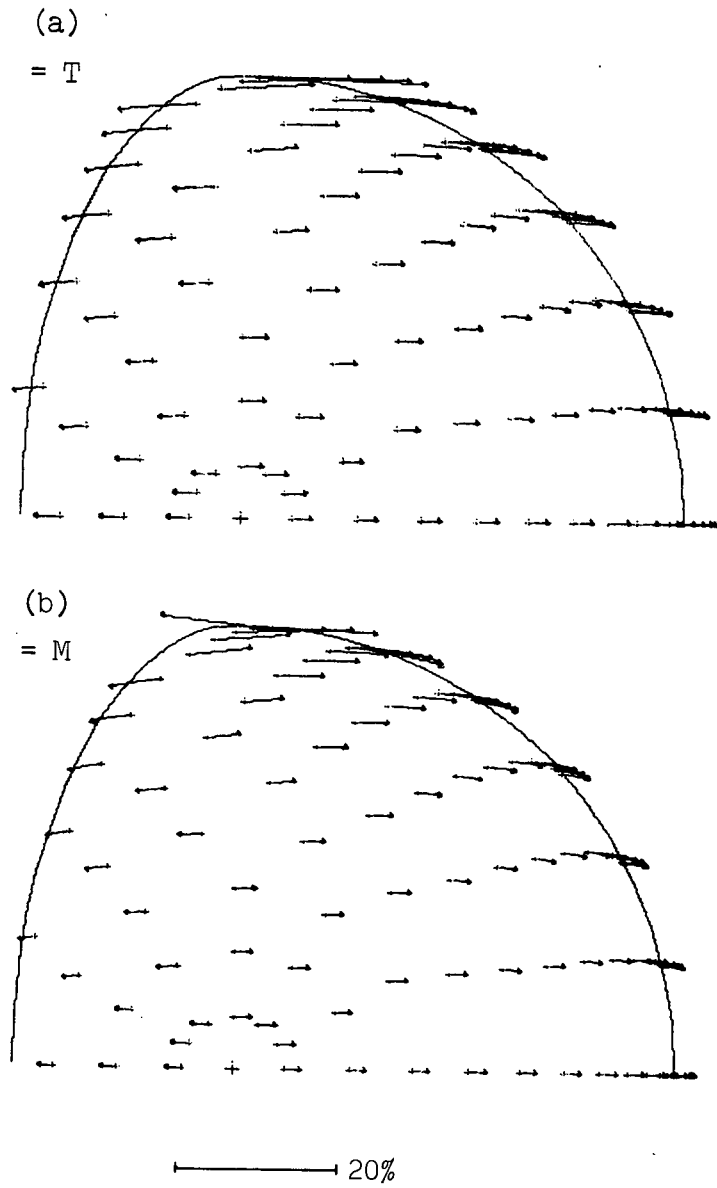
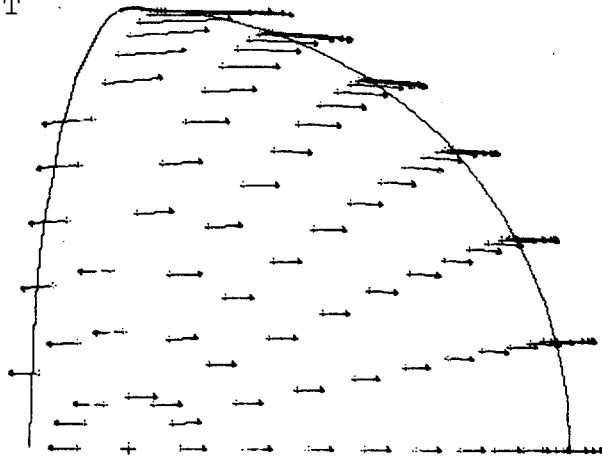
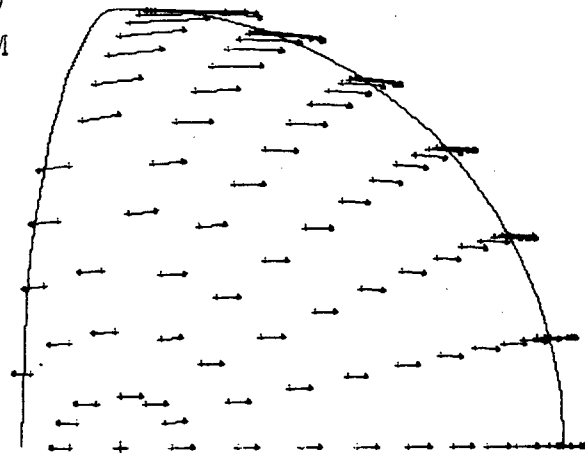


Figure 2.46 Case C.  $\psi = 60^\circ$ . Data is available for comparison here.  
See figure 2.52.

(a)

 $= T$ 

(b)

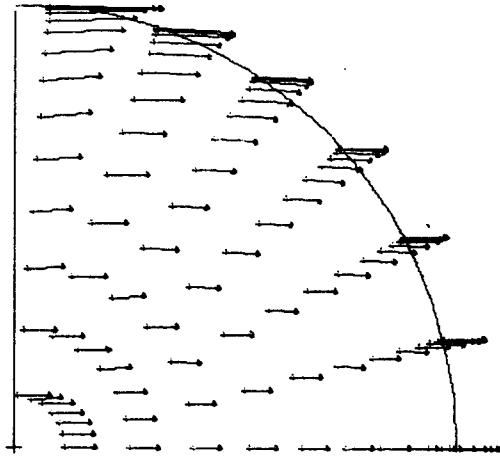
 $= M$ 

20%

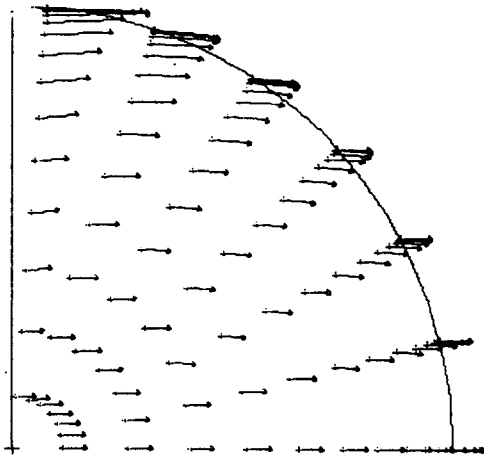
Figure 2.47 Case C.  $\psi = 77^\circ$ . Data is available for comparison here.  
See figure 2.53.



48(a)

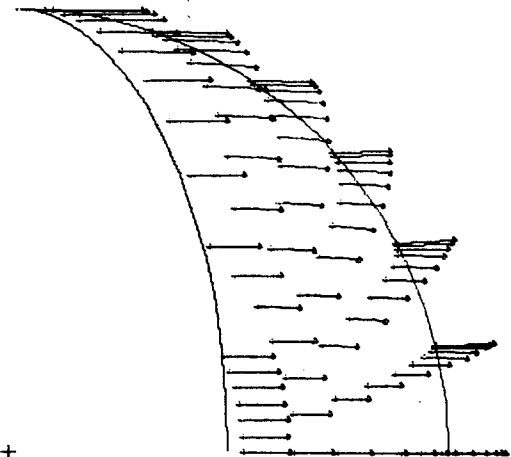
 $= T$ 

48(b)

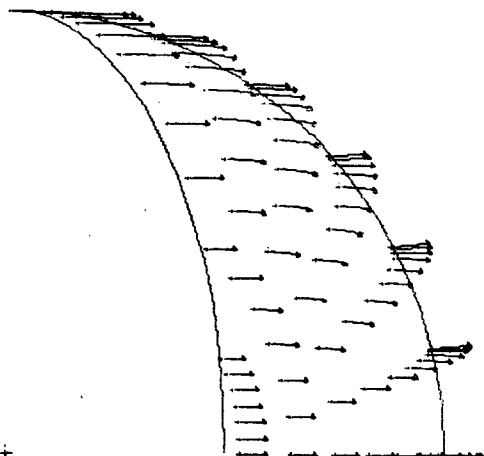
 $= M$ 

20%

49(a)

 $= T$ 

49(b)

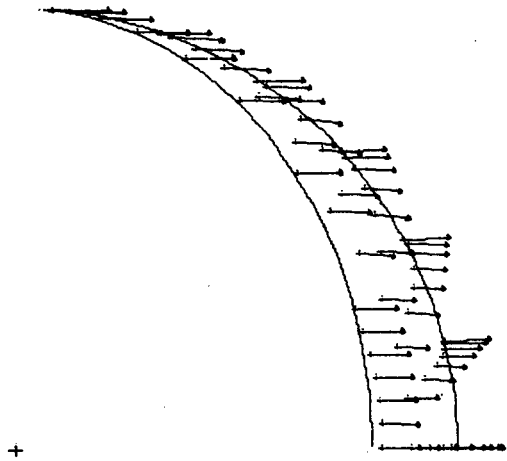
 $= M$ 

20%

Figure 2.48. Case C.  $\psi = 90^\circ$   
 Figure 2.49. Case C.  $\psi = 120^\circ$

50(a)

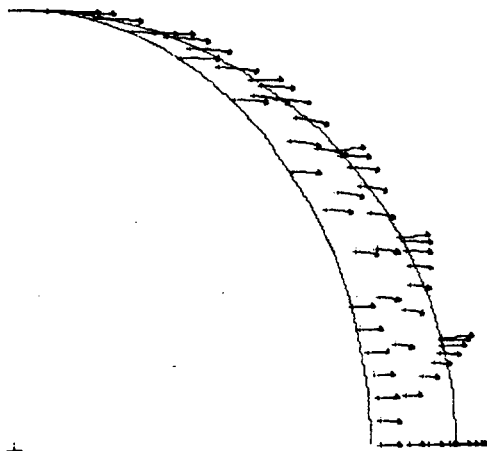
= T



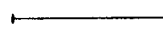
+

50(b)

= M

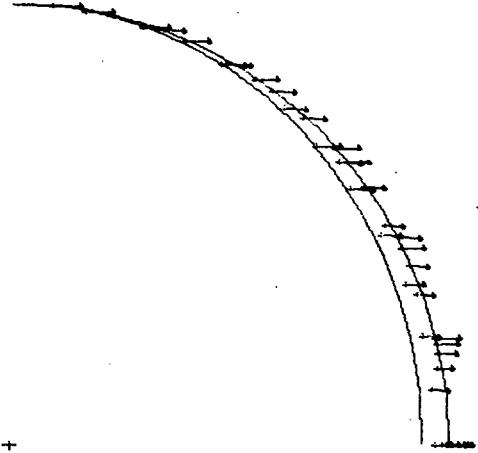


+

 20%

51(a)

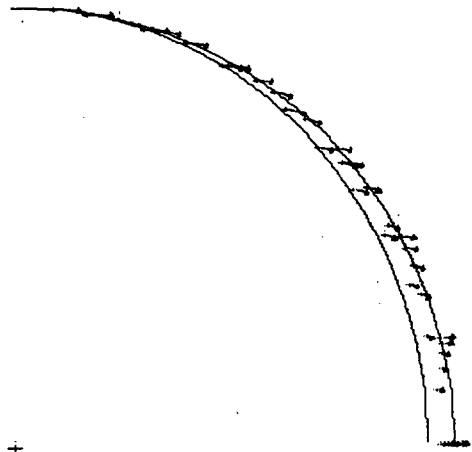
= T



+

51(b)

= M



+

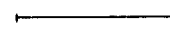
 20%
Figure 2.50 Case C.  $\psi = 144^\circ$ .Figure 2.51 Case C.  $\psi = 160^\circ$ . Tangential negative not yet apparent at this the largest phase angle computed. M polarization does show some tendency in this direction.

Figure 2.52

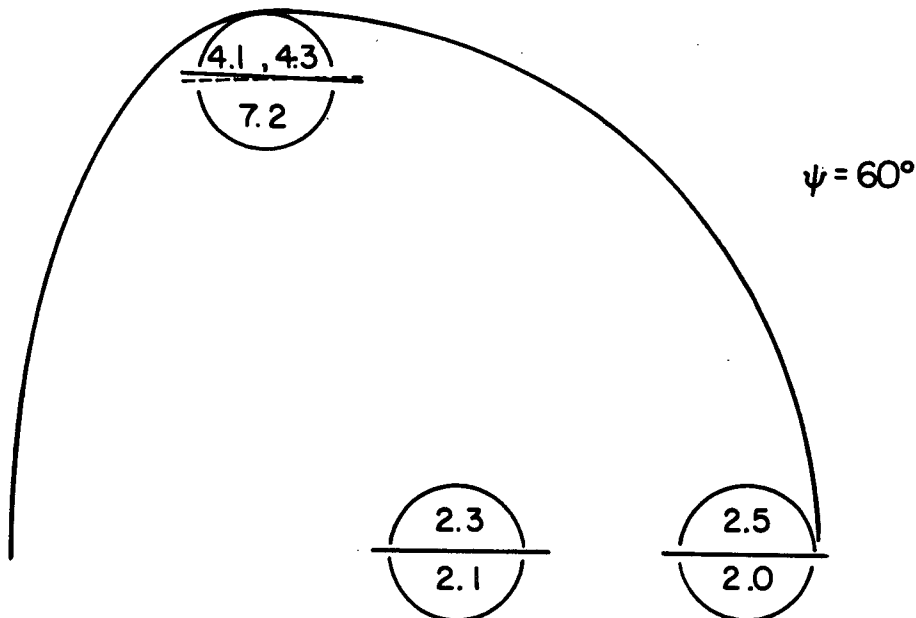


Figure 2.53

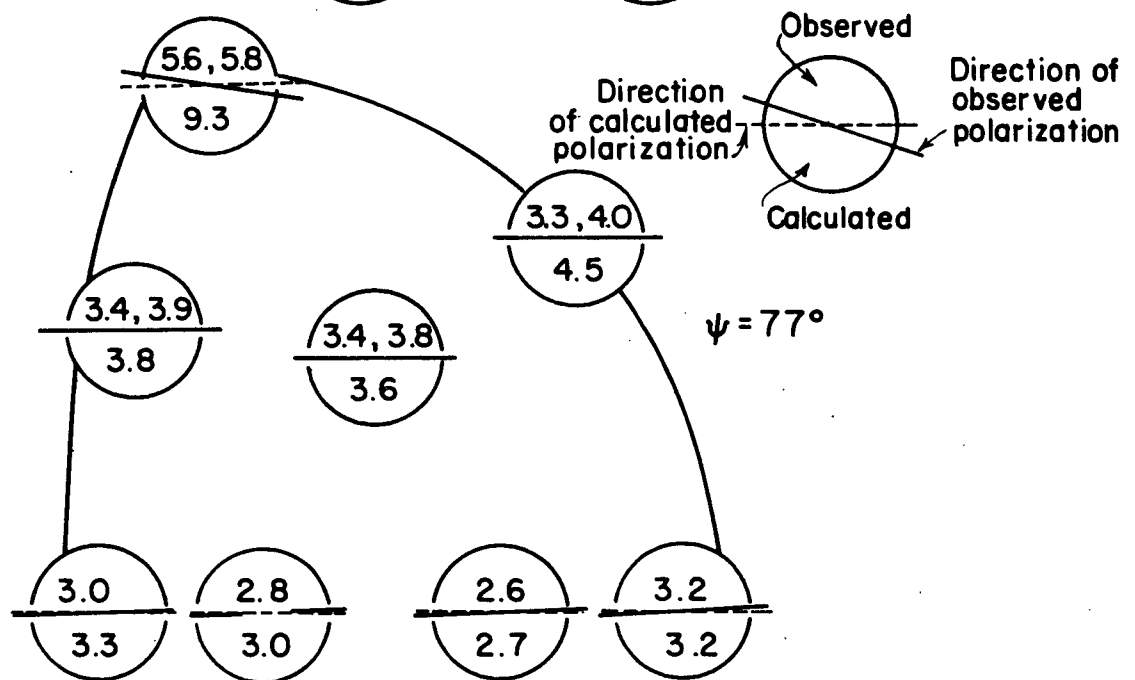


Figure 2.52 and 2.53 Coffeen's observations of Venus polarization at  $0.99 \mu$  and calculations compared. Data taken north and south have both been given. Circles indicate approximate size of physical diaphragms used in the observations. Calculations at limb, terminator and especially at poles overestimate polarization due to integration scheme used.

## V LOCALIZED POLARIMETRIC OBSERVATIONS OF JUPITER AND VENUS - DISCUSSION

Much of the discussion in section IV, while gleaned from three very specific examples, may in fact be quite general in its application. For now we have a better a priori sense of what to expect from the distribution of polarization across a planet and we may compare the discussion of section IV with the observations. We will see many of the calculations have observational counterparts. We also will make some tentative suggestions about the scattering behavior of the particles polarizing the light of Jupiter and Venus. The suggestions are tentative because it must be realized that no model calculations have been performed.

Polarization observations over the disk have been few and separated by decades in time. Lyot (1929) did the first principal work in the field, performing extensive visual light observations of Venus, Jupiter, Saturn as well as of Mercury, the Moon and Mars using a Savart polariscope. Years later Dollfus (1955) did a thorough study of these planets at a variety of wavelengths with a Lyot polarimeter. A history of the work in the intervening years may be found in Dollfus's (1955) thesis. His work included observations of disk integrated and regional polarizations as well as their secular variations over time with an accuracy of  $\pm .1\%$ . In

more recent years localized polarization studies of Venus have been published by Dollfus (1966) and Coffeen and Gehrels (1969); Jupiter was studied by Gehrels, Herman and Owen (1969) and Hall and Riley (1968) who also make observations of Saturn as well (Hall and Riley, 1969).

# 1. Jupiter

Many of the observations show effects we have seen in our calculations. All of the studies of Jupiter and Saturn have revealed a radial polarization pattern in the ultraviolet especially near the edges of the disk. Our Rayleigh scattering calculations show this behavior. The polarization at the poles is always observed to be greater than at the limbs. While our calculations show this, the effect is only noticeable for phase angles  $\gtrsim 12^\circ$  for the Rayleigh atmosphere. On Jupiter this effect is more probably due to a difference in cloud top altitudes from equator to pole such that a much greater molecular atmosphere overlies the clouds at the poles (Gehrels et al., 1969). The polarization increases from the center of the disk to the limbs as in our calculations. There is a N-S versus E-W asymmetry however such that the polarization is greater in the N-S direction even at small phase angles (Gehrels, 1969).

The central regions of Jupiters disk exhibit a less radial pattern which is much more chaotic than our calcu-

lations (Hall and Riley; 1968,1969) and may be useful in modeling lateral inhomogenities in the distribution of cloud particles or of cloud top altitudes. The position of the electric vector maximum changes from positive to negative in the central regions as the wavelength increases from ultraviolet to infrared (Gehrels et al., 1969; Dollfus, 1955). If we take cases A and B to represent ultraviolet and infrared respectively then this phenomena is present in our calculations; compare figure 2.6a for Rayleigh scattering and figure 2.25a for case B. In the infrared the negative polarization increases from the center outwards as the phase angle increases (Dollfus, 1955). Compare figures 2.24a and 2.25a for case B where this phenomena appears. These figures show that while the center of the disk has a negative polarization the edges display a radial positive direction. The observations, on the other hand, while showing a radial polarization near the poles, show a tangential negative polarization at the West (and presumably East) limbs in the infrared (Gehrels et al., 1969). Since Rayleigh scattering is more important at the North and South poles than at the limbs, perhaps a more meaningful example of the phase variation of the central regions which reproduces the phenomena at the West limb would be figures 2.43 and 2.44. (The negative tangential nature would be more apparent at smaller phase angles, but the diagrams of the M light show what the behavior would be like.)

A uniform homogeneous single layer model cannot explain the disk polarization of Jupiter. In visible light the optical depth of the molecular scattering layer is about 0.5 above latitude  $45^\circ$  while it is about 0.05 at smaller latitudes and along the equator (Gehrels et al., 1969). An optical depth of 0.05 is insufficient to blanket the effects of the cloud polarization and we find that along the equator the polarization in the infrared behaves in a characteristically negative manner. In the ultraviolet, on the other hand, the equatorial polarization behaves in a characteristically positive manner. The optical depth in the ultraviolet of the equatorial Rayleigh atmosphere above the clouds would be 0.3 according to the usual  $\lambda^{-4}$  law. This depth of Rayleigh scatterers may be sufficient to account for the positive polarization. Two layer model calculations may be required to confirm this, however. With the removal of the effect of the Rayleigh atmosphere there may be enough data as a function of position on the equator, phase angle and wavelength to be able to meaningfully model the cloud composition.

## 2. Venus

Turning now to Venus, there are many more observations available than for Jupiter, including variable features over many years and secular daily changes as well. We shall discuss only a fraction of the observations.

In our calculations we have seen the polarization increase towards the poles, as is observed. All the observations of Coffeen and Gehrels (1969) show polarizations mostly perpendicular or parallel to the plane of scattering over the disk in agreement with all three of our cases at the angles observed. Deviations from these directions, however, is not always in the sense predicted from the nature of the integrated phase function even allowing for the scatter in the observed directions. Thus at 3400A, where the integrated polarization is always positive, Coffeens observations show a turn towards the negative tangential near the limb. This is not understandable within the plane parallel uniform models we have derived. In addition to these unpredicted deviations, there are secular changes in the Stokes intensity from day to day that require the formulation of more complex models. At 60° phase angle Dollfus (1955) observed polarized spots changing from day to day as well as a changing distribution of negative and positive regions. We would not expect to see both negative and positive re-



gions on the same disk for one uniform layer except near a null.

Near  $\Psi = 60^\circ$  Dollfus, as Lyot before him, observed the polarization of the poles to change, the position of the maximum shifting off the poles and suffering deviations in direction of up to  $18^\circ$ . Dollfus interprets this as being due to cloud structure: bands, striations and coils. We remark that while this is certainly possible similar effects can result from a changing index of refraction (as in a two layer model) or particle size distribution.

Near  $\Psi = 10^\circ$  the polarization was observed by Dollfus to pass through a null in the disk integrated light. This may be compared to figures 2.26, 2.27 and 2.28 for case B. The polarization observed is non-uniform, being positive in some regions and negative in others as well as displaying considerable variability. Near the terminator the direction is more tangential negative than at  $\Psi = 60^\circ$ . The more tangential behavior of higher order scattered light probably dominates in this region. The observations (Dollfus, 1955) as well as the calculations here (figures 2.27 and 2.28) show that small changes in the phase angle can cause large changes in the direction of polarization. The observed polarization across the planet near the null is not as uniform as in the calculations nor is it symmetrical north and south. If we assume the localized polarimetric obser-

vations can be matched in detail by Hansen's (1971) model of the cloud particles--as we have shown probable in case C--then behavior at null points becomes an important tool to probe for more refined structure. The particles size distribution, index of refraction, cloud structure and the effect of variable cloud altitudes all affect the direction of polarization and the position of the null point. The variability of these conditions might be investigated at the null points.

Dollfus (1966) has also observed the polarization across Venus when it appears as a thin crescent at large phase angles. He observed that the electric vector maximum is oriented parallel to the limb, i.e. tangential negative, in both green and red light. The polarization was not maximum as the poles, but elsewhere along the crescent. Dollfus does not believe this tangential orientation can be explained by multiple scattering in the atmosphere. The integrated polarization is positive at these phase angles, thus seeming to imply radial, not tangential, polarization. He concludes that this tangentialism and similar tangential tendencies observed near the limb at other phase angles can be explained only by banded or striated cloud structures.

We disagree. The positive polarization at large phase angles is most probably due to the process which causes neg-

ative polarization for  $\Psi > 164^\circ$  for Rayleigh scattering as calculated by Kattawar and Adams (1971). This was explained in section IV A. As the planetary phase increases we have seen (figures 2.11, 2.12, 2.13, 2.20, 2.33, 2.34, 2.51) the polarization across the disk goes from negative (or positive) to tangential negative (or radial positive). The integrated polarization, however, where we now rely on Kattawar's calculations, would go from negative (or positive) to positive (or negative), due to the larger weight given the illuminated crescent in the equatorial regions. This appears to be the explanation of what Dollfus has observed.

The smaller polarization at the poles, in contrast to the behavior at other phase angles, may be due simply to the larger polarization of the multiply scattered light which is more visible towards the equator.

Polarization studies are a potentially powerful source of information on particle composition, size and distribution in the atmospheres as well as on the surfaces of the planets. The interpretation of these data is still in its infancy. The potential for successful interpretation is high because multiple scattering does not wash out polarization features as it does intensity features. The future will bring faster electronic computers, and faster computation schemes as well so that many model calculations may be easily performed. The

next few years can be expected to bring an order of magnitude increase in polarization observations of a type not possible a few years ago. The polarization experiments aboard the Mariner 9 mission to Mars, the Mariner 10 swing-by mission to Venus and Mercury, the Pioneer F and G missions to Jupiter and the Grand Tour missions to Jupiter and the rest of the solar system will provide accurate ( $\pm$  a few %) regional and disk integrated observations of the planets at a wide range of phase angles. The missions to the outer planets will permit viewing at phase angles not accessible from the earth. Meaningful disk integrated and regional model calculations will then be possible.

## APPENDIX

The investigation of cases A, B, and C in the main text involved, in part, a parameterization in  $\tilde{\omega}_0$ . The effects of varying  $\tilde{\omega}_0$  was not fully investigated above, nor do we do a complete study here. It was felt, however, that some of the information we obtained in varying  $\tilde{\omega}_0$ , while not useful to our argument, would be worthwhile summarizing here.

Below in Table A.1 we give the geometric albedo,  $p$ , the phase integral,  $q$ , the Bond albedo,  $A_B$ , and the quantity  $q/p(50^\circ)$ , supposed to be a constant from Russell's (1916) law. The quantities were defined in the text. The results were calculated by scalar intensity methods (designated INT) and by matrix methods for the Stokes intensity (designated POL). Both sets of results are shown in the table.

The geometric albedo decreases as we would expect as  $\tilde{\omega}_0$  decreases for all three cases. There is a difference between the values of  $p$  calculated by scalar and matrix methods, the difference being greatest for Rayleigh scattering and small or non-existent for the other two cases. The quantities  $q$  and  $q/p(50^\circ)$  show the same behavior in the comparison of scalar and matrix derived quantities. The magnitude of the differences correlate with the degree of forward scattering given by  $\langle \cos \theta \rangle$ . Experience with var-

TABLE A.1

	$\tilde{\omega}_0$	p		q		$A_B$	q/p(50°)	
		POL	INT	POL	INT	POL INT	POL	INT
<u>CASE A:</u> Rayleigh, $\langle \cos\theta \rangle = 0.0$	$\sim 1$	0.790	0.744	1.25	1.33	0.990	2.09	2.22
	0.9999	0.778	0.733	1.25	1.33	0.975	2.09	2.23
	0.999	0.743	0.697	1.25	1.33	0.929	2.10	2.24
	0.995	0.682	0.637	1.25	1.33	0.850	2.11	2.26
	0.990	0.640	0.596	1.24	1.33	0.794	2.12	2.27
	0.975	0.565	0.522	1.23	1.33	0.695	2.13	2.30
	0.950	0.491	0.451	1.22	1.32	0.597	2.14	2.33
	0.900	0.400	0.366	1.20	1.31	0.479	2.15	2.35
	0.800	0.293	0.268	1.17	1.28	0.343	2.16	2.36
	0.600	0.172	0.160	1.15	1.23	0.196	2.18	2.38
<u>CASE B:</u> $\alpha = 5.0$ $\langle \cos\theta \rangle = 0.842$	0.9995	0.558	0.558	1.57	1.57	0.878	2.32	2.32
	0.997	0.446	0.446	1.64	1.64	0.730	2.39	2.39
	0.993	0.365	0.365	1.70	1.70	0.621	2.47	2.47
	0.990	0.326	0.326	1.74	1.74	0.567	2.51	2.51
	0.950	0.142	0.142	2.07	2.07	0.294	2.95	2.95
<u>CASE C:</u> $\alpha = 6.6$ $\langle \cos\theta \rangle = 0.694$	0.9995	0.675	0.674	1.35	1.35	0.911	2.28	2.28
	0.999	0.649	0.647	1.35	1.35	0.877	2.29	2.30
	0.995	0.550	0.548	1.36	1.36	0.747	2.35	2.36
	0.985	0.445	0.443	1.36	1.37	0.605	2.43	2.44

ious phase functions has shown that only in the case of very Rayleigh-like phase functions does a substantial difference exist, both in these quantities and in the intensities themselves. Curiously, the Bond albedo is not affected by the method of computation, at least to the accuracy of the tabulated values.

The quantity  $q/p(50^\circ)$  has been found to be approximately constant for many astronomical bodies, and a values of 2.2 is usually taken as its value. Veverka (1971) has shown this to be a consequence of the rapid decrease of a planets brightness as the phase angle increases. The variation with  $\tilde{\omega}_0$  in the table indicates that for non-Rayleigh planetary atmospheres at least the result also depends on the fact that the albedo is high.

## REFERENCES - II

- S. Chandrasekhar, Radiative Transfer, Dover Publications, New York (1960)
- D.L. Coffeen and T. Gehrels, Astron. J., 74, 433 (1969)
- K.L. Coulson, J.V. Dave, and Z. Sekera, Tables Related to Radiation Emerging from a Planetary Atmosphere with Rayleigh Scattering, U. of Cal. Press (1960)
- D. Deirmendjian, Electromagnetic Scattering on Spherical Polydispersions, American Elsevier Pub. Co., New York (1969)
- A. Dollfus, Doctoral Thesis (1955); Technical translation in NASA TT F-188
- A. Dollfus, in Proceedings Caltech-JPL Lunar and Planetary Conference, JPL Tech. Memo. 33-266 (1966)
- T. Gehrels, Icarus, 10, 410 (1969)
- T. Gehrels, B.M. Herman, and T. Owen, Astron. J., 74, 190 (1969)
- J.S. Hall and L.A. Riley, Lowell Obs. Bull., 7, 83 (1968)
- J.S. Hall and L.A. Riley, J. Atmospheric Sciences, 26, 920 (1969)
- J.E. Hansen, Science, 171, 669 (1971)
- J.W. Hovenier, Astron. and Astrophys., 13, 7 (1971)
- H.C. van de Hulst and K. Grossman, in The Atmospheres of Venus and Mars, ed. by J.C. Brandt and M.B. McElroy, Gordon and Breach, (1968)
- H.C. van de Hulst, A New Look at Multiple Scattering, NASA Inst. for Space Studies, New York, mimeographed report (1963)
- W.M. Irvine, J. Atmospheric Sciences, 25, 610 (1968)
- G.W. Kattawar and C.N. Adams, Ap. J., 167, 183 (1971)



B. Lyot, Doctoral Thesis and Annals of Meudon Observatory  
(1929; Technical translation in NASA TT F-187

H.N. Russell, Ap. J., 43, 173 (1916)

C. Sagan, in Planetary Atmospheres, ed. by Sagan et al.,  
I.A.U. (1971)

J. Ververka, Icarus, 14, 284 (1971)

### Part III

#### RADAR OBSERVATIONS OF THE MOON AND THEIR INTERPRETATION: A MULTIPLE SCATTERING APPROACH

##### Abstract

It is proposed that the average diffuse component of lunar radar echoes results from the effect of multiple scattering by rocks buried beneath the surface of the interior and exterior ejecta blanket of fresh young craters. The multiple scattering polarization computer program that was developed in Part I is used to calculate the scattering matrix of a plane parallel layer of buried rocks. The scattering matrix is then integrated over the surface of a crater and the results of crater and ejecta blanket combined. A single choice of parameters produces a model which shows good agreement with observations. Inferred mean indices of refraction of 1.3 and 1.6 for the ejecta blanket at wavelengths of 3.8 cm. and 23 cm., respectively, are consistent with measurements on an Apollo 11 fine sample and indicate an increasing density with depth beneath the surface. Tests are proposed to settle the question of multiple vs. single scattering. If the model is correct then the difference in diffuse reflectivity between maria and highland is due chiefly to a difference in the single scattering albedo of buried rocks. Then properly prepared radar maps could serve as geological maps of that mineral or minerals, perhaps ilmenite, which dominate microwave absorption processes.

## I INTRODUCTION

The typical lunar radar experiment consists of illuminating the moon or a portion of it with a circularly or linearly polarized beam and receiving the power in the sense expected from a perfectly smooth dielectric sphere. In the case of circular illumination the expected sense is opposite to that transmitted, while for linear it is the same sense. More sophisticated experiments have also measured the power returned in the unexpected sense. This is usually referred to as the depolarized component, and is the least well explained and, at the same time, potentially the most informative datum on the nature of the lunar surface.

The returned power may be analyzed according to its time delay relative to the first return from the subradar point and to its frequency spread relative to the frequency of transmission. Power with a given delay is returned from a circular annulus centered on the subradar point. (Strictly speaking, the annulus is only an approximation since features such as mountains which are large when measured in fractions of a resolution element, can contribute even though slightly outside the annulus.)

This provides a one-to-one mapping of delay space onto  $\theta$  space, where  $\theta$  is the angle between the line of sight and the local surface normal. The doppler spread of the frequency provides the second coordinate needed to localize the returned power.

The moon appears to rotate or librate during an observation due to the combined motion of the observer on the earth due to the earth's rotation, the non-circularity of the moon's orbit, and the inclination of the moon's orbital plane and the earth's equator. Thus at any given time a unique axis of libration is defined. The locus of constant doppler shift is a series of lines parallel to this axis. The intersection of strips of constant doppler shift with annuli of constant delay provides localization of features with a two-fold degeneracy. The degeneracy may be removed by pointing an antenna whose beam width is small compared to the angular size of the moon to illuminate only one area at a time. In this way maps have been prepared for most of the side of the moon visible to the earth.

The results from the resolution in delay are quite interesting. The polarized component shows a pronounced peak in intensity for small delays, followed by a much slower decline at larger delays, the dependence on  $\theta$  being

approximately  $\cos^{1.5} \theta$  until near the limb, when a  $\cos \theta^{1.0}$  dependence is approached. The depolarized component has no such central peak and follows a  $\cos \theta$  law for most of the range of  $\theta$ . This slowly varying component of the polarized and depolarized data is called the diffuse component. It is this component which we hope to explain. The peaked return is similar to that expected from a polished specularly reflecting sphere and is called the quasi-specular component due to its similarity to the results expected from a smooth sphere.

We hope to show that the diffuse component of the polarized and depolarized power is due to multiple scattering from wavelength sized rocks lying above and beneath the surface of areas inside and in the ejecta blanket of fresh young craters. To do this we apply the multiple scattering program developed in Part I of this thesis to spherical rocks buried beneath the surface of an absorbing layer of dust having an index of refraction  $n_s$ . The scattering law that results is integrated over the assumed parabolic surface of a fresh rocky crater and combined with the scattering from the ejecta blanket itself, appropriate weights being given to each scattering source. Using data on the nature of fresh craters, their size distribution and the distribution of boulders in their vicinity we are able to match to a plausible degree

not only the angular data provided by delay-doppler techniques, but also wavelength dependence of the cross sections, maria-highland differences, and the absolute value of the cross sections. Our main emphasis will be on the average properties of the lunar surface integrated over large areas -- either annuli of constant delay or Maria-highland properties. The model, however, naturally explains the data for large ( $\gtrsim 10$  km) fresh young craters seen as enhanced areas on radar maps.

The work here differs in three significant respects from all previous work although some authors do discuss some of the points we raise. The first and most important departure is the invocation of multiple instead of single scattering, though this has been discussed briefly by Thompson et al. (1970). This is also the first detailed multiple scattering attempt to explain the polarized-depolarized data. First order theories using a dipole single scattering mechanism have been put forth previously by Hagfors (1967a) and Burns (1969). Lastly we differ in our description of the actual physical placement of the scattering elements. We assume that the sources are discretely rather than uniformly located across the lunar surface and that the locations coincide for the most part with the areas near fresh young craters.

In the following section we will present a summary of observations and previous theoretical work and discuss more fully our departures from previous work. Sections III and IV derive and discuss the single scattering behavior of the scattering model. Sections V and VI derive the scattering matrix for subsurface multiple scattering in a crater and its ejecta blanket. Much of the work in the last three sections we have mentioned is not necessary for a complete understanding of the argument and may be skipped over in a cursory reading. The comparison of the observations with our computations for data taken as a function of position on the disk is presented in sections VII and VIII. Section IX is devoted to a discussion of the high single scattering albedo required by the results in section VIII. Observational tests of the model are proposed. Section X deals with the absolute diffuse cross section, its wavelength dependence and variation from highland to maria. The discussion in IX and X implies that maps of the polarized/depolarized power ratio may serve as mineralogical maps of the lunar surface.

## II THE OBSERVATIONS AND PREVIOUS INTERPRETATIONS

In this section we will present a survey of the relevant radar data. The work of other investigators will be examined and the differences between previous theories and our present hypothesis will be pointed out. Basically the differences are single scattering vs. multiple scattering and homogeneous sources vs. discrete sources. At the end of the section we present some non-radar data which suggests the hypothesis of multiple scattering from boulders beneath the surface near fresh craters.

There are three basic types of observations with one radar unit as transmitter and receiver (the monostatic case): absolute cross section measurements, measurements as a function of delay averaged over a range ring, and measurements as a function of position on the disk averaged over a range-doppler cell. We discuss each type below in a separate subsection. A fourth type of observation making use of delay, doppler shift and phase to give height differences will not be considered. The transmitter can be set up to illuminate the moon with either circularly or linearly polarized radiation and the radar return can be analyzed, independent of the polari-



zation mode transmitted, into two linear components or two circular components. Unfortunately most experimenters have only measured that sense of polarization that would be expected from a smooth sphere, the polarized component. The polarized component has been observed over a wide range of radar wavelengths, from 8.6mm to 12m. A smaller subset of these contain data on the unexpected or depolarized component as well.

### 1. Cross Section

Cross section measurements provide information on the dielectric constant of the surface layers. The dielectric constant follows from the cross section derived using Fresnel's laws of reflection once proper account is taken of undulations of the surface and the amount of energy returned in the non-specular or diffuse component. Hagfors (1967a) obtained a value of  $\epsilon_s = 2.64$  ( $n_s = 1.62$ ) for his work at 23cm wavelength. (We shall use the dielectric constant,  $\epsilon$ , and the index of refraction,  $n = \epsilon^{1/2}$ , interchangeably from now on so quantities will sometimes be expressed in terms of both. Strictly speaking this is only true of minerals with a small amount of ionic polarizability.) The dielectric constants obtained in this way at 3.8cm and 70cm are similar.

Hagfors has also developed a more realistic depth dependant model for the dielectric constant, thus providing for power returned from some distance into the surface as well. We shall neglect this refinement in our calculations and derive only equivalent uniform layer results.

The total cross section of the moon as measured by Evans and Hagfors (1966) at 23cm in the polarized component for circular transmitted and received radiation is  $\sigma_t = (0.065 \pm 0.008) \pi R^2$  where  $R$  is the radius of the moon. This is the most accurate measurement to date because the LCS, the Lincoln Calibration Sphere, a polished metal sphere in earth orbit for absolute calibration of the antenna, was employed. In this way they were able to keep their errors to within  $\pm 1$  db. Cross sections obtained at other wavelengths include two-way calibration difficulties bringing the error to at least  $\pm 3$  db.

The data show very little if any change in the total cross section in over 3 decades in wavelength, from 8.6mm to 12m. See figure 3.1. At the larger wavelengths the cross section appears to increase along with the error bars, radar systems being intrinsically less sensitive at longer wavelengths. Some of the uncertainty here is due to the exact placement of the subradar point

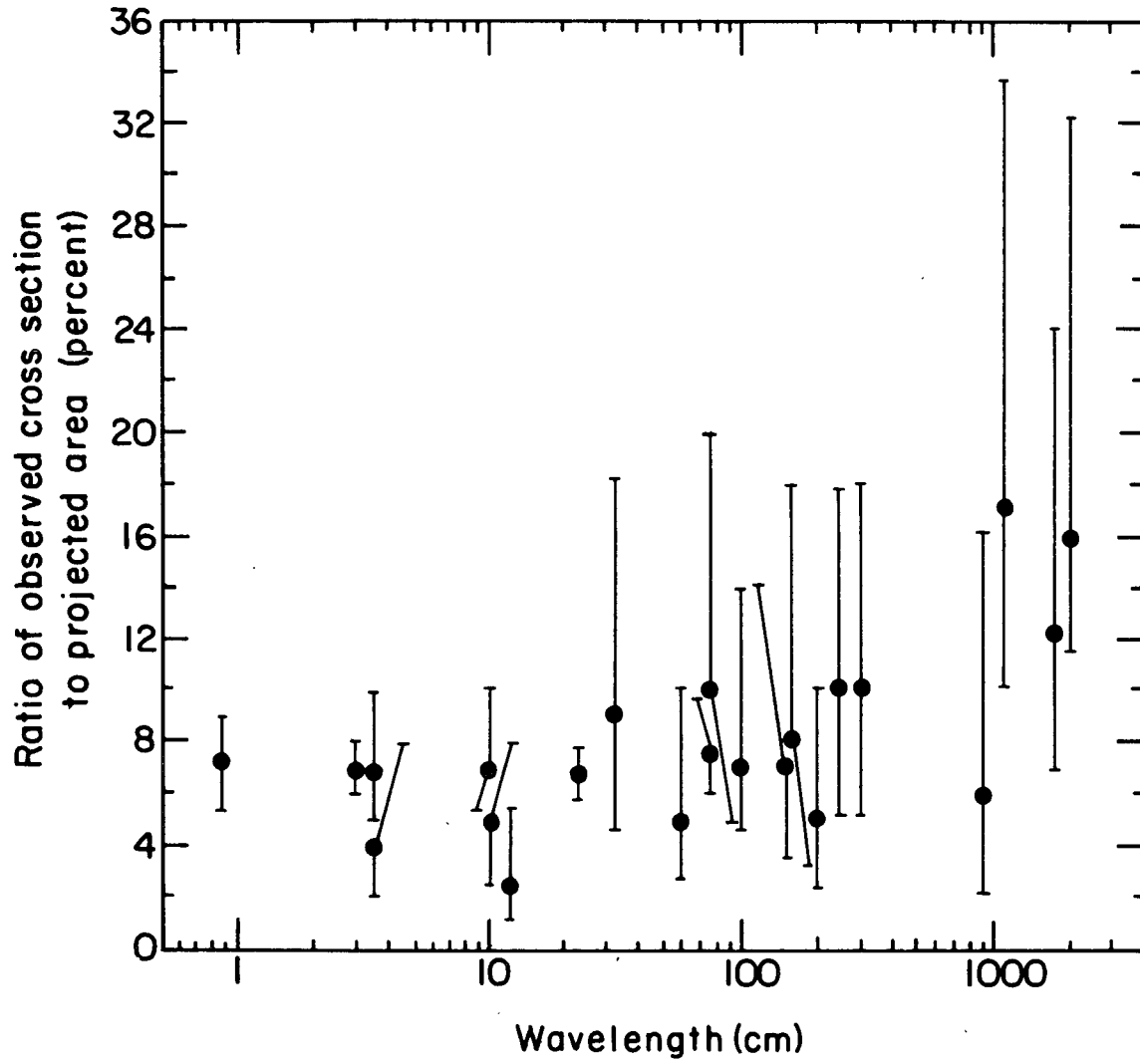


Figure 3.1 The variation of the total cross section of the moon as a function of radar wavelength. From Hagfors (1967a)

(Burns, 1970), the cross section being higher at 12m in maria regions than in highland regions. Note that this refers essentially to the quasi-specular component and says nothing about the diffuse component.

The diffuse component of the radar cross section is of more interest to the present work, since it is the diffuse component of the radar return we are attempting to explain. The diffuse cross section is obtained by extrapolating the diffuse component backwards to zero delay and subtracting out the quasi-specular peak. The method of extrapolation is not unambiguous, however, since it depends on the model of the quasi-specular component. The diffuse cross section has a significant wavelength dependence. The data are given in Table 3.1 below taken from Hagfors (1967a).

TABLE 3.1

## Diffuse Cross Section in Polarized Component

$\lambda(\text{cm})$	% of power in diffuse polarized return	diffuse cross section assuming total cross section = $0.065\pi R^2$
0.86	85	0.055
3.6	35	0.023
23.	25	0.016
68.	20	0.013

Using other assumptions as to the character of the diffuse component, Pettengill and Thompson (1968) have obtained 12% for their 70 cm results. Hagfors gives the wavelength dependence of the diffuse component as:

$$\begin{aligned}\sigma &\propto \lambda^{-0.32} & 3.8\text{cm} < \lambda < 23\text{cm} \\ &\propto \lambda^{-0.26} & 23.\text{ cm} < \lambda < 68\text{cm}\end{aligned}$$

The wavelength dependence of the diffuse cross section can be derived quite easily if the diffuse component is attributed to single scattering from wavelength sized rocks lying on (and in) the lunar surface. This calculation has been done with varying degrees of success by Hagfors (1967a), Burns (1969), Thompson et al. (1970), and Zisk (1970). We shall follow the development by Thompson et al. because their work is more general and to some degree encompasses the work of others.

We will find that if only single scattering is considered then the diffuse cross section varies as  $\lambda^{3-5}$  where  $s$  is the exponent of the power law distribution function of rock sizes. Specifically, if  $n_A(a) = n_0 a^{-s}$ , then  $n_A(a)da$  is the number of rocks per unit area between  $a$  and  $a + da$ , where  $a$  is the radius of the rock. The cross section per unit area due to these rocks

$$3.1 \quad \sigma(\lambda) = \int_0^{\infty} n_A(a) Q\left(\frac{2\pi a}{\lambda}\right) \pi a^2 da$$

$Q$  is the backscattering efficiency, and can be approximated via Mie theory for scattering from spherical objects in free space. It is a function of  $\alpha = \frac{2\pi a}{\lambda}$ , the size parameter. With the substitution of " $\alpha$ " for " $a$ " the integral becomes wavelength independent and we get

$$3.2 \quad \sigma(\lambda) \propto \lambda^{-5}$$

Hagfors (1967a), Zisk (1970) and Burns (1969) have used a cruder approximation for  $Q$ , though this is easily seen to have no effect on the wavelength dependence for the very special case of the power law distribution that is usually used. Their different assumptions do however have a large effect on the absolute value of the cross section. This will be discussed shortly.

The value of  $s$  derived from the wavelength dependence matches quite nicely the value of  $s$  observed in Surveyor studies of rocks lying near the spacecraft (Surveyor Project Final Report, 1968). This has been used (Thompson et al., 1970) to argue in favor of single scattering from rocks as the source of the diffuse component. Unfortunately multiple scattering requires modification of this simple approach. The wavelength dependence will be seen to be a related to the simple scattering albedo of the rocks as

well as wavelength changes in the index of refraction and wavelength dependent crater parameters. The need for a multiple scattering model will be discussed later.

The absolute value of the diffuse cross section per unit area is a source of serious concern for the multiple scattering approach we shall take. It is not at all clear that the entire diffuse cross section cannot be explained by single scattering from surface rocks seen in Surveyor photographs. There is however good evidence to believe that the success of this calculation is fortuitous. Later, after presenting some pertinent observations, we shall discuss why it should not work.

Hagfors (1967a), using the cross section of the moon as a whole to estimate rock cross sections, concluded that the Surveyor rock counts were more than sufficient to explain the observed cross section. His treatment has been criticized by Thompson et al. (1970), who found numerical errors in the derivation of the rock density function and conceptual errors in the approximation of boulder cross sections. Burns (1969), using the approximation that the reflectivity was independent of size, derives a cross section insufficient to match observations. This assumption is in serious discord with Mie theory results which show a rapid rise to 5 or 10 times the

geometric cross section as the size parameter,  $\alpha = \frac{2\pi a}{\lambda}$ , becomes greater than 1. This is followed by a first rapid, then slow decline to the cross section of a large dielectric sphere given by Fresnel's laws. Zisk (1970) uses a more realistic approximation for the variation of cross section with  $\alpha$ , but his results seriously overshoot the observed values. A closer approximation to the Mie theory would lower his results. Thompson et al. (1970), however, have used the Mie theory in conjunction with Surveyor rock counts, and they derive a smaller cross section than observed.

My results paralleling the calculations discussed above, using the backscatter cross section from the Mie theory, proves to be higher than observed values. The actual backscatter cross section of the rocks is not known for the rocks are not spherical as we have assumed. The actual cross sections may be smaller by 40% (Greenberg et al., 1971) or more. The "average" of all these calculations appears to show that Surveyor rock counts alone are sufficient to explain the diffuse cross section. As we discuss later, however, the rocks counted by the Surveyor spacecraft seriously underestimate the total number of rocks lying on the lunar surface. Thus none of the above calculations could be valid, and their success is accidental.



Cross section calculations by Thompson et al. (1970) and Zisk (1970) using the different rock size distributions at the Surveyor sites have shown that the sense of the observed radar enhancements in these regions is obeyed. We note, however, that from our point of view, enhanced regions would contain more fresh craters which would increase the amount of general debris in the area. Thus both our hypothesis and earlier hypotheses are able to explain this observation.

Thompson et al. discuss a multiple scattering model for the diffuse cross section. However they assume a homogeneous model, whereas ours is inhomogeneous, allowing for discrete scattering centers. The present calculations will show that single scattering albedos small enough to produce the observed cross section are far too small to produce the observed depolarization. It was in fact this calculation that led to the present inhomogeneous model.

Any model for the diffuse component of the radar return must be consistent with the observed cross section and the observed wavelength dependence. In addition it should be able to explain Thompson's (1968) estimate that the highlands are twice as bright as the maria in the diffuse component.

## 2. Delay Measurements

The radar return as a function of delay provides information on the average lunar scattering law since the results average over a range ring. The angular dependence of the polarized and depolarized cross section per unit surface area in rings of constant delay is presented in figures 3.2 and 3.3 for 23cm, for circular and linear polarization transmitted and received (Hagfors, 1967a). For the polarized data, the diffuse return varies as  $\cos^{3/2} \theta$  for angles  $\theta$  between  $25^\circ$  and about  $80^\circ$ , where a transition to a  $\cos \theta$  law takes place. The depolarized data may be approximated by  $\cos \theta$  over a wider range of angles. The above statements apply as well to the 68cm data, although the 3.8cm data indicates a greater tendency towards a  $\cos \theta$  dependence (Zisk, 1970).

The ratio of polarized to depolarized power in the diffuse tail equals about 3db for circular and 7db for linear polarization. It is important to note that for circular polarization at least (where the data is available) the ratio of polarized to depolarized power is almost constant for 68cm, 23cm and 3.8cm; the difference

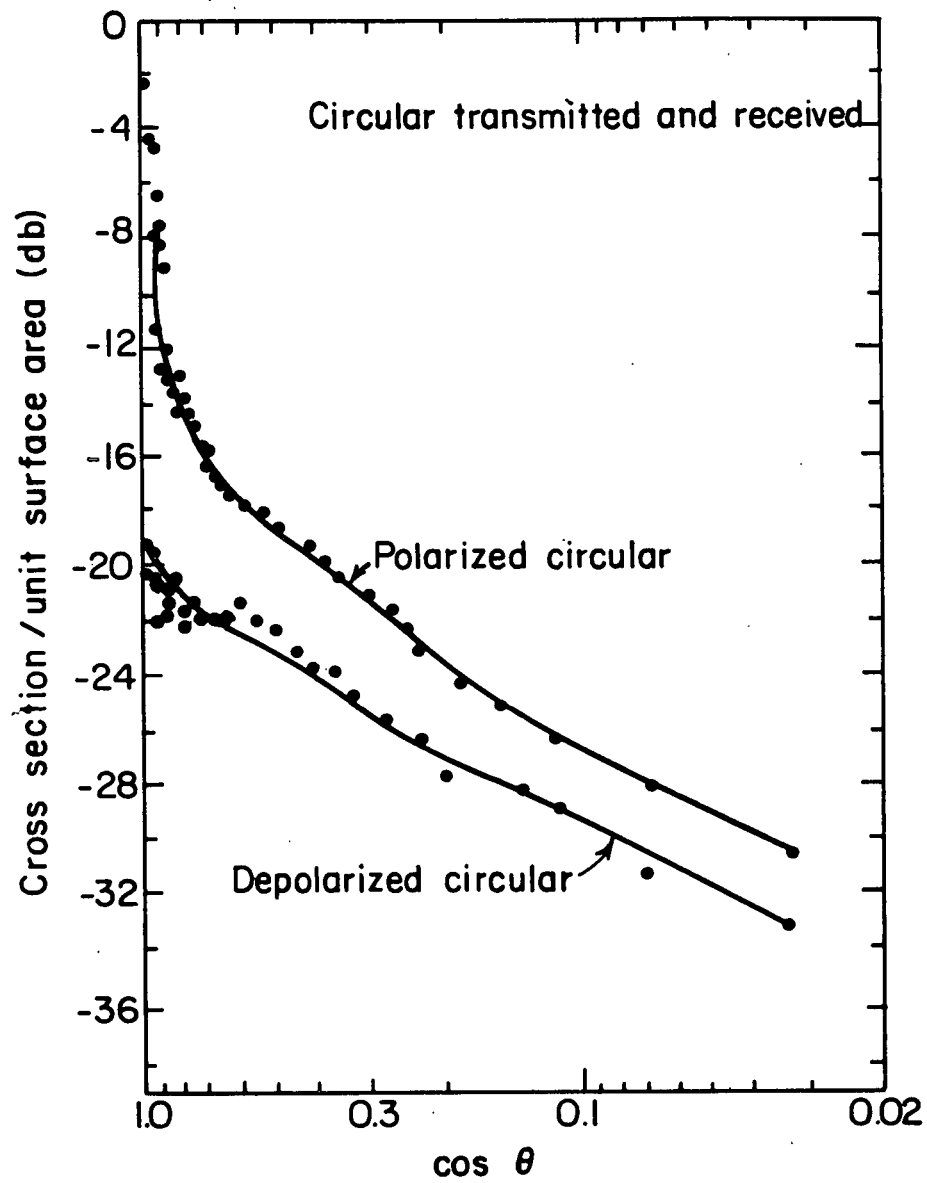


Figure 3.2 Cross section per unit surface area at 23 cm for polarized and depolarized circular returns vs  $\cos \theta$ . From Hagfors (1967a).

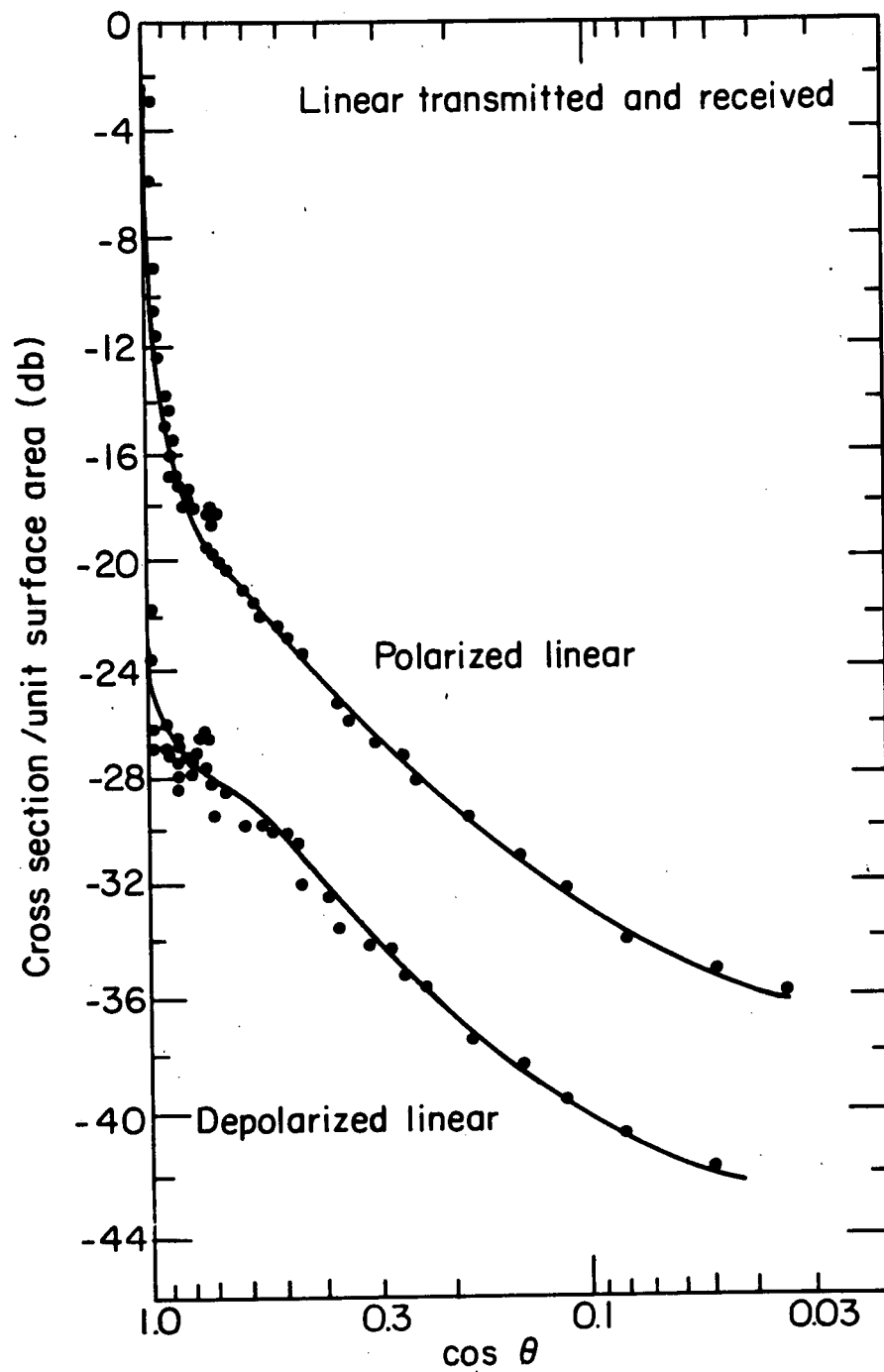


Figure 3.3 Cross section per unit surface area at 23 cm for polarized and depolarized linear returns vs  $\cos \theta$ .

between 3.8cm and 68cm is only 0.75db.

A theory that attempts to explain the diffuse return must cope with these results. In order to produce this much depolarization Hagfors suggests, as a first approximation, that the scattering behavior is due to randomly oriented linear dipoles. By dividing the power between dipole scatterers and scatterers that do not depolarize at all he finds that both the linear and circular depolarization data lead to the conclusion that the linear dipoles contribute about 70 percent of the observed diffuse power. This consistency check, while certainly a happy one, does nothing to validate the model, since as Hagfors admits, the model is somewhat naive. Burns (1969) does a similar more extended treatment of the same model, adding to it the hypothesis, which we use as well, that the scatterers are buried. This model too is ad hoc, for Burns fails to deal with the question of what causes the dipole-like behavior of the scatterers. Burying the rocks, however, allows him to explain the angular behavior of the diffuse component by Fresnel's laws. However Burns achieved a fit to the  $\cos^{3/2} \theta$  law of the polarized component which contains the effects of specular reflection, but did not fit

the  $\cos^1 \theta$  law of the depolarized component which is more characteristic of the diffusely scattered radar return.

A similar treatment of the angular scattering law has been achieved by Zisk (1970).

### 3. Delay Doppler Measurements

We come to a set of measurements which makes use of the localization capabilities of the range-doppler techniques. We gain the ability to define a local plane of incidence and measure power polarized in and normal to this plane. The data will be interpreted to imply that the scattering takes place beneath the surface.

In one experiment the moon was illuminated by a circularly polarized beam and linear polarization was measured as a function of doppler position in the range rings. The antenna was aligned so that one direction of polarization coincided with the instantaneous position of the libration axis, that is, parallel to the local plane of incidence. The incident circular beam may be considered as two linear beams of equal intensity with a physical delay in space of a quarter wavelength. If the relative phase of the scattered wave is not measured the incident circular produces the same effects as an unpolarized beam.

Figure 3.4 shows the results for four range rings. The limbs are marked L and C marks the points where the curves for the two linears cross. Points C fall just at these points on the disk where both linears make an angle of  $45^\circ$  with the local plane of incidence. This corresponds to 0.707 times the maximum doppler shift at the limb. A likely possibility, supported by other evidence we shall present, is that this is due to the radar beam having penetrated the top of the regolith, the difference in the linear power being due to the effects of the Fresnel transmission coefficients for the two orientations of the electric field vectors (Hagfors, et al., 1965). The difference in the linear components is in the same sense as predicted by Fresnel's laws. Note the anomalous peak in the second graph near +4cps doppler frequency. This is the crater Tycho, a large rayed crater and one of the youngest large features on the moon.

The fact that the difference in the linears disappears near Tycho seems to indicate that the scattering is occurring at or near the surface in this region (Hagfors, 1965). Another possibility, however, is that the considerable variability of the local plane of incidence in the crater walls and chaotic crater floor averages over both

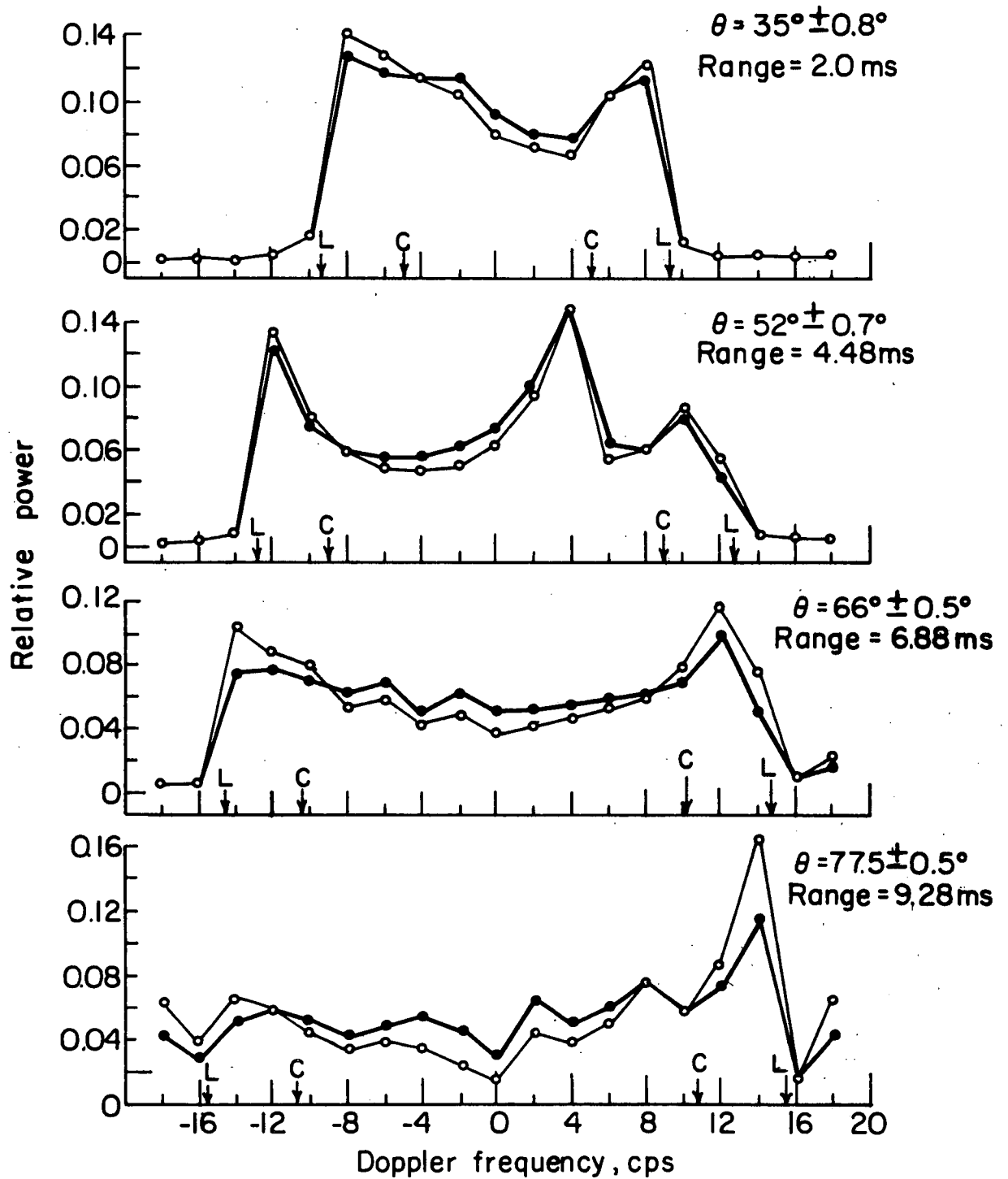


Figure 3.4 Normalized frequency spectra of the moon at 23 cm; L, maximum frequency; C cross-over point. Curves:  $\bullet$  —, E-field aligned with libration axis;  $\circ$  —, E-field normal to libration axis. From Hagfors (1965)



linear components. We shall return to this point in section VIII.

To further illustrate that the diffuse scattering occurs within the lunar regolith consider figures 3.5 for 23 and 3.8cm. The experimental setup is the same as for the previous experiment but the data is presented as a power ratio for the region along the libration axis as a function of  $\cos \theta$ . Thus one linear has its electric vector always parallel to the local plane of incidence. Hagfors assumed that the buried scatterers return power in the same linear mode as was transmitted. He thus was able to derive an index of refraction because the ratio of the power returned to the two linear modes is then equal to the square of the Fresnel transmission coefficients. His result, assuming a constant index of refraction, is

$n_s \cong 1.3$  at 23 cm, which is lower than the value of  $n_s \cong 1.6$  derived from cross section data, although it fits rather well with the value derived from radiometric observations of the polarization of thermal emission from the lunar surface (Hagfors, 1967a). A much smaller value of  $n_s$  is indicated for the 3.8cm data. Hagfors states that it is possible to reconcile the two radar values of  $n_s$  by postulating a two layer model. We will find instead that

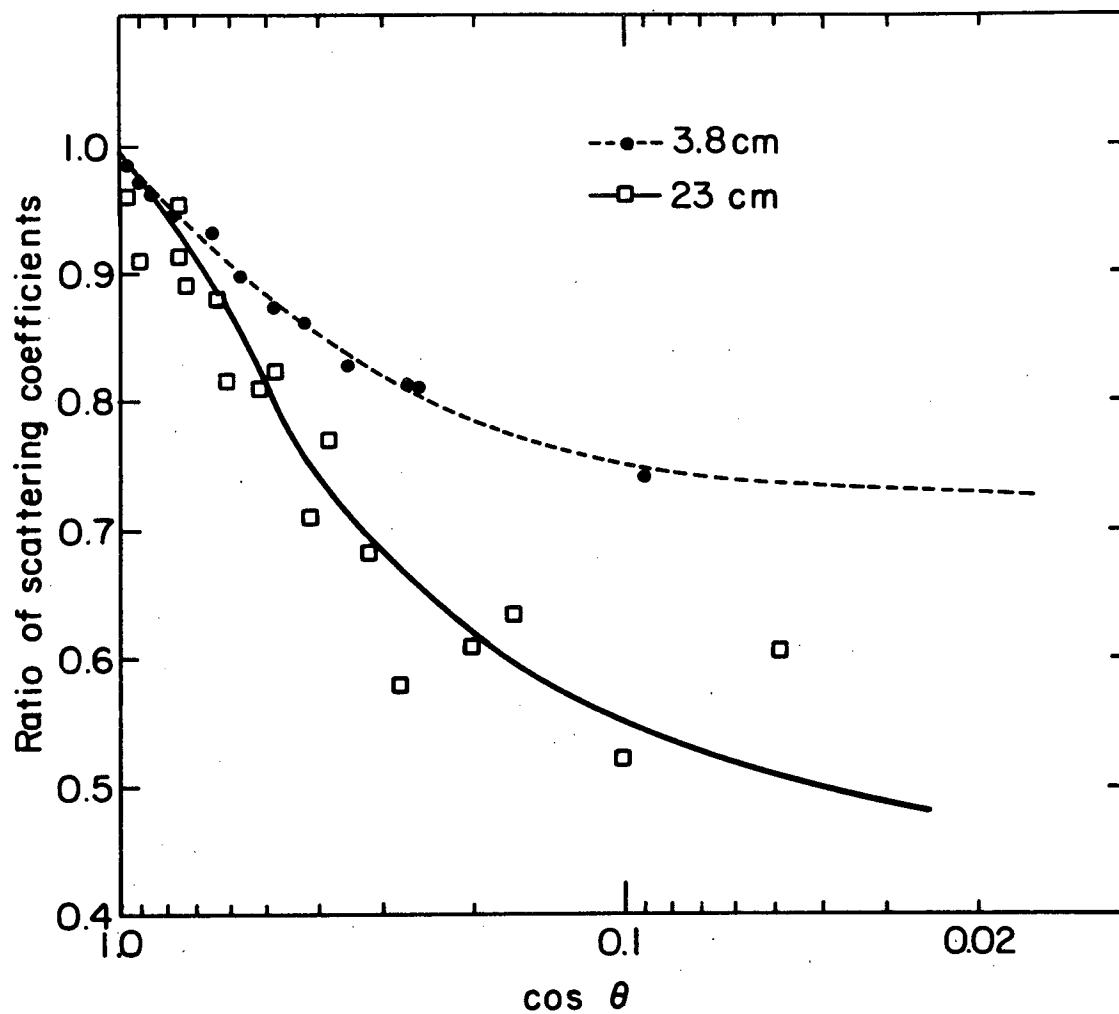


Figure 3.5 Ratio of backscattered power at 23 cm and 3.8 cm in two orthogonal linearly polarized components from a small region of the lunar surface for circularly polarized illumination. From Hagfors (1967a).

$n_s = 1.6$  is consistent with our calculations since the averaging of the local planes of incidence within fresh craters and the depolarization within the surface requires us to increase the index of refraction of the dust to get the same angular dependence.

Another significant but unexplained observation is shown in figure 3.6. The small square data points represent the ratio of polarized to depolarized power in two linear modes from the libration axis for linear polarization incident parallel to the libration axis and in the local plane of incidence. The triangular points are the experimental results for averaging over all points in a range ring at the same value of  $\theta$ . That experiment was described above. There appears to be a real increase in the depolarization ratio, although the scatter in the data points is greater. We shall find that this phenomena is explained by Fresnel's laws when combined with the multiple scattering reflection matrix, and gives further evidence of the subsurface nature of the scattering process.

The phenomena apparent in the delay doppler measurements can have an alternate explanation. The same differences in the linear components could result from a preferential orientation of the scattering centers such

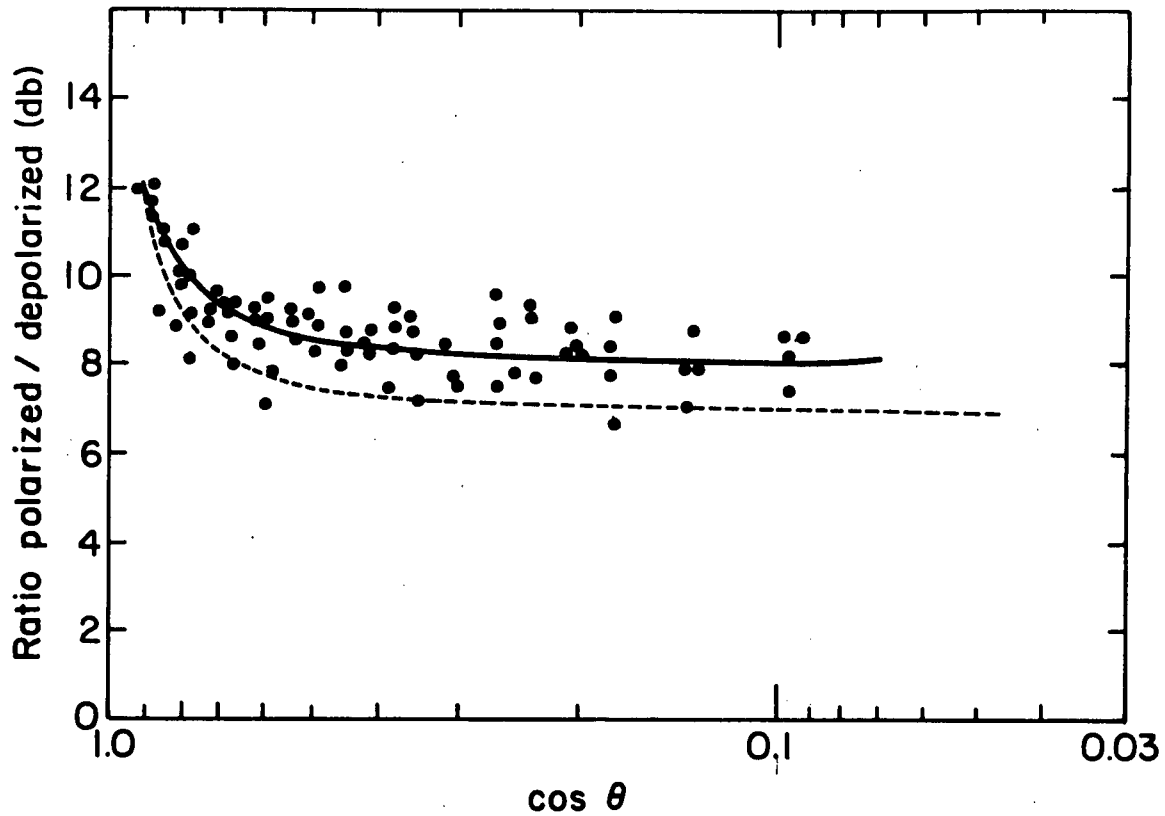


Figure 3.6 Ratio of backscattered power at 23 cm in two orthogonal linearly polarized components for linearly polarized illumination with polarization parallel to plane of incidence. Dashed curve shows depolarization when polarization of illumination is averaged over all angles for the same data. From Hagfors (1967a).

that their long axes are vertical, as was suggested by Hagfors (1967a). We reject such a situation as being inherently unstable.

#### 4. Discrete Model vs. Homogeneous Model

Most previous discussions of the diffuse component have shared the basic assumption that only single scattering need be considered. The explanation given is that the rocks are so widely scattered that absorption between scattering events in the regolith reduces the single scattering albedo to a point where multiple scattering can be neglected. This argument, however, depends on the tacit assumption that on the average each small area of the moon contributes as much as any other. This leads to the slightly more explicit assumption that the rocks counted in all the Surveyor missions are representative of large areas of the moon and, with a certain amount of care, of the moon as a whole. Thus the Surveyor rocks, or similarly distributed rocks beneath the surface, are taken as the source of the diffuse component.

Pollack (personal communication) has shown otherwise, and we take his argument, given below, as motivation for the discrete source, multiple scattering approach. We

use the data of Moore (1969), who made boulder and crater counts from lunar orbiter photographs.

Fresh craters are seen to possess large numbers of rocks and boulders in their interiors and for a distance of 2 or 3 crater radii outwards into the ejecta blanket. Data is given for the fraction of the area covered by boulders larger than a certain size in annuli one crater radius wide out to 5 or 6 radii. Fresh craters occupy about 1% of the lunar surface, so circles 10 crater radii large centered on fresh craters will approximately cover the entire surface of the moon. If we extrapolate Moore's data to 10 radii outwards we find a very interesting result. We find that there is about 8 times as many rocks from 0 to 3 radii as there are from 3 to 10 radii; or, put another way, there are about 10 times as many rocks in 10% of the lunar surface than in the other 90%. Thus the data from all the Surveyors are basically useless in determining absolute cross sections or deciding the question of single scatterings vs. multiple scattering, though the exponent of the distribution functions may be significant. Using data from fresh craters we will find that single scattering albedos greater than 80% are plausible and thus that multiple scattering is important.

We do the calculation of single scattering albedo in Section IX, making use of the complex index of refraction of lunar rocks and dust brought back by Apollos 11 and 12. The skeptical reader is encouraged to skip ahead to Section IX to allay any doubts that such high values are realistic.

The multiple scattering in the crater and ejecta blanket would tend to enhance the difference between the crater and the background even further. Depolarized enhancements of more than a factor of 10 are common for many of the larger young craters at 70 cm wavelength (Thompson et al., 1970). Zisk (1970), working at 3.8 cm, also finds significant enhancement around fresh craters which he is able to resolve far better than other workers at longer wavelengths. Some of his remarks follow:

"Most craters that are 'fresh' in geological appearance show a well-developed halo (of ejecta?) in the depolarized maps. In some cases, the halo is strong enough to obscure on the depolarized map other features that are clear on the polarized map. There also appear on the depolarized map, and even more distinctly on the ratio map, a number of bright patches -- perhaps as many as 1000 on the earthside hemisphere -- with diffuse outlines but no obvious central crater. In all these cases the Lunar Orbiter photographs show a bright, fresh crater or clump of craters at the center of the bright patch, although some of the craters may be only a fraction of a percent of the diameter of the patch."

### III THE DIFFERENCE BETWEEN THE SINGLE SCATTERING MODEL AND REALITY AND ITS INFLUENCE ON THE MULTIPLE SCATTERING RESULTS

The multiple scattering results we derive in later sections are predicated of course on how we choose to describe the single scattering from a rock or group of rocks. At opposite ends of the range of models we can either assume the scatterers are randomly oriented linear dipoles or perfectly spherical dielectric spheres. Clearly, neither model is the correct one and rocks having random shapes fall somewhere in between. Unfortunately, scattering theory for randomly oriented, randomly shaped particles is not developed at all and we must make do with the Mie theory, which has been fully developed only for spheres and infinite cylinders. The applicability of Mie theory to the real situation is discussed below.

The approximation of lunar rocks by dielectric spheres is at first sight a severe one, though certainly much less severe than the approximation by linear dipoles. In evaluating the effect of this approximation on our final results two aspects must be considered, intensity and polarization.

No one non-spherical object will have the same intensity phase function as any one sphere chosen to be



most equivalent, due to the detailed dependence of the phase function on phase reinforcements and cancellations inside, at the boundaries and outside the object. The phase function of any particle which is wavelength-sized or larger shows many ripples in the intensity as a function of scattering angle, the number of ripples being approximately equal to the value of the size parameter  $\alpha = \frac{2\pi a}{\lambda}$ , where  $a$  is the particle radius and  $\lambda$  the wavelength. It is only by averaging over many different sized particles that a smooth phase function is obtained. For non-spherical particles we also expect a smooth phase function, although the detailed shape may be different from a set of spherical particles of equivalent size distribution. The ability of spherical particles to mimic the phase function of non-spherical particles depends on their departure from sphericity. Specially filled angular particles are found to do a reasonable job (Hodkinson, 1963), while fourlings (objects like the jacks children play with) of the same index of refraction, are found to not work very well at all (Donn and Powell, 1963). We may expect that convex objects work better than concave objects. Lunar rocks are mostly convex, so we are helped in this respect.

With respect to multiple scattering we are in a much better position in using the intensity phase function of spheres. It has been shown (Van de Hulst and Grossman, 1968) that through the use of similarity relations, multiple scattering from particles with different sizes may be related by appropriate scaling of the single scattering albedo,  $\tilde{\omega}_0$ , and the value  $\langle \cos \theta \rangle$  of  $\cos \theta$  averaged over the phase function. Thus even though the detailed form of the phase function is different, the multiple scattering is similar for phase functions with the same  $\tilde{\omega}_0$  and  $\langle \cos \theta \rangle$ . If we now make the more reasonable assumption that  $\tilde{\omega}_0$  and  $\langle \cos \theta \rangle$  for lunar rocks are similar to that derived for spheres of the same size, then we may expect the multiple scattering intensity results to be a valid representation of the real situation.

We are not so fortunate in the case of polarization. The scattering matrix for spherical particles has only 6 non-zero elements, 4 of them independent. Lunar rocks will be described by a matrix with 16 non-zero elements, all of them independent. The additional elements result from the total lack of symmetry expected for real rocks. There is no theory to describe these additional elements,

nor any experiments that have measured them except in very special cases such as backscattering or scattering from well defined geometrical metallic objects. We can only hope that effects due to non-sphericity will be superimposed on the results we get for spherical objects and that they will be of magnitude and direction such as to not invalidate the results. Certainly we do expect depolarization by single scattering alone due to the non-symmetric quality of the scatterers. This effect is absent for spheres in the case of direct backscattering since we then have a perfectly symmetrical situation.

Although we must admit virtual failure in calculating the full single scattering polarization matrix, this does not obviate the results in any way. This surprising statement comes from a comparison of single scattering polarizations of initially unpolarized radiation with multiple scattering depolarizations of initially fully polarized radiation. Figure 3.9 shows percent polarization of some of the phase functions used with the index of refraction of the rock relative to the dust, as a parameter. The maximum polarization varies from a maximum of 60% to a minimum of 7% for different phase functions. Yet there is only a small difference in the

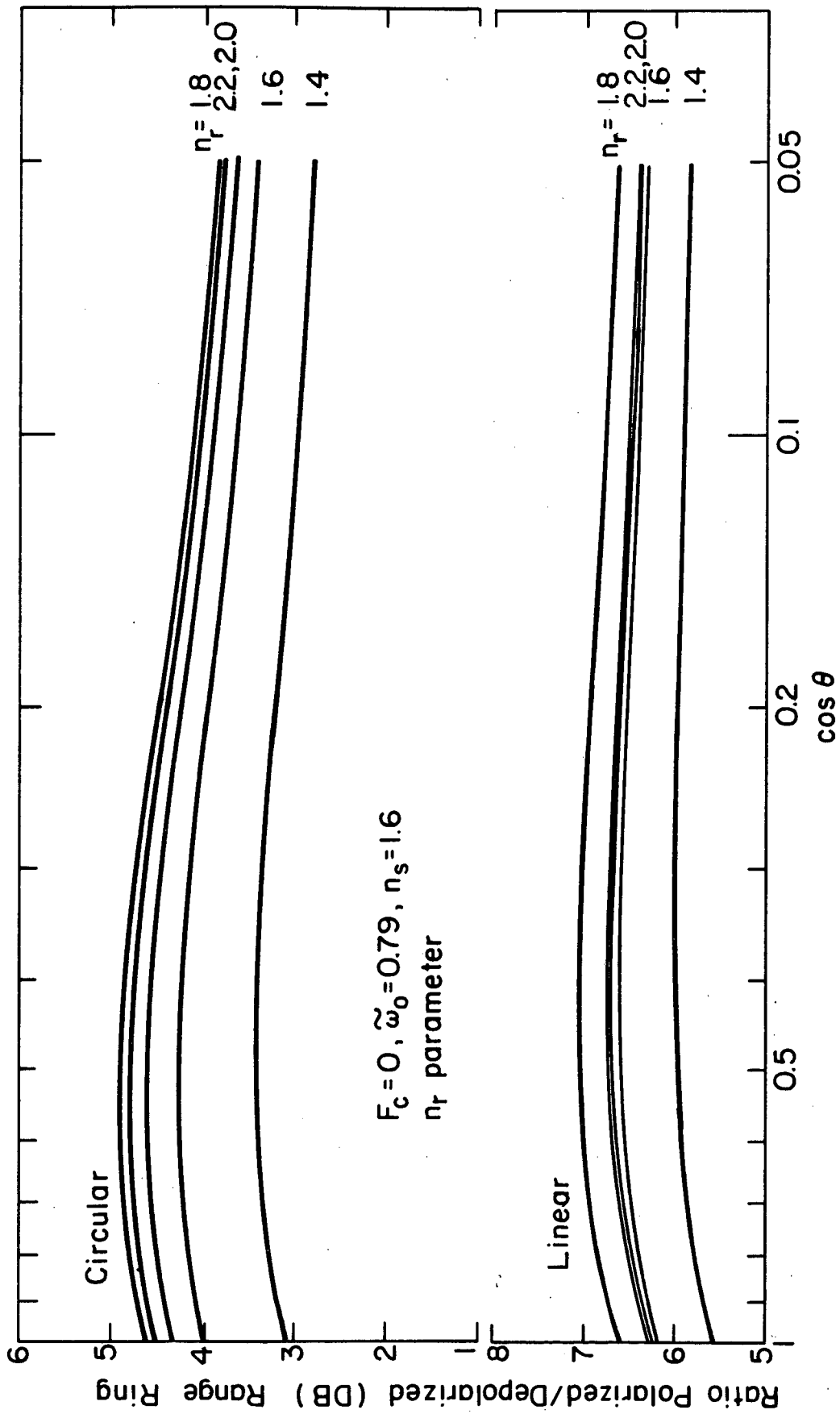


Figure 3.7 Ratio of polarized to depolarized power in range ring for circularly and linearly polarized power transmitted and received.  $n_r$  varied.

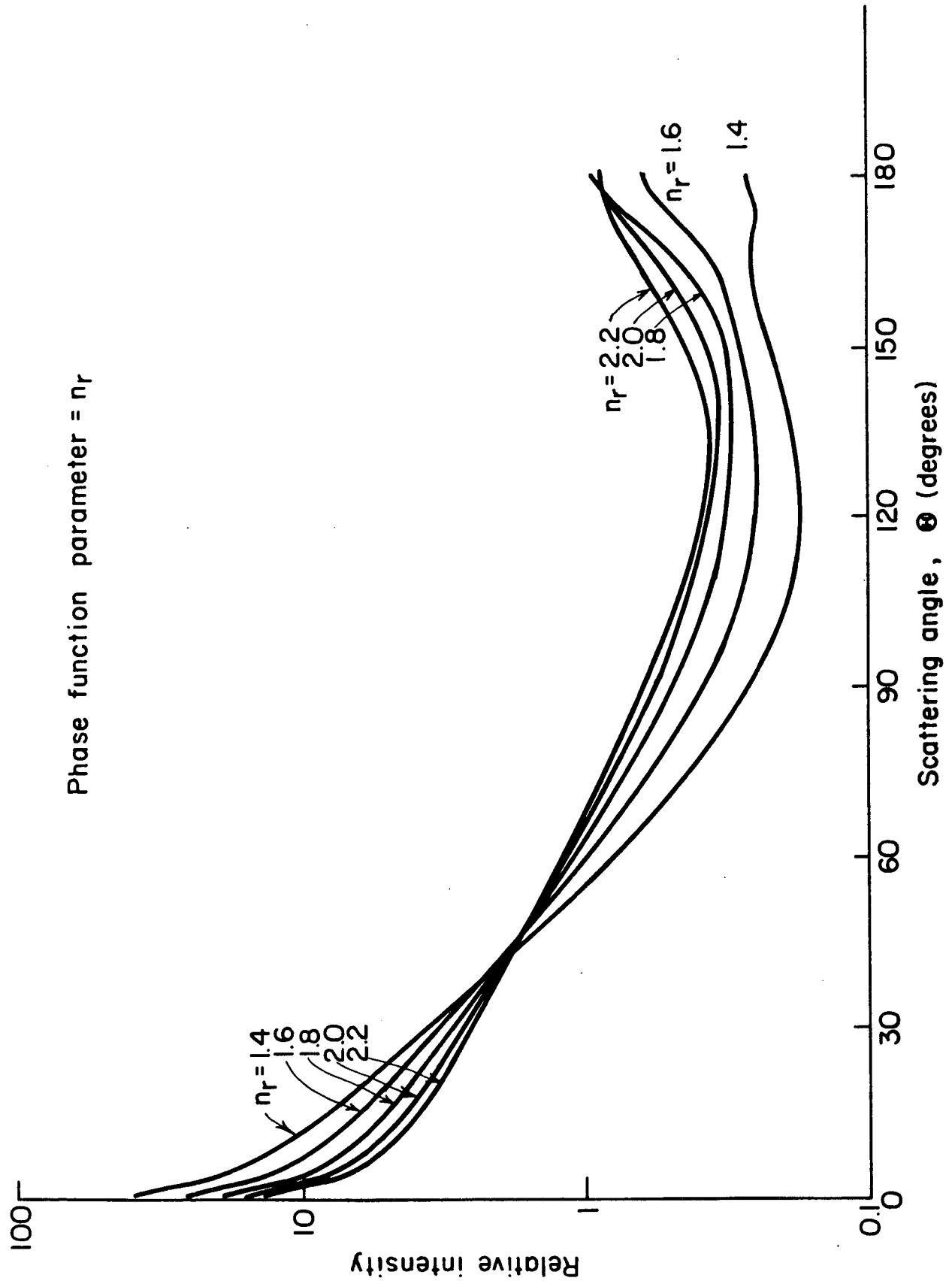


Figure 3.8 Variation of single scattering phase function with  $n_r$ .

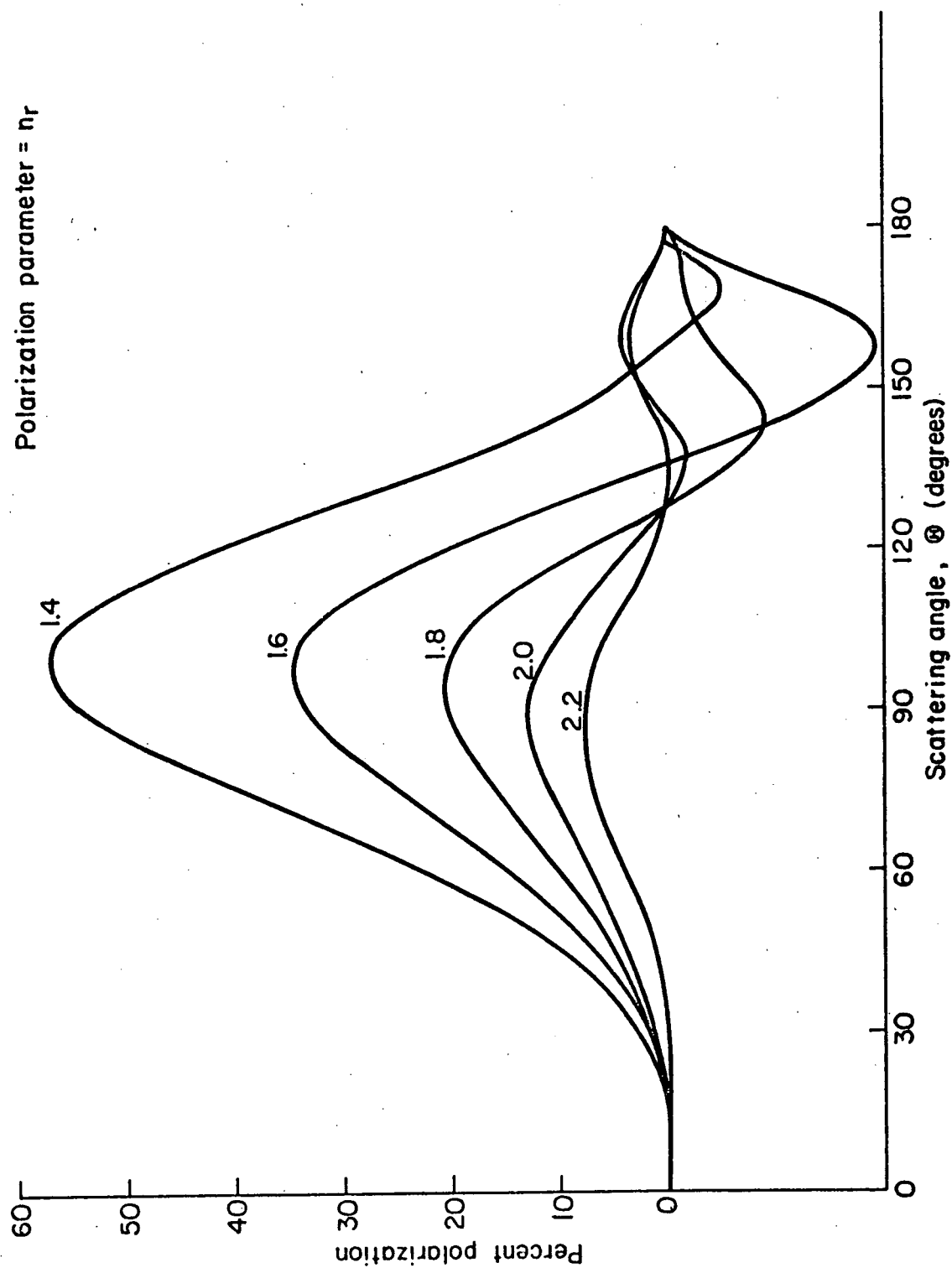


Figure 3.9 Variation of the single scattering polarization for the phase functions in figure 3.8.  $\eta_r$  is varied.

multiple scattering depolarization (see figure 3.7) and the differences are correlated one to one with the backscatter cross section (see figure 3.8) and not the single scattering polarization (see figure 3.9). Figure 3.7 gives the ratio of polarized to depolarized power returned in range rings for circular and linear polarized power transmitted and received. The backscatter cross section is evident in Figure 3.8 as the backscattering peak in the plot of the single scattering intensity phase function.

This argument implies that the depolarization results from the randomization in direction of the incident beam. As we have argued above, we calculate the randomization in direction correctly. We also argue that we have calculated the backscatter cross section correctly because it correlates fairly well with the reflectivity of a dielectric surface given by Fresnel's laws for ray optics. We expect non-spherical rocks to follow Fresnel's laws so we expect that the backscatter cross sections we calculate will be similar to those of the actual rocks.

#### IV SINGLE SCATTERING - CALCULATIONS

Below we develop the single scattering phase function and albedo for a collection of absorbing particles embedded in an absorbing medium. We assume that the bulk of the scattering comes from rocks buried beneath the surface of a layer of dust of uniform index of refraction,  $n_s$ . The rocks have an index of refraction relative to the dust of  $\tilde{n}_r = n_r - in_i$  in terms of the real and imaginary parts of the index of refraction. The imaginary part,  $n_i$ , is unaffected by  $n_s$  since the absorption per unit length in the rock is dependent on  $n_i$  alone, independent of  $n_r$  and hence  $n_s$ .

$$3.3 \quad n_i = \frac{\lambda}{4\pi\ell_a} \quad \text{where } \ell_a \text{ is the absorption length.}$$

We assume the dust to be absorbing, the functional dependence of the absorption length with wavelength being given approximately by  $\ell_a = \ell_0 \lambda$  (Cambell and Ulrichs, 1969).  $\ell_a$  may be proportional to a slightly higher power of  $\lambda$  than 1, but we shall ignore this possible difference to decrease the number of parameters. It is not an important effect.

Lastly we take for our distribution of sizes the law

$$3.4 \quad n_V(a) = n_0 a^{-s}$$



The number of rocks per unit volume with a radius between  $a$  and  $a + da$  is  $n_V(a)da$ . Having specified  $n_V(a)$ ,  $\tilde{n}_r$ ,  $\ell_a$  and  $\lambda$ , the single scattering phase function albedo, etc. are completely determined.

In developing the simple scattering phase functions that were used throughout this work, a computer program written by J. V. Dave (communicated through I.B.M.) was used to provide the mie scattering information for single spheres. The only inputs necessary for this program are the index of refraction  $\tilde{n}_r$  and the size parameter  $\alpha$ . Briefly, the program obtains the far field scattered rays by matching boundary conditions in the interior, on the surface, and at infinity for the incident, internal and scattered rays.

In terms of the mie scattering phase functions  $p_1$ ,  $p_2$ ,  $p_3$ ,  $p_4$  and the scattering and extinction efficiency factors  $Q_s$  and  $Q_x$  for single particles we can derive the results for a polydispersion of particle sizes as follows: The unnormalized phase functions are, for  $i = 1, 4$

$$3.5 \quad P_i'' = \int_0^\infty P_i(a; \theta, \lambda) n_V(a) da$$

The phase functions  $P_i''$  are normalized to a single scattering albedo of 1 such that they satisfy the equation

$$3.6 \quad 1 = \frac{1}{4\pi} \int_0^{2\pi} \int_0^\pi \left( \frac{P_1'(\theta) + P_2'(\theta)}{2} \right) \sin \theta d\theta d\phi$$

where  $\sin \theta d\theta d\phi$  is a differential solid angle. The single scattering albedo, neglecting absorption in the dust, is

$$3.7 \quad \tilde{\omega}_0 = \frac{\int_0^\infty Q_S(a; \lambda) \pi a^2 n_V(a) da}{\int_0^\infty Q_X(a; \lambda) \pi a^2 n_V(a) da}$$

Note that  $P_1'$  and  $\tilde{\omega}_0$  are not functions of  $\lambda$ , only in the very special case of a power law distribution of particle sizes of the form we have chosen. This is true because we may remove  $\lambda$  from the above integral and change the integration variable from "a" to " $\alpha$ ".

The single scattering albedo  $\tilde{\omega}_0$  is only a function of  $\tilde{n}_r$  and  $s$ , the exponent of the power law distribution. The absolute value of number density of particles given by the coefficient  $n_0$  is nowhere included since so far we have assumed that there is no absorption between particles and hence their relative packing is irrelevant, assuming point particles. With the introduction of absorption between scattering events the single scattering albedo becomes

$$3.8 \quad \tilde{\omega}_0 = \frac{\int_0^\infty Q_S(a; \lambda) \pi a^2 n_V(a) da}{\int_0^\infty Q_X(a; \lambda) \pi a^2 n_V(a) da + 1/\ell_0 \lambda}$$

It is worthwhile to note that now  $\tilde{\omega}_o$  is also a function of  $n_o$  and  $\lambda$ , the dependence being given by

$$3.9 \quad \tilde{\omega}_o = \frac{n_o A^{4-s}}{n_o B \lambda^{4-s} + C}$$

Since  $\tilde{\omega}_o$  now depends on many parameters, we have chosen instead to parameterize our results in terms of arbitrary choice of  $\tilde{\omega}_o$ . We show in the section IX that while the choices of  $\tilde{\omega}_o$  used are arbitrary, they are by no means unrealistic. Thus the phase functions  $P_1$  used in the first chapter of the thesis are normalized such that

$$3.10 \quad \tilde{\omega}_o = \frac{1}{4\pi} \int_0^{2\pi} \int_0^\pi \left( \frac{P_1(\theta) + P_2(\theta)}{2} \right) \sin \theta d\theta d\theta$$

We take  $P_1$  as the starting point in the polarization doubling program.

## V SCATTERING MATRIX FOR BURIED ROCKS

In the previous section we described the transition from single scattering on single spheres to single scattering on many spheres. We obtained the phase functions  $P_1$  necessary as input to the polarization doubling program. With the computer program developed in Part I in hand, we obtain the scattering matrix  $\bar{\bar{S}}(\mu', \mu_0, \phi_0 - \phi')$ , defined in Part I in terms of the Stokes vector  $\bar{I} = (I_1, I_2, U, V)$  where  $(\mu_0, \phi_0)$  and  $(\mu, \phi)$  refer to directions of incidence and emergence respectively. With this as our starting point we will adapt  $\bar{\bar{S}}$ , in this and subsequent sections, to our model of the lunar surface. In this section we shall derive the scattering matrix for scatterers imbedded within a medium with index of refraction  $n_s$ . We discuss the form of  $\bar{\bar{S}}$  for our special case and derive the transmission matrixes from Fresnel's laws of reflection.

We first examine the scattering matrix we shall be working with. We use the variable  $\mu' = \cos \theta'$  to remind us that we have described scattering inside the layer, the variable  $\mu = \cos \theta$  being reserved now for radiation outside the layer. We no longer need the scattering process to be defined for all angles  $\mu'$ ,  $\mu_0$ ,  $\phi_0$  and  $\phi'$  since we are only interested in backscattering. In this case  $\mu' = \mu_0$  and

$\phi_0 - \phi' = 180^\circ$ , and we may speak in terms of the restricted matrix  $\bar{S}(\mu')$  only. It is an almost diagonal matrix, the only non-diagonal elements lying in the 12 and 21 positions when the Stokes intensity is written  $[I_1, I_r, U, V]$ . See Part I of the thesis where these quantities and  $\bar{S}$  are described in detail. The notation is basically the same as that used in Chandrasekhar's (1960) book on radiative transfer (see, e.g., pp. 24-42). Eight of the sixteen elements are zero because they are odd functions of  $\phi$  and since  $-180^\circ$  and  $+180^\circ$  are equivalent values of  $\phi$ , the values of the functions there must be zero. This does not explain why the elements 34 and 43 are zero however, since they are even functions of  $\phi$ .

The nullness of these elements is apparent from the following "Gedanken Experimente" due to Hagfors (1967b).

We expect that if the surface is illuminated with either right or left handed circularly polarized light the excess of one linear component over another will be the same in both cases. The incident ray then is  $I = [1, 1, 0, +\sqrt{2}]$  in the  $[I_1, I_r, U, V]$  representation we have been using. Then taking into account the zero terms already mentioned we have for the two polarizations

$$3.11 \quad U \sim S_{34} = -S_{43}$$

where  $U$  is the excess of the two linears on axes  $45^\circ$  to the normal axes. Thus  $S_{34} = 0$  and  $S_{43} = 0$  by symmetry.<sup>1</sup>

Matrix  $\bar{S}(\mu')$  is now of the form

$$3.12 \quad \bar{S} = \begin{pmatrix} S_{11} & S_{12} & 0 & 0 \\ S_{21} & S_{22} & 0 & 0 \\ 0 & 0 & S_{33} & 0 \\ 0 & 0 & 0 & S_{44} \end{pmatrix}$$

We wish to combine  $\bar{S}$  with Fresnel's Laws of transmission and reflection for a layer of dust with index of refraction  $n_s$ . In deriving the transmission coefficients explicit account must be taken of the change in the solid angle of the beam as it enters and leaves the medium. This is usually not done. Transmission coefficients derived in most optics texts are applied to the magnitude of the electric field squared which is not strictly a measure of the intensity as we have been using it. The definition of intensity here, which is more properly called the specific

---

<sup>1</sup> The zeroness of  $S_{34}$  is an important check on computational accuracy. Each Fourier coefficient is non-zero in this element. It is only the sum of all the Fourier coefficients that produces the null value. This is the only a priori known quantity in all the computations and can serve as a check on the choice of all the internal parameters needed to actually run the polarization doubling program on the computer.

intensity, is a measure of the energy passing through a surface per unit time per unit solid angle. The question for our purposes is perhaps academic because the product of the transmission coefficients in and out of the layer is the same for both derivations, although the actual transmission coefficients differ from those usually seen by factors of  $n_s$ .

Let  $\theta$  and  $\theta'$  be, respectively, the angles of incidence and refraction that the radiation makes with the surface normal as it enters the dust from space. We derive the transmission coefficient from the reflection coefficient by writing the equation for conservation of energy across the interface, taking explicit account of the change in solid angle of the radiation.

$$3.13 \quad I^r \cos \theta \, d\omega + I^t \cos \theta' \, d\omega' = I^i \cos \theta \, d\omega$$

where  $r, t, i$  refer to reflected, transmitted, and incident respectively and  $d\omega$  and  $d\omega'$  are the differential solid angle occupied by the beam outside and inside the layer.

$$3.14 \quad R \cos \theta \sin \theta \, d\theta + T \cos \theta' \sin \theta' \, d\theta' = \cos \theta \sin \theta \, d\theta$$

Now,

$$3.15 \quad n \sin \theta' = \sin \theta$$

by Snell's law, where we have dropped the subscript s from  $n_s$  for the remainder of the derivation. Differentiating 3.15 and substituting in equation 3.14 we find

$$3.16 \quad T = n^2(1-R)$$

The usual Fresnel reflection coefficients as a function of the angle of incidence  $\theta$  for polarized parallel and perpendicular to the meridian plane of incidence are

$$3.17 \quad R_l = \left( \frac{n^2 \cos \theta - \sqrt{n^2 - \sin^2 \theta}}{n^2 \cos \theta + \sqrt{n^2 - \sin^2 \theta}} \right)^2$$

$$R_r = \left( \frac{\cos \theta - \sqrt{n^2 - \sin^2 \theta}}{\cos \theta + \sqrt{n^2 - \sin^2 \theta}} \right)^2$$

where l and r refer to the last letter of parallel and perpendicular. Then we get from 3.16 and 3.17

$$3.18 \quad T_l^i = \frac{4n^4 \cos \theta \sqrt{n^2 - \sin^2 \theta}}{(n^2 \cos \theta + \sqrt{n^2 - \sin^2 \theta})^2}$$

$$T_r^i = \frac{4n^2 \cos \theta \sqrt{n^2 - \sin^2 \theta}}{(\cos \theta + \sqrt{n^2 - \sin^2 \theta})^2}$$



The superscript  $i$  refers to transmission into the layer.

The two coefficients  $T_1^i$  and  $T_r^i$  describe the transformation of the two Stokes parameters  $I_1$  and  $I_r$  as the radiation enters the medium. We derive the transformation of the Stokes parameters  $U$  and  $V$  from their definitions in equation 1.2. If we take note of the tacit assumption which we have been making in the derivation of the transmission coefficients, that the imaginary part of the index of refraction is zero, no phase changes are introduced across the boundary. The derivation then is straightforward.

The definitions of  $[I_1, I_r, U, V]$  in equation 1.2 yield

$$\begin{aligned}
 I_1^t &= E_1^t{}^2 = T_1 E_1^o{}^2 = T_1 I_1^o \\
 I_r^t &= E_r^t{}^2 = T_r E_r^o{}^2 = T_r I_r^o \\
 U^t &= 2\text{Re} (E_r^t E_1^{t*}) = (T_r T_1)^{1/2} U^o \\
 V^t &= 2\text{Im} (E_r^t E_1^{t*}) = (T_r T_1)^{1/2} V^o
 \end{aligned}
 \tag{3.19}$$

Superscripts  $t$  and  $o$  refer to the transmitted and originally incident rays respectively,  $*$  means complex conjugate and  $E$  is the electric field strength. The superscript  $i$  on  $T$  was suppressed. These results show that

$$3.20 \quad T_u^i = T_v^i = (T_l^i T_r^i)^{1/2}$$

and the transmission matrix for the four stokes parameters is a diagonal matrix which we shall call  $\bar{T}^i(\theta)$ .

The transmission matrix for radiation leaving the medium,  $\bar{T}^o(\theta)$ , is derived from  $\bar{T}^i(\theta)$  by inverting the index of refraction writing  $\theta'$  for  $\theta$  in equation 3.18 and using Snell's law to re-express  $\theta'$  as  $\theta$ . The result is

$$3.21 \quad \bar{T}^o = \bar{T}^i / n^4.$$

The final step in deriving the scattering matrix of buried scatterers,  $\bar{B}$ , is to combine the transmission and scattering matrices.

$$3.22 \quad \bar{B}(\theta) = \bar{T}^o(\theta) \bar{S}(\theta) \bar{T}^i(\theta)$$

We mean by  $\bar{S}(\theta)$  that we have changed the dependent variable from  $\theta'$  to  $\theta$  so that  $\bar{S}(\theta)$  is related to  $\bar{S}(\theta')$ , the result of the doubling program, through Snells law. This required interpolation of values in the computer program. The form of  $\bar{B}$  is the same as that of  $\bar{S}$  given by equation 3.13 since both transmission matrices are diagonal.

## VI SCATTERING MATRIX FOR A CRATER

The model for radar scattering in the lunar surface has begun to take shape. Already in the modeling we have accounted for the subsurface nature of the scattering process. But up to this point there has been no need to decide whether the scattering is occurring in discrete locations or quasi-uniformly over the entire surface. In the development of the model the choice was made for us.

It was found, contrary to expectations, that a very high single scattering albedo,  $\tilde{\omega}_0 > 0.7$ , was needed to match the ratio of polarized to depolarized return power. This would give a radar cross section 2 orders of magnitude higher than what is observed. The need for discrete sources is immediately apparent, and the areas in and around fresh young craters a logical choice.

In this section we shall obtain the scattering matrix of the crater. To do this we discuss the meaning and use of  $\bar{\bar{B}}$  in greater detail and show how to integrate it over the surface of a crater. We require a matrix  $\bar{\bar{C}}$  which describes the scattering from a crater occupying the same area element that matrix  $\bar{\bar{B}}$  is referred to. We must take account not only of the angle that the radar beam makes with the local crater normal, but also of the angle that the average local lunar meridian plane of incidence makes with

the local meridianal plane of incidence inside the crater. These are the basic points involved in the integration over the crater. The derivation is as follows.

In order to do the crater integration we must first understand the physical meaning of  $\bar{\bar{B}}$  and  $\bar{\bar{C}}$ . The diffuse intensity scattered by an area element  $dA$  back towards the observer from the buried scatterers is

$$3.19 \quad \bar{I} = \frac{1}{4\mu} \bar{\bar{B}} \cdot \bar{F}$$

where  $\bar{F}$  is the incident flux and  $\mu$  is the cosine of the angle that the direction of propagation makes with the local normal. The energy that is observed from this area element is proportional to the intensity,  $\bar{I}$ , and the projection of the area onto the plane normal to the line of sight,  $\mu dA$ . Thus the energy returned from a randomly oriented surface element  $dA$  is proportional to  $\bar{\bar{B}} dA$  and it is this quantity we wish to integrate over the crater. In an equivalent manner, we define the crater scattering matrix  $\bar{\bar{C}}$  such that the energy coming from the crater as a whole is proportional to  $\bar{\bar{C}} A_0$ , where  $A_0$  is the area of the smooth lunar surface removed by the crater.

Before we write down the form of the integral for  $\bar{\bar{C}}$  we must more completely understand how to make proper use of  $\bar{\bar{B}}$ . These considerations would be absent if we were discussing intensity only. The scattering matrix  $\bar{\bar{B}}$  is express-

ed in terms of a local coordinate system defined by directions parallel and perpendicular to the local meridian plane of incidence and emergence, that is, the plane (or planes) defined by the direction(s) of propagation and the local normal to the surface. We want to refer each scattering element in the crater to the local meridian plane of the craterless surface. We must therefore rotate the coordinate system fixed on the lunar surface into the coordinate system of the crater scattering element and, the scattering having been completed, rotate it back again to the craterless surface coordinate system. If  $\Omega$  is the angle in the plane transverse to the direction of propagation that the meridian plane of the crater element makes with the meridian plane of the craterless lunar surface element then the scattering matrix of an infinitesimal portion of the crater is, in average lunar surface coordinates,  $\bar{L}(-\Omega) \cdot \bar{B} \cdot \bar{L}(\Omega)$  where  $\bar{L}$  is the rotation matrix of equation 1.9.

We may now write down the form of the integral for  $\bar{C}$ .

$$3.20 \quad \bar{C}(\mu) = \frac{\iint_{A_0} \bar{L}(-\Omega) \cdot \bar{B}(\eta) \cdot \bar{L}(\Omega) \, dA}{A_0}$$

where  $\eta$  is the cosine of the angle that the local crater normal makes with the line of sight.

The integral for  $\bar{C}$  is quite general for any crater shape. What remains is to discuss  $\Omega$ ,  $\eta$ ,  $dA$  and the integration limits for a particular model.

We assume that the crater is parabolic with a diameter to depth ratio of 4 following Moore (1969). This is approximately true for small fresh craters, but fails to hold increasingly as flat bottomed floors develop in larger craters. The crater has a depth  $h$  and a diameter  $d$ . If  $x$  and  $y$  are measured along orthogonal directions on the flat lunar surface and  $z$  is positive upwards, then the equation of the paraboloid is

$$3.21 \quad f(x,y,z) = z - ax^2 - ay^2 = 0$$

where  $a = 4h/d^2$ .

To express  $\eta$ ,  $\Omega$  and  $dA$  in terms of the variables  $x$  and  $y$ , consider the unit vector  $\hat{n}$  parallel to the local normal to the surface of the paraboloid.

$$3.22 \quad \hat{n} = \frac{\nabla f}{|\nabla f|} = \frac{-2ax\hat{i} - 2ay\hat{j} + \hat{k}}{\sqrt{4a^2x^2 + 4a^2y^2 + 1}}$$

where  $\hat{i}$ ,  $\hat{j}$ ,  $\hat{k}$  are unit vectors in the  $x$ ,  $y$ ,  $z$  directions respectively. Assume the radar beam is incident in the  $x$ - $z$  plane. The direction of propagation is parallel to the unit vector  $\hat{l}$  given by

$$3.23 \quad \hat{l} = \sin\theta \hat{i} + \cos\theta \hat{k}$$

where  $\theta$  is the angle between the normal to the  $x$ - $z$  plane and  $\hat{l}$ . Note that  $\cos\theta = \mu$ , the variable used previously. The cosine of the angle between the local normal to the surface and the direction of the beam is

$$3.24 \quad \eta = \hat{l} \cdot \hat{n} = \frac{-2ax \sin \theta + \cos \theta}{\sqrt{4a^2 x^2 + 4a^2 y^2 + 1}}$$

The area element  $dA$  is the real area on the surface of the paraboloid above the area element  $dxdy$  in the  $x$ - $y$  plane. Using unit vector  $\hat{n}$  normal to the crater surface, and unit vector  $\hat{k}$  normal to the  $x$ - $y$  plane we have

$$3.25 \quad dA = \frac{dxdy}{\hat{n} \cdot \hat{k}} = \sqrt{4a^2 x^2 + 4a^2 y^2 + 1} \, dxdy$$

The derivation of  $\Omega$  requires a bit more thought.  $\Omega$  is the angle that the projection of  $\hat{n}$  and the projection of  $\hat{k}$  make in the plane normal to  $\hat{l}$ . Noting the form of the vector  $\hat{l}$ , the direction of propagation, we may write down immediately two mutually orthogonal vectors  $\hat{L}_1$  and  $\hat{L}_2$  which define the transverse plane  $L$ .

$$3.26 \quad \begin{aligned} \hat{L}_1 &= \cos \theta \, \hat{i} - \sin \theta \, \hat{k} \\ \hat{L}_2 &= \hat{j} \end{aligned}$$

The sum of the projections of  $\hat{n}$  and  $\hat{k}$  on  $\hat{L}_1$  and  $\hat{L}_2$  determines the projected vectors. The projected vectors are then

$$3.27 \quad \begin{aligned} \hat{n} \rightarrow \hat{N} &= \frac{(2ax \cos \theta + \sin \theta) \hat{L}_1 + 2ay \hat{L}_2}{\sqrt{4a^2 x^2 + 4a^2 y^2 + 1}} \\ \hat{k} \rightarrow \hat{K} &= -\sin \theta \, \hat{L}_1 \end{aligned}$$

We find  $\Omega$  by the vector theorem

$$\cos \Omega = \frac{N \cdot K}{|N| |K|}$$

After a little algebra the equation for  $\Omega$  becomes

$$3.28 \quad \Omega = \tan^{-1} \left( \frac{2ay}{(2ax \cos \theta + \sin \theta)} \right)$$

Note that  $\Omega$  is an odd function of  $y$ . Because the beam is incident in the  $x$ - $z$  plane the crater is symmetric about this plane. Thus for every point  $(x, y)$  there is a point  $(x, -y)$ , and for every  $\Omega$  there is a  $-\Omega$ . In the computations therefore all odd functions of  $\Omega$  will be zero and can be discarded before the integration begins.

The integration limits remain. We will not derive them here as it is a question of simple though tedious analytic geometry. With the inclusion of the integration limits the equation for the crater scattering matrix is

$$3.29 \quad \bar{C}(u) = \int_{-h/a}^{\frac{m-\sqrt{ha}}{a}} \int_0^{q(x)} q(x) + \int_{\frac{m-\sqrt{ha}}{a}}^{\frac{m/2a}{g(x)}} \int_{g(x)}^{q(x)} L(-\Omega) \cdot B(\eta) \cdot L(\Omega) \\ \cdot \sqrt{4a^2x^2 + 4a^2y^2 + 1} \, dx dy$$

where

$$g(x) = \sqrt{\frac{h}{a} - \left(x - \frac{m}{a}\right)^2}, \quad q(x) = \sqrt{\frac{h}{a} - x^2}$$

and  $m = \cot \theta$ , and  $\eta(x, y)$  and  $\Omega(x, y)$  are given by equations 3.24 and 3.28.

The integration was performed numerically using Gauss-



ian quadrature in the variables  $x$  and  $y$ . Unfortunately using  $x$  and  $y$  as Gaussian points in variable intervals meant that  $\eta(x,y)$  did not necessarily coincide with the points at which matrix  $\bar{B}$  was known. Consequently the value of the functions at each integration point was determined by fitting a parabola to the three nearest points. We can write the formula for this interpolation in a very compact form, since it is a special case of the Lagrange interpolation formula. If the function  $f(\mu)$  is known at 3 points  $\mu_1, \mu_2, \mu_3$  surrounding the desired point  $\eta$ , then

$$3.30 \quad f(\eta) = \sum_{i=1}^3 f(\mu_i) \times \prod_{j=1}^3 \frac{(\eta - \mu_j)}{(\mu_i - \mu_j)}$$

This formula has been used extensively throughout much of this work, although we explicitly mention its use only here.

To conclude this section on the integration of the scattering matrix over the crater we discuss below the form of the matrix product  $\bar{C}' \equiv \bar{L}(-\Omega) \cdot \bar{B} \cdot \bar{L}(\Omega)$  and hence the form of the equivalent crater scattering function  $\bar{C}$ . Combining equation 3.12 for  $\bar{S}$  and equation 1.9 for  $\bar{L}$  and neglecting all odd functions of  $\Omega$  we get the components of the matrix product. The non-zero elements are the same as those for  $\bar{S}$  given in equation 3.12 and the components are, explicitly

$$C_{11}^1 = B_{11} \cos^4 \Omega + (B_{12} + B_{21}) \sin^2 \Omega \cos^2 \Omega + B_{22} \sin^4 \Omega + \frac{1}{2} B_{33} \sin^2 2\Omega$$

$$C_{22}^1 = B_{22} \cos^4 \Omega + (B_{12} + B_{21}) \sin^2 \Omega \cos^2 \Omega + B_{11} \sin^4 \Omega + \frac{1}{2} B_{33} \sin^2 2\Omega$$

$$3.31 \quad C_{11}^2 = B_{21} \cos^4 \Omega + (B_{11} + B_{22}) \sin^2 \Omega \cos^2 \Omega + B_{12} \sin^4 \Omega - \frac{1}{2} B_{33} \sin^2 2\Omega$$

$$C_{33}^1 = B_{33} \cos^2 2\Omega + \frac{1}{2} (B_{11} + B_{22} - B_{12} - B_{21}) \sin^2 2\Omega$$

$$C_{12}^1 = C_{21}^1$$

$$C_{44}^1 = B_{44}$$

We note in passing that if the crater is asymmetrical with respect to the meridianal plane of the line of sight, then the form of  $\bar{C}$  is changed from a non-zero 2x2 matrix situated on the upper diagonal to a 3x3 matrix on the diagonal.

## VII THE MATRIX ELEMENTS AND THE RADAR EXPERIMENTS

We are now capable of relating scattering matrices  $\bar{\bar{B}}$  and  $\bar{\bar{C}}$  to most of the observations that can be made from the earth. The only exception is that we cannot give absolute cross sections since we have not as yet accounted for the distribution of craters across the lunar surface. We will do this in section X. We here discuss the relation between the matrix elements we have derived and the radar experiments themselves. The comparisons between calculated and observed values will be discussed in the next section. Some of the discussion given here parallels in part a paper by Hagfors (1967b), but was independently arrived at.

We shall be discussing the matrix elements of a new matrix  $\bar{\bar{M}}$  which combines the scattering properties of the crater and ejecta blanket through the equation

$$3.32 \quad \bar{\bar{M}} = \bar{\bar{C}} + \frac{(1-F_c)}{F_c} \bar{\bar{B}}$$

where  $F_c$  is the fraction of the total power returned from the crater. For want of a very detailed description of the average fresh crater, we also take  $F_c$  to be the fraction of the area of the crater and its ejecta blanket occupied by the crater.

There are five independent matrix elements. Therefore five independent experiments are required to measure them. They fall into two categories --- measurements averaged over a range annulus and localized measurements of small area elements requiring the full power of the range-doppler technique (or other methods). We discuss below the averaging of  $\bar{M}$  over an annulus.  $\bar{M}$  is sometimes referred to as the Mueller matrix, although strictly speaking we should reserve the term for the properly normalized matrix.

Define  $\phi$  to be the angle in the plane transverse to the direction of propagation that the vector parallel to the local meridian or plane of incidence makes with an arbitrary direction, the direction of the libration axis for example. Then with the considerations of the previous section as to the meaning and use of the scattering matrix we may write down that the scattered Stokes intensity at any point is

$$3.33 \quad \bar{I}^S = \frac{1}{4\mu} \bar{L}(-\phi) \cdot \bar{M}(\mu) \cdot \bar{L}(\phi) \bar{I}^i$$

The scattering matrix for the entire annulus is then proportional to  $\bar{M}^a$  where

$$3.34 \quad \bar{M}^a = \frac{1}{2\pi} \int_0^{2\pi} \bar{L}(-\phi) \cdot \bar{M} \cdot \bar{L}(\phi) d\phi$$

and the result is, once again, an almost diagonal matrix

whose elements are:

$$\begin{aligned}
 M_{11}^a &= M_{22}^a = \frac{1}{8} (3M_{11} + M_{12} + M_{21} + 3M_{22} + 4M_{33}) \\
 M_{12}^a &= M_{21}^a = \frac{1}{8} (M_{11} + 3M_{12} + 3M_{21} + M_{22} - 4M_{33}) \\
 3.35 \quad M_{33}^a &= \frac{1}{8} (2M_{11} - 2M_{12} - 2M_{21} + 2M_{22} + 8M_{33}) \\
 M_{44}^a &= M_{44} \\
 \text{and} \quad M_{33}^a &= M_{11}^a - M_{12}^a
 \end{aligned}$$

This matrix, however, is different from previous matrices in that in the  $[I, Q, U, V]$  representation it is diagonal, with  $M_{22}^a = M_{33}^a$  as expected from the quite similar physical meanings of  $Q$  and  $U$ . ( $Q$  and  $U$  it will be remembered are the differences in the linear polarizations in two orthogonal coordinate systems making an angle of  $45^\circ$  with each other.) The equations to follow would be slightly more compact if written in this representation, but we will avoid this to reduce the incidence of new notation.

The averaged Mueller matrix,  $\bar{M}^a$ , is examinable by two experiments. In the first, circularly polarized power is incident and both right and left circulars are received. The incident intensity is  $[\frac{1}{2}, \frac{1}{2}, 0, 1]$  in the  $[I_1, I_r, U, V]$  representation. The ratio of polarized to depolarized power,

$r_c$ , can be written down immediately if we remember that  $V$  is the excess of right-handed over left-handed circular polarized power.

$$r_c = \frac{I + V}{I - V}$$

3.36

$$r_c = \frac{M_{11}^a + M_{12}^a + 2M_{44}^a}{M_{22}^a + M_{21}^a - 2M_{44}^a}$$

In another conceptually similar, although physically more difficult experiment (due to Faraday rotation in the Earth's ionosphere) a linearly polarized beam,  $[1, 0, 0, 0]$ , is used to illuminate the moon and both linears are received. The ratio of polarized to depolarized power,  $r_l$ , is

$$r_l = \frac{I_l}{I_r} = \frac{I + Q}{I - Q}$$

3.37

$$r_l = \frac{M_{11}^a}{M_{21}^a}$$

Implicit in the two equations is the total power received per unit area,  $\sigma$ , which is given by the proportionality

$$3.38 \quad \sigma(\mu) \propto M_{11}^a + M_{21}^a$$

For the second of the two categories of experiments we use the unaveraged Mueller matrix,  $M$ , to describe scattering

from local areas. In one experiment circular polarization is incident and the two linears are received from the libration axis (or any other suitable axis), the antenna polarization oriented parallel to this axis. The ratio of the power in the linear polarizations,  $r_{cl}$ , is

$$3.39 \quad r_{cl} = \frac{M_{11} + M_{12}}{M_{22} + M_{21}}$$

Note that this ratio is equal to unity for the data averaged over an annulus.

The last of these experiments measures the depolarization of linear incident power. The incident radiation is linearly polarized parallel to the libration axis and the state of linear polarization of the returned power is measured. The ratio of the two linears,  $r_{ll}$ , is given by,

$$3.40 \quad r_{ll} = \frac{M_{11}}{M_{21}}$$

From the point of view of the experimentalist, equations 3.36 to 3.40 are five equations in five unknowns for the determination of the Mueller matrix elements. That they are independent is not immediately clear from the form we have written them in. If we were to write them in matrix form, the uniqueness of the solution would become immediately obvious. To save space we will not pursue this matter any further.

### VIII THE ANGULAR VARIABLES-OBSERVATIONS AND CALCULATIONS COMPARED

We come now to the first of the results. We shall present in this section, mostly in graphical form, a parameterization of the end product of the computer calculations and comparisons with observations. The variables  $r_c$ ,  $r_l$ ,  $r_{cl}$ ,  $r_{ll}$ , and  $\sigma(\mu)$  defined in section VII will be discussed. We shall see the degree to which a consistent and physically reasonable set of parameter values is able to match the observations. Unfortunately, since there are many more variables than there are knowns, the choice will not be unique. The usefulness of our results will lie in their ability to explain differences from the average lunar scattering behavior. The section ends with a discussion of the applicability of this model to Mars and Venus. We reserve till section X the discussion of absolute cross sections.

There are two types of parameters involved here. The first set are those that were given as input to the computer program and whose effects we will examine below. They will be varied independently. The second set includes the first but shows more clearly the interdependence of the parameters. The parameters that we vary are  $n_s$ ,  $n_r$ ,  $\tilde{\omega}_o$ ,  $F_c$ ,  $s$  and  $\tau$ . The more complete set includes  $n_o$ ,  $\ell_a$ ,  $\lambda$ ,  $n_i$  as well as  $\tilde{\omega}_o(n_o, \ell_a, \lambda, n_i, n_r, s)$ . We take a detailed look



at  $\tilde{\omega}_0$  in section IX. The definitions of these quantities have been given before, but will be repeated here:  $n_s \equiv$  index of refraction of surface layer;  $n_r \equiv$  index of refraction of rock relative to  $n_s$ ;  $\tilde{\omega}_0 \equiv$  single scattering albedo;  $F_c \equiv$  fraction of crater and its ejecta blanket covered by crater;  $s \equiv$  exponent of power law distribution of rock sizes;  $\tau \equiv$  optical depth of scattering layer;  $n_0 \equiv$  coefficient of power law distribution;  $\ell_a \equiv$  absorption length in the dust;  $n_i \equiv$  imaginary part of the index of refraction of the rocks.

The non-uniqueness of the solution means that one choice of parameters to fit the observations may do quite as well as another. Yet we are forced to make a choice because the large number of parameters to be investigated makes it impracticable to display or calculate the whole hyper-space of solutions. Therefore we have selected a "good" set of values that make a reasonable fit to the observations and we display the result of varying each parameter independently while the other parameters are kept constant. The "good" parameter values are then the origin or "zero point" of a coordinate system and we shall investigate the results along axes centered at this point.

An exception to investigating conditions along these axes is our decision to display much of the results with-

out the addition of crater scattering. We do this because the crater destroys much angular dependence that might be of interest at some later date in connection with boulder fields unrelated to craters.

The zero point set of parameters is:  $\tilde{\omega}_0=0.79$ ,  $n_s=1.6$ ,  $n_r=1.6$ ,  $F_c=0.5$ ,  $\tau=\infty$ ,  $s=4.4$ . We shall discuss the physical plausibility of this choice in this and later sections. Briefly the choices are justified as follows:  $\tilde{\omega}_0$  corresponds to a point in a range of values calculated in section IX on the basis of Surveyor and Orbiter rock size distributions and Apollo 11 and 12 data for the complex index of refraction of rock and dust. The Apollo data give a range for  $n_s$  and  $n_r$  that includes our choices.  $F_c$  agrees with the value calculated from the radar return from Tycho and its ejecta blanket (section X). Finally we will see in this section that results for  $\tau=\infty$  are close to results for  $\tau=4$ , the optical depth of the smallest crater we consider (section X). The choice of the parameter  $s$  follows the observed distribution function for Surveyors I, III, V, and VI (Surveyor Mission Final Report, 1968) which gives  $s=4.1, 4.5, 4.6, 4.5$  respectively. The effect of  $s$  over a range  $s=4.0-4.6$  was found to have little effect on any of the computational results; we will discuss this later in this section.

The most important single question is whether our calculations can match the observed depolarization ratio in the different experiments. Figures 3.10 and 3.11 each give observed and calculated values at 23 cm. for circular in and out (i.e., transmitted and received) and linear in and out respectively, averaged over range rings. The single scattering albedo is varied. Here, as in all subsequent comparisons involving the polarized component, we must ignore the observations in the region near  $\cos\theta = 1$ . The quasi-specular return dominates the polarized component in this region. Also, the calculations for  $\cos\theta \lesssim 0.1$  should not be taken too seriously since the effect of an undulating terrain and surface rocks, not accounted for in the model, most certainly becomes important here.

The 23 cm. and 68 cm data shown in figure 3.10 as well as the 3.8 cm. data (not shown) have a circular depolarization ratio,  $r_c$ , of about 3 db (Hagfors, 1967a; Zisk, 1970). The linear depolarization ratio,  $r_l$ , measured only at 23 cm. is about 7 db, or 4 db greater than  $r_c$ . For  $\tilde{\omega}_0 = 0.79$  as well as for other choices of zero point parameters for best fit,  $r_l - r_c = 2\text{db}$ , and thus no one choice of  $\tilde{\omega}_0$  can exactly match both sets of data simultaneously. We see that although a single choice of  $\tilde{\omega}_0$  can explain the large depolarization and even the correct sign for  $r_l - r_c$ ,

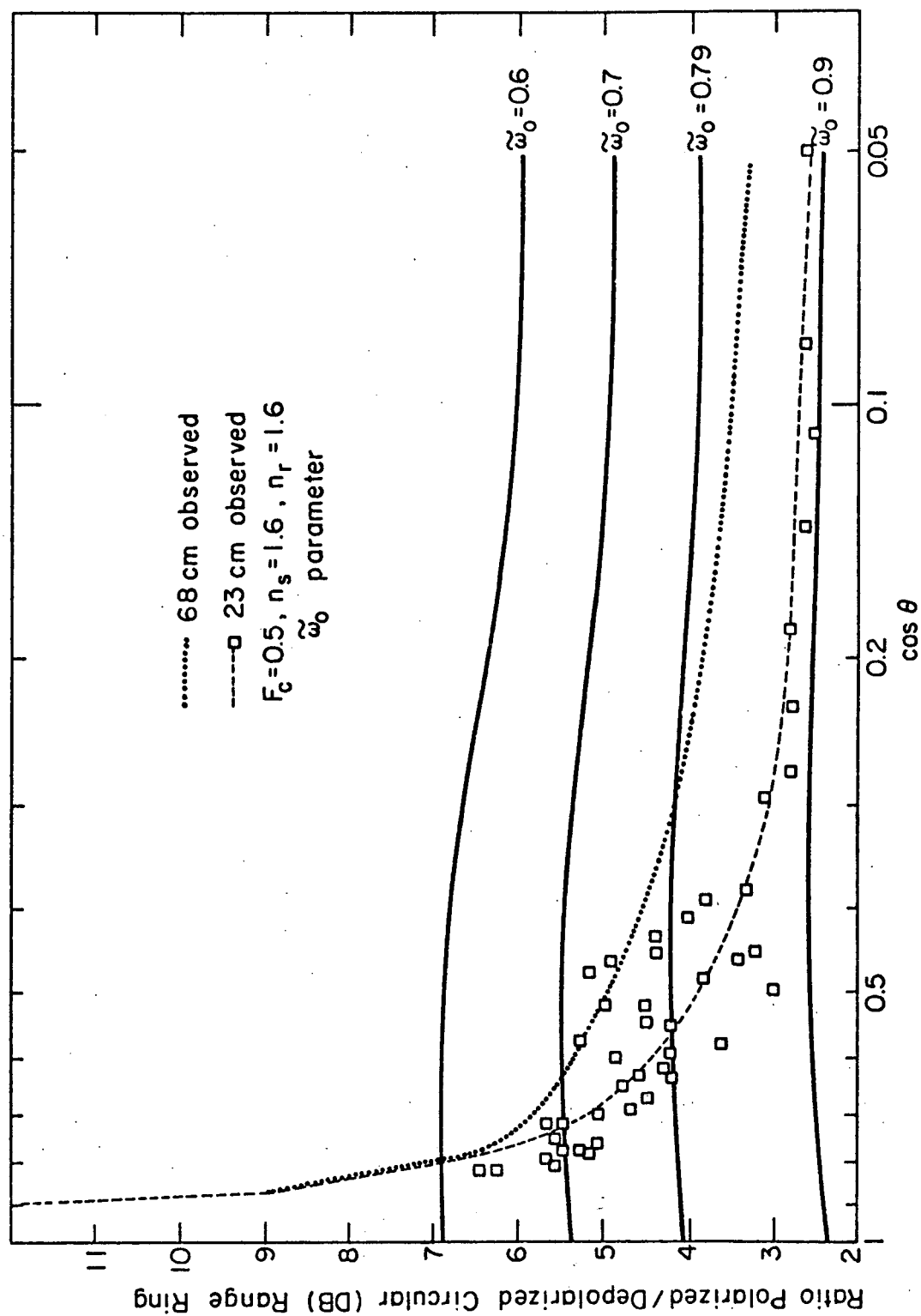


Figure 3.10 Calculated ratio of polarized to depolarized power in range ring from circular polarization transmitted and received. Data included for comparison. Single scattering albedo,  $\omega_0$ , varied.  
 $F_c = 0.5, n_s = 1.6, n_r = 1.6$  Data from Hagfors (1967a).

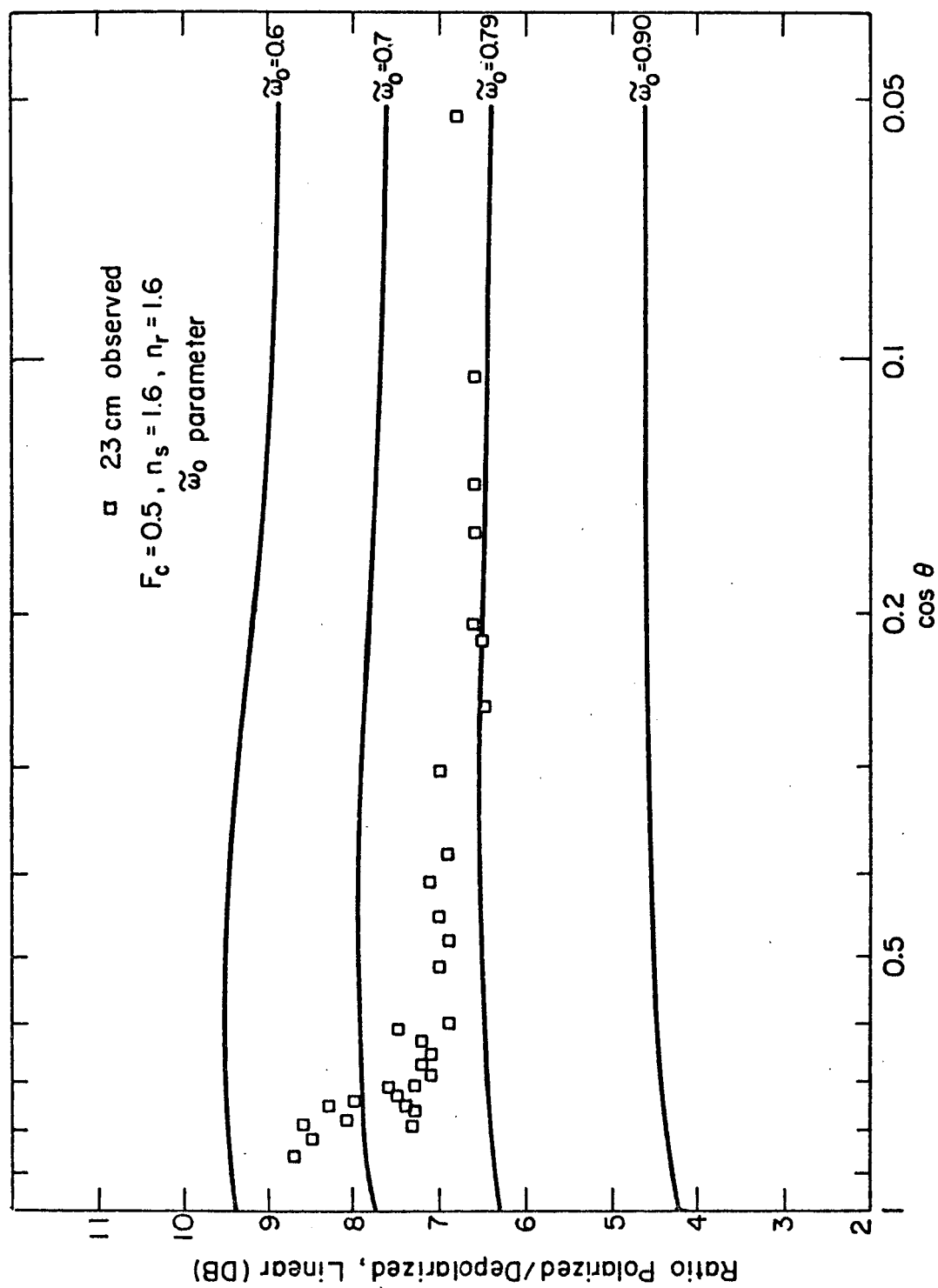


Figure 3.11 Calculated ratio of polarized to depolarized power in range ring for linear polarization transmitted and received. Data included for comparison. Single scattering albedo,  $\tilde{\omega}_0$ , varied.  $F_c = 0.5, n_s = 1.6, n_r = 1.6$  Data from Hagfors (1967a).

it falls slightly short of a perfect explanation. This may be reasonable given the obvious departure of lunar rocks from perfect spheres. Single scattering then still must play a role in the depolarization.

We have succeeded in obtaining more circular than linear depolarization with multiple scattering between spheres just as Hagfors (1967a) has succeeded using single scattering from dipoles. A combination of the two effects could add in the correct sense and account for the other 2 db. We envision the dipole like depolarization as follows. At any given wavelength most of the power is returned from rocks with  $\alpha \approx 2$ . For  $\alpha > 2$  and  $s > 3$  the total cross section decreases due to the power law distribution of rocks, while for  $\alpha < 2$  and  $s < 7$  the decrease is due to the rapid decrease of the rock cross section with  $\alpha$ . A rock with a long dimension such that  $\alpha \approx 2$  may have a much smaller cross section along its short dimension where  $\alpha < 2$ . The decrease of cross section with  $\alpha$  is very rapid for  $\alpha < 2$ , much more so than for  $\alpha > 2$ . The dipole effect then is due to those elongated rocks with  $\alpha \approx 2$ . Elongated rocks such as those invoked in this discussion may be seen in many of the pictures taken in all the Surveyor missions (Surveyor Project Final Report, 1968).

We next present the effect on  $r_c$  of changing the zero point parameters one at a time. The effect on  $r_1$  is completely similar where not shown. Figure 3.12 shows how  $r_c$  varies with the dielectric constant of the surface  $n_s$ , for  $F_c = 0$ . The striking difference between  $n_s = 1$  and  $n_s > 1$  is easily explained by Snell's law to be due to the very large change in the range of angles of incidence as the radiation penetrates the surface. We will see this effect often. The crater has the effect of removing much of the angular dependence. We see this in figure 3.13 where  $F_c = 0.5$ .

The depolarization ratio can also be influenced slightly by the choice of the index of refraction of the rock relative to the dust,  $n_r$ . This is shown in figure 3.7, section III. The non-monotonic behavior with  $n_r$  was discussed previously in section III and found to be the result of the backscatter cross section. The depolarization decreases as the backscatter cross section increases. We would expect this result for radiation multiply scattered back towards the source by objects that exhibit no single scattering depolarization.

Figure 3.14 shows  $r_c$  for  $\tilde{\omega}_0 = 0.9$  as the optical depth is varied. The depolarization increases less quickly as  $\tau$  increases and reaches its limit near  $\tau = 4$ . Thus we will be justified in using the results for  $\tau = \infty$ . The parame-

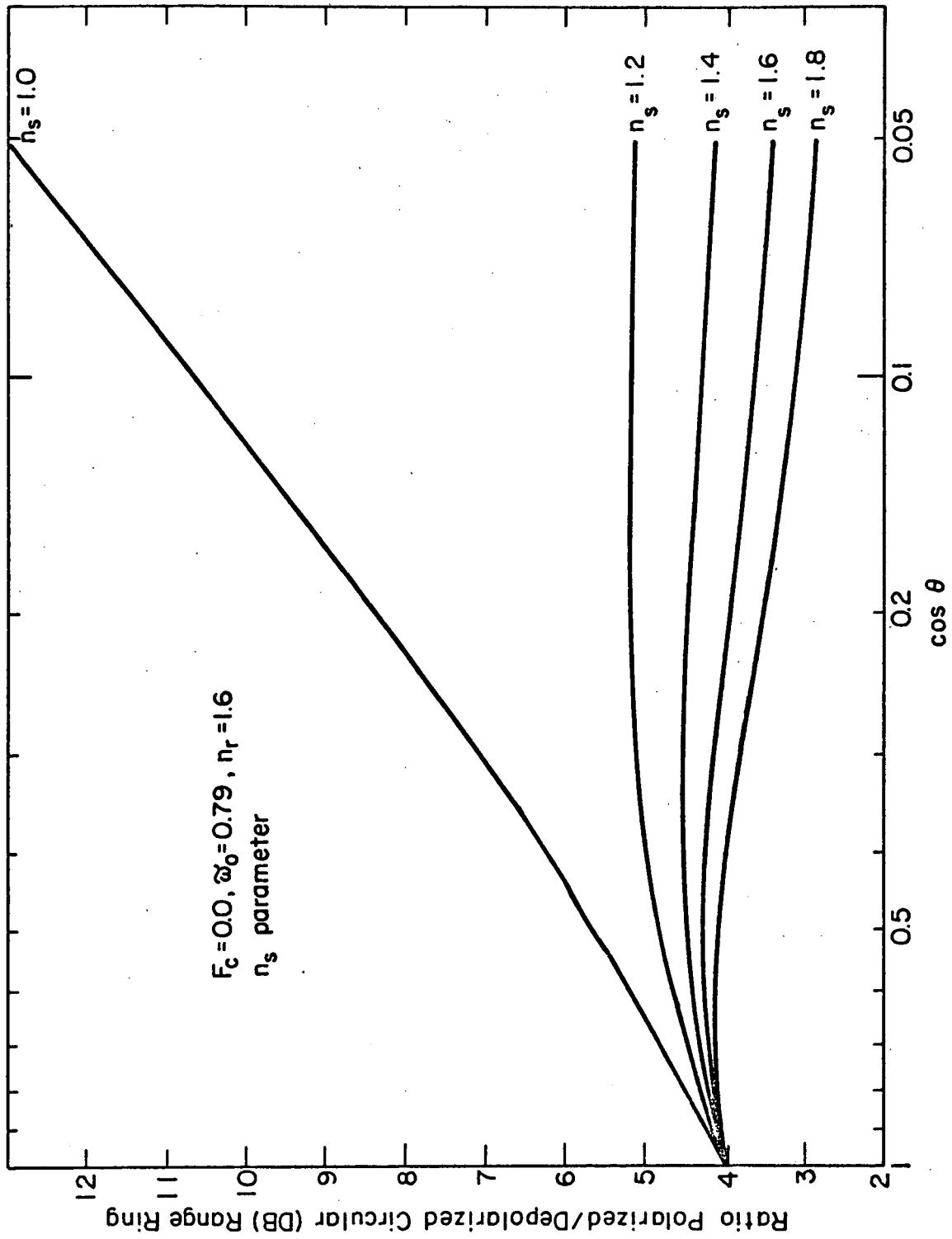


Figure 3.12 Curves have same meaning as theoretical curves in figure 3.10.  $F_c = 0.0$   $n_s$  is varied.



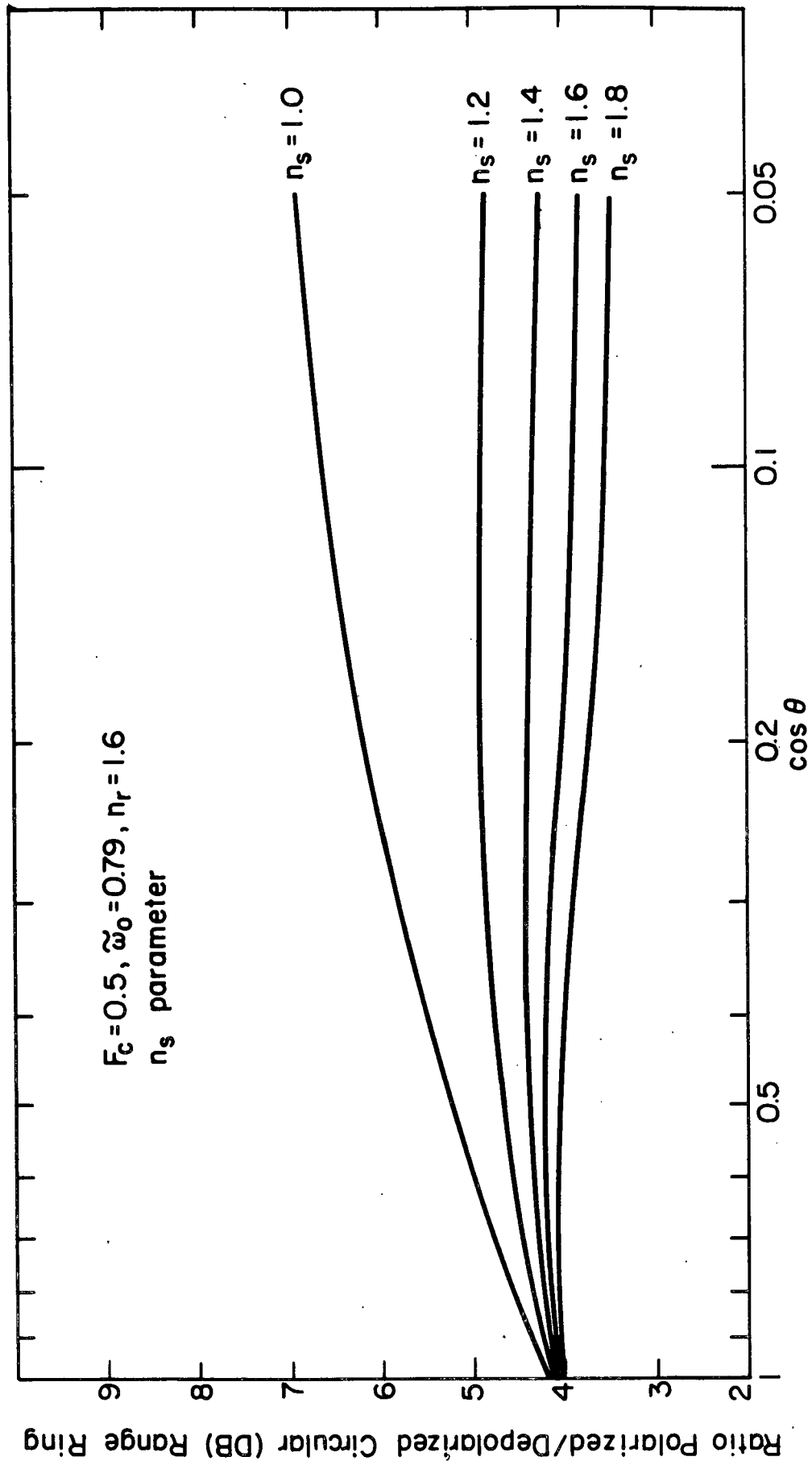


Figure 3.13 Curves have same meaning as theoretical curves in figure 3.10.  $F_c = 0.5$ ,  $n_s$  is varied.

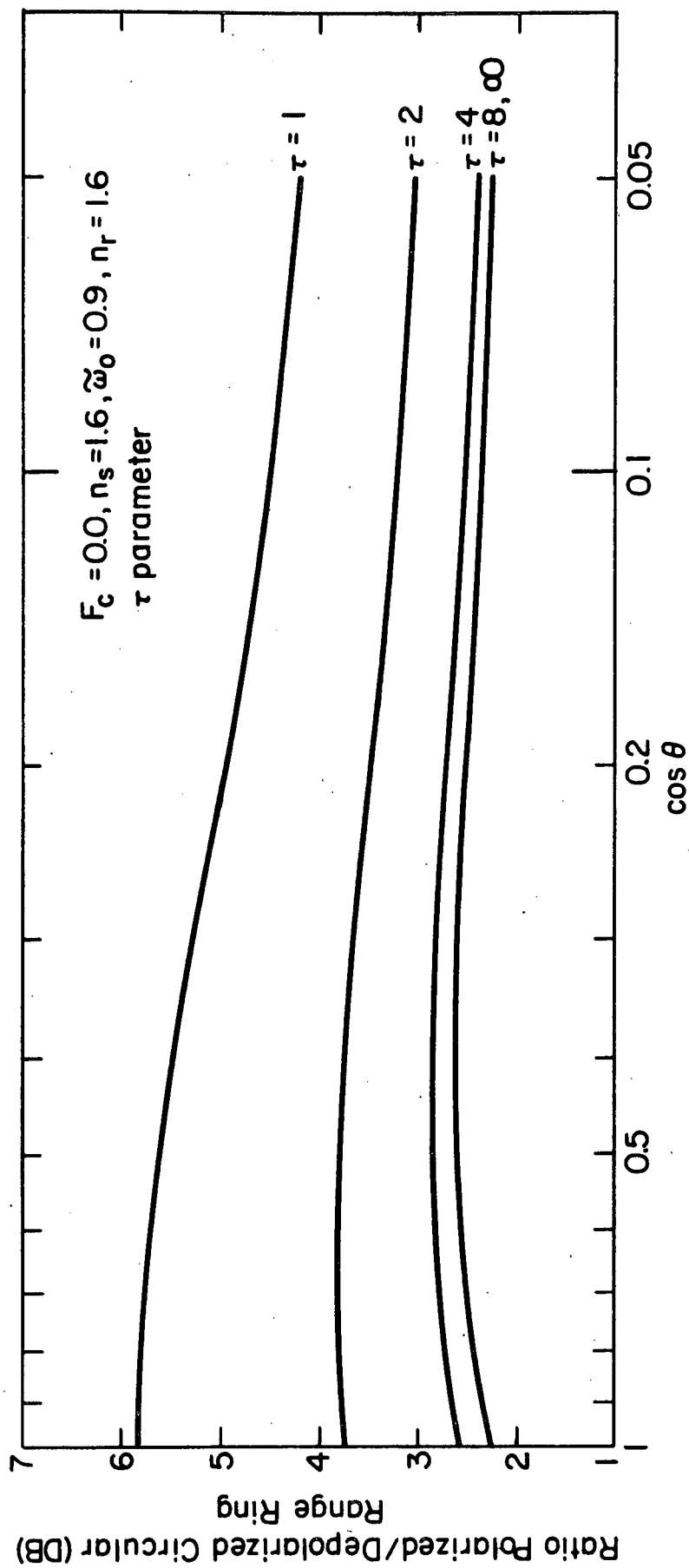


Figure 3.14 Curves have same meaning as theoretical curves in figure 3.10.  $\tilde{\omega}_0 = 0.9$ . Optical depth,  $\tau$ , is varied.

ter  $s$  has practically no influence on the results for  $s$  between 4.0 and 4.6. This is not surprising because the backscatter cross sections are all about the same for the different values of  $s$ , even though the maximum percent polarization changes by a factor of 2.

Another touchstone of our success in explaining the observations is the depolarization ratio,  $r_{11}$ , for linear in and out measured along the libration axis. Figure 3.15 shows calculated and observed values for this case. The average over a range ring,  $r_1$ , is included for comparison. There appears to be a real upwards shift in  $r_{11}$  over  $r_1$  although the spread in the data points is greater. The calculated values also show this effect. The spread in the data points may be due to noise, or, may be real. In the latter case, the spread may be analyzed according to a single or multiple scattering approach. If one attributes the scatter to a single scattering mechanism then must suppose systematic differences in the shapes of large numbers of rocks from place to place. On the other hand our explanation would be that there are systematic differences in the rock distribution and/or rock composition from crater to crater. We feel this is far more plausible.

The increase in the calculated and observed values of  $r_{11}$  over  $r_1$  is just the result of Fresnel's laws and is fur-

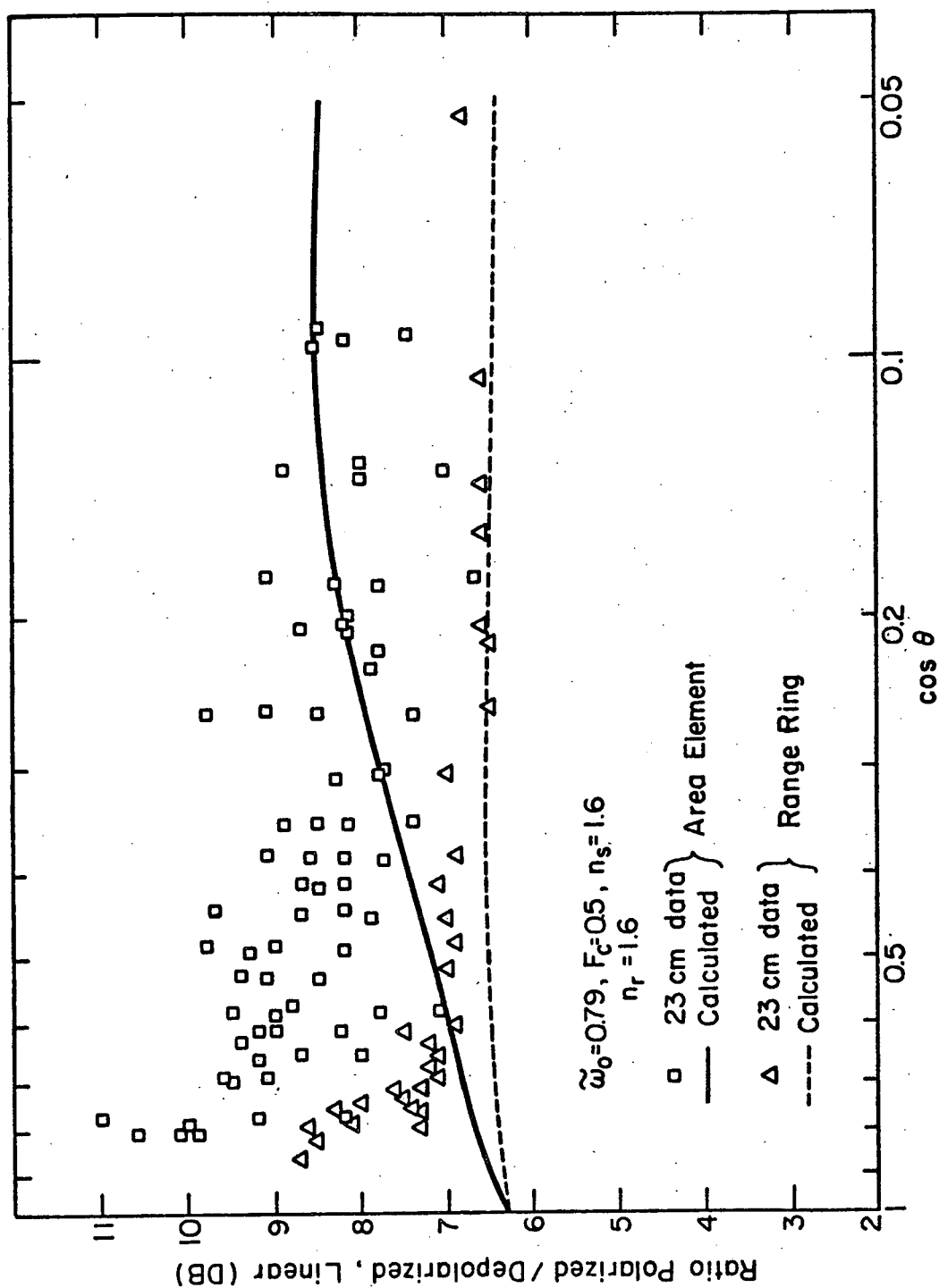


Figure 3.15 Calculated ratio of polarized to depolarized power averaged over area elements along libration axis and in annuli of constant delay. Data from Hagfors (1967a) included for comparison.

ther proof of the subsurface nature of the scattering process. We can see this readily if we compare the variation of  $r_1$  and  $r_{11}$  with  $n_s$  in figures 3.12 and 3.16. (Figure 3.12 is really drawn for  $r_c$ , but only the variation with  $n_s$  is of interest here.)  $r_1$  decreases monotonically with  $n_s$  mostly as a consequence of Snell's law, as we mentioned previously. This is not the whole story for  $r_{11}$ . The effect is still there as witnessed by the behavior of  $n_s = 1.0$  and  $n_s = 1.2$ . But as  $n_s$  increases further the depolarization decreases, not increases (i.e.,  $r_{11}$  increases).

For  $r_{11}$  data is taken along the libration axis where a plane of incidence may be defined, unlike data taken for  $r_1$  where the average over a range ring makes the definition of a plane of incidence impossible. Radiation polarized in the plane of incidence is preferentially transmitted through the surface. Thus any radiation that crosses over to the other polarization will find it harder to escape the subsurface layers than radiation polarized in the same mode as was transmitted. Any depolarization would be decreased, the effect increasing as  $n_s$  increases.

In line with the previous discussion we would predict that incident radiation polarized perpendicular to the libration axis would give more depolarization than the average over a range ring. The conclusion from all this, that the

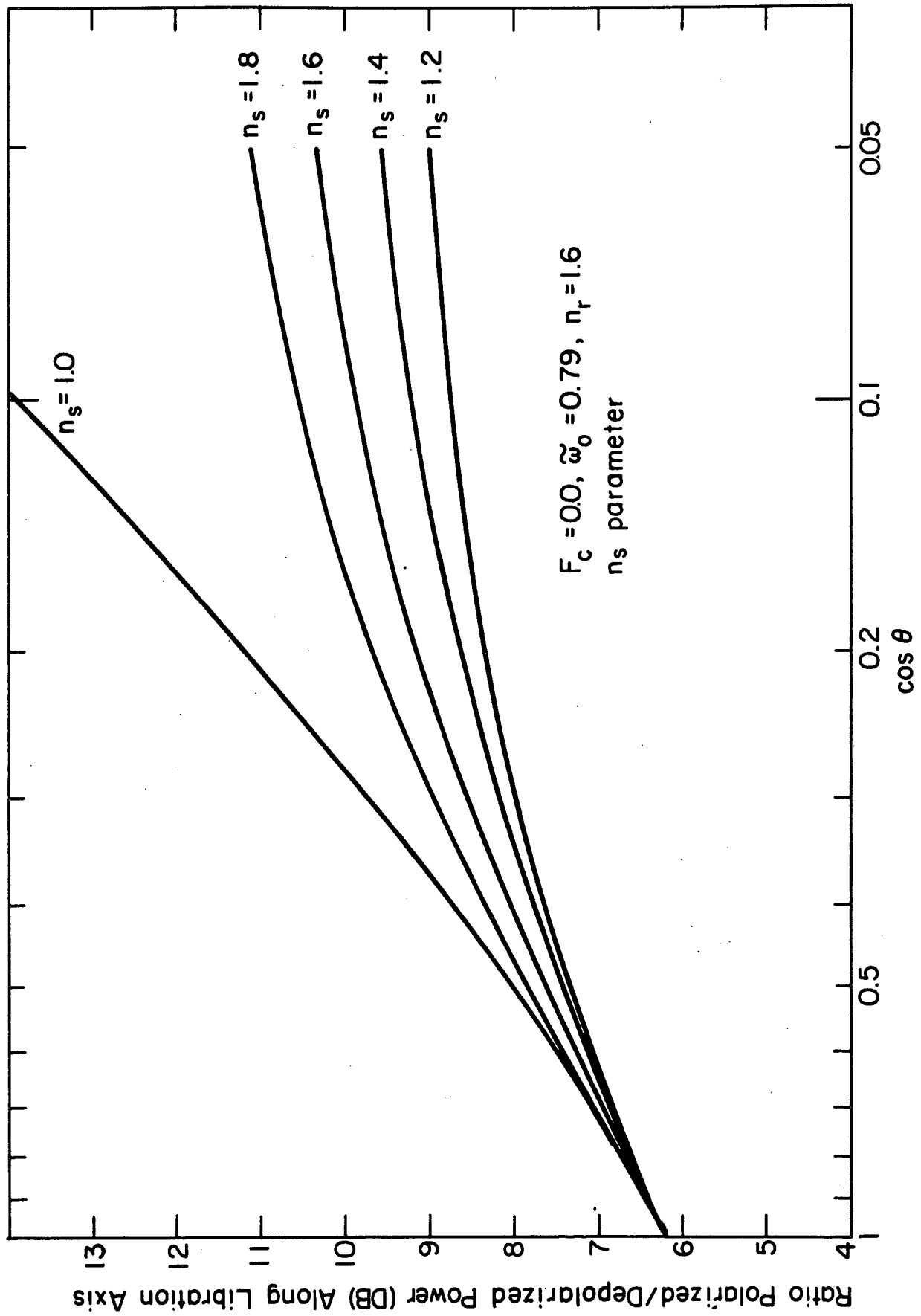


Figure 3.16 Ratio of polarized to depolarized power received from libration axis for linear polarization incident.  $n_s$  is varied.

scattering process is subsurface in nature, is certainly not a new one (see, e.g., Hagfors et al., 1965). However, we emphasize that the set of data we have been analyzing has never before yielded this result. Presently we shall discuss an experiment that shows the subsurface scattering more clearly.

It is mostly of passing interest to discuss the effect of the crater on the depolarization ratio  $r_{11}$ . The other parameters,  $\omega_0$ ,  $n_r$ ,  $s$ , and  $\tau$ , act exactly as they do for  $r_c$  and  $r_l$ .  $F_c$  too acts the same, but since there is more angular dependence here, we can see its influence more readily. Figure 3.17 shows the variation of  $r_{11}$  with  $F_c$ . The statement that can be made from these graphs is that averaging over a crater removes almost 100% of the angular activity of  $r_{11}$ ,  $r_l$ , and  $r_c$ , except where  $\cos\theta \approx 1$ . This also holds true for  $r_{c1}$ , to which we now turn.

The experiment that measures  $r_{c1}$  gives strong evidence that the radar has been scattered beneath the lunar surface. The problem with the interpretation, however, has been that for 23 cm. wavelength an index of refraction,  $n_s$ , of about 1.3 ( $\epsilon = 1.7$ ) is obtained rather than the value of 1.6 ( $\epsilon = 2.6$ ) that cross section data, taken at the same wavelength, gives. Hagfors et al. (1965) state that the two conflicting values can be reconciled if a two layer model is postulated.

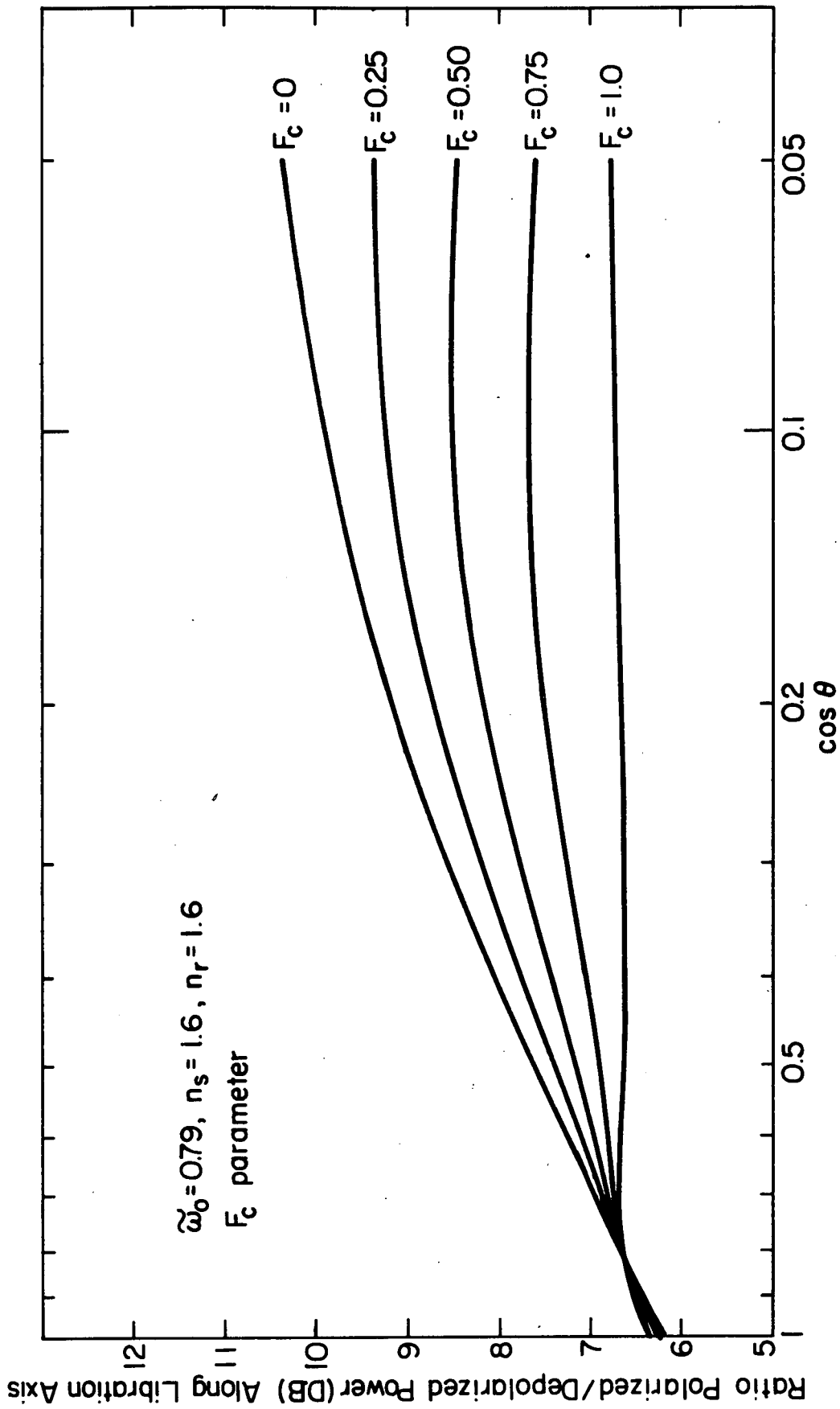


Figure 3.17 Ratio of polarized to depolarized power received from libration axis for linear polarization incident.  $F_c$  is varied.



The larger value of  $n_s$  due to observations of the absolute value of the radar cross section would then be due to an upper layer with  $n_s = 1.3$  and a lower layer with  $n_s \approx 2.2$ . Unfortunately, it is difficult to achieve this high a value for  $n_s$  from lunar dust. Combining the value given by Costes et al. (1970) for the maximum density achieved in packing the lunar dust returned by Apollo 11 with the curve of density vs. dielectric constant given by Gold et al. (1970) for Apollo 11 fines, the maximum index of refraction is  $n_s = 1.7$  ( $\epsilon = 2.9$ ). Values as high as  $n_s = 2.2$  could only be achieved under much higher pressures than would be expected one half an absorption length down. The depth corresponding to the two way absorption length of 2.3 m at 23 cm. is 1.2m, so that Hagfors would need to postulate bedrock just a meter into the surface. Estimates of the depth of the regolith, however, are generally greater than this (Quaide and Oberbeck, 1968)

We shall show that it is possible to interpret all the 23 cm. data in terms of one value for the index of refraction. The radar experiment that measures  $r_{cl}$ , consists of illuminating the moon with a circularly polarized beam and measuring the ratio,  $r_{cl}$ , of the two linear components aligned perpendicular and parallel to the libration axis. If the radar was being returned by single scattering

from surface rocks, no difference in the linears would be expected. The situation would be expected to change in the scattering is subsurface since Fresnel's laws of transmission are different for the two linear polarizations aligned in and normal to the plane of incidence. The data for 3.8 cm. and 23 cm. along with a parameterization of the calculations in  $n_s$  for zero point conditions, is shown in figure 3.18. The lack of a strong upturn in the data near the limb shows that our neglect of surface rocks is justified since there the slant optical depth is greatest and transmission through the surface should have its smallest influence.

The actual position of the curves depends to a very large degree on the choice of  $F_c$  and to a lesser extent on  $\tilde{\omega}_0$ . (See figure 3.19), and not at all on  $n_r$  and  $s$ . Thus while figure 3.18 implies that taking  $n_s = 1.6$  for 23 cm (and  $n_s = 1.3$  for 3.8 cm) is consistent with the calculations, it by no means says that these are the correct values. In fact the variation with  $F_c$  is so large that we instead have used figures 3.18 and 3.19 to determine that  $F_c = 0.5$ . This choice of  $F_c$  is consistent with a value determined from measurements across the crater Tycho, discussed in section X.

The variation of  $r_{c1}$  with  $\tilde{\omega}_0$  is also shown in figure 3.19 for  $F_c = 0$ . If no depolarization occurred in the scat-

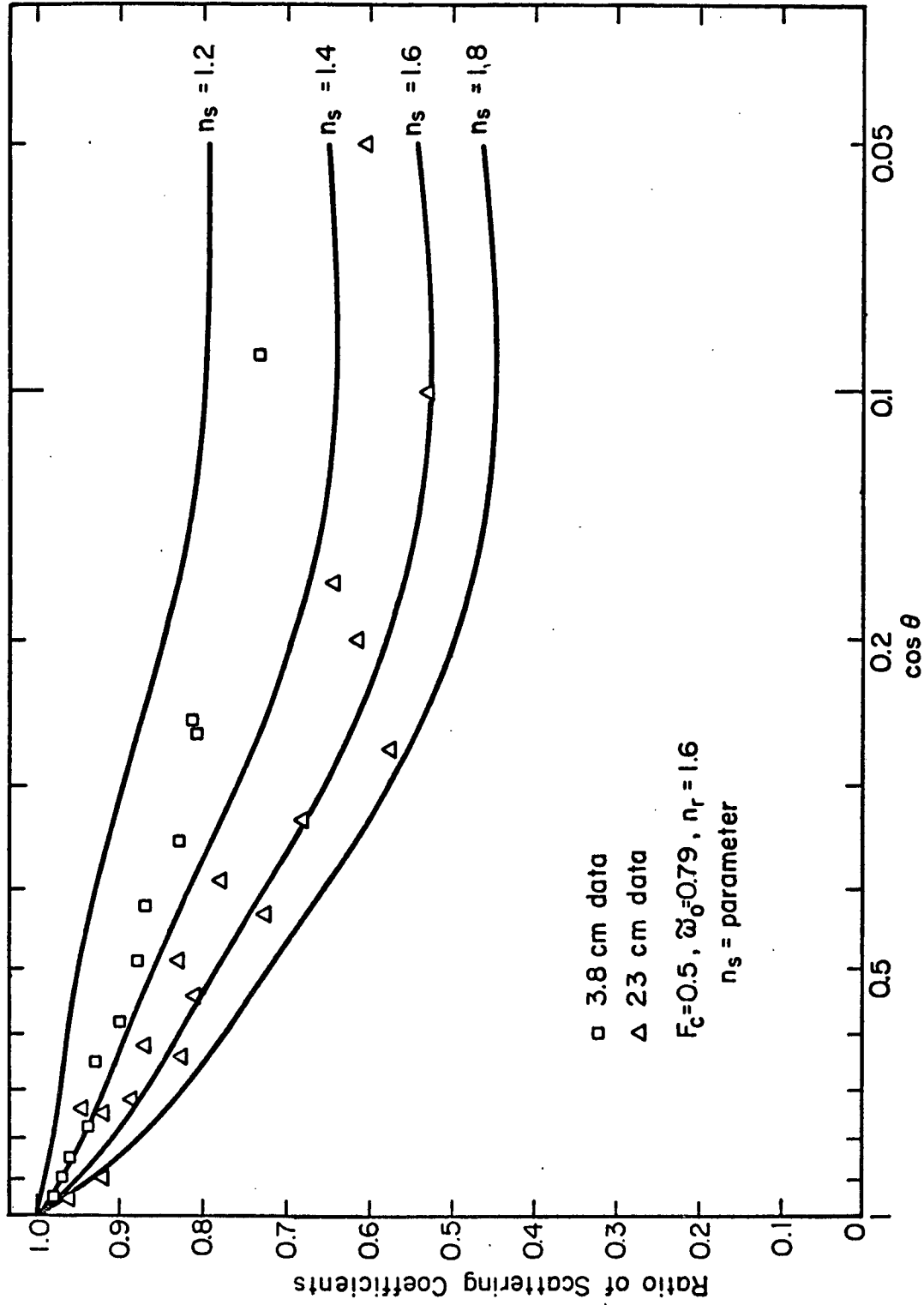


Figure 3.18 Calculated ratio of backscatter coefficients received from libration axis in two orthogonal linearly polarized components for circularly polarized illumination. Data from Hagfors (1967a) included for comparison. Index of refraction of surface,  $n_s$ , is varied.

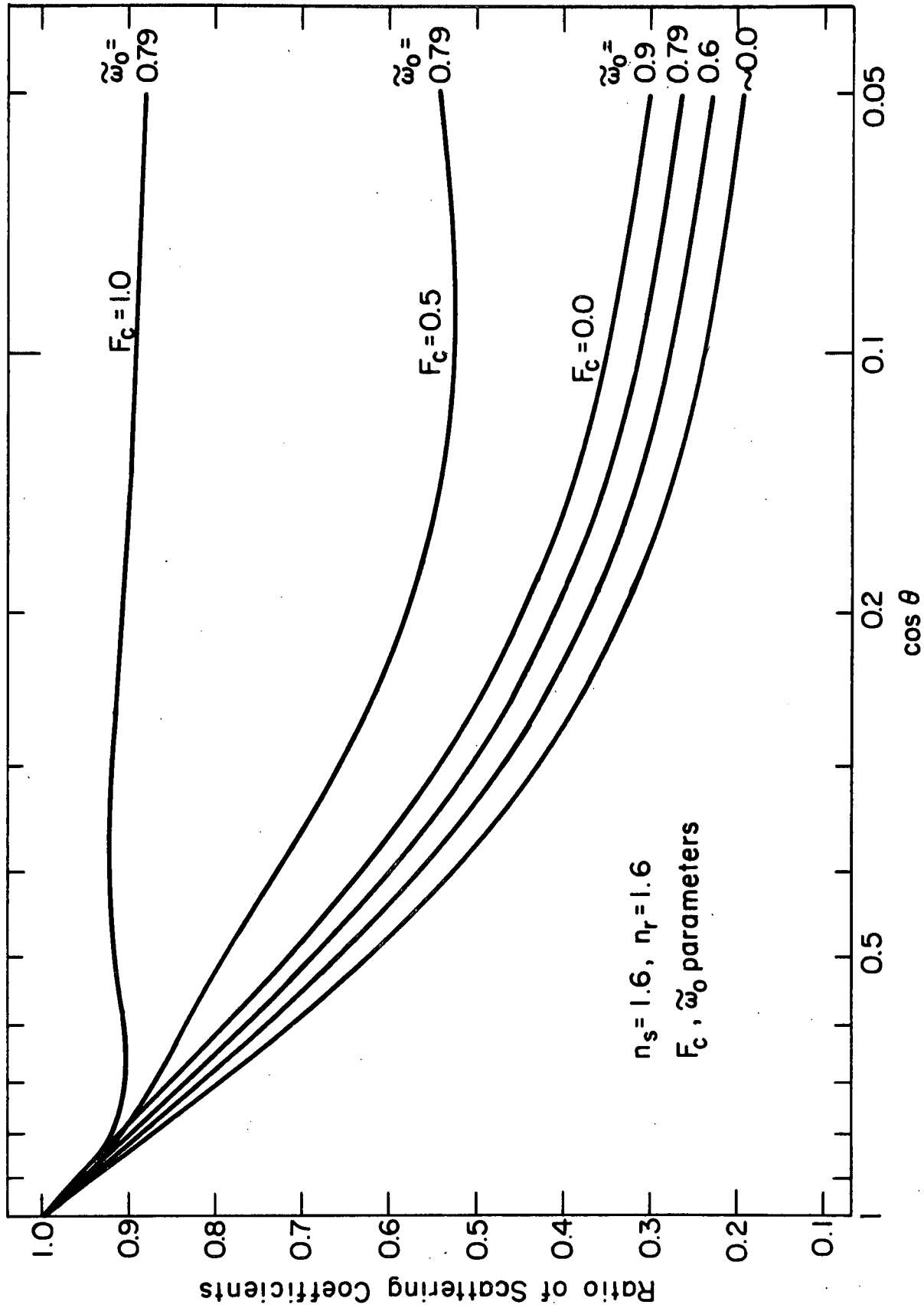


Figure 3.19 Theoretical curves have same meaning as in figure 3.18.  $F_c$  and  $\omega_0$  are varied.

tering then  $r_{cl}$  would vary as  $T^2$  where  $T$  is the transmission coefficient. The scattering has the effect of blurring the polarization induced by transmission into the layer, and thus  $r_{cl}$  varies as  $T$  to a smaller power than 2, though not quite 1.

Finally noting the rather small polarization occurring when the crater is the only source of the scattering,  $F_c = 1$ , it is very difficult to say whether an observation showing  $r_{cl} \approx 1$  means the scattering is not subsurface or that the terrain is very crater filled or chaotic. Thus we disagree with the statement of Hagfors et al. (1965) that "the fact that no systematic difference in the backscattering coefficients of the two polarizations is seen in the Tycho region may be interpreted to mean that this region does not have a tenuous layer..." . We feel that the averaging effect of the crater walls and the chaotic crater floor are at least an equally plausible explanation. The high rock number density in that region, which we have taken as characteristic of fresh craters in general, leads to a multiple scattering approach. The multiple scattering occurring beneath the surface would lead to a difference in backscattering coefficients were it not for the averaging process over the crater.

We come finally in our graphical presentation of angular variables to the discussion of the diffuse power returned per unit area averaged over a range ring. The success we have had is mostly due to the influence of the dielectric constant of the surface and the shadowing and averaging effect of a crater. The influence of the multiple scattering in determining the power  $n$  of  $\cos^n \theta$  is restricted to reducing the  $T^2$  dependence arising from the two way transmission through the surface to one between  $T^2$  and  $T^1$ . The shadowing in the crater introduces approximately a  $\cos^1 \theta$  dependence for intermediate and large values of  $\theta$ .

Figure 3.20 is a comparison between the observed 23 cm. circular depolarized cross section/unit area and our curve for the zero point parameters for best fit to this and previous data. The curve, given in db, has been shifted with respect to the data points to achieve a good fit. This is necessary since so far we have included no information on the actual fresh crater distribution that serves to determine the absolute cross section.

The fit is reasonable. While the actual shape of the curve does not closely parallel the data points, the decrease in the calculated cross section/unit area from  $\cos \theta = 1.0$  to  $\cos \theta \approx 0.1$  is about right. The failure to match the data more closely is understandable in view of the consid-

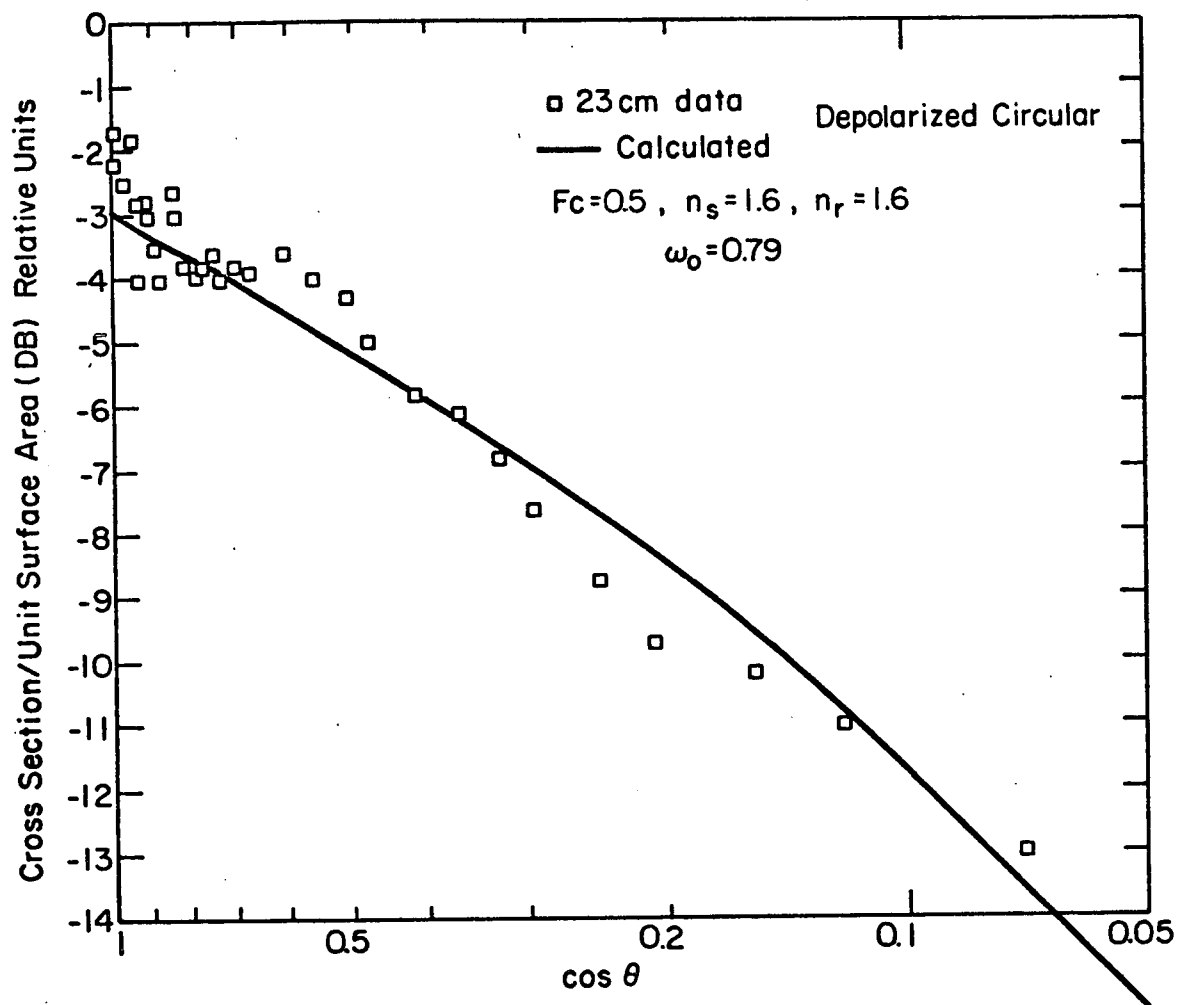


Figure 3.20 Theoretical depolarized cross section per unit area for circular polarization transmitted and received. Observations (Hagfors, 1967a) included for comparison.

erable topographic differences in lunar terrain and the unknown angular variation of the absolute reflectivity of the surface rocks which have not been accounted for in our model. The possibility exists, for example, that on the average a rock lying on the surface will have a larger cross section near the subradar point than it will towards the limb due to the fact that a lower center of gravity is inherently more stable so that the large end of the rock is in contact with the ground. The region beyond  $\cos \theta \approx 0.2$  is most susceptible to the effects of surface rocks and surface roughness and probably accounts for the positive slope change at large  $\theta$ .

The following graphs show the polarized and depolarized cross section/unit area for circular in and out. Where not shown polarized cross sections are similar to depolarized cross sections and follow the depolarized ones almost exactly as can be seen and derived from the curves of  $r_c$  and  $r_l$ . The linear results as well will not be shown since there is no essential difference between circular and linear other than the polarized-depolarized power difference given by  $r_c$  and  $r_l$ .

The two most important parameters that affect the shape of the theoretical curves are  $F_c$  and  $n_s$ . Figure 3.21 shows that parabolic craters alone give an average cross



section/unit area that varies as  $\cos^1\theta$  while a flat surface is closer to  $\cos^{0.7}\theta$  and approaches  $\cos^{1.5}\theta$  near the limb. We have chosen, on the basis of our discussion of  $r_{cl}$ , to use  $F_c = 0.5$  as the fraction of the power returned from craters alone. Thus the exponent of  $\cos\theta$  is between these two extremes.

Figure 3.22 shows the effect of  $n_s$  with  $F_c = 0$ . It is evident that we owe a great deal of the angular variation to  $n_s$ . Multiple scattering occurring on top of the regolith interface, supposing the calculations to be valid here, would give more limb darkening than beneath the interface. The two factors at work here, Fresnel's laws of transmission and the decreased range of the angle of incidence within the medium from Snell's law, combine in opposite directions to give the results in figure 3.22.

The parameters  $\tilde{\omega}_0$ ,  $s$ , and  $\tau$  have little effect on the angular dependence of the diffuse cross section per unit area over a wide range of values. This effect, as we have mentioned, is due to the strong reduction in angular variation caused by the index of refraction of the surface. We note that qualitatively the relative cross sections are affected to a small extent by  $n_s$ ,  $F_c$ , and  $s$  and to a very large extent by  $\tilde{\omega}_0$ ,  $\tau$ , and  $n_r$ . The increase in cross section is, as we would expect, in the direction of increasing

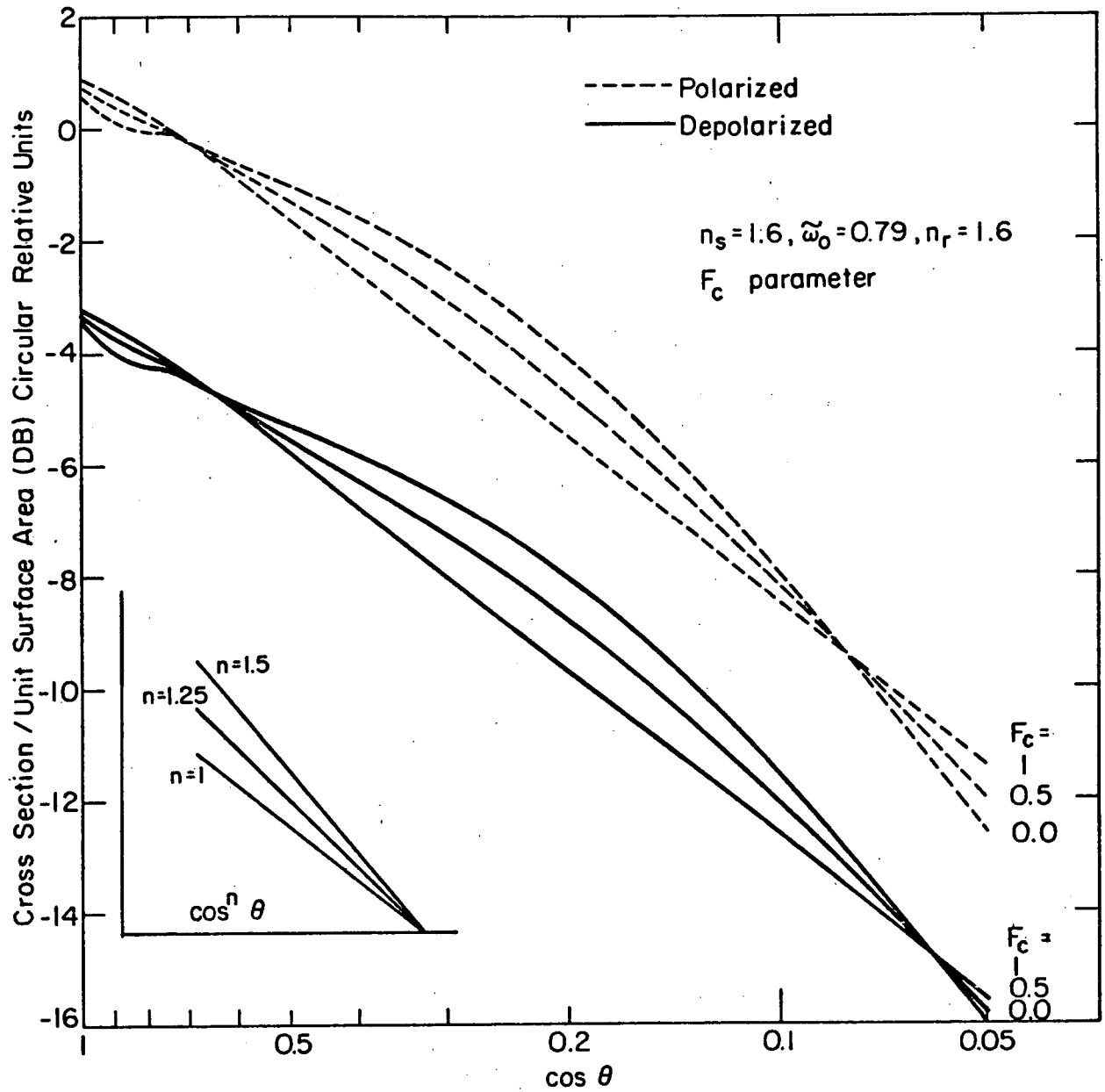


Figure 3.21 Cross section / unit surface area for circularly polarized power transmitted and received.  $F_c$  is varied.

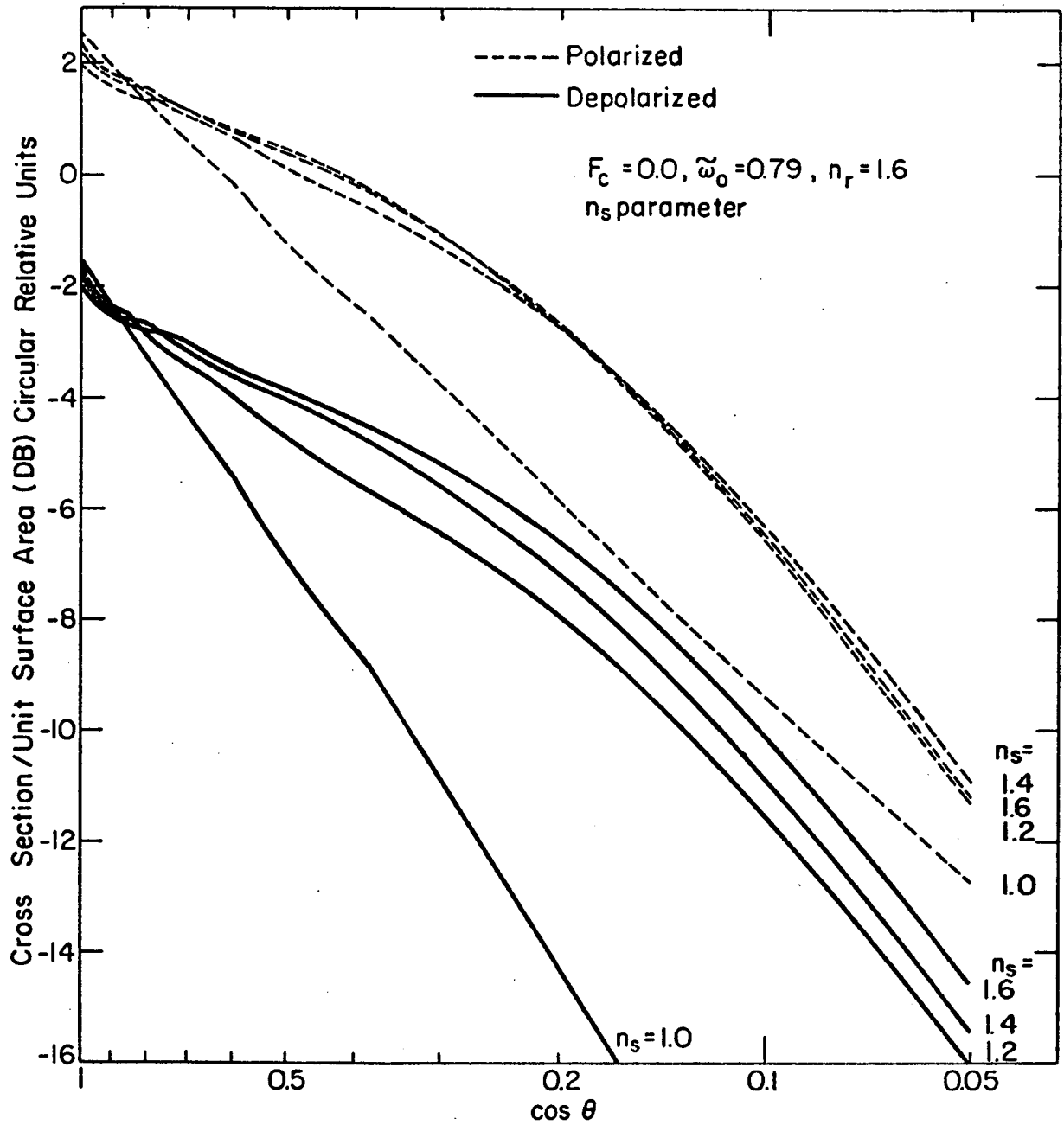


Figure 3.22 Curves are defined in figure 3.21.  $F_c = 0$  and  $n_s$  is varied.

$\omega_0$ ,  $\tau$ , and  $n_r$ . We shall discuss these points again in section X when we consider the absolute cross sections.

We have had much success in explaining the lunar radar data. Mars, which appears to share many surface characteristics with the moon, may be amenable to a similar interpretation. Future observations of Mars with improved ground based radar as well as bistatic radar observations employing spacecraft near the planet may yield much information on fresh craters, boulder populations, and surface composition. We would advise caution, however, in any attempt to apply a variation of this model to the planet Venus--the most un-moonlike of all the terrestrial planets. Observations of Venus show most of the terrain depolarizes less than the moon (Jurgens, 1970). This could be interpreted as smooth relatively boulderless terrain, rounded scatterers, or in the context of our model a lack of multiple scattering from burying rocks. The higher radar derived index of refraction of the surface of Venus implies that the surface is considerably more compacted than that of the moon thus arguing against multiple subsurface scattering (Campbell, 1971). There are also localized regions on the planet where the depolarization is much greater than is found anywhere on the lunar surface. We would be very reluctant to try to force our lunar model to ex-

plain this. Instead we believe the depolarization is due to rough broken terrain, a product of tectonic and volcanic activity unlike anything found on Mars or the moon. In this view the depolarization would be caused by multiple scattering from surface facets and surface rocks.

## IX THE SINGLE SCATTERING ALBEDO-THE PIVOTAL POINT OF THE MODEL

We saw in section VIII that our model revolves around a single main point - a single scattering albedo that most would agree is rather high. All the observations we discussed in section II were fitted in the previous section by assuming  $\tilde{\omega}_0 \approx 0.8$ . On the basis of data brought back by Apollos 11 and 12 and Lunar Orbiter and Surveyor results we will show that high  $\tilde{\omega}_0$  values are likely.

The dependence of  $\tilde{\omega}_0$  on  $n_r$ ,  $n_1$ ,  $n_s$ , and  $s$  will be noted and values for  $\tilde{\omega}_0$  will be calculated for observed lunar rocks distributed according to a fresh crater rock distribution function we shall develop. Possible correlation of the depolarization with heavy metal abundance will be suggested. We will see that we are able to reproduce the observed constancy of the depolarization with wavelength, yet predict a marked decrease with increasing wavelength - an effect not predicted by a single scattering model. We also will suggest another test of the model.

The calculations discussed previously were done by assigning a value of the single scattering albedo to the phase function and varying  $n_r$ ,  $n_s$ , and  $s$  independently even though  $\tilde{\omega}_0$  is a function of them. We found, however, that the depolarization is virtually unaffected by  $s$  over the

range 4.0 to 4.6; variations in  $n_s$  change the angular dependence by only a small amount; and  $n_r$  over a realistic range from 2.2 to 1.4 changes the depolarization by only 1 db. Moreover, with the single exception of absolute cross sections, all the multiple scattering calculations are relatively insensitive to  $s$  and  $n_r$  over the above ranges. On the other hand  $n_s$  does affect the polarization along the libration axis for circular in linear out,  $r_{cl}$ , but as we shall argue in this section and the next,  $n_s$  is rather well restricted and we shall take it to be 1.6 for 23 cm. This is the value used in our discussion of  $r_{cl}$ .

Since the fit of our calculations is unaffected by  $s$ , we are free to model  $\tilde{\omega}_0$  with a rock distribution function that departs somewhat from the one actually used to produce the graphs. Specifically we take a more realistic model to be one that exhibits a break in the power law distribution similar to what is observed. We now derive  $n_V(a)$ .

In our model we assume that fresh young craters are the source of the diffuse component. Consequently we must take  $n_V(a)$  to represent the volume distribution within and near fresh craters. Unfortunately in those regions where we have good data on surface rock frequencies from the Surveyor series of lunar landers there are no fresh craters in the vicinity. The possible exception to this is Surveyor

VII which landed near the rim of Tycho, one of the youngest large lunar features. The area covered in the photographs, however, is quite small compared to the area coverage in Lunar Orbiter photographs. The Lunar Orbiter photographs, on the other hand, do not permit boulder counts below 0.5 m radius. Therefore we use Lunar Orbiter data to determine the absolute number densities for large rocks and Surveyor data to determine the break point and slope of the power law distribution for small rocks. The coefficient of the small rock distribution function was determined by matching the absolute value of the number densities at the break point. The calculation follows.

From the data of Moore (1969) we have for Tycho

$$n_a(a) = 1.013a^{-4}/\text{cm}^2$$

between  $a$  and  $a + da$  where  $n_a$  is the surface number density. From the Surveyor Project Final Report (1968), we have

$$n_a(a) = n_0 a^{-2.82}/\text{cm}^2, \quad a < 25 \text{ cm}.$$

Equating the number density at 25 cm we derive the coefficient  $n_0$ .

We have a size distribution of surface rocks but we require a volume distribution function. The two distributions may be related through the use of the Rosin (1898) principle: the ratio of the area occupied by the particles of a



given size to the total area studied is equal to the ratio of the volume of the particles of this size to the total volume assuming the particles exposed at the surface are representative of the particles in the subsurface and the layer is uniformly mixed. In a non-rigorous fashion we may use this law in its differential form:

$$3.41 \quad n_V(a) \frac{4\pi a^3}{3} da = n_a(a) \pi a^2 da$$

The result of all this is

$$3.42 \quad n_V(a) = 0.017a^{-3.82}/\text{cm}^3, \quad a < 25 \text{ cm.} \\ = 0.76 a^{-5}/\text{cm}^3, \quad a > 25 \text{ cm.}$$

In view of the present data this is our best guess as to the average rock distribution function. There will undoubtedly be areas with higher number density which will have higher  $\tilde{\omega}_0$ 's than those we shall calculate, as well as areas with lower  $\tilde{\omega}_0$ 's. Since the depolarization and cross section depend on  $\tilde{\omega}_0$  to a higher power than 1, we may expect that the predictions based upon  $\tilde{\omega}_0$  calculated below are more uncertain in the direction of increasing  $\tilde{\omega}_0$  than in the opposite direction.

A good intuitive feeling for the physical appearance of rocks distributed according to  $n_V(a)$  is obtained from the calculation of  $f_V$ , the fraction of the total volume occupied.

For rocks larger than 1 mm.,  $f_V = 0.58$ . The fraction of the volume occupied by rocks contributing to the scattering at any wavelength gives a good feeling for the relative magnitude of  $\ell_0$ . Thus integrating from  $\alpha = 1$  to  $\alpha = 20$ ,  $f_V$  is 0.03, 0.21, 0.29, 0.26, 0.20 for 7.5m, 68cm, 23cm, 3.8cm and 8mm respectively. The single scattering albedo, as we shall see below, even though convolved with the Mie theory, follows the above pattern quite well. We see that on the basis of the size distribution alone  $\tilde{\omega}_0$  is fairly constant from 68 cm. to 8 mm., but  $\tilde{\omega}_0$  for 7.5 m is down by a large factor.

The next parameter of interest in the calculation of  $\tilde{\omega}_0$  is the absorption length in the dust,  $\ell_a = \ell_0 \lambda$ . We can obtain  $\ell_0$  in two ways: from thermal models of the lunar surface and by direct measurement of lunar fines brought back by Apollo's 11 and 12.

Linsky (1966) has derived a set of models to fit the curves of radiothermal temperatures versus phase angle. We get  $\ell_0 = 10$  and  $\ell_0 = 16$  from two of his best fit models. The other models all give  $\ell_0 \approx 10$ .

Measurements of  $\ell_a$  from Apollo data has been carried out by Gold et al. (1970, 1971). The absorption length decreases as the degree of packing increases. Using the data of Costes et al. (1970) for densities and porosities observ-

ed in core-tubes and under maximum packing and referring this to the curves of Gold et al. (1970,1971) for absorption length versus density we get  $\ell_0 = 10$ . This is the value we shall use. We note, however, that terrestrial basalts with similar powder densities have absorption lengths from 2 to 5 times greater (Campbell and Ulrichs, 1969). This difference may be due to the high ilmenite content observed in the rock and dust (Chung et al., 1970; Katsube and Collett, 1971). We shall return to this point shortly.

We can readily calculate  $n_s$ , the index of refraction of the dust, from the same set of measurements used above. The densities in two core tubes and the density of maximum compaction all give  $n_s = 1.6 \pm 0.05$ . This is the index of refraction of the surface that we used in section VIII to derive  $F_c = 0.5$ . We show in section X that this value of  $F_c$  can be calculated a priori, although the uncertainty is larger than for  $n_s$  calculated a priori. Thus we have used  $n_s$  to determine  $F_c$ .

We come finally to the complex index of refraction of the rock relative to the dust,  $\tilde{n}_r = n_r - in_i$ . In what follows we have divided the real part of the index of refraction of the rock relative to vacuum by  $n_s$  to obtain  $n_r$ . The imaginary part, however, is not divided by  $n_s$ . This is because

for small values of  $n_i$  relative to  $n_r$  (i.e., small loss tangent,  $\tan\delta = \epsilon_i/\epsilon_r$ ), the absorption length in the rock is inversely proportional to  $n_i$  and independent of  $n_r$ . Since the absorption in the rock does not change with  $n_s$ , neither does  $n_i$ .

The uncertainty in the values we shall use for  $\tilde{n}_r$  are the greatest source of error in determining  $\tilde{\omega}_0$ . Terrestrial rocks exhibit large variations in  $n_r$  and  $n_i$  in samples taken in the same area and even greater variations in samples taken in different areas (Campbell and Ulrichs, 1969). There is no "average" terrestrial rock, although an extraterrestrial observer might try to define one. This is just what we are trying to do for lunar rocks. Consequently it is useful to emphasize the variability of theoretical  $\tilde{\omega}_0$ 's before defining a most probable value.

Table 3.2 give the subsurface single scattering albedo for 10 lunar rocks brought back by Apollo's 11 and 12. The complex index of refraction relative to the dust has been derived from published graphs. M. Campbell (personal communication) has emphasized that the values read from these graphs are more accurate than the data itself; hence the reluctance to publish tables as we do below. The albedos indicated as lower limits were derived from  $\tilde{n}_r$  measured at 30m wavelength. For shorter wavelengths  $n_r$  remains relatively constant, but  $n_i$  decreases and  $\tilde{\omega}_0$  increases.

TABLE 3.2

$\tilde{\omega}_0$  CALCULATED FROM MEASURED  $\tilde{n}_r$  AT 23 CM. WAVELENGTH

$\tilde{n}_r = n_r - n_i$	$\tilde{\omega}_0$	REFERENCE	COMMENTS
1.7 - 0.081	0.58	Gold, O'Leary & Campbell (1971)	Measured at 68 cm. wavelength.
1.6 - 0.081	0.55		
1.3 - 0.051	0.49		
1.5 - 0.051	0.61		
1.8 - 0.031	0.75	Katsube & Collett (1971)	Igneous; ilmenite con- tent 15-20%
1.8 - 0.021	0.81		Igneous; ilmenite con- tent 3-4%
1.7 - 0.031	0.74		Breccia
1.9 - 0.141	0.52		Dense crystalline igneous; ilmenite 16%
2.0 - 0.141	0.54	Westphal & Simmons (1970)	Dense crystalline ilmenite 15%
1.5 - 0.061	0.57		Fine grained breccia; ilmenite 9%
1.7 - 0.041	0.70		N Hawaiian Oahu Basalt
1.5 - 0.061	0.57		O Cape Neddick Gabbro
1.5 - 0.00241	0.87		A Simulated sample, P similar to Apollo O rocks of this ref. L but ilmenite 4%
1.6 - 0.021	0.80	Wood (1970)	L O Proposed material for lunar highlands; anorthosite

Also given in the table are two earth basalts, a simulated lunar sample with similar chemical analysis but reduced ilmenite content and an anorthositic rock such as that proposed by Wood et al. (1970) as a major constituent of the highlands.

Katsube and Collett (1971) and Chung et al. (1970) have suggested that large  $n_r$  and  $n_i$  may be correlated with increased ilmenite content. These factors act in opposite ways on  $\tilde{\omega}_0$ , but referring to table 3.2 there appears to be some correlation in the direction of decreasing ilmenite yielding higher  $\tilde{\omega}_0$ 's. The Surveyor alpha scattering experiments of Surveyors V and VI, both of which landed in maria regions, and Surveyor VII which landed in the lunar highlands (Surveyor Project Final Report, 1968) imply the highlands have less heavy metals than the maria. We would expect a smaller ilmenite abundance in those regions. This expectation coincides with the speculation of Wood et al. (1970) and Wood (1971) that the lunar highlands have a higher abundance of anorthositic rocks. The idea is based in part on observations of Apollo 11 and 12 fines and the fact that such rocks have lower densities than maria basalt. Since highlands cover 2/3 of the visible face of the moon we suggest that rocks with small ilmenite abundance are the principle depolarizing agents. From these considerations

and table 3.2 we suggest that  $\tilde{\omega}_0 = 0.8^{+0.1}_{-0.3}$  in the highlands, lower in the maria.

The limits on  $\tilde{\omega}_0$  imply that at best multiple scattering in the lunar surface can explain almost all of the observed depolarization. At worst, figure 3.10 implies that at least 30% of the circular depolarized power is due to multiple scattering and 70% is due to single scattering while figure 3.11 implies that at least 50% of the linearly depolarized power is due to multiple scattering. As we have mentioned in section VIII we would expect some of the observed depolarization to be due to single scattering, no matter how high a single scattering albedo is observed or deduced.

Before leaving the subject at hand we pause to consider whether the wavelength dependence of  $\tilde{\omega}_0$  in our model can explain the observed wavelength dependence of the absolute diffuse cross section and the circular depolarization ratio. As we have suggested before,  $\tilde{\omega}_0$  is approximately constant from 68 cm. to 8 mm., but is significantly lower at 7.5m. Specifically, for the simulated lunar sample of Chung et al. (1970)  $\tilde{\omega}_0 = (0.45, 0.86, 0.87, 0.85, 0.82)$  at (750, 68, 23, 3.8, 0.8) cm. respectively. We see that on the basis of  $\tilde{\omega}_0$  alone we are unable to explain the increase of the diffuse cross section with decreasing wavelength. An explanation is proposed in the next section where we discuss the nature of the crater scattering more closely.

We are successful, however, in explaining the observed relative constancy of the depolarization from 68 cm. to 3.8 cm. Single scattering would imply the same result. But single scattering would predict that towards 7.5 m. and at longer wavelengths the depolarization would remain constant provided there is no systematic change of rock shape with size. We predict a rapid decrease of depolarization with wavelength beyond 1 m., the exact rate being highly dependent on the amount of multiple scattering. A curve of depolarization vs. wavelengths greater than 1 m. could yield immediately from our model the degree of multiple vs. single scattering. In view of the possible geological significance of the multiple scattering model we urge such measurements be made.

We propose one final test of our model. Since the depolarization is highly dependent on the random existence of large rock concentrations we predict that as the resolution element of the radar observations decreases the depolarization will begin to fluctuate more than would be expected from decreased signal to noise. This effect may be present in figure 3.15, as was discussed in section VIII. Further, we predict that the sense of the fluctuations will be in the direction of decreased depolarization in the absence of large boulder fields. If such an effect is observed only multiple scattering could account for it. We urge that this observation also be performed.



## X THE TOTAL DIFFUSE RADAR CROSS SECTION OF THE MOON

Until now we have been discussing the relative angular behavior of the diffuse component. No effort has been made to describe the fresh crater distribution and the detailed nature of real lunar craters. Consequently we have not been able to discuss the total diffuse cross section, to which we now turn.

This section is divided into five subsections. In the first we develop the equation relating the scattering matrix for a typical crater site and the distribution function of lunar craters to the diffuse cross section. Next we describe a model for the observed crater distribution and some characteristic features. In the final three parts we discuss, in turn, the total diffuse cross section, the wavelength dependence of the cross section, and the observed differences between highland and maria regions. We suggest that highland-maria differences may be due to mineralogical differences and thus propose that the depolarization ratio may be used to map the moon geologically.

### 1. Diffuse Cross Section - Theory

We have chosen to derive the diffuse cross section in two steps. First we use the Mueller matrix for crater and ejecta blanket,  $M$ , to calculate the gain from a complete-

ly cratered planet. Then the gain is combined with a cratering law to produce the gain (or cross section) for the moon. In what follows we take  $M$  to be a scalar scattering function instead of a matrix since we are interested in intensity only.

Let  $P_t$  be the power transmitted and  $P_r$  the power received at the radar unit;  $A_r$ , the area of the receiver;  $G_r$ , the gain of the receiver;  $L$ , the lunar distance;  $g_c$ , the gain of the fully cratered lunar surface; and  $a$ , the lunar radius. Then the flux incident at the moon, normal to the direction of propagation is  $P_o$ .

$$3.43 \quad P_o = \frac{P_t G_t}{4\pi L^2}$$

The power per unit solid angle or intensity radiated back to the receiver from an element of area  $dA$  is

$$3.44 \quad dI_r = \frac{M(\mu) P_o \mu dA}{4\pi \mu}$$

The total intensity reflected back to earth is

$$3.45 \quad I_r = \frac{P_o}{4\pi} \int_0^{2\pi} \int_0^1 M(\mu) a^2 d\mu d\eta$$

where  $\eta$  is the azimuthal coordinate. The power received by the antenna is the intensity times the solid angle occupied by the receiver as seen from the moon.

$$3.46 \quad P_r = I_r \frac{A_r}{L^2}$$

On the other hand the power received is given by the radar equation

$$3.47 \quad P_r = \frac{P_t G_t A_r}{(4\pi L^2)^2} g_c \pi a^2$$

Substituting equations 3.43 and 3.45 into 3.46 and comparing 3.46 and 3.47 we find

$$3.48 \quad g_c(\tau) = 2 \int_0^1 M(\mu; \tau) d\mu$$

For a Lambert surface where  $M = 4\mu^2$  the gain would be 8/3. We also note that this definition of  $g_c$  equals 4 times the geometric albedo of a planet which scatters according to M. The parameter  $\tau$ , the optical depth, has been reintroduced in equation 3.48 for use below.

In our model of the lunar surface we will assume that only craters greater than a diameter  $D_0$  are blocky enough to contribute to the cross section. This conforms to the observations of Moore (1969) who observed that small fresh craters have a much smaller proportion of their area covered by rocks. We take the depth of the scattering layer to be uniform inside and outside the crater and to be only a function of the crater diameter,  $D$ . Thus  $\tau = \tau(D)$ . The distribution of fresh craters is given by  $n(D)$  such that the number of craters per unit area with diameters between  $D$  and  $D + dD$  is  $n(D)dD$ . Then the gain of the model moon is

$$3.49 \quad g = \int_{D_0}^{\infty} g_c(\tau(D)) \frac{\pi D^2}{4} n(D) dD$$

## 2. The Fresh Crater Distribution Function

The discussion below is based upon the work of Moore (1969) and his discussion of crater frequencies and morphologies. From his work we find that for rough maria as well as for some highland regions the number of craters with diameters greater than  $D$  is given by the general law

$$3.50 \quad \begin{aligned} N(D) &= 10^{-1} D^{-2}, \quad D < D_c \\ &= 10^{-1} D_c D^{-3}, \quad D > D_c \end{aligned}$$

Smooth maria which we will not consider in any detail, display a slightly more complicated behavior but the general behavior is like that of equation 3.50. The  $D^{-2}$  law refers to a steady state surface which is the result of an equilibrium between crater production and erosion by extensive cratering. The  $D^{-3}$  law reflects the rate of crater production for a particular model of impacting asteroids over geologic time.

We are interested in the distribution function for fresh craters. This can be derived from the distribution function for all craters because steady state frequency distributions exist not only for all craters but also for craters with given morphologies. Our definition of a fresh

crater, however, differs from Moore's in that we differentiate on the basis of scattering properties, not morphologies. Moore defines a fresh crater as one in which  $31/32$  of the original relief has been preserved. We shall define a fresh crater as having an ejecta blanket capable of significant scattering. For that purpose we define  $t^*$  to be the depth to which bombardment by small meteorites causes a crater to cease being a strong radar anomaly. Now Moore states that crater lifetimes are proportional to their depths. This can be derived with some discussion from equation 3.50. What this means for our development is that the depth of steady state pulverization of the rocks in the ejecta blanket (which we take as covering the inside of the crater as well) is proportional to the age of the crater. Thus a fraction  $t^*/d$  of all steady state craters with diameters  $D$  will be among those we shall consider fresh, where  $d$  is the crater depth. For fresh craters we will take  $D = 4d$  following Moore.

The position of the break point,  $D_c$ , is also a function of crater morphology.  $D_c$  is the smallest size crater that has not been completely eroded over the lifetime of the moon. If we demand instead a depth of erosion  $t^*$ , the break point would come at a larger diameter  $d_c/t^* D_c$ , where  $d_c$  is the depth corresponding to a diameter  $D_c$ . The  $D^{-2}$  law of

the steady state distribution now becomes a  $D^{-3}$  law after multiplication by  $t^*/d$ . On the other hand the exponent of the original  $D^{-3}$  portion of the cratering law remains unchanged because a constant fraction, independent of  $D$ , would be among those we would consider fresh. This follows when we note that craters with  $D > D_c$  have not been destroyed in the history of the moon and when we assume that the exponent of the power law distribution of impacting bodies has not changed over time. Then the fraction of craters with  $D > D_c$  that has been eroded to a depth  $t^*$  will be independent of  $D$ .

With the above considerations the distribution function no longer has a break-point and we may write for all fresh craters

$$3.51 \quad N(D) = 0.4t^*D^{-3}$$

and the crater density function becomes

$$3.52 \quad n(D) = 1.2t^*D^{-4}$$

Not all of these craters, however, will possess ejecta blankets blocky enough or deep enough to cause significant scattering. The crater must penetrate the regolith to have blocks. For highland regions this lower limit,  $D_o$ , is 100 m. diameter while for maria regions the limit is 10 m. Not all craters larger than these limits produce sufficient blocks to be of interest. From the small amount of data available on the fraction of area covered by blocks larger than 1 m.

for various crater diameters we take  $D_0$  to be 400m. The value may be different for the maria and highlands. This estimate is very crude and is based upon poor statistics. From the limited data available, the lower limit scales approximately as the wavelength so we write the lower limit as  $D_{0\lambda} = D_0\lambda$ .

The optical depth of the ejecta blanket can be estimated by taking the depth of the ejecta blanket to be  $1/2$  the rim height. The depth of the ejecta blanket is then  $2 \times 10^{-2} D$ , since the rim height is directly proportional to  $D$ . The optical depth for a 400 m crater at 70 cm. wavelength is 12 for the rock composition and distribution discussed previously. As we have seen in figure 3.14 the limit for infinite optical depths is approached near  $\tau = 4$ . Thus it will be sufficient to use only the results for infinite optical depth in deriving the cross section. This is also the justification for displaying only the results for  $\tau = \infty$  in section VIII. The ad hoc assumption that the depth of the ejecta is  $1/2$  the crater rim height is not crucial to this analysis, though a much lower value might somewhat alter the cross section we calculate next.

The depth  $t^*$  may be estimated by taking it to be that depth with a two way optical depth due to dust alone of 1. For the dust obtained by Apollos 11 and 12,  $t^* \approx 5$ . This

value for  $t^*$  is valid when we expect that the meteoritic flux pulverizes all rocks to this depth and stirs up no rocks from below.

### 3. The Total Diffuse Cross Section

Using the previous choice of parameters the equation for the diffuse cross section becomes

$$\begin{aligned}
 \sigma(\lambda) &= \pi a^2 \int_{D_0 \lambda}^{\infty} g_c(\tau=\infty) \frac{\pi D^2}{4} (6. \lambda D^{-4}) dD \\
 3.53 \qquad &= 4.71 g_c / D_0 \pi a^2 \\
 &= 0.012 \pi a^2
 \end{aligned}$$

The cross section above, while being independent of wavelength as written, is more strictly true for 70 cm. wavelength.  $D_0$  may be  $\lambda$  dependent, but was derived for  $\lambda = 1m$ . Also,  $g_c$  was expressed for  $n_r = 1.6$  at 70 cm. and this too varies with  $\lambda$  as discussed below.

The observed diffuse cross section at 70 cm. is  $0.011 \pm 0.005 \pi a^2$  (Pettingil and Thompson, 1968). Our value agrees with this quite well, but the agreement must be in part fortuitous. There are large uncertainties here. We do not know  $\tilde{\omega}_0$  very well due to uncertainties in  $n_v(a)$  and  $\tilde{n}_r$ . The value of  $\tilde{\omega}_0$  is not expected to remain constant across the crater or from crater to crater as we have assumed.  $D_0$  is not well known and, to a lesser extent, neither is  $t^*$ .



The cross section is, respectively, inversely and directly proportional to these last two parameters. Other uncertainties are introduced by the crater shape, which is not precisely parabolic as we have assumed, and by the fraction of the area covered by the ejecta blanket,  $1 - F_c$ . It is difficult to assign error limits to most of the above factors, but we estimate, conservatively, that the limits on the calculated diffuse cross section are  $\times \div 3$ .

A study of the crater Tycho lends more weight to our results, but cannot be used for error estimates since the crater is very large and constitutes a statistical sample of one. Pollack (personal communication, 1971) has calculated the diffuse cross section of the crater interior to be  $0.4 \frac{\pi D^2}{4} \times \div 2$  whereas our calculations give  $0.5 \frac{\pi D^2}{4}$ . He used the observed depolarized enhancement along E-W swaths across the crater, allowing for the difference in the background near Tycho from the mean background. He also calculates that the interior of the crater is responsible for  $50 \pm 10\%$  of the total diffuse reflectance. This is further justification for our use of  $F_c = 0.5$  and lends additional weight to the choice of  $n_s = 1.6$ .

#### 4. The Wavelength Dependence

The observed diffuse cross section is about a factor of 2 higher at 3.8 cm than at 70 cm (Pettingill and Thompson, 1968), and approximately obeys a  $\lambda^{-0.3}$  law (Hagfors, 1967a). Equation 3.53 for the diffuse cross section displays no wavelength dependence, however. This is due to some of the approximations we have used. We expect the observed wavelength dependence to arise from three factors: the single scattering albedo, the refractive index of the rock relative to the dust and the fraction of the lunar surface covered by fresh craters.

The single scattering albedo, as we have calculated in section IX, is relatively constant between 3.8 and 70 cm. This is largely the result of the rock distribution we have chosen, and the position of the break point. There is evidence, however, from the depolarization ratio  $r_c$  shown in figure 3.10, section VIII, that  $\tilde{\omega}_0$  decreases from 0.88 to 0.83 as  $\lambda$  increases from 23 cm. to 68 cm. This implies (see figure 3.23) a decrease of a factor of 1.3 in the cross section, which is similar to the actual observations within the error bars. The decrease of  $\tilde{\omega}_0$  with  $\lambda$  is expected on the basis of measurements of Apollo 11 and 12 rock samples (Chung et al., 1970; Katsube and Collett, 1971). Their work implies that the loss tangent increases as  $\lambda$  increases, but approaches a constant value for  $\lambda$  near 1-10 cm. Thus we would not ex-

pect much change in  $\tilde{\omega}_0$  from 23 cm. to 3.8 cm. The constancy of the depolarization ratio at these wavelengths (Zisk, 1970) adds weight to this argument.

But a variation in  $\sigma$  is observed between 23 cm. and 3.8 cm. The second factor,  $n_r$ , becomes more important in this interval. We expect  $n_r$  to increase as  $\lambda$  decreases because a large fraction of the radiation will be returned in the upper meter of the dust where the density and refractive index of the dust can be expected to be smaller than at greater depths. Thus  $n_r$  increases as  $\lambda$  decreases. Fresnel's laws, along with the more complete Mie theory, predict that  $\sigma$  increases as  $n_r$  increases. This is shown in the single scattering phase function in figure 3.8, section III, and the cross section per unit area in figure 3.24. A factor of 1 - 2 in cross section is thus predicted, depending upon the refractive index of the rocks relative to vacuum.

The third factor in the wavelength dependence is the fraction of area covered by fresh craters. According to our derivation it is proportional to  $t^*/D_{0\lambda}$ . To a first approximation we took both  $t^*$  and  $D_{0\lambda}$  to be directly proportional to  $\lambda$ . The absorption length and hence  $t^*$  is known from terrestrial rocks to vary as between  $\lambda^{1.00}$  and  $\lambda^{1.15}$  (Thompson et al., 1970). The dependence of  $D_{0\lambda}$  on  $\lambda$ , however, is only speculative since Lunar Orbiter and Surveyor photographs

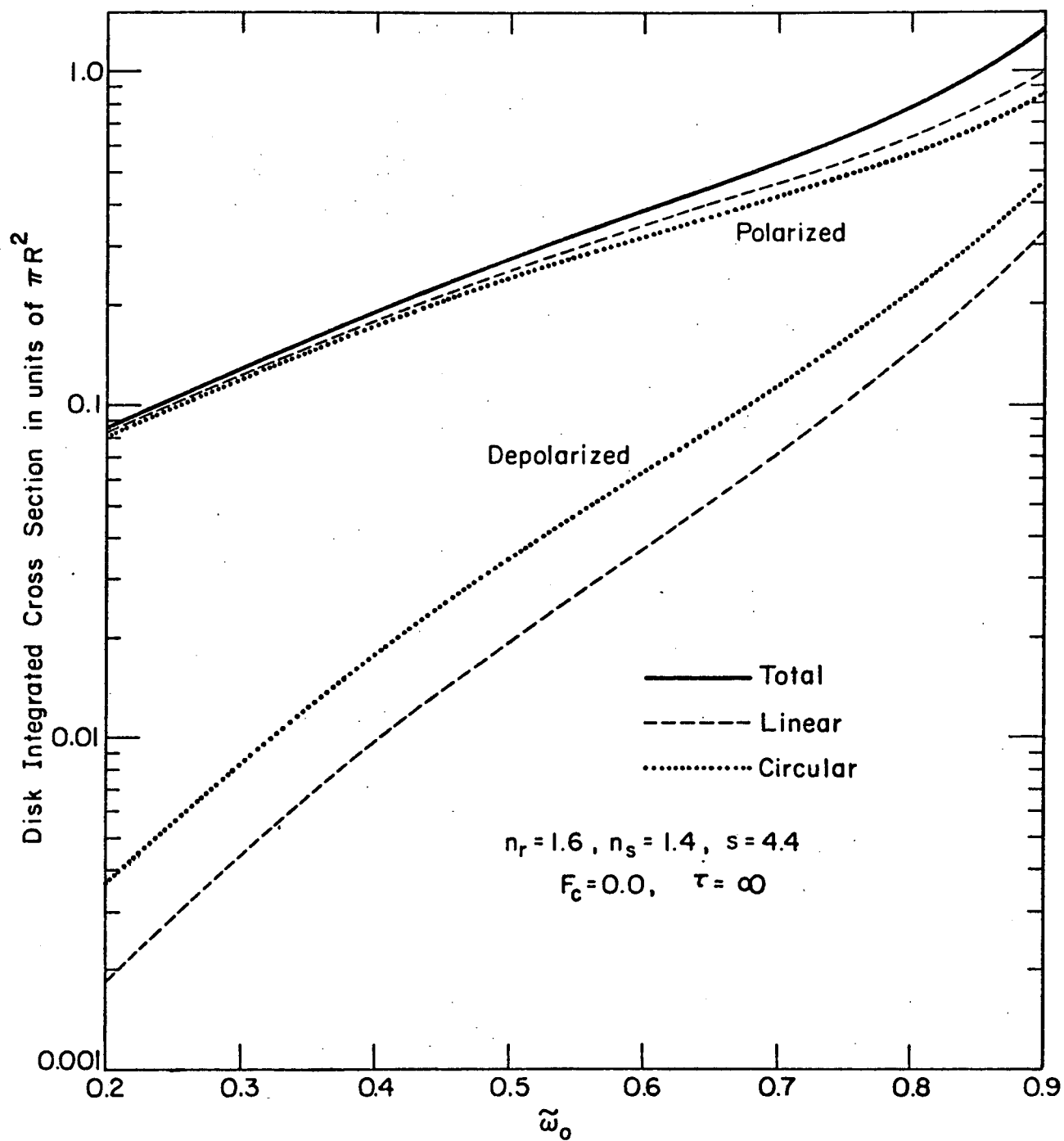


Figure 3.23 Disk integrated polarized and depolarized diffuse cross section as a function of  $\tilde{\omega}_0$ . The cross sections are calculated assuming the lunar surface is uniformly covered with an optically thick scattering layer.

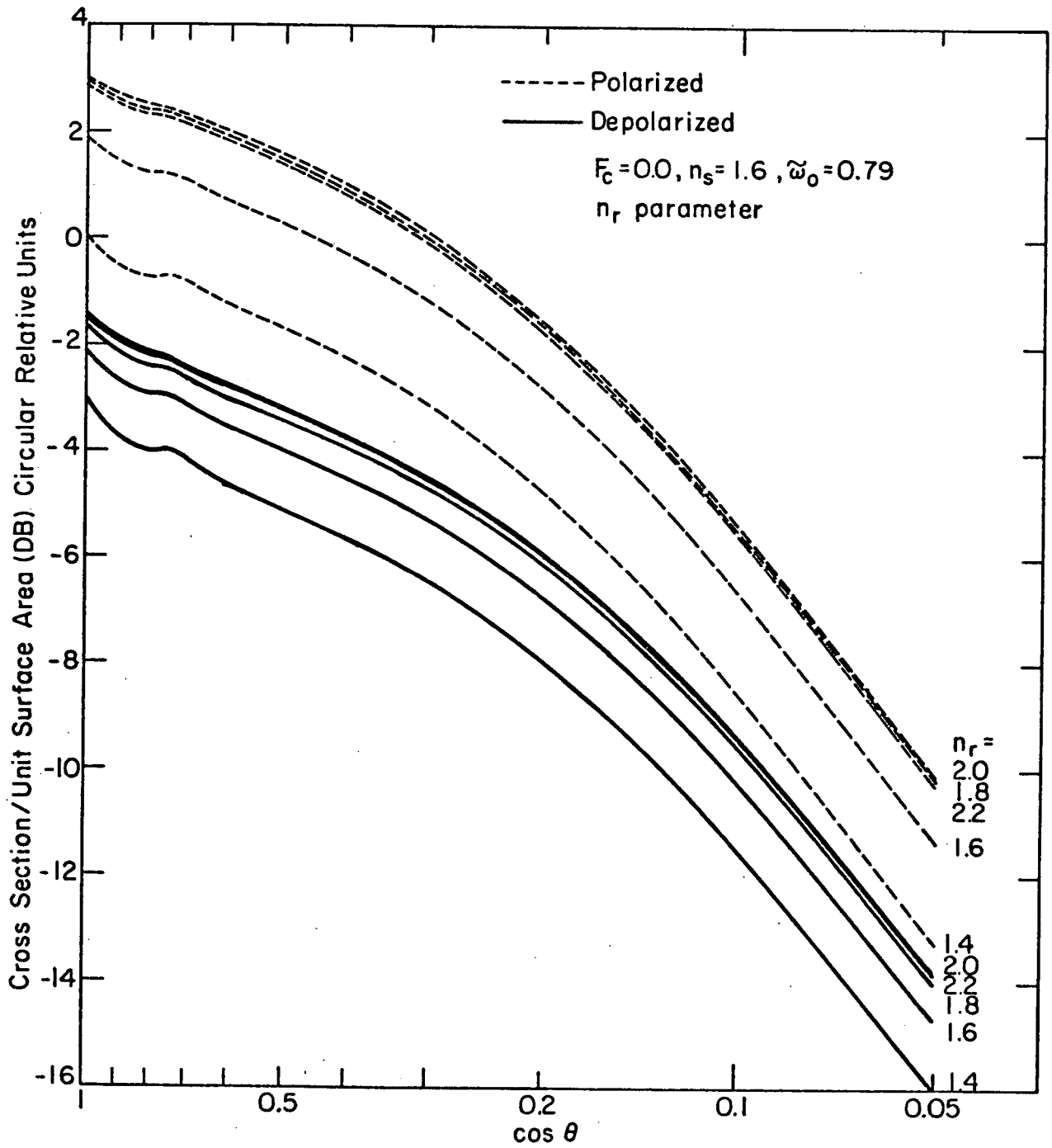


Figure 3.24 Diffuse cross section / unit surface area with the index of refraction of the rock relative to the dust,  $n_r$ , as a parameter. Compare with figure 3.8.

give little information on fresh craters in the rock size regime in which we are interested. There is evidence that the largest rock size produced in a cratering event is directly proportional to the size of the crater (J.B. Pollack, personal communication, 1971). This is the source of the assumed  $\lambda^{1.0}$  variation for  $D_{0\lambda}$ . Thus the fractional area covered by fresh craters has little effect on the wavelength dependence, although the exact effect is uncertain.

#### 5. Maria-Highland Differences and Implications for Future Radar Experiments

Highland regions are consistently observed to have a larger depolarized return than maria regions. Observations at 70 cm. wavelength (Thompson, 1968) reveal variations of from 2 to 5, and similar results have been obtained from a preliminary analysis of 3.8 cm. data (Zisk, 1970). The explanation for this phenomenon, within the context of our model, is probable differences in the single scattering albedo between the types of regions due to differences in mineralogy.

We suggest that the most important single parameter affecting maria-highland differences is the single scattering albedo,  $\tilde{\omega}_0$ . Figure 3.23 shows that a factor of 5 increase in the depolarized cross section results by changing  $\tilde{\omega}_0$  from 0.65 to 0.90. This range of  $\tilde{\omega}_0$  is within the range

calculated for the refractive index of Apollo 11 and 12 rock samples obtained from maria regions alone. (See table 3.2). Alternatively  $\tilde{\omega}_0$  may be varied over this range by changing the absorption length in the dust,  $\ell_a$ , by a factor of 3.5, since to a first approximation  $1-\tilde{\omega}_0$  is inversely proportional to  $\ell_a$ . This and larger variations in  $\ell_a$  are observed for different terrestrial rock powders (Campbell and Ulrichs, 1969).

The above hypothesis leads us to ask whether a systematic difference in  $\tilde{\omega}_0$  exists between highland and maria. At present there is no direct evidence. There is evidence, however, that there may be a systematic difference in the percentage of ilmenite between the two types of surface and that the ilmenite content is directly related to  $\tilde{\omega}_0$ . The Surveyor alpha scattering experiments have shown significantly less titanium at the Surveyor VII highland site than at the maria areas sampled. Measurements by Chung et al. (1970), and Katsube and Collett (1971) on returned lunar rocks reveal differences in the ilmenite ( $\text{FeO} \cdot \text{TiO}_2$ ) content from rock to rock. Their data for the complex index of refraction coupled with our calculations for  $\tilde{\omega}_0$  show a one to one correlation between ilmenite content and  $\tilde{\omega}_0$ , such that the less ilmenite the higher  $\tilde{\omega}_0$ . Table 3.2 of section IX displays the results of the computation. For example, a sim-

ulated lunar sample, with 4% ilmenite gives  $\tilde{\omega}_0 = 0.87$  while the lunar sample with similar mineralogy but 16% ilmenite gives  $\tilde{\omega}_0 = 0.52$ . Too much emphasis should not be placed on this, however, because the effects of crystalline structure and composition have not been well separated. The "average"  $\tilde{\omega}_0$  of ten lunar rocks measured is 0.62 while the average of the low ilmenite simulated lunar sample and an anorthosite proposed by Wood(1970) for the lunar highlands is 0.84. The data for anorthosite was taken from the paper by Campbell and Ulrichs (1969).

The possible correlation of  $\tilde{\omega}_0$  with the ilmenite or heavy metal abundance deserves further investigation. If it can be shown that there is significant correlation then maps of the depolarization ratio across the lunar surface could be interpreted, in light of our model, as mineralogical maps. Not only could general differences from maria to highland be interpreted this way, but fresh craters of the same morphology and apparent rock distribution could serve as localized probes of the mineralogy across the visible face of the moon. Thus radar could be used to map the moon geologically.



# REFERENCES - III

- A.A. Burns, J.G.R., 74, 6553 (1969)
- A.A. Burns, J.G.R., 75, 1467 (1970)
- D.B. Campbell, Radar Interferometric Observations of Venus, Thesis, Cornell Univ. (1971)
- M.J. Campbell and J. Ulrichs, J.G.R., 74, 5867 (1969)
- S. Chandrasekhar, Radiative Transfer, Dover Publications, Inc., New York (1960)
- D.H. Chung, W.B. Westphal, G. Simons, J.G.R., 75 (1970)
- N.C. Costes, W.D. Carrier, J.K. Mitchell and R.F. Scott, Science, 167, 739 (1970)
- J.D. Dave, Program # 360-D-174002, I.B.M. Programing Dept.
- B. Donn and R.S. Powell, in ICES Electromagnetic Scattering, ed. by M. Kerker, Pergamon Press (1963)
- J.V. Evans and T. Hagfors, J.G.R., 71, 4871 (1966)
- T. Gold, M.J. Campbell and B.T. O'Leary, Science, 167, 707 (1970)
- T. Gold, B.T. O'Leary and M.J. Campbell, in Proceedings of the Second Lunar Science Conference, 3, M.I.T. Press, 2173 (1971)
- J.M. Greenberg, R.T. Wang, and L. Bangs, Nature Phys. Sci., 230, 110 (1971)
- T. Hagfors, R.A. Brockelman, H.H. Danforth, L.B. Hanson, and G.M. Hyde, Science, 150, 1153 (1965)
- T. Hagfors, Radar Studies of the Moon, M.I.T. Lincoln Lab. Final Rep., 1, Lexington, Mass. (1967a)
- T. Hagfors, Radio Science, 2, 445 (1967b)
- J.R. Hodkinson, in ICES Electromagnetic Scattering, ed. by M. Kerker, Pergamon Press (1963)

H.C. van de Hulst and K. Grossman, in The Atmospheres of Venus and Mars, ed. by J.C. Brandt and M.B. McElroy, Gordon and Breach, (1968)

R.F. Jurgens, Radio Science, 5, 435 (1970)

T.J. Katsube and L.S. Collett, in Proceedings of the Second Lunar Science Conference, 3, M.I.T. Press, 2367 (1971)

J.L. Linsky, Icarus, 6, 606 (1966)

H.J. Moore, in Lunar Terrain and Traverse Data for Lunar Roving Vehicle Design Study, U.S. Geological Survey Preliminary Report (1969)

G.H. Pettengill and T.W. Thompson, Icarus, 8, 457 (1968)

W.L. Quaide and V.R. Oberbeck, J.G.R., 73, 5247 (1968)

A. Rosiwal, Verh. Kaiserliche Konigliche, Geol. Reichsanstalt, 143-175, Vienna (1898)

Surveyor Project Final Report, JPL Technical Report 32-1265 (1968)

T.W. Thompson, C.R.S.R. Research Report RS 73, Cornell University, (1968)

T.W. Thompson, J.B. Pollack, M.J. Campbell, and B.T. O'Leary, Radio Science, 5, 253 (1970)

J.A. Wood, J.S. Dickey Jr., U.B. Marvin and B.N. Powell, Geochim. Cosmochim. Acta, Suppl. 1, 34, 965 (1970)

J.A. Wood, to be published in Icarus, (1971)

S. Zisk, Radar Studies of the Moon, M.I.T. Lincoln Lab. Rep., Lexington, Mass. (1970)